

DESIGN AND OPTIMIZATION OF A SWITCHED RELUCTANCE MOTOR FOR A TWO-WHEELER AND THREE-WHEELER APPLICATION

Thesis

Submitted in the partial fulfillment of the requirements for the Degree
of

DOCTOR OF PHILOSOPHY

by

SANDESH BHAKTHA B



DEPARTMENT OF MECHANICAL ENGINEERING
NATIONAL INSTITUTE OF TECHNOLOGY KARNATAKA SURATHKAL
MANGALORE - 575 025
KARNATAKA, INDIA
October, 2024

**DESIGN AND OPTIMIZATION OF A
SWITCHED RELUCTANCE MOTOR FOR
A TWO-WHEELER AND THREE-
WHEELER APPLICATION**

Thesis

Submitted in the partial fulfillment of the requirements for the
Degree of

DOCTOR OF PHILOSOPHY

by

SANDESH BHAKTHA B

Under the guidance of

Dr. KV Gangadharan
Professor

Dr. Jeyaraj P
Professor



DEPARTMENT OF MECHANICAL ENGINEERING
NATIONAL INSTITUTE OF TECHNOLOGY KARNATAKA SURATHKAL
MANGALORE - 575 025
KARNATAKA, INDIA
October, 2024

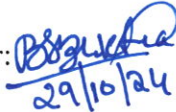
DECLARATION

I hereby declare that the research thesis entitled "**Design and Optimization of a Switched Reluctance Motor for a Two-wheeler and Three-wheeler Application**" which is being submitted to the **National Institute of Technology Karnataka, Surathkal** in partial fulfillment of the requirements for the award of the Degree of **Doctor of Philosophy** in the **Department of Mechanical Engineering** is a *bonafide report of the research work carried out by me*. The material contained in this research thesis has not been submitted to any University or Institution for the award of any degree.

Registration number: **187ME503**

Name of the Research Scholar: **Sandesh Bhaktha B**

Signature of the Research Scholar:


29/10/24

Department of Mechanical Engineering

CERTIFICATE

This is to certify that the research thesis entitled “**Design and Optimization of a Switched Reluctance Motor for a Two-wheeler and Three-wheeler Application**” submitted by **Mr. SANDESH BHAKTHA B** (Register No.187ME503) as the record of the research work carried out by him, is accepted as the Research Thesis submission in partial fulfillment of the requirements for the award of the degree of **Doctor of Philosophy**.

Research Guides

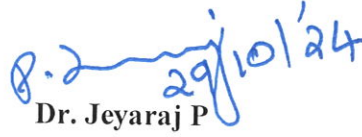


Dr. KV Gangadharan

Professor

Department of Mechanical Engineering

NITK, Surathkal



Dr. Jeyaraj P

Professor

Department of Mechanical Engineering

NITK, Surathkal



Chairman-DRPC

Date: 29/10/24



ACKNOWLEDGMENTS

“Courage isn’t having the strength to go on – it is going on when you don’t have strength.”

-Napoleon Bonaparte

Courage, relentless perseverance, and endless hope, I believe, have made my dream of a Doctorate a reality. It is also the culmination of the concerted efforts of many individuals who inspired, motivated, guided, and supported me at various junctures and for whom words’ would not suffice to express my gratitude.

With immense humility and respect, I express my sincere gratitude to my guide, **Prof. K V Gangadharan**. He always motivated me to work hard with his unforgettable remark “Let us find one reason to work rather than finding 101 reasons not to work”. He instilled confidence in me throughout with his reassuring words such as “It is okay even if the first prototype of the motor fails and it does not work.” Critical inputs coupled with words of inspiration boosted my morale when I was low. Sir, I remain indebted to all the knowledge you have shared and will always remain an inspiration in my life.

With deepest respect and regard, I would like to express my gratefulness to my co-guide **Prof. Jeyaraj P**. Sir’s help in meticulously planning my PhD helped me achieve all timelines. Sir’s valuable input in the technical aspects of the manuscript writing is cherished and his eye for detail is magnificent. I am grateful for all your support sir.

I am also grateful to the **Director**, National Institute of Technology Karnataka (NITK), Surathkal, and the **Head of the department**, Department of Mechanical Engineering, NITK for providing all the facilities required for carrying out my research.

I also express my sincere gratitude to the esteemed members of the RPAC, **Dr. Navin Karanth P.**, Associate Professor, Department of Mechanical Engineering, NITK, and **Dr. Yashwant Kashyap**, Assistant Professor, Department of Electrical and Electronics Engineering. The critical comments and valuable suggestions that were provided helped me to improve my thought process and elevate my work a step further.

I am sincerely grateful to **Prof. B Venkatesa Perumal**, Department of Electrical and Electronics Engineering for providing me with the test facilities and technical inputs and to **Dr. Pruthviraj U.**, Associate Professor, Department of Water Resource and Ocean Engineering for equipping me with the best test facilities.

I am truly obliged to **Mr. Srinivas Kudligi**, Chief Technical Officer, Aditya Avartan Technologies Private Limited, Bangalore for his valuable technical inputs regarding SRM design. I am also grateful to **Mr. Gautam Prabhu**, Assistant Manager, Aditya Avartan Technologies Private Limited for being a patient ear and having endless discussions and deliberations at each step of my PhD. I remain indebted to **Mr. Jagadish** and **Mr. Madhusoodhan**, Aditya Avartan Technologies Private Limited for their assistance in the design of the child parts of the SRM and their assembly respectively.

I am grateful to have wonderful seniors in the lab like **Dr. Praveen Shenoy**, **Dr. Susheel Kumar**, and **Dr. Kiran Katari** who motivated and held discussions with me. I am also grateful to **Dr. Sriharsha Hegde**, Associate Professor, Department of Aeronautical and Automobile Engineering, MIT Manipal for motivating me to pursue my doctorate under Prof. K V Gangadharan.

I would like to thank the funding support provided by the **Ministry of Heavy Industries, Government of India** under its project titled ‘Switched Reluctance Motor for 2W and 3W’ on the TPDM and FAME – India scheme [Grant no – F.No. 3(5)/2018-NAB-II(AUTO) (20331)]. I would also like to thank the **Centre for System Design (CSD): A Centre of Excellence** at NITK, Surathkal for providing the experimental facilities required for motor testing.

I would like to thank the wonderful M.Tech students **Mr. Satish Kumawat**, **Mrs. Aishwarya Pillai**, **Mr. Anil Jogi**, **Ms. Monika Sahu**, **Mr. Rahul Gupta**, **Mr. Satyam Sharma**, **Mr. Mukesh Kumar**, and **Mr. Arunlal** for their overall support in the execution of this project.

I would also like to thank the CSD members **Mr. Neil Jose**, **Mr. Akhilesh G**, **Mr. Rajat Kotekar**, **Mr. Sarath Kannan**, **Mr. Nagaraja Kamath**, and **Mr. Ashutosh Prabhu** for all the technical and non-technical assistance.

I would also like to thank **M/s Ashutosh Engineering Works**, Mangalore, and **Mr. Roopesh** in particular for his immense help during the manufacturing of fixtures for the motor.

Finally, and most importantly, I am thankful to my parents **Yashavanth Bhaktha** and **Bharathi Bhaktha** for their encouragement and support throughout my life and education. I am deeply indebted to my wife, **Dr. Apoorva Bhaktha**, for her unwavering emotional support and immense motivation during the challenging times I faced while carrying out my doctoral work. I would also like to thank my son **Shlok Bhaktha**. I also thank my sister **Sangeetha Bhaktha** for her moral support. I also would like to thank all my extended family members especially my in-laws for their moral support.

(SANDESH BHAKTHA B)

ABSTRACT

Among the available traction motors, switched reluctance motors (SRMs) are gaining a lot of attention as a potential choice to propel electric vehicles (EVs) since they are magnet-free, and mechanically robust with a longer constant power range. Although SRM has several benefits, high torque ripple causing abnormal noise and vibrations has proven to be a major hindrance to its wide-scale use. Moreover, SRMs possess a lower torque density as compared to other permanent magnet-based motors. A motor solution with a higher torque density is highly preferred for in-wheel (IW) EV applications due to limited space inside the wheel hub. The performance of an SRM is commonly assessed using a variety of electromagnetic performance metrics such as starting torque, torque density, efficiency, and torque ripple. The electromagnetic performance metrics are highly sensitive to the type of SRM topology, their design, and excitation control parameters. Any modification to these excitation control or design factors has a distinct effect on the performance metrics, with varying degrees of potential benefit and drawback. As a result, within the design and development framework of an SRM, numerous optimization techniques have been widely employed to optimize these design and excitation control parameters.

This thesis comprehensively investigates the sensitivity of the electromagnetic performance metrics with the dimensions of the geometric design variables for an SRM. The influence of the dimensions of the various geometric design variables such as rotor diameter, pole arc angles, and yoke thicknesses on the electromagnetic performance metrics such as average torque and torque ripple has been analyzed using static two-dimensional (2D) electromagnetic finite-element analysis (FEA). The reason for the change in static characteristics due to variation in reluctance between SRM designs has not been detailed so far in the literature. This is addressed in the present work by the magnetic equivalent circuit (MEC) model that simplifies the design analysis. Results indicate that stator pole reluctance needs to be given due importance while studying the influence of rotor diameter. Also, it is imperative to set an adequate thickness of the stator and rotor yokes to minimize the effect of saturation on the performance. Rotor diameter and stator pole arc angle have a pronounced influence on the average torque and torque ripple while the influence of rotor pole arc angle and yoke thicknesses was relatively less.

Further, previously published research articles on SRM optimization intended to be used for EV applications have mostly focused on the optimization of their design and control variables only at the rated conditions. In EV applications, the load operating points (LOPs) of a traction motor are dynamic and spread widely across the torque speed envelope. To enhance their overall performance, it is vital to include them in the design optimization process. Therefore, in this thesis, a novel procedure for implementing the multi-objective design optimization (MODO) of an SRM based on a driving cycle has been demonstrated for an Electric rickshaw (E-rickshaw) application. Higher starting torque, and torque density with reduced electromagnetic losses throughout the driving cycle are established as the design objectives, subject to practical restrictions on current density and slot fill factor. The design objectives have been accurately evaluated through transient finite element analysis (FEA) and a computationally efficient SRM drive model (developed in MATLAB/Simulink) with consideration of the excitation control parameters. Kriging models have been constructed to reduce the computation cost of FEA during the optimization process. Then, a nondominated sorting genetic algorithm II (NSGA II) based multi-objective optimization coupled with the constructed Kriging models is conducted to generate a Pareto-optimal set. An optimal design that offers the best balance between the design objectives is selected from the Pareto-optimal set and the dimensions of corresponding design variables are used to build a prototype. Finally, the static and dynamic performance of the SRM prototype are experimentally evaluated and validated with the FEA simulations.

Working conditions and design restrictions are more challenging for IW motors (typically used in electric two-wheeler applications) since a reducer is not utilized. Among the available SRM topologies, Multi-teeth (MT) SRM topology is a promising candidate for IW applications since it retains the inherent simplicity and cost-effectiveness offered by traditional SRM designs. However, the design of IW-MTSRM topologies and their electromagnetic performance have not been explored sufficiently. In this thesis, a design formula governing the selection of the number of MT and rotor poles for MTSRMs has been proposed. Using this, a novel four-phase 8/18 IW-MTSRM is derived. The characteristics of the 8/18 IW-MTSRM SRM are numerically compared with a conventional 8/10 SRM based on magnetic characteristics,

efficiencies, and steady-state operation for the complete torque-speed range for an electric scooter (E-scooter) application. Results indicate that the 8/18 MTSRM has a higher peak torque capacity, torque density, superior drive cycle efficiency, and reduced torque ripple.

Keywords: Electric vehicles (EVs), Switched reluctance motor (SRM), Finite element analysis (FEA), driving cycle-based design optimization, Multi-teeth (MT) topology, prototype machine, Electromagnetic performance metrics

Contents

ACKNOWLEDGMENTS	i
ABSTRACT	v
LIST OF FIGURES	xi
LIST OF TABLES	xv
ACRONYMS	xvii
NOMENCLATURE	xix
Chapter 1 INTRODUCTION	1
1.1 Need for an alternative means to power vehicles in India	1
1.2 Electric vehicles	2
1.3 Typical characteristics of an electric traction motor and their types and comparison	5
1.4 Fundamentals of Switched Reluctance Motor	7
1.5 Classification of SRMs	22
1.6 Outline of the thesis	23
Chapter 2 LITERATURE SURVEY	25
2.1 Introduction	25
2.2 Influence of the design and excitation control parameters on the SRM's electromagnetic performance metrics	26
2.3 Different Electromagnetic Analysis Techniques for SRMs	35
2.4 Employment of SRMs for EV applications	38
2.5 Implementation of optimization techniques to optimize the dimensions of the geometric design variables to enhance the overall performance of SRMs.	41
2.6 Topological characterization of In-wheel (IW) SRMs for E-2Ws	46
2.7 Summary of Literature Survey	49
2.8 Motivation and Scope of the Present Work	53
Chapter 3 INFLUENCE OF GEOMETRICAL DESIGN VARIABLES ON SRM PERFORMANCE	55
3.1 Introduction	55
3.2 Theoretical background	56
3.3 Methodology	59
3.4 Results and Discussions	66
3.5 Summary	74
Chapter 4 DRIVING CYCLE-BASED DESIGN OPTIMIZATION OF AN SRM	77
4.1 Introduction	77
4.2 Investigated EV application and estimation of motor specifications	78

4.3 Implementation of the <i>k</i> -means algorithm to determine the representative points (RPs)	83
4.4 SRM initial design	87
4.5 Multi-objective design optimization (MODO)	90
4.6 Prototyping	107
4.7 Experimental validation	111
4.8 Summary	119
Chapter 5 COMPARATIVE ASSESSMENT OF AN 8/18 MULTI-TEETH WITH CONVENTIONAL 8/10 IN-WHEEL SRM FOR AN E-SCOOTER	121
5.1 Introduction	121
5.2 Theoretical Background	122
5.3 Investigated EV application and estimation of motor specifications	124
5.4 Electromagnetics design process of the two configurations	128
5.5 Results and Discussions	138
5.6 Thermal analysis	148
5.7 Summary	150
Chapter 6 SUMMARY AND CONCLUSIONS	151
6.1 Summary	151
6.2 Conclusions	152
6.3 Scope for Future Work	154
References	157
List of Publications based on Research work	169
Appendixes	171

LIST OF FIGURES

Figure 1.1 Power train arrangement of an (a) ICE-driven vehicle (b) Electric motor-driven vehicle.....	3
Figure 1.2 (a) Total EV sales in India (b) Category-wise sales of EVs in India (SMEV 2023)	4
Figure 1.3 Price variation of rare-earth materials like dysprosium oxide and Neodymium oxide over the years (Statistica 2023).....	6
Figure 1.4 Structure of an SRM and its components	8
Figure 1.5 Torque production in an SRM.....	8
Figure 1.6 Components of an SRM drive	9
Figure 1.7 Axis positions in a rotor of an SRM.....	10
Figure 1.8 Phase inductance and the corresponding torque variation for a constant phase current	10
Figure 1.9 Positions of the rotor poles 1 and 4 (a) at the beginning of overlap with stator poles A1 and A2 (b) overlapped with A1 and A2 (c) leaving the overlap region of A1 and A2 (d) completely leaving the overlap with A1 and A2.....	11
Figure 1.10 Idealized phase inductances, phase currents, and the total torque profile of the SRM.....	13
Figure 1.11 An SRM's single-phase equivalent circuit.....	14
Figure 1.12 Magnetic field energy and co-energy storage with respect to current.....	17
Figure 1.13 (a) Phase inductance linear variation (b) Ideal phase current waveform (c) Hysteresis current control method (d) Chopped phase voltage (e) Variation of flux linkage corresponding to HCC method.	19
Figure 1.14 (a) Linear variation of phase inductance (b) Phase current profile corresponding to SPC (c) Phase voltage profile corresponding to SPC (d) Variation of flux linkage corresponding to SPC.	20
Figure 1.15 Four-phase SRM drive	21
Figure 1.16 Hard chopping (a) Both Q1 and Q2 are ON (b) Both Q1 and Q2 are OFF.....	22
Figure 1.17 Soft chopping (a) Both Q1 and Q2 are ON (b) Q1 is OFF and Q2 is ON.....	22
Figure 1.18 Classification of SRMs (a) Internal rotor type SRM (b) External rotor type SRM	23
Figure 2.1 Geometric design variables of the four-phase 8/6 SRM.....	32
Figure 3.1 Outline of the procedure to study the influence of geometrical design variables on the electromagnetic performance metrics of an SRM.....	56
Figure 3.2 Flux linkage vs current characteristics	57

Figure 3.3 (a) Flux path (b) MEC for the flux path	58
Figure 3.4 B-H curve of M270_35A (Cogent, 2023).....	59
Figure 3.5 Geometric design variables of an 8/6 SRM.....	60
Figure 3.6 (a) FEA model of the SRM (b) Mesh quality in the airgap region.....	63
Figure 3.7 (a) Flux density plot (b) Flux paths at the aligned position	64
Figure 3.8 Flux paths at the unaligned position (a) 1-5, (b) 6-7	65
Figure 3.9 Influence of change in D_r ; (a) Static torque profile, (b) and (c) Co-energy comparison between 80 and 88 mm designs (d) and (e) Flux density comparison (f) Average torque and torque ripple	68
Figure 3.10 Influence of change in β_s ; (a) Static torque profile, (b) and (c) Co-energy comparison between 18 and 23° designs (d) and (e) Flux paths at 8° rotor position (f) Average torque and torque ripple	70
Figure 3.11 Influence of change in β_r ; (a) Static torque profile, (b) and (c) Co-energy comparison between 22.5 and 27° designs (d) and (e) Flux paths at 5° rotor position (f) Average torque and torque ripple.....	71
Figure 3.12 Influence of change in b_{sy} ; (a) Static torque profile, (b) and (c) Co-energy comparison between 11 and 17 mm designs (d) and (e) Flux density comparison, (f) Average torque and torque ripple	72
Figure 3.13 Influence of change in b_{ry} ; (a) Static torque profile, (b) and (c) Co-energy comparison between 9 and 19 mm designs (d) and (e) Flux density comparison (f) Average torque and torque ripple	74
Figure 4.1 Outline of the MODO of an SRM based on a driving cycle.....	78
Figure 4.2 Forces acting on an E-rickshaw.....	80
Figure 4.3 (a) CSIR-IIP driving cycle speed profile (Pathak et al. 2017) (b) Operating points of the E-rickshaw obtained from CSIR-IIR driving cycle	82
Figure 4.4 Determination of representative points (RPs) using k-means algorithm.....	85
Figure 4.5 Selection of the appropriate number of clusters (a) Elbow approach (b) Silhouette analysis.....	86
Figure 4.6 Design variables of the four-phase 8/6 SRM.....	88
Figure 4.7 Influence of the number of turns per phase on the (a) Static torque and (b) Dynamic torque.....	90
Figure 4.8 Flowchart of the Multi-objective design optimization (MODO).....	91
Figure 4.9 Flowchart indicating the calculation of the performance metrics of the design candidates.....	94

Figure 4.10 Pareto-optimal set obtained from NSGA II	99
Figure 4.11 Pearson's correlation coefficient of the design variables	101
Figure 4.12 Comparison of dynamic torque waveforms obtained from FEA and SRM drive model at RP4.....	103
Figure 4.13 (a) Optimized Turn-ON angles LUT (b) Optimized Turn-OFF angles LUT	104
Figure 4.14 Torque-speed characteristics of the design D2.....	105
Figure 4.15 Motor efficiency map	106
Figure 4.16 Flux density map of the optimized design at the base point.....	106
Figure 4.17 Drawings for fabrication (a) Stator and (b) Rotor core	108
Figure 4.18 Exploded view of SRM components.....	109
Figure 4.19 Views of the assembled SRM model (a) Isometric view (front) (b) Right side view (c) Isometric view (Rear)	109
Figure 4.20 (a) Stator core with the phase windings (b) Rotor assembly (c) Basic components of the motor assembly (d) IR sensor array with target plate (e) Prototype SRM mounted on the fixture (top view)	111
Figure 4.21 (a) Schematic and (b) Photograph of the experimental setup for determining the static performance of the SRM prototype.....	113
Figure 4.22 Measured phase current and voltage at (a) Unaligned (b) Partially aligned position and (c) Comparison between FEA and measured flux linkages.	114
Figure 4.23 (a) Experimental setup for determining the dynamic performance of the SRM prototype (b) AHB inverter controlled by WAVECT controller.....	116
Figure 4.24 Closed loop hysteresis current control (HCC) block diagram.....	116
Figure 4.25 Experimental phase current and voltage waveforms at RP1 ($I_{ref} = 23$ A, $\theta_{ON} = 54$ elec. deg. and $\theta_{OFF} = 144$ elec. deg.).....	117
Figure 4.26 Experimental phase current comparison with transient FEA at RP1.....	118
Figure 4.27 Average torque comparison between experiments and FEA at the 4 RPs.....	118
Figure 4.28 Experimental phase current waveforms at (a) RP1 (b) RP2 (c) RP3 (d) RP4....	119
Figure 5.1 Outline of the procedure to carry out the comparative assessment of 8/18 MT with conventional 8/10 SRM	122
Figure 5.2 Flux path comparison of SRM configurations with (a) $n = 1$ (Conventional SRM) (b) $n = 2$ (MTSRM)	124
Figure 5.3 (a) Forces acting on an E-Scooter (b) WMTC driving cycle speed profile (Steven 2002) (c) Torque-speed envelope and load operating points of the E-scooter obtained from the vehicle dynamics equations.	126
Figure 5.4 SRM design methodology	129

Figure 5.5 B-H curve of M270_35A (Cogent 2023).....	130
Figure 5.6 Initial design of (a) 8/18 MT (n = 2) and (b) 8/10 (n = 1) SRM configurations...	131
Figure 5.7 Influence of the number of turns per phase on the (a) Static torque and (b) Dynamic torque of the 8/18 MTSRM.....	133
Figure 5.8 Flowchart of the MODO.....	134
Figure 5.9 Convergence characteristic of the PSO	136
Figure 5.10 LUTs of optimized (a) θ_{on} (b) θ_{off} of the 8/18 MTSRM	137
Figure 5.11 Static torque of the 8/18 and 8/10 SRM at varied currents (a) $i = 20$ A (b) $i = 60$ A (c) $i = 100$ A (d) $i = 140$ A.....	139
Figure 5.12 Flux linkage curves of the 8/18 MT and 8/10 SRM	140
Figure 5.13 Average static torque of the 8/18 MT and 8/10 SRMs.....	140
Figure 5.14 The flux density of the 8/18 MT and 8/10 SRM at the midway position at (a) 20 A and (b) 140 A	142
Figure 5.15 Comparison of efficiency maps (a) 8/18 MTSRM and (b) 8/10 SRM	144
Figure 5.16 Comparison of copper loss maps (a) 8/18 MTSRM and (b) 8/10 SRM	144
Figure 5.17 Comparison of Iron loss maps (a) 8/18 MTSRM and (b) 8/10 SRM	144
Figure 5.18 Comparison of RMS current maps (a) 8/18 MTSRM and (b) 8/10 SRM	144
Figure 5.19 Torque and current waveforms operating on CCC at 200 rpm.....	146
Figure 5.20 Torque and current waveforms operating on SPC at 600 rpm	147
Figure 5.21 2D FEA thermal model of the 8/18 MTSRM.....	149
Figure 5.22 Temperature rise of the windings for peak torque condition at 200 rpm.....	149
Figure 5.23 Temperature distribution of the 8/18 MTSRM after five minutes of running at 200 rpm	150

LIST OF TABLES

Table 1.1 Evaluation of BLDC and SRM for EV applications (Bilgin et al. 2015) (Zeraoulia et al. 2006).	7
Table 2.1 Notations of the design variables and their description	32
Table 3.1 Description of Reluctance.....	58
Table 3.2 Description of the geometric design variables.....	60
Table 3.3 Predetermined design entities	61
Table 3.4 Mesh details	63
Table 3.5 Inductance (mH) comparison.....	67
Table 3.6 Reluctance variation with the change in D_r	68
Table 3.7 Reluctance variation with the change in β_s	70
Table 3.8 Reluctance variation with the change in β_r	71
Table 3.9 Reluctance variation with the change in b_{sy}	73
Table 3.10 Reluctance variation with the change in b_{ry}	74
Table 4.1 Performance comparison between commercial E-rickshaw BLDC motors and the prototype machine.....	79
Table 4.2 Parameters of the E-rickshaw (RetroEV 2023) (Sreejith and Rajagopal 2017).....	80
Table 4.3 Target performance specifications and design restrictions for the SRM	83
Table 4.4 Representative points (RPs) and Energy weights	86
Table 4.5 Initial SRM dimensions	88
Table 4.6 Design variables and their ranges for optimization	92
Table 4.7 NSGA II Optimization model parameters	99
Table 4.8 Design variables and Performance metrics of the initial and the optimized designs	100
Table 4.9 Excitation control parameters and the average output torque of the optimal design D2 at the RPs	102
Table 4.10 Comparison between FEM and Kriging model results.....	107
Table 4.11 Different parts of the motor assembly, their purpose, material used, and manufacturing process employed.	110
Table 5.1 Comparison between the specifications of the commercially available IW-BLDC motors and the proposed IW-SRM considered in the present work	125
Table 5.2 Parameters of the E-scooter (Andrada et al. 2016)	126
Table 5.3 Design and electrical constraints for the SRM	127
Table 5.4 Optimization limits of the design for the 8/18 MTSRM.....	134

Table 5.5 Parameters of the two optimized SRMs.....	138
Table 5.6 Comparison of steady-state performance of two SRM topologies	147
Table 5.7 Material properties of the different components (ALTAIR 2023).....	149

ACRONYMS

AHB	Asymmetric Half-Bridge
BEM	Boundary Element Method
BLDC	Brushless DC
CCC	Current chopping control
CSIR-IIP	Council of Scientific and Industrial Research - Indian Institute of Petroleum
DAQ	Data acquisition
E-bicycle	Electric bicycle
E-rickshaw	Electric rickshaw
E-scooter	Electric scooter
E-2W	Electric two-wheeler
E-3W	Electric three-wheeler
ECU	Electric Control Unit
EV	Electric Vehicle
FEA	Finite Element Analysis
FDM	Finite Difference Method
FEM	Finite Element Method
GA	Genetic Algorithm
GHG	Greenhouse Gas
GoI	Government of India
HCC	Hysteresis Current Control
HSRM	Hybrid Switched Reluctance Motor
ICCT	International Council on Clean Transportation
IM	Induction Motor
IPCC	Intergovernmental Panel on Climate Change
IW	In-Wheel
LHD	Latin Hypercube Design
LOP	Load Operating Point

LUT	Look Up Table
MEC	Magnetic Equivalent Circuit
MMF	Magnetomotive force
MODO	Multi-Objective Design Optimization
MTSRM	Multi-teeth Switched Reluctance Motor
NEDC	New European Driving cycle
NSGA II	Nondominated Sorting Genetic Algorithm II
OR	Outer rotor
PE	Power electronic
PM	Permanent Magnet
PMM	Permanent Magnet Machine
PMSM	Permanent Magnet Synchronous Motor
PSO	Particle swarm optimization
RP	Representative Point
SEM	Stochastic Evolutionary Method
SMEV	Society of Manufacturers of Electric Vehicles
SOO	Single objective optimization
SPC	Single pulse control
SRM	Switched Reluctance Motor
SRSRM	Segmented Rotor Switched Reluctance Motor
WMTC	World harmonized motorcycle test cycle

NOMENCLATURE

A	Area of the cross-section of the flux path	mm^2
A_f	The frontal area of the vehicle	m^2
A_z	Magnetic vector potential	Wb/m
a	Vehicle acceleration	m/s^2
B_{sp}	Elementary value of flux density at the stator pole	T
b_{sy} and b_{ry}	Stator and rotor yoke thicknesses	mm
C_d	Drag coefficient	-
D	Stator bore Diameter	mm
D_{or}	Rotor outer diameter	mm
D_r	Rotor diameter	mm
D_s	Stator outer diameter	mm
D_{sh}	Diameter of the shaft	mm
F_1	Applied MMF	AT
F_c	Calculated MMF	AT
F_g	Climbing force	N
F_j	Inertia force	N
F_{rr}	Rolling force	N
F_t	Traction force	N
F_w	Drag force	N
f_r	Rolling resistance coefficient	-
g	Acceleration due to gravity	m/s^2
H	Magnetic field intensity	A/m
h_s and h_r	Stator and rotor pole height	mm
h_{s1}	Slot depth in the stator pole	mm
I_{ref}	Reference current	A
I_{rms}	RMS value of phase current	A
$I_{\text{rms_limit}}$	Maximum RMS phase current	A
i_{peak}	Peak phase current	A
i	Instantaneous phase current	A
J_c	Current density	A/mm^2

j	Operating point	-
L	Stack length	mm
$L(\theta)$	Phase inductance with respect to rotor position	mH
l	Length of the magnetic path	mm
l_g	Air-gap length	mm
$Loss_{Cu}$	Copper loss	W
m	The total mass of the vehicle	kg
N	Number of turns per phase	-
N_m	Total number of multi-tooth	-
N_{ph}	Number of phases	-
N_s and N_r	Number of stator and rotor poles respectively	-
n	Number of multi-teeth per stator pole	-
P_{Cu}	Copper loss	W
$P_{ironcoreloss}$	Ironcore loss	W
P_{loss}	Total loss	W
$P_{loss,j}$	Total loss at the operating point j	W
P_w	Weighted power loss	-
R	Magnetic reluctance	AT/Wb
R_{eq}	Equivalent reluctance	AT/Wb
R_g	Reluctance of the airgap	AT/Wb
R_{ph}	Phase resistance	Ω
R_{rp}	Reluctance of the rotor pole	AT/Wb
R_{ry}	Reluctance of the rotor yoke	AT/Wb
R_{sp}	Reluctance of the stator pole	AT/Wb
R_{sy}	Reluctance of the stator yoke	AT/Wb
sf	Slot fill factor	-
$T_{average}$	Static average torque	Nm
T_{avg}	Average torque calculated from the dynamic torque waveform	Nm
T_e	Instantaneous torque	Nm
T_m	Torque density	Nm/kg

T_{\max}	Maximum value of torque for the best 15 degrees in the static torque waveform	Nm
T_{\min}	Minimum value of torque for the best 15 degrees in the static torque waveform	Nm
T_{rip}	Torque ripple calculated from static simulation	-
T_{ripple}	Torque ripple calculated from the dynamic torque waveform	-
W_{rp}	Width of the rotor pole	mm
W_{sp}	Width of the stator pole	mm
α	Gradient of the road	°
β_s and β_r	Stator and rotor pole arc angle	°
γ	Magnetic reluctivity	H ⁻¹
δ	Smallest angle of the triangular surface element	°
∂W	Magnetic co-energy	J
∂W_m	Total magnetic co-energy	J
ΔF	Error in MMF	AT
ε	Stroke angle	°
η	Efficiency	-
η_{cycle}	Drive cycle efficiency	-
θ	Rotor position	°
$\theta_1, \theta_2, \theta_3, \theta_4$	Angular positions of the rotor	°
θ_{on}	Turn-on angle	°
θ_{off}	Turn-off angle	°
θ_{sp}	Stator pole pitch	-
μ_0	Permeability of free space	H/m
μ_r	Permeability of the magnetic material	H/m
v	Velocity of the vehicle	km/h
ρ	Density of air	kg/m ³
ϕ	Flux	Wb
ψ	Flux linkage	Wb
ω	The angular speed of the rotor	rad/s

Chapter 1 INTRODUCTION

1.1 Need for an alternative means to power vehicles in India

The air quality of the megacities in India has deteriorated immensely in recent times owing to a tremendous increase in the number of vehicles (Bhandarkar 2010). Major pollutants emitted from the tailpipe of a vehicle driven by an internal combustion engine (ICE) comprise carbon monoxide, nitrogen oxides, carbon dioxide, sulfur dioxide, hydrocarbons, and particulate matter (Sharma et al. 2020). The severity of these emissions is dependent on the vehicle type and its maintenance routine. The World Quality Report states that New Delhi, India, is the most polluted capital city in the world. Moreover, India accounts for six of the ten most populous cities worldwide (Broom 2020). Owing to a higher vehicle density in these cities, vehicular emissions are known to be a major source (62-85%) of the depreciated air quality. This has a negative impact on both the environment and human health. Inferior air quality is known to cause respiratory and cardiovascular disorders (Cohen et al. 2013). Further, as per the International Council on Clean Transportation (ICCT), annually, many people die in India due to the ill effects caused by air pollution (Miller et al. 2019).

Further, carbon dioxide (CO₂, a greenhouse gas) released from vehicles based on fossil fuel is also one of the major reasons for climate change. As per climate scientists, it is required to bring down the levels of greenhouse gas (GHG) emissions by 72% of 2010 by 2050 to restrict the rise of temperature globally to 2°C only. India is ranked in 3rd place in terms of GHG emission load (Intergovernmental Panel on Climate Change 2014). In the 2015 Paris Climate Change Agreement, India agreed to a 33–35% curtailment in greenhouse gas emissions.

The uncertainty surrounding the oil supply and its future availability are the main challenges of today. It is well known that oil fields are majorly situated in Middle Eastern countries, USA, Russia, and China. With India being one of the rapidly growing economies in the world, it is evident that India must depend on the import of crude oil. From India's perspective, days ahead are going to be challenging considering that the oil production in India is low and there are fewer non-renewable fuel sources. India is susceptible to a global oil supply crisis in the setting of political turmoil given the

enormous requirement for crude oil (Babajide 2018). In India, only 25% of the oil needs can be met by domestic production; the rest 75% ought to be imported. Also, the global crude oil prices are rising at an enormous pace. Roughly 1.642 trillion barrels of oil are available globally, according to a January 2014 estimation. Given that 90.5 million barrels of oil are consumed per day, the Earth can only sustain itself for 50 years on its current reserves (Oamen F. 2018).

Considering these adverse effects of air pollution caused by vehicles, GHG emissions leading to global warming and climate change, dependency of India on crude oil from other countries, and a limited reserve of fossil fuel, exploring alternative means to power the vehicles as compared to the conventional ICEs is deemed essential.

1.2 Electric vehicles

Using Electric vehicles (EVs) can eliminate the tailpipe emissions and the import of oil. EVs as compared to conventional vehicles have no tailpipe emissions. A comparison between ICE-powered vehicles and electric vehicles can be drawn by assessing their powertrain layout (Ehsani et al. 2018). A conventional ICE-based powertrain with a front engine and rear wheel drive is shown in Figure 1.1a. It can be noticed that the engine (prime mover) is situated at the front and the mechanical output power produced by it is transmitted to the rear wheel of the vehicle through the clutch, gearbox, propeller shaft, and differential gear respectively. Figure 1.1b depicts the layout of a conventional EV powertrain which primarily comprises an electric motor, power converter, inverter, battery, battery management system, and electric control unit (ECU). In comparison to the ICE power train, the ICE is replaced by an electric motor, that is used to propel the vehicle. The ECU governs the motor. The ECU receives signals through the operator via the accelerator and brake pedals etc. Further, feedback signals from the sensors which consist of information pertaining to the vehicle speed and the acceleration are also fed into the ECU. Based on this information, the power requirement is computed, and the demanded power is regulated amid the electric motor and the battery respectively through a power converter.

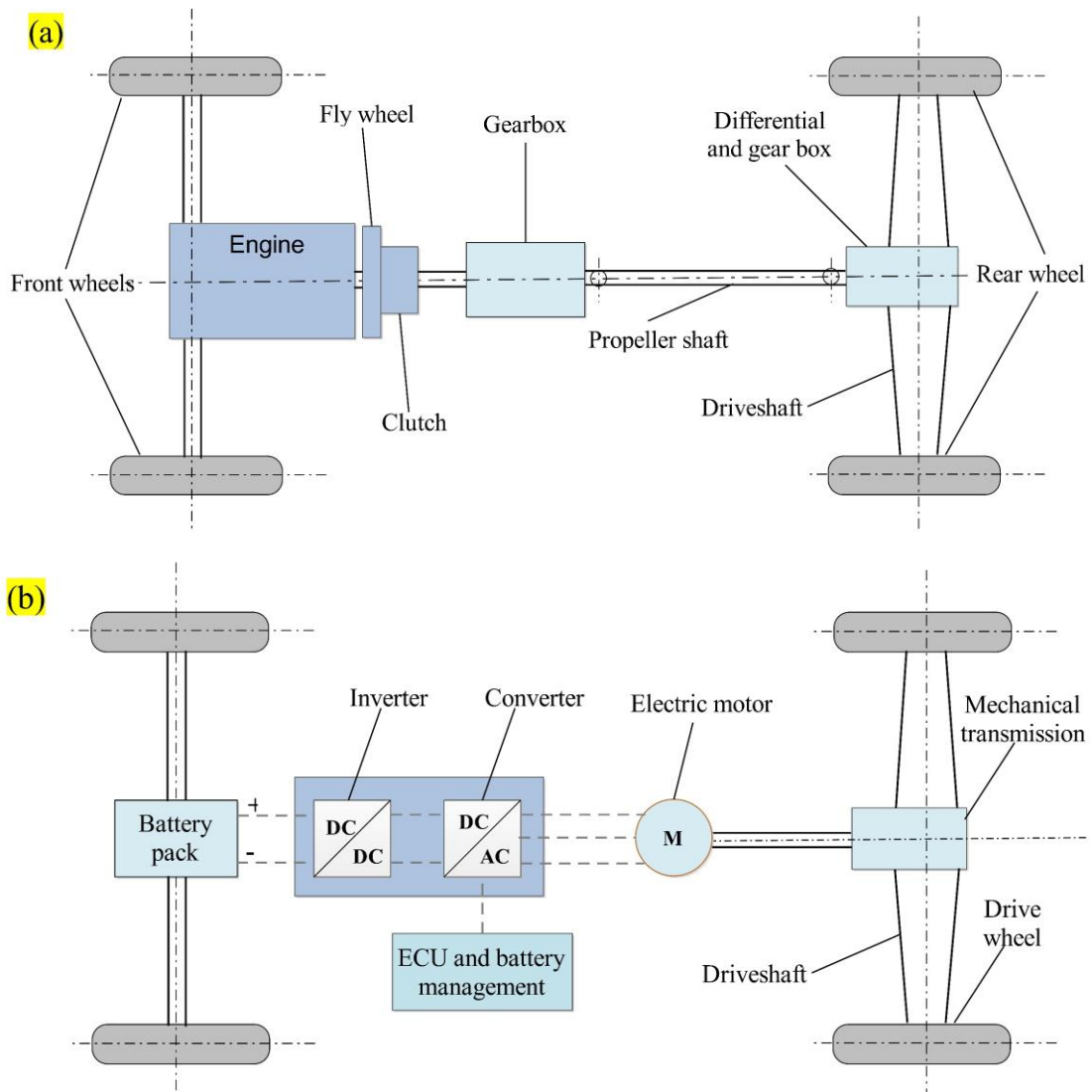


Figure 1.1 Power train arrangement of an (a) ICE-driven vehicle (b) Electric motor-driven vehicle

EVs possess higher efficiency, thereby resulting in a lower requirement of energy. EVs have a faster response time, require less maintenance, and generate less noise than conventional vehicles. Moreover, their torque-speed characteristics very well match the typical traction requirements of a vehicle (Ehsani et al. 2018). Owing to these advantages, EVs can be a potential alternative to conventional ICE-powered vehicles in the future. In light of this, the Government of India (GoI) has chalked out and implemented various vehicle electrification schemes (Singh et al. 2021). Due to the impetus provided for this process, a surge in domestic EV sales has been noted recently (Figure 1.2a) (SMEV 2023). The chart displays the sales data for EVs in India for each of the financial years (FYs). The vehicle category-wise sales are provided in Figure

1.2b. It can be inferred that electric two-wheelers (E-2Ws) and three-wheelers (E-3Ws) constitute the clear majority of the total domestic EV sales.

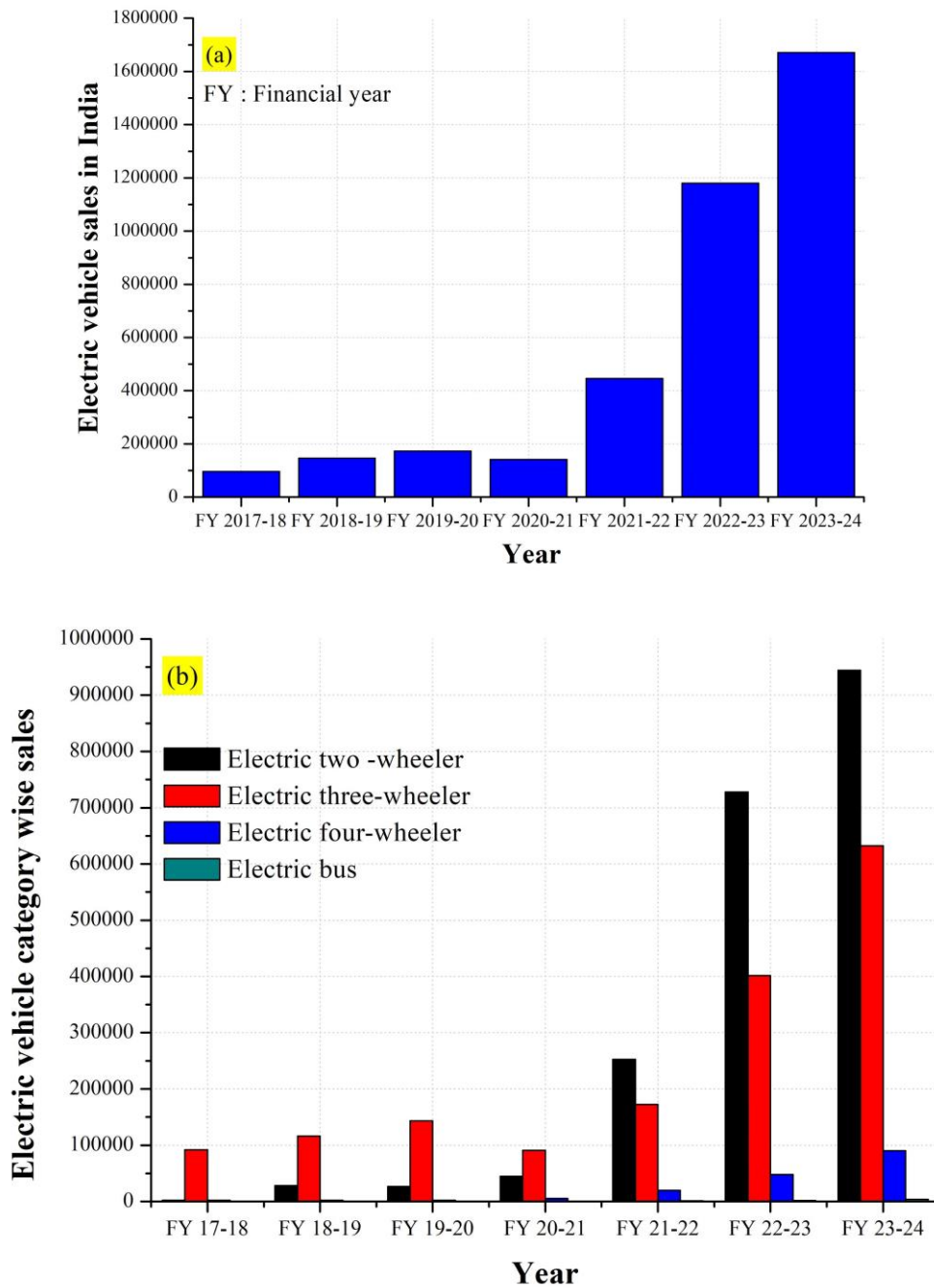


Figure 1.2 (a) Total EV sales in India (b) Category-wise sales of EVs in India (SMEV 2023)

1.3 Typical characteristics of an electric traction motor and their types and comparison

An electric motor used to propel an EV should possess the following features (Bilgin et al. 2015) (Ehsani et al. 1997):

- a) A high torque at lower operating speeds for starting, obstacle negotiation, and hill climbing. The electric motor must deliver a high starting torque to ensure that the operating points with higher torque duty cycles at lower speeds are achieved. The motor's capacity to produce torque in these circumstances is also known as its overload capability or the peak torque capacity.
- b) A high torque density to ensure that the motor's average torque output rises without increasing its overall mass. Any increase in motor mass adds to the overall mass of the EV which affects their energy consumption and the driving range
- c) A high power at higher operating speeds for cruising.
- d) Superior field weakening capabilities. This is vital to ascertain that the electric motor has an extensive operating speed range to accommodate driving scenarios on both urban and highway routes.
- e) A high efficiency in most regions of the torque-speed envelope to elevate the driving range.
- f) A low torque ripple to enhance ride comfort and lower noise and vibration levels.
- g) High reliability and robustness for working under challenging working environments.
- h) Lower cost.

Currently, a large proportion of the E-2Ws and E-3Ws in India are propelled by permanent magnet (PM) Brushless DC (BLDC) motors. Among BLDC motors, the interaction between the magnetic fields of the rotor and stator aids in the production of torque. The magnetic field in the stator is produced due to the excitation of the winding whilst the PMs create the magnetic field within the rotor (Hughes and Drury 2013). These traction motors hold an edge over others owing to a superior torque density and efficiency, both of which are by virtue of rare-earth PMs. However, the price of these

materials (Dysprosium oxide/Neodymium oxide) used to manufacture PMs is exorbitant and fluctuant (Figure 1.3), given the volatility of the world markets. Further, the removal and processing of rare earth oxides have a negative environmental impact (Widmer et al. 2015). A large share of the PM reserves is concentrated in China and India must depend on Chinese imports which can be a constraint to localization in indigenous motor manufacturing. BLDC motors showcase poor reliability owing to the sensitivity of PMs to temperature and vibrations (Xuan et al. 2017). They also have a limited constant power range because of their poor field-weakening capabilities (Bilgin et al. 2015).

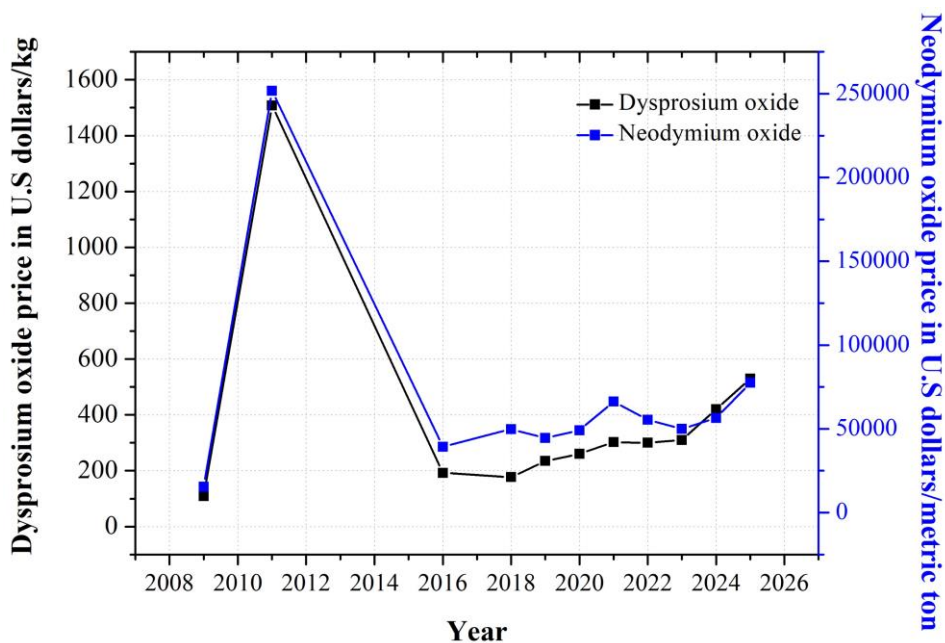


Figure 1.3 Price variation of rare-earth materials like dysprosium oxide and Neodymium oxide over the years (Statistica 2023)

To overcome all the shortcomings, particularly in the Indian context, it is deemed essential to explore a magnet-free motor solution. At present, such alternatives comprise induction motor (IM) and switched reluctance motor (SRM) amongst which IM possesses lower efficiency and torque density in comparison to SRM (Turner et al. 1997). By virtue of its simplicity, ruggedness, fault tolerance, and capability to operate at higher temperatures, SRM is apt for EV applications. Additionally, due to their extended field weakening capabilities, they exhibit excellent power-speed characteristics (Ehsani et al. 2003). However, they have lower torque density,

efficiency, and higher torque ripple in comparison to BLDC motors. A comparison of various aspects between the BLDC and the SRM is enlisted (Table 1.1). A higher value signifies that the device most effectively satisfies the requirements. The comparison shows that SRM may still be improved in aspects like power density, efficiency, controllability, noise, and torque ripple.

Table 1.1 Evaluation of BLDC and SRM for EV applications (Bilgin et al. 2015) (Zeraoulia et al. 2006).

Parameter	BLDC	SRM
Power density	5	3.5
Overload	3.5	4
Efficiency	5	3.5
High-speed range	2.5	4.5
Controllability	4	3
Noise	4	3
Torque ripple	3.5	2
Size and weight	4	3.5
Ruggedness	3.5	4.5
Maintenance	4	4.5
Maturity	5	4
Cost	8	10
Total	52	50

1.4 Fundamentals of Switched Reluctance Motor

1.4.1. Torque production mechanism

SRM belongs to the category of special electrical machines that transform electrical energy to mechanical energy, employing the principle of varying reluctance (Vijayakumar et al. 2008). The stator and the rotor cores of doubly salient construction consist of laminated electrical steel sheets which are welded or riveted to form lamination stacks. The concentrated coils mounted on the diametrically opposite stator poles are connected in series or parallel to form a phase (Figure 1.4). On energizing the

appropriate stator phase, the rotor pole tends to orient itself into a state of minimum reluctance, thus producing torque (Figure 1.5) (Bostanci et al. 2017).

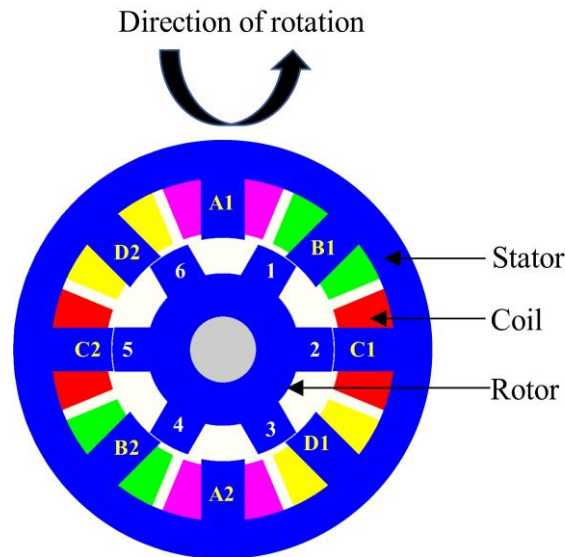


Figure 1.4 Structure of an SRM and its components

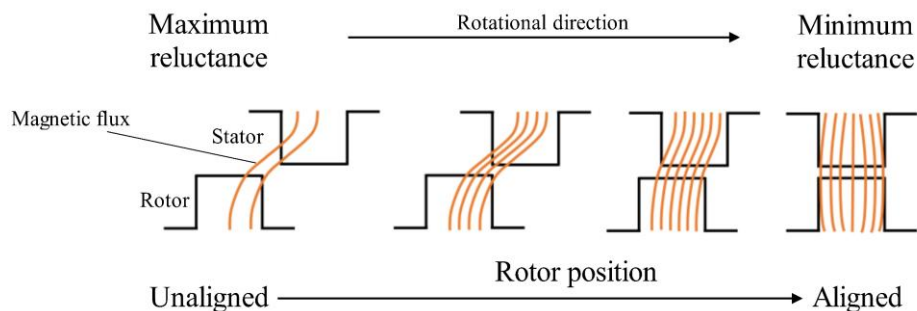


Figure 1.5 Torque production in an SRM

In Figure 1.4, when phase D (which constitutes the stator pole pair D1-D2) is energized, a magnetic field is created which attracts the pole pair 3-6 and causes the rotor to turn in the anti-clockwise direction. The reluctance pertaining to the flux path will be least when stator pole pair D1-D2 aligns itself with the rotor pole pair 3-6. The stator phases are successively energized accurately in accordance with the rotor position in the sequences A, B, and C respectively to put the rotor into continuous motion in the counter-clockwise direction. Based on this, it is evident that the phase energization relies on the rotor's angular position indicating that SRM necessitates the positional information of the rotor for its effective operation.

An SRM is designated as N_s/N_r (Krishnan 2001), where N_s indicates the pole count on the stator and N_r denotes the pole count on the rotor. An SRM with eight stator and six rotor poles (Figure 1.4) is designated as an 8/6 SRM. Figure 1.6 shows the integral components of an SRM drive system (Rashid 2011). An inverter is used to drive the SRM. The positional information of the rotor in the SRM is obtained using a mechanical angle transducer or an encoder. The phase currents and voltages are sampled using current and voltage sensors respectively. The control system employed in the controller creates the driving signals for each phase to drive the switches in the inverter based on the measured phase current and voltages, position feedback, and input commands. Accordingly, the inverter regulates the phase currents of the SRM to follow the desired waveforms and thus produce the necessary load torque. It is vital to design and develop both the drive and motor in a consolidated mode to enhance the overall performance of the system. The choice of specification/configuration of each component is application-specific and needs to be chosen judiciously to achieve a trade-off between various parameters enlisted in Table 1.1.

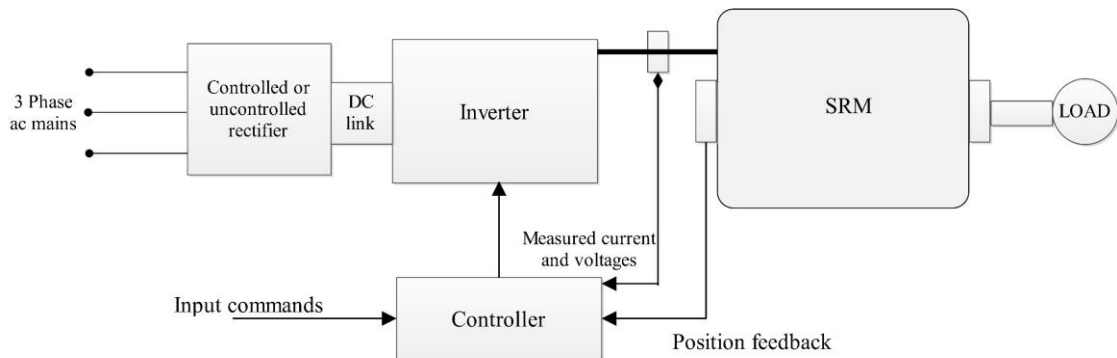


Figure 1.6 Components of an SRM drive

1.4.2. Working principle of an SRM

To comprehend the working of an SRM, it is imperative to define the two positions in the analysis of the SRM; Unaligned and the aligned position. An unaligned position refers to the angular position while the rotor's inter-pole axis aligns with the stator pole's center axis (stator pole pair A1 and A2 with rotor pole pair 1 and 4, 3 and 6) (Figure 1.4). The axis positions of the rotor are indicated in Figure 1.7. Further, at this position, the phase inductance is the least with no saturation in the magnetic circuit. An aligned position refers to the angular position when the rotor pole's center axis

coincides with that of the stator pole (stator pole pair C1 and C2 with rotor pole pair 2 and 5 in Figure 1.4). At this angular position, the phase inductance is maximum, and the magnetic circuit is prone to significant saturation. A classic phase inductance variation about the rotor position, $L(\theta)$ is depicted in Figure 1.8. It is assumed that there is no mutual inductance between the phases while constructing this curve. Further, the magnetic circuit is assumed to be linear (phase inductance is independent of the current, i) and the effects of flux fringing are also completely neglected. The phase inductance profile depicted in Figure 1.8 is segregated into four segments. Each segment has a peculiar inductance behavior based on relative positions between the rotor and the stator pole.

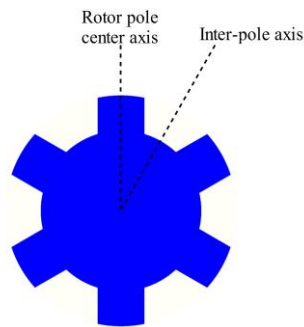


Figure 1.7 Axis positions in a rotor of an SRM

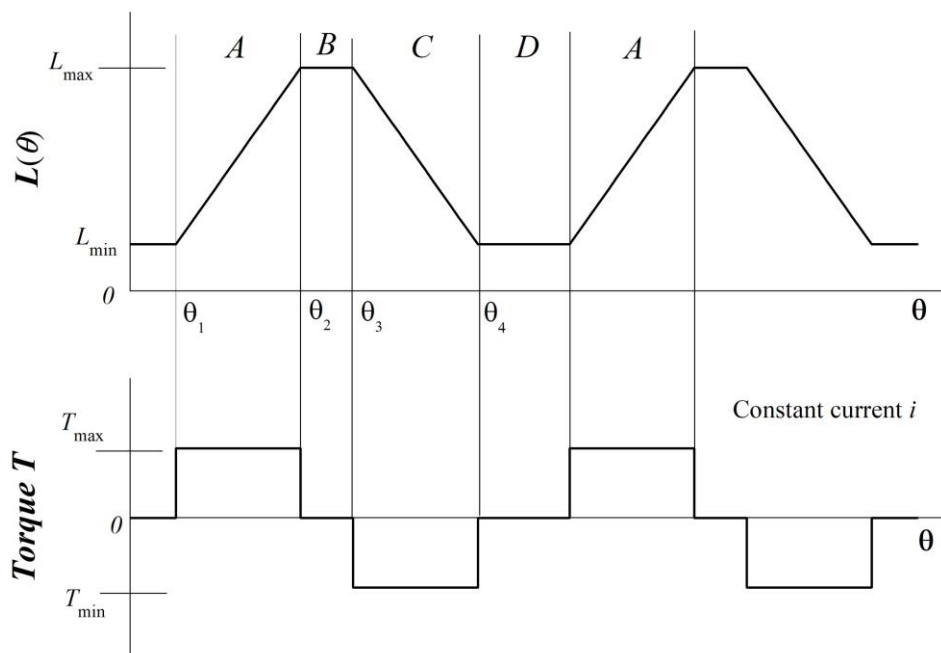


Figure 1.8 Phase inductance and the corresponding torque variation for a constant phase current

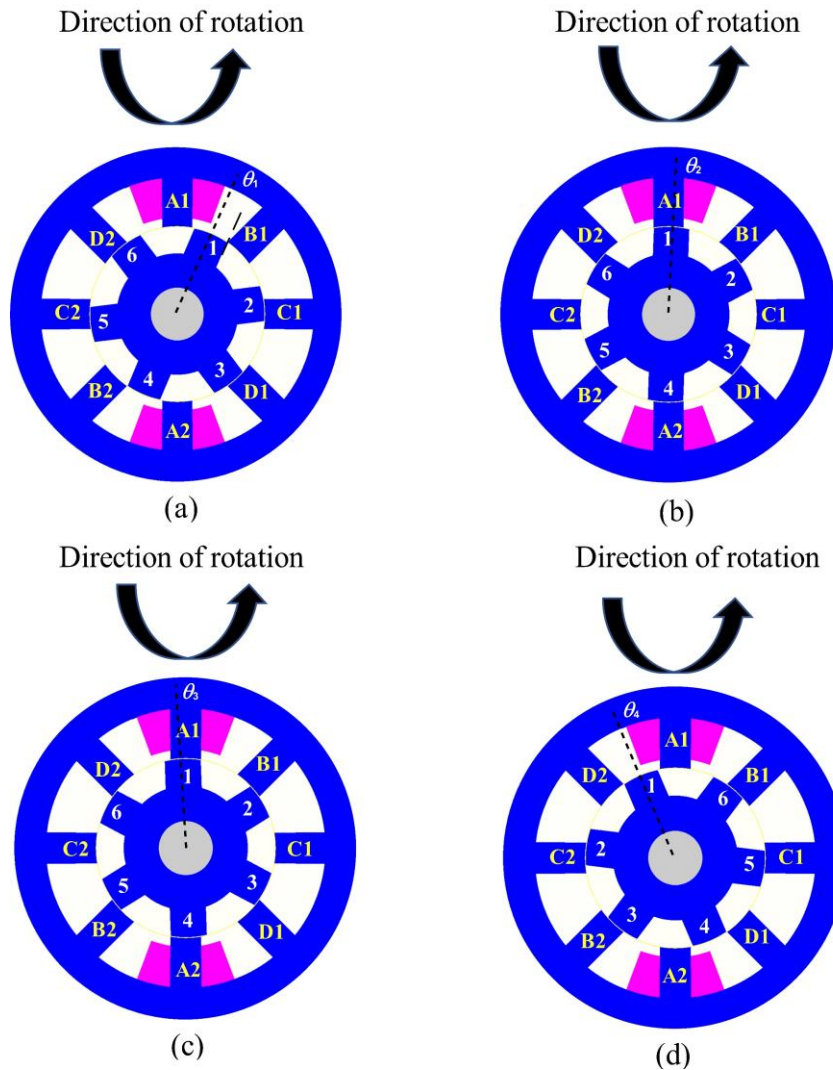


Figure 1.9 Positions of the rotor poles 1 and 4 (a) at the beginning of overlap with stator poles A1 and A2 (b) overlapped with A1 and A2 (c) leaving the overlap region of A1 and A2 (d) completely leaving the overlap with A1 and A2

a) Segment A

This segment spans from the rotor positions θ_1 to θ_2 (Figure 1.8 and Figure 1.9). The rotor angle at the beginning of the overlap amidst the rotor and stator pole corners is represented by θ_1 (Figure 1.9a). θ_2 corresponds to the rotor position when both the poles are completely overlapped. The rotor positions are indicated in Figure 1.9b for an 8/6 SRM where the rotor poles 1 and 4 align with the poles A1 and A2. During this course, it can be observed that the inductance linearly varies between θ_1 and θ_2 (Figure 1.8). At the angular instance θ_2 , the reluctance corresponding to the flux path is least thereby correlating to a maximum phase inductance.

b) Segment B

Segment B lies between the rotor positions θ_2 and θ_3 . In this segment, the phase inductance is constant (Figure 1.8) as the overlap area between the corresponding rotor and the stator pole is the same. At rotor position θ_3 , the rotor pole starts to go away from the overlap region leading to a decrease in the overlap area between the corresponding poles (Figure 1.9c).

c) Segment C

In this region, the rotor pole moves beyond θ_3 . Due to this, the overlap area between the poles decreases causing a linear decrease in the phase inductance (Figure 1.8). At rotor position θ_4 , the rotor pole completely departs the overlapping region between the poles (Figure 1.9d). At this angular instant, the phase inductance is the least.

d) Segment D

In this segment, the phase inductance remains the same (least throughout) till segment A is approached once more as there is no overlap between the poles (Figure 1.8 and Figure 1.9).

The torque output (T) of an SRM is expressed as (Krishnan 2001) (will be derived later in the sub-section 1.4.3 of this chapter);

$$T = \frac{1}{2} i^2 \frac{dL}{d\theta} \quad (1.1)$$

Equation 1.1 is derived based on the assumption that the magnetic core is unsaturated, or the variation of flux linkage is linear with current for different positions of the rotor. This leads to the observation that the output torque is directly correlated with the square of the phase current (i) and the inductance change rate as a function of rotor position. Further, the torque is unaffected by the polarity of the phase current and relies on the sign of $dL/d\theta$. A positive torque is produced when the stator phase is energized in the rising inductance region (it is assumed that the direction of the motor is in the direction of rising θ). Contrarily, a negative torque is created when the phase is energized in the decreasing inductance region. As a result, the rotor turns against the direction of the motoring action. The change in torque with the rotor position at a constant phase current

excitation is depicted in Figure 1.8. The torque remains constant in the rising and falling inductance region, while it is nil in the constant inductance region. In Figure 1.10, the continuous total torque profile produced as a result of the successive phase energizations (A, B, C, and D) of an 8/6 SRM according to the rising inductance regions has been depicted.

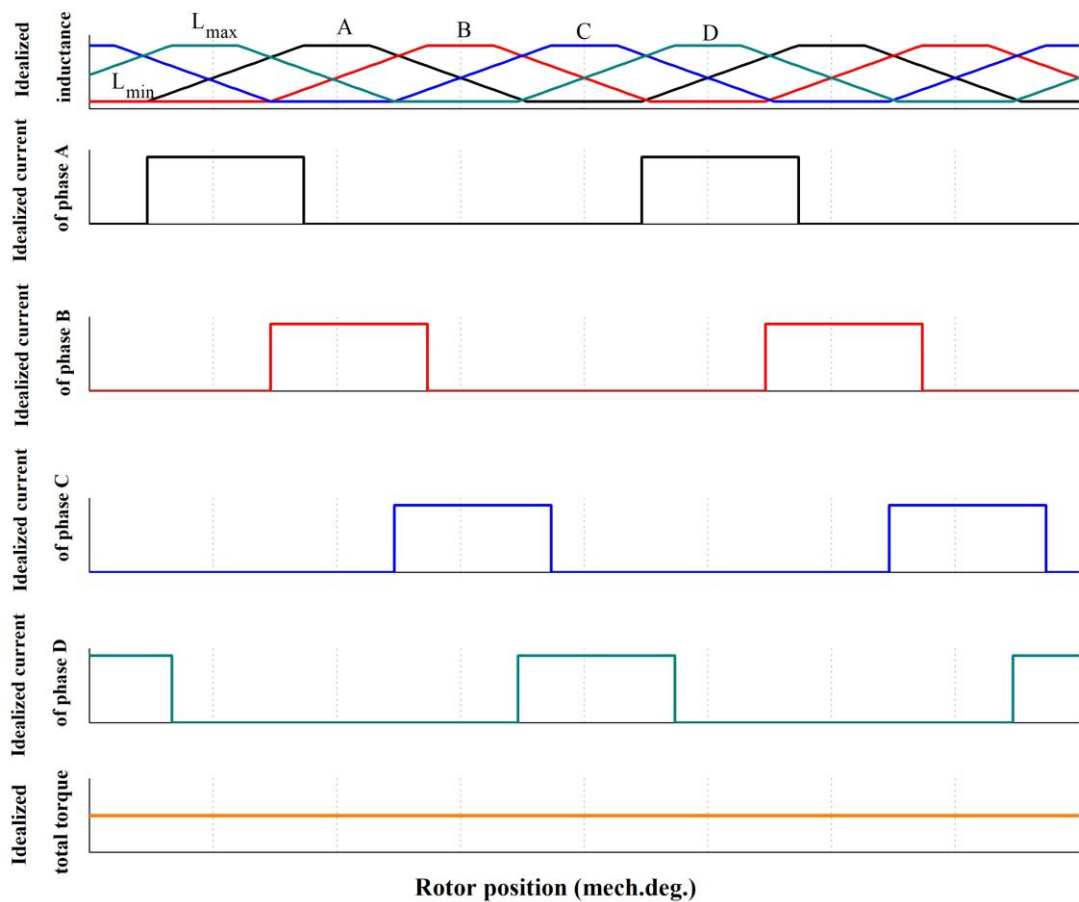


Figure 1.10 Idealized phase inductances, phase currents, and the total torque profile of the SRM

1.4.3 Electromagnetic energy conversion

The analytical equations pertaining to the instantaneous torque output of an SRM (T) can be derived based on the voltage equation applied to the SRM equivalent circuit and the Co-energy principle. The same is elucidated as follows (Bilgin et al. 2019);

- a) Voltage equation applied to the SRM equivalent circuit (no saturation of the SRM's magnetic circuit)

As depicted in Figure 1.11, the equivalent circuit for an SRM's single phase can be modeled.

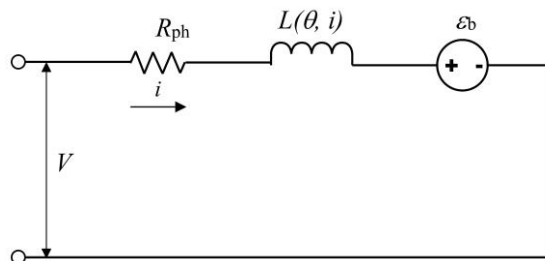


Figure 1.11 An SRM's single-phase equivalent circuit

According to Faraday's law, the voltage V across the stator windings (as shown in Figure 1.11) is expressed as

$$V = iR_{ph} + \frac{d\psi}{dt} \quad (1.2)$$

where R_{ph} denotes the phase resistance, i indicates the phase current, and ψ signifies the flux linkage of the coil. In SRMs, the phase inductance is dependent on the angular position of the rotor for a specified phase current i . Also, the flux linkage is dependent on both current (i) and rotor position (θ) as per Equation (1.2). Neglecting motor saturation (assuming that the change of ψ is linear with I and θ), the variation of flux as:

$$\psi = L(\theta, i)i \quad (1.3)$$

Putting Equation (1.3) in Equation (1.2),

$$V = iR_{ph} + L(\theta, i)\frac{di}{dt} + i\frac{dL(\theta, i)}{dt} = iR_{ph} + L(\theta, i)\frac{di}{dt} + i\frac{dL(\theta, i)}{d\theta}\frac{d\theta}{dt} \quad (1.4)$$

Angular speed (ω) is given as

$$\omega = \frac{d\theta}{dt} \quad (1.5)$$

Substituting Equation (1.5) in Equation (1.4),

$$V = iR_{ph} + L(\theta, i)\frac{di}{dt} + i\frac{dL(\theta, i)}{d\theta}\omega \quad (1.6)$$

The first term is the resistive voltage drop, 2nd term is the inductive voltage drop, and 3rd can be interpreted as the back Electromotive Force (EMF) (\mathcal{E}_b).

For simplification, $L(\theta, i)$ being used in the above expressions is depicted as L .
Multiplying Equation (1.6) with the phase current i , we get

$$iV = i^2 R_{ph} + iL \frac{di}{dt} + i^2 \frac{dL}{d\theta} \omega \quad (1.7)$$

The energy stored in an inductor (E) is given as

$$E = \frac{1}{2} Li^2 \quad (1.8)$$

Differentiating the above expression with respect to time,

$$\frac{dE}{dt} = \frac{d}{dt} \left(\frac{1}{2} Li^2 \right) = \left(\frac{1}{2} i^2 \frac{dL}{dt} + iL \frac{di}{dt} \right) \quad (1.9)$$

$$iL \frac{di}{dt} = \frac{d}{dt} \left(\frac{1}{2} Li^2 \right) - \frac{1}{2} i^2 \frac{dL}{dt} \quad (1.10)$$

Writing the 2nd term on the RHS in the form of angular speed,

$$\frac{1}{2} i^2 \frac{dL}{dt} = \frac{1}{2} i^2 \frac{dL}{d\theta} \omega \quad (1.11)$$

Substituting this in expression (1.10),

$$iL \frac{di}{dt} = \frac{d}{dt} \left(\frac{1}{2} Li^2 \right) - \frac{1}{2} i^2 \frac{dL}{d\theta} \omega \quad (1.12)$$

Substituting in the Equation (1.7)

$$iV = i^2 R + \frac{d}{dt} \left(\frac{1}{2} Li^2 \right) - \frac{1}{2} i^2 \frac{dL}{d\theta} \omega + i^2 \frac{dL}{d\theta} \omega \quad (1.13)$$

$$iV = i^2 R_{ph} + \frac{d}{dt} \left(\frac{1}{2} Li^2 \right) + \frac{1}{2} i^2 \frac{dL}{d\theta} \omega \quad (1.14)$$

where iV = Input electrical power

$i^2 R_{ph}$ = Resistive power loss

$\frac{d}{dt} \left(\frac{1}{2} Li^2 \right) =$ Magnetic power stored as magnetic field energy in the core

$\frac{1}{2} i^2 \frac{dL}{d\theta} \omega =$ Mechanical power (power in the air gap region transformed to mechanical power)

Therefore, the Input electrical power is transformed to electrical, magnetic, and mechanical power on the RHS. The Mechanical power (P_{mech}) is given as

$$P_{mech} = T\omega \quad (1.15)$$

Comparing the mechanical power in Equation (1.14) with the Equation (1.15), the output torque

(T) is given as

$$T = \frac{1}{2} i^2 \frac{dL}{d\theta} \quad (1.16)$$

Equation 1.16 is applicable when the magnetic core is unsaturated, or the variation of flux linkage is linear with current for different positions of the rotor. If the core is working in the saturated region or the flux linkage variation is non-linear with current for different positions of the rotor, the principle of magnetic co-energy is used to derive the expression for torque output.

b) Co-energy (considers the effect of saturation in the magnetic circuit of the SRM)

The power supply equals the sum of the power dissipated through the resistor, the output mechanical power from the SRM, and the stored power in the magnetic field (as per the law of conservation of energy).

$$Vi = i^2 R_{ph} + \frac{d\psi}{dt} i = i^2 R_{ph} + \frac{dW_m}{dt} + \frac{dW_f}{dt} \quad (1.17)$$

where, W_m is the instantaneous mechanical power and W_f corresponds to the stored energy in the magnetic field.

Further, the instantaneous mechanical power is given as:

$$\frac{dW_m}{dt} = T \frac{d\theta}{dt} \quad (1.18)$$

where, T refers to the instantaneous torque produced, and $\frac{d\theta}{dt}$ indicates the rotational speed. Next, the instantaneous torque can be expressed as:

$$T = i \frac{d\lambda}{d\theta} - \frac{dW_f}{d\theta} \quad (1.19)$$

The equation depicting the association of the magnetic field energy storage $W_f = \int_0^i id\psi$ and the co-energy $W_c = \int_0^i \psi di$ can be described as

$$W_f + W_c = i\psi \quad (1.20)$$

Differentiating the Equation 1.20, we get

$$dW_f + dW_c = id\psi + \psi di \quad (1.21)$$

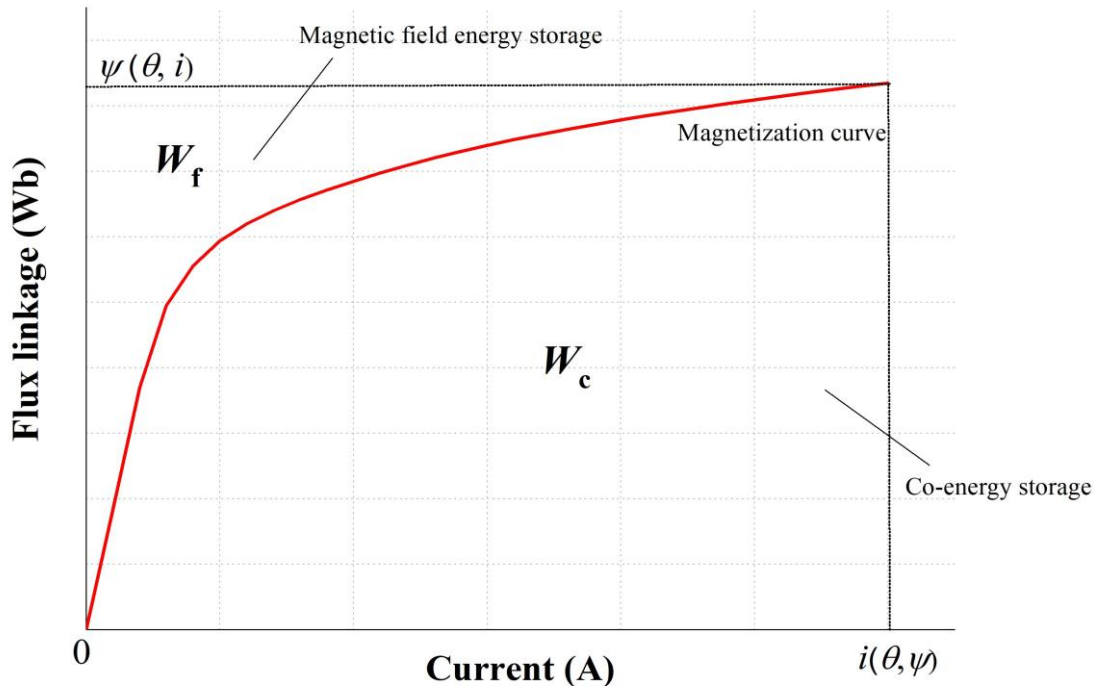


Figure 1.12 Magnetic field energy and co-energy storage with respect to current
Substituting the above differential field energy in Equation (1.21) into Equation (1.19), we get

$$T = \frac{-\psi di + dW_c}{d\theta} \quad (1.22)$$

Equation (1.18) can be simplified by employing a constant current to

$$T = \frac{dW_c}{d\theta} \quad (1.23)$$

The aforementioned expression holds true regardless of whether the SRM's magnetic circuit is linear or non-linear.

1.4.4 Control Approaches for the SRM

As per the previous discussion, an ideal waveform of phase current for producing a motoring torque is a square waveform of constant magnitude passing during the rising inductance region (Figure 1.13b). However, it is practically difficult to generate such a waveform of this nature as the current is provided through a fixed DC supply and the phase inductance is known to retard the rise the fall of the current. A practically viable current waveform produced using a hysteresis current control (HCC) method is depicted in Figure 1.13c. It is observed that it closely approximates the ideal current waveform. Practically, two kinds of waveforms for current approximate the ideal current waveform. The waveforms can be categorized based on the operating speed of the motor as follows: (a) Hysteresis current control (HCC) for low and medium operating speeds and (b) Single pulse control (SPC) for high operating speed.

(i) Hysteresis current control (HCC)

The HCC is also termed chopping mode control (CCC) (Bilgin et al. 2019). This control method is adopted for low and medium operation speeds of the SRM. The control parameters associated with HCC are chopping current (also termed as the reference current, I_{ref}), turn-on angle (θ_{on}), and turn-off angle (θ_{off}) (commutation angles). During the conduction period (i.e. between θ_{on} and θ_{off}), the current is managed between a predefined hysteresis band (Figure 1.13c). This is incorporated by using an inverter that switches OFF and ON the phase voltage whenever the phase current hits the highest and lowest value of the set hysteresis band respectively. The illustration of the voltage waveform corresponding to HCC is shown in Figure 1.13d. The DC voltage (V) is subjected to a varied switching frequency during the conduction period owing to a

rising inductance behavior of the corresponding phase which delays the ascent and descent of the current. The HCC technique can be further divided into two categories: soft chopping and hard chopping, which are covered in more detail in Section (1.4.5). The voltage and current waveforms depicted in Figure 1.13 correspond to hard chopping. As discussed previously, it is desired that the phase is energized in the increasing inductance segment to create a motoring torque. To ensure this, θ_{on} is located slightly prior to the location where the inductance begins to rise such that the current is at the desired highest magnitude in the least inductance segment well prior to the increasing inductance segment begins. Correspondingly, θ_{off} is located behind the highest inductance segment in order to give enough time for the current to fall to zero value prior to the start of the negative inductance segment. The angular position corresponding to zero current is referred as θ_q (Figure 1.13).

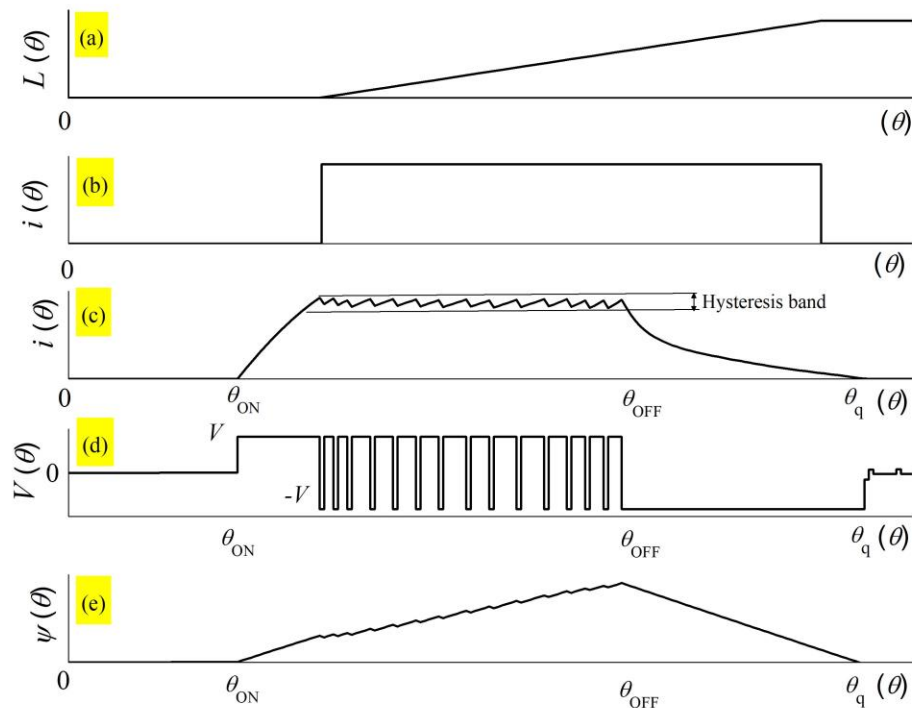


Figure 1.13 (a) Phase inductance linear variation (b) Ideal phase current waveform (c) Hysteresis current control method (d) Chopped phase voltage (e) Variation of flux linkage corresponding to HCC method.

(ii) Single pulse control (SPC)

At greater running speeds, the phase currents corresponding to the set hysteresis band will never be reached, hence the HCC approach cannot be used. This is mainly due to

a higher motor back-EMF at higher operating speeds. In the region of rising inductance, the back-EMF is either equal to or higher than the supply voltage, which curtails the growth in current and, consequently, the corresponding phase torque (Figure 1.14). Consequently, it is necessary to position θ_{on} prior to the growing inductance zone to ensure that the current has enough time to ascent prior to the back-EMF reaching a higher level. Moreover, there is less time for the current to rise because of higher operating speeds. With further increase in speed, there will be an instance when the current cannot reach the chopping level. At this juncture, SPC comes into effect where the current either drops or stays the same throughout the zone of increasing inductance (Rashid 2011). This is seen in Figure 1.14. There are two control parameters related to SPC: θ_{on} and θ_{off} . The motor back-EMF determines the magnitude of the maximum current during SPC. When the power inverter switches turn on the phase (θ_{on}), a full voltage (V) is applied across it. Consequently, when the phase is turned off (θ_{off}), $-V$ is thrown across it.

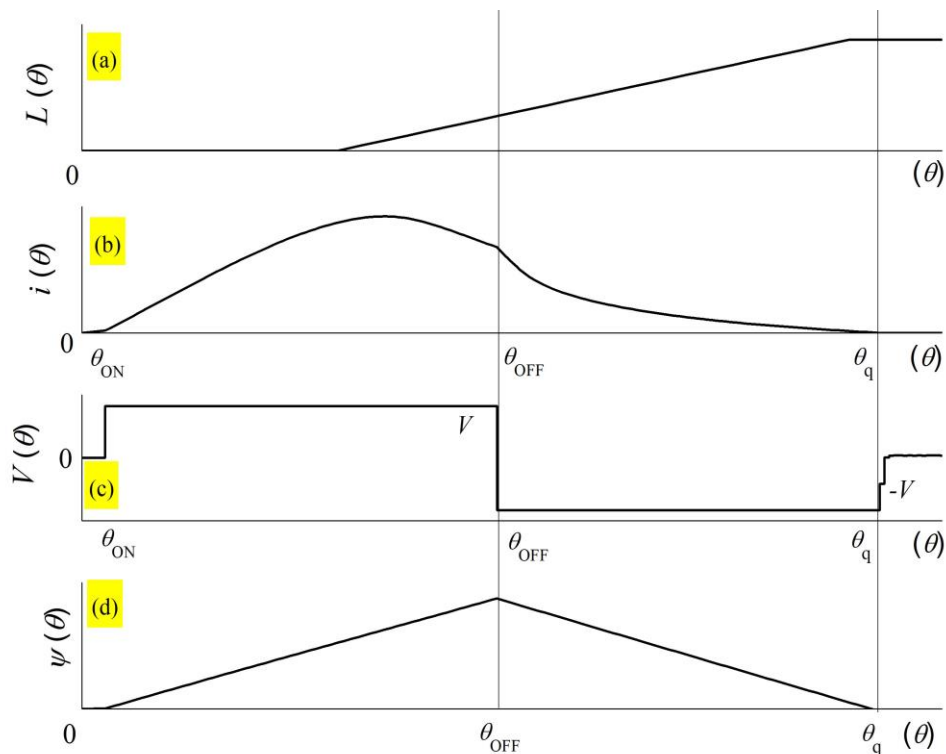


Figure 1.14 (a) Linear variation of phase inductance (b) Phase current profile corresponding to SPC (c) Phase voltage profile corresponding to SPC (d) Variation of flux linkage corresponding to SPC.

Therefore, it can be concluded that the HCC method is adopted to control the motor at lower and medium operating speeds, while at higher operating speeds, SPC is employed.

1.4.5 Hard chopping and soft chopping

There are two possible schemes within the HCC method. These are referred to as hard and soft chopping (Bilgin et al. 2019). With the aid of the asymmetric half-bridge (AHB) inverter topology, which is commonly employed to drive the SRM, the schemes can be explained. The diagram of a four-phase AHB power inverter is depicted in Figure 1.15. It can be seen that each phase consists of two switches and two diodes. Under the hard-chopping approach, both switches are always in the same switching state and are switched simultaneously. With both switches in the ON position (Q1 and Q2), the phase winding sees the entire positive supply (Figure 1.16a). Furthermore, by shutting OFF both switches, a full negative supply is supplied across the phase, reducing the current in the phase winding (Figure 1.16b). During soft-chopping, one of the switches is kept ON throughout the full conduction period (Figure 1.17a), and the other switch is alternately turned ON and OFF to regulate the necessary current magnitude. Figure 1.17b illustrates this. When both the switches are ON, the phase experiences a full voltage while the phase encounters a zero-voltage freewheeling loop that reduces the phase current while just one switch is ON.

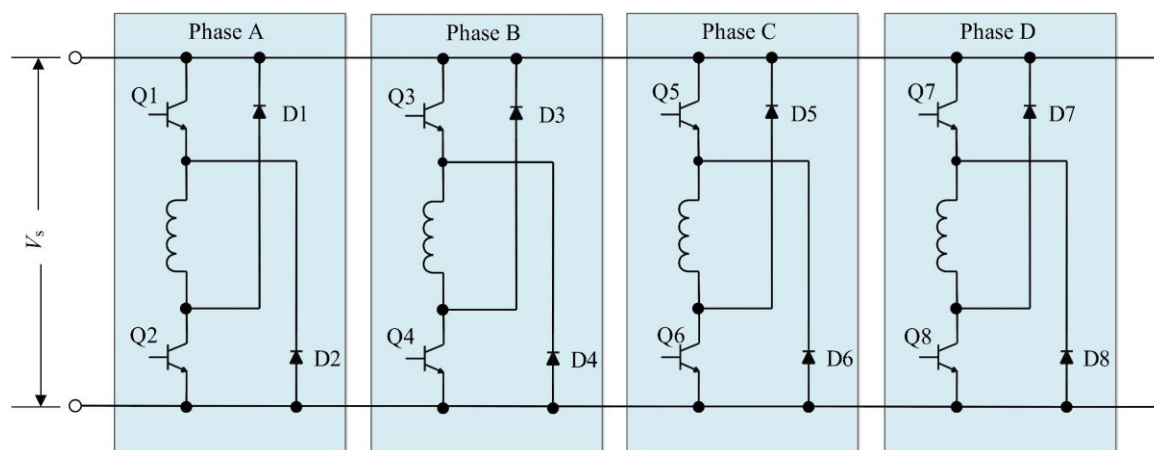


Figure 1.15 Four-phase SRM drive

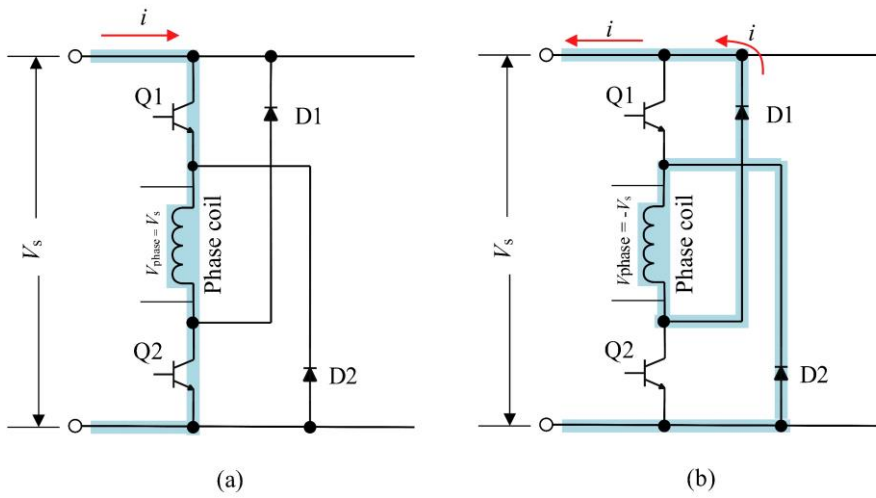


Figure 1.16 Hard chopping (a) Both Q1 and Q2 are ON (b) Both Q1 and Q2 are OFF

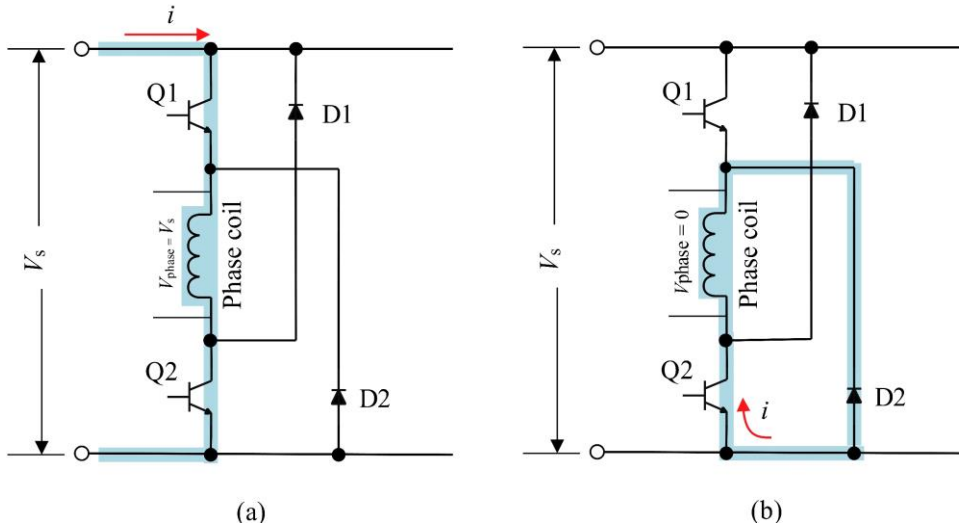


Figure 1.17 Soft chopping (a) Both Q1 and Q2 are ON (b) Q1 is OFF and Q2 is ON

1.5 Classification of SRMs

Like any other motor, SRMs are categorized as outer rotor and inner rotor type SRMs based on how the rotor is positioned in relation to the stator. In an outer rotor type SRM, the rotor is located outside the stator while the rotor in an inner rotor type SRM is positioned inside the stator (Figure 1.18). There are various names for the outer rotor motor, including external, hub, and in-wheel (IW) motor. An outer rotor-type motor layout makes it possible to directly couple to the EV's wheel rim, preserving the space and removing the need for a mechanical transmission system and the associated mechanical losses (Xue et al. 2010). Conversely, among inner rotor-type motors, the power is transmitted to the wheel via a mechanical transmission system such as the

gearbox, chain and sprocket, belt and pulley, etc. Compared to an inner rotor type SRM, an outer rotor type SRM has a higher torque output because its design permits a larger airgap diameter, which raises the lever arm and, in turn, the torque output. In contrast, the inner rotor type SRM's maximum airgap diameter is limited by the area required for the coils (Hennen and De Doncker 2007). One advantage of the outer rotor-type SRM is that it has coils close to the shaft for improved cooling. Inner rotor-type SRMs may need sophisticated cooling systems to control the heat produced by the motor since the inner rotor design may restrict airflow (Howey et al. 2017).

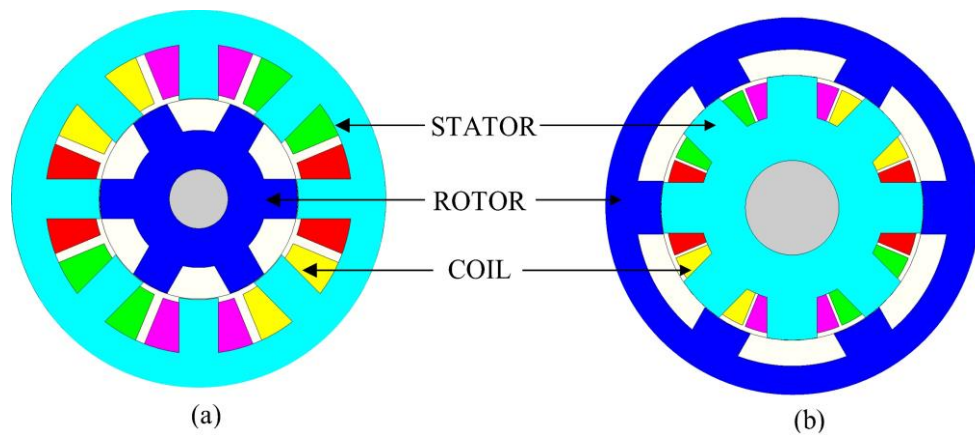


Figure 1.18 Classification of SRMs (a) Internal rotor type SRM (b) External rotor type SRM

1.6 Outline of the thesis

The thesis is grouped into 6 chapters. The present chapter provided a brief overview of the working principle, components, control method, electromagnetic energy conversion process, and classification of an SRM. In Chapter 2, the literature on the design of SRMs is thoroughly and critically reviewed. Various topologies, optimization techniques, and the use of SRMs for EV applications are all covered, along with a variety of electromagnetic modeling approaches for studying the static and dynamic behavior of SRMs. A gap in the research is highlighted at the end of this chapter. Further, the scope of the work is established based on the unanswered questions from the literature survey. A thorough parametric analysis examining the impact of geometric design variable dimensions on an SRM's performance is presented in Chapter 3. The MEC model and a comparison of the flux densities have been used to identify the key reluctance segments of an SRM that are responsible for the performance

change. In Chapter 4, a novel procedure for implementing the multi-objective design optimization (MODO) of an SRM based on a driving cycle is demonstrated. In Chapter 5, a comprehensive electromagnetic comparison is carried out between the four-phase 8/18 MT and the conventional 8/10 IW-SRMs. A summary of the work and recommendations for further field research are included in Chapter 6.

Chapter 2 LITERATURE SURVEY

2.1 Introduction

Amongst the traction motors available, SRMs show great promise for use in EVs owing to certain benefits such as magnet-free construction, simplicity, mechanical robustness, and a longer constant power range. Although the SRMs' structures are simpler than those of other AC or DC machine designs, their extremely nonlinear behavior resulting from both localized and substantial saturation in different segments of the rotor and stator, respectively, makes the design process and analysis more difficult. A high starting torque, torque density, and efficiency, with reduced torque ripple are some of the electromagnetic performance metrics desirable for an SRM intended to be employed for an EV application. Recent research has shown that the performance of the SRM is competitive when compared to other permanent magnet-based motors while adhering to the same volumetric (stator outer diameter and stack length) and electrical constraints (battery voltage and peak phase RMS current) (Kiyota and Chiba 2012) (Zayed et al. 2021).

Successfully implementing an SRM for an EV application requires a thorough understanding of its design and excitation control parameters and how they impact electromagnetic performance metrics. A change in any of these design or excitation control parameters has a specific impact on the performance metrics which may be beneficial or detrimental, with varied strengths. Owing to this, many optimization methods have been extensively used to optimize these design and excitation control parameters within the SRM's design and development framework.

This chapter contains a comprehensive and critical analysis of the existing literature that has been done on the design and development of SRMs for EV applications. The literature survey offers more information about SRM design and control parameters, the development of SRMs for EV applications, the application of optimization techniques in SRM design, and the topological characterization of in-wheel (IW) SRMs. The results of the literature survey also provide the direction and road map for the proposed study. The evaluation of the literature in this chapter is divided into the general categories mentioned below.

1. Influence of the design and excitation control parameters on the electromagnetic performance metrics of the SRM.
2. Different electromagnetic analysis techniques for SRMs
3. Employment of SRMs for EV applications
4. Implementation of optimization techniques to optimize the dimensions of the geometric design variables to improve the overall performance of SRMs.
5. Topological characterization of In-wheel (IW) SRMs for E-2Ws

2.2 Influence of the design and excitation control parameters on the SRM's electromagnetic performance metrics.

The number of phases, pole count on the stator and rotor, lamination material's characteristics, the number of turns in each phase, and the dimensions of the geometric design variables encompass the design parameters of an SRM. Further, their excitation control parameters include the reference current, turn-on, and turn-off angles. The present section is focused on the studies carried out to analyze the effects of the design and excitation control parameters on the electromagnetic performance metrics of the SRM.

2.2.1 Number of phases (N_{ph})

In the context of an SRM, a phase represents a distinct motor winding set within the motor that is energized to produce torque. Apart from its influence on electromagnetic performance metrics, they also affect the starting capability, directional capability, fault-tolerance capability, and the overall cost and packaging size of the SRM drive. Both the conventional single-phase and two-phase SRMs do not possess self-starting and bi-directional capabilities (Miller 2002). Both these configurations have significant torque ripple issues and require external assistance to start because there is no intrinsic starting torque produced. These limitations can be overcome by employing SRM configurations with three phases or more. The two-phase 4/6 SRM can only operate in one direction, while the three-phase 6/4 SRM can operate in two directions (Krishnan 2001). An increase in the number of phases of an SRM improves the fault-tolerance capability of the machine (Lin et al. 2015). A motor with more phases will have more independent windings. If one of the phases experiences a malfunction, the motor can

still run on the remaining phases. An increase in the number of phases improves the average torque, and torque density and reduces the torque ripple without the loss of the saliency ratio. The improvement is mainly due to an increase in the overlap region between the successive phases during commutation. In comparison to the three-phase 6/4 and four-phase 8/6 SRMs, respectively, a five-phase 10/8 SRM produced a greater average torque and a lower torque ripple (Petrus et al. 2010). For high-speed applications, an increase in the number of phases reduces the efficiency. Due to a larger iron core loss, the 10/8 SRM's efficiency was lower than that of the 6/4 and 8/6 SRMs, respectively (Petrus et al. 2010). An increase in the number of phases elevates the torque density. Compared to the four-phase 16/20 SRM, the five-phase 20/16 showed a greater torque density (Anvari et al. 2016). The cost and package size of the SRM drive rise as the number of phases increases (Miller 2002). This is because, the requirement of the number of converter phase units, corresponding drivers, control units, voltage and current sensors, etc. increase in proportion to the increase of phases.

2.2.2 Pole count on the stator (N_s) and rotor (N_r)

The number of poles on the stator (N_s) and rotor (N_r) has a significant influence on the electromagnetic performance metrics of an SRM. The equation governing the selection of the stator and the rotor pole count is expressed as (Lawrenson et al. 1980);

$$LCM(N_s, N_r) = N_{ph} N_r \quad (2.1)$$

where LCM represents the least common multiple. Equation 2.1 has been used to derive some of the most widely used SRM configurations such as the 6/4 SRM (three-phase), 8/6 SRM (four-phase), and 10/8 SRM (five-phase). It is important to note that in these configurations, there are fewer rotor poles than stator poles. Increasing the rotor pole count of an SRM configuration lowers its saliency ratio, but increases the average torque owing to a higher number of strokes per revolution and an increased number of turns per phase (facilitated by an increased winding space). Furthermore, an increased pole count on the rotor results in a reduced stroke angle, which decreases torque ripple. In contrast to the 6/4 SRM design, the 6/10 SRM (both three-phase designs) configuration (derived using the pole design formula, $N_r = 2N_s - 2$) produced a higher average torque and a reduced torque ripple (Desai et al. 2010) (Zhu et al. 2017a) within

the same geometrical constraints. Similar findings were reported for four-phase designs (Smaka et al. 2012), wherein the 8/14 SRM outperformed the 8/6 SRM considering the torque ripple and average torque. Moreover, SRM configurations with more rotor poles have higher torque densities because to their reduced core mass. Under conditions of constant copper loss, the 6/10 SRM had a lesser core mass as compared to the 6/4 SRM. Compared to the 6/4 SRM design, the 6/10 SRM's torque density was higher due to the combined effect of a lower core mass and an increased average torque (as previously explained) (Desai et al. 2010). The influence of the rotor pole count on the efficiency of an SRM is dependent on the speed range of the intended EV application. From an efficiency standpoint, adding more rotor poles to an SRM design is detrimental to high-speed applications. A larger iron core loss because of a higher stator frequency resulting from the incorporation of more rotor poles results in decreased efficiency. On the other hand, low-speed applications (IW-motor applications) benefit from an SRM design with more rotor poles. Copper loss decreases significantly with the increase in the number of rotor poles owing to an increase in the winding space. Though an increase in the number of rotor poles elevates the iron core loss, its influence on net loss is not pronounced due to the low-speed nature of the application (Vandana et al. 2012). When compared to the 8/6 IW-SRM design, the 8/10 design (derived using Miller's formula, $N_r = N_s + 2$) demonstrated a higher efficiency (Zhu et al. 2017a). The overloading capability of an SRM is reduced by increasing the rotor pole count. The SRM core is prone to magnetic saturation because of the need to decrease the pole widths and yoke thicknesses due to the rise in rotor pole count. The 12/28 IW-SRM demonstrated lesser overloading capabilities than the 12/20, 12/16, and 12/8 IW-SRM designs, in that order, because of magnetic saturation (Howey et al. 2020b). Moreover, the field-weakening capabilities of an SRM are influenced by the number of rotor poles. Increasing the rotor pole count of an SRM deteriorates its field weakening capabilities (Nikam et al. 2013). Furthermore, to obtain the desired output power, the inverter VA rating grows in tandem with the increase in rotor poles. The field-weakening capabilities of the 12/28 IW-SRM were found to be lower than those of the 12/20, 12/16, and 12/8 IW-SRM designs, respectively (Howey et al. 2020b).

2.2.3 Characteristics of the lamination material

Typically, the stator and rotor of the SRM are made of non-orientated soft magnetic electrical steel. The lamination profile of the stator and rotor made up of electrical steel is shaped using either laser cutting (for low-volume prototypes) or stamping (for mass manufacturing). The laminations are then stacked axially and secured together via lamination bonding, lamination interlocking, riveting, or welding. The electromagnetic performance metrics of an SRM are known to be significantly impacted by the properties of the lamination material such as the magnetic permeability, saturation flux density, and core losses (Yu et al. 2016). To ease the process of magnetization and demagnetization during the motor's operation, the lamination material should have a high magnetic permeability. As a result, efficiency rises, and energy losses are reduced. Further, it is preferable to employ core material with a high saturation flux density to boost the torque density since an SRM's torque production capability improves when it is worked under saturation. A 15% increase in average torque was seen between the lamination materials 10JNEX900 (Super Core with 0.1 mm steel thickness) and 35A300 (conventional silicon steel with 0.35 mm steel thickness) when utilized in a three-phase 18/12 SRM arrangement. This was mostly caused by the 35A300's greater saturation flux density than the 10JNEX900 (Chiba et al. 2011). The 12/8 SRM design with M19 lamination material generated a higher average torque than those using M4 and TR66, due to its superior saturation flux density (Prabhu et al. 2023). An 8/6 SRM design with Si 1010 produced a higher average torque than those using M43, JNEX, JNF, Si 50H 100, and M19 due to its higher saturation flux density (Deepak et al. 2022). Additionally, employing a low core loss electrical steel ensures higher efficiency and reduced heat generation in the motor, improving the overall performance, since the stator and rotor cores of SRMs usually operate at higher frequencies. The primary components of the iron core loss are the eddy current loss and the hysteresis loss. The hysteresis losses generated by the core material are dependent on the concentration of the silicon. For motor applications that operate at higher frequencies, a higher silicon content in the core material lowers the hysteresis loss. However, this reduces the core material's saturation flux density. Further, the eddy current loss can be lowered by reducing the thickness of the electrical steel. But, because it takes longer to cut

additional laminations, this comes at the penalty of higher costs. The lamination material 10JNEX900 employed with a three-phase 6/4 SRM showed a roughly 5% higher efficiency than the lamination material 35A300 at the maximum efficiency point. The primary causes of this efficiency gain were a higher silicon content and thinner laminations on the 10JNEX900 lamination material, which cumulatively decreased the iron core loss. However, this caused the cost of the 10JNEX900 to rise three times more than that of the 35A300 (Hayashi et al. 2009). Thus, it is evident that choosing the appropriate lamination core material for a certain EV application is important, considering the desired electromagnetic performance metrics across the torque-speed envelope as well as the overall cost constraint.

The selection of lamination material in EV motors is not fixed and depends on the specific application. Given the low-speed requirements of the E-bike application, a lamination material with high magnetic saturation flux density was prioritized to maximize torque output rather than focusing on minimizing core losses (Howey et al. 2020). M19 lamination material was chosen for the SRM core in the E-bicycle application because of its higher saturation flux density (Lin et al. 2015). 10JNEX900 lamination material was employed in a high-speed inner rotor type SRM (Jiang et al. 2017). The selected lamination material provided the best balance between the torque production capability and efficiency. The 35JNE300 lamination material was used in a high-speed 12/8 inner rotor SRM (Zayed et al. 2021). The chosen lamination material offered an optimal balance between torque production and efficiency.

2.2.4 Geometric Design Variables

The dimensions of the geometric design variables are known to have a substantial impact on electromagnetic performance metrics as they alter the magnetic circuit. Figure 2.1 shows the design variables of a four-phase inner rotor 8/6 SRM. The notation along with the description of the design variables and the respective units are provided in Table 2.1. Significant restrictions exist on the packing dimensions (stator outer diameter and stack length for inner rotor type SRM) of an electric motor in EV applications because of the presence of battery packs, electronic systems, and passenger accommodations. The packaging dimensions of the SRM have an impact on its electromagnetic performance metrics (Smaka et al. 2013a). A longer stack length

enhances the average torque. An increase in the stack length increases flux linkage and reduces reluctance for a given input magnetomotive force (MMF). An increased average torque is produced by a higher rate of change of this flux linkage with respect to the rotor position (Bilgin and Emadi 2012). The disadvantage of increasing the stator outer diameter (D_s) and stack length (L) is that it increases the motor volume and, in turn, the motor mass. The average torque and the torque density improved with an increase in rotor diameter (D_r) because of a rise in the lever arm that extends from the motor's center to the airgap (Jiang et al. 2017) (Bieńkowski et al. 2004). Nevertheless, this enhancement was at the expense of a smaller slot area, which raises copper loss and may cause motor efficiency to decline. Increasing the stator pole arc angle (β_s) leads to a greater overlap region between the stator pole and the corresponding rotor pole leading to a lower torque ripple and improved average torque (Mamede et al. 2019). The drawback of this is a smaller slot area (Miller 2002). Enlarging the rotor pole arc angle (β_r) improved the average torque until the point where the saliency ratio is high (Jiang et al. 2017). Further, providing a larger rotor pole arc angle (β_r) than the stator pole arc angle (β_s) creates a dead zone around the aligned position which aids in providing more time for the flux to nullify after commutation ensuring that no negative torque is generated (Miller 2002). Also, the field weakening capabilities of the SRM are significantly affected by the pole arc angles. This is mostly because changes in the pole arc angles have an impact on the length of the dead zone and the minimum inductance region of the phase inductance profile. A shorter minimum inductance zone reduces the scope for advancing the turn-on angle at higher operating speeds, thereby leading to a drop in the average torque. A 6/4 SRM design with a rotor pole arc angle of 30.31° was found to have a larger extended constant power range (5.7) than one with a rotor pole arc angle of 36° (4.7). The stator pole arc angles were set at 30° for both designs. The design with the stator pole arc angle of 19° and the rotor pole arc angle of 21° in an 8/6 SRM displayed a greater extended constant power range (4.125) than the design with the stator pole arc angle of 21° and the rotor pole arc angle of 23° (3.2), respectively (Rahman et al. 2000). The average torque is enhanced by increasing the yoke thicknesses of the rotor and stator (b_{ry} and b_{sy}). It is critical to provide enough thickness to the yoke sections to prevent magnetic saturation. Further, to strengthen the

stator's stiffness against the ovalizing force and lower the acoustic noise levels, it is imperative to maximize the stator yoke thickness (b_{sy}) (Miller 2002). The drawbacks are a reduction in the slot area and an increase in motor weight (Smaka et al. 2013a). An SRM needs good concentricity and a constant airgap (l_g) to guarantee balanced phase currents and minimize acoustic noise. Setting the airgap to a low value maximizes the torque density and average torque (Bieńkowski et al. 2004). An enhancement in the above performance metrics can be attributed to the decrease in airgap reluctance (Mamede et al. 2019). Although minimizing the amount of airgap is important, the process employed to manufacture the stator and rotor core limits the least value of feasible airgap (Miller 2002). Furthermore, a very small airgap value is not appropriate for EV applications since the drive train assembly is prone to increased mechanical stress and vibrations depending on the operating circumstances (Bilgin and Emadi 2012).

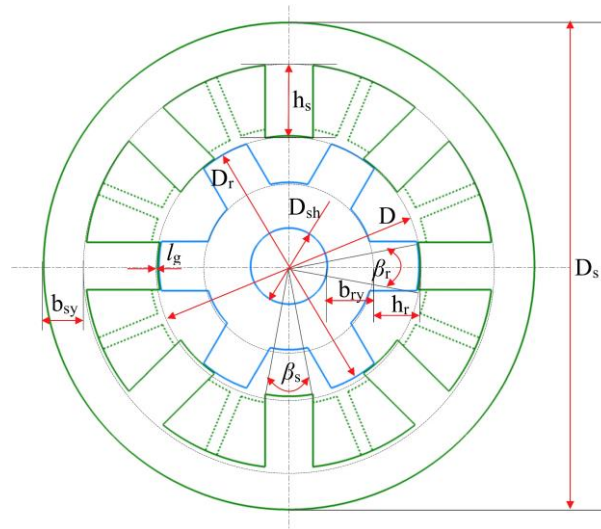


Figure 2.1 Geometric design variables of the four-phase 8/6 SRM

Table 2.1 Notations of the design variables and their description

Notation	Description	Unit
β_s	Stator pole arc angle	$^\circ$
β_r	Rotor pole arc angle	$^\circ$
b_{sy}	Stator yoke thickness	mm
b_{ry}	Rotor yoke thickness	mm

h_s	Stator pole height	mm
h_r	Rotor pole height	mm
D_s	Stator outer diameter	mm
D	Stator bore diameter	mm
D_r	Rotor diameter	mm
D_{sh}	Shaft diameter	mm
l_g	Air-gap length	mm

2.2.5 Number of turns per phase (N)

SRM comprises of concentrated coils that are wound around each stator pole. A phase winding can be created by connecting these coils in various ways (Bilgin et al. 2019). The coils consist of several turns wound using hand winding or an automated winding process (Hughes and Drury 2013). The slot fill factor and current density are dependent on the number of turns and the available slot area. An increase in the number of turns per phase reduces the peak and root mean square (RMS) current rating of the inverter to meet the peak torque requirements below the rated speed. However, because of an increase in back-EMF, this lowers the SRM's power output at higher operating speeds (Chiba et al. 2012) (Yu et al. 2016). The voltage equation for an SRM is given as;

$$V = iR_{ph} + L(\theta, i) \frac{di}{dt} + i \frac{dL(\theta, i)}{d\theta} \omega \quad (2.2)$$

where R_{ph} denotes the phase resistance and V indicates the phase terminal voltage. In the above expression, $i \frac{dL(\theta, i)}{d\theta} \omega$ corresponds to the back-EMF (ε_b). It is evident that ε_b is a linear function of speed. Neglecting the resistive voltage drop and on re-arranging, the above expression can be re-written as;

$$\frac{V - \varepsilon_b}{L} = \frac{di}{dt} \quad (2.3)$$

The aforementioned expression suggests that if ε_b is greater than V , $\frac{di}{dt}$ will become negative, with V being a constant. This restricts the increase in current, thereby

decreasing the motor's output power. As the number of turns per phase increases, $\frac{dL}{d\theta}$ term also increases (Equation 2.2). Consequently, there is a restriction on the output power. This decrease in output at higher running speeds can be overcome by employing the continuous current operation mode which elevates the RMS phase current (Schofield et al. 2009). Because of increased copper loss from higher RMS current, SRM operating in continuous current operation mode exhibits decreased efficiency compared to discontinuous current operation mode (Chiba et al. 2012). As N increases, the efficiency of the SRM running in continuous current operation mode falls at higher operating speeds (Chiba et al. 2012).

2.2.6 Excitation control parameters

The excitation control parameters namely the reference current (I_{ref}), turn-on (θ_{ON}), and turn-off angle (θ_{OFF}) (also referred to as the commutation angles) have a significant influence on the electromagnetic performance metrics of an SRM over the entire operating range. Larger reference currents have been shown to help reduce torque ripple and increase average torque as well as average torque per RMS current (a measure of efficiency for low-speed motors) (Xue et al. 2010a). The dwell angle ($\theta_{ON} - \theta_{OFF}$), expressed in terms of rotor angular position, is the duration of time that each phase winding carries current. The control of this dwell angle mainly determines the resultant torque profile of the SRM drive. A correct choice of commutation angles is essential since they may be beneficial or detrimental to the aforementioned performance metrics with varied strengths. Although a set of carefully considered commutation angles might maximize average torque, they could also minimize average torque per RMS current and increase torque ripple, or vice-versa (Xue et al. 2010a). When conducting at the rotor positions where the inductance is flat (near the unaligned and the aligned rotor position), torque is not produced; instead, the copper loss is increased, which lowers motor efficiency (Mademlis and Kioskeridis 2003). Further, conduction in the falling inductance region produces a generating torque (negative torque) which could reduce the magnitude of the average torque and average torque per RMS current (Jiang et al. 2016). Conduction in the falling inductance region creates a large amount of oscillations

in the dynamic torque waveform which could deteriorate the torque ripple (Bhuvaneswari et al. 2008).

2.3 Different Electromagnetic Analysis Techniques for SRMs

An electromagnetic model is necessary for the design and performance analysis of an SRM (Mousavi-Aghdam et al. 2016). Owing to its doubly salient construction and operation under magnetic saturation, the flux linkage characteristics have extremely nonlinear interactions with the rotor angular position and phase current, making the modeling and analysis of SRMs challenging. Thus, a highly accurate model is necessary to realize a superior design and make accurate performance predictions. The model is used to predict several significant electromagnetic performance characteristics including magnetic flux density, flux linkage, and electromagnetic torque. Additionally, the model can be used to estimate electromagnetic losses such as iron-core and copper losses. Furthermore, it can be employed in an optimization procedure to accomplish several objectives like reducing torque ripple, increasing efficiency, and minimizing motor weight. Electromagnetic modeling in the context of SRMs has three main subcategories: analytical modeling, numerical modeling, and magnetic equivalent circuit (MEC) modeling (Yilmaz and Krein 2008). Depending on the required level of accuracy and available computation time, the designer needs to choose a suitable electromagnetic modeling technique.

Most analytical models are built on the basis of Maxwell's equations. In these models, the partial differential equations are solved analytically to determine the magnetic scalar potential or the magnetic vector potential inside the SRM (Bianchi 2005). These models ignore the leakage flux, the impact of mutual coupling, and local saturation. Therefore, these techniques face challenges in approximating complex geometries, modeling the end-winding inductance, approximating iron-core losses, and comprehending core saturation thereby reducing its accuracy and practicality. However, in terms of computing cost, analytical models are less expensive than numerical models.

Electromagnetic modeling of SRMs uses a variety of numerical techniques, including the Finite Element Method (FEM), Boundary Element Method (BEM), and Finite Difference Method (FDM). Owing to its high accuracy, FEM is the most widely

used numerical technique (Bianchi 2005). Taking into account the nonlinearity of the core materials, complexity in motor geometries, and three-dimensional (3D) effects, it can accurately estimate a variety of electromagnetic characteristics. Further, it is also useful for accurately predicting machine losses. However, there's a higher computational cost associated with this technique. It is possible to employ BEM as a substitute for FEM because it requires less computational time. In BEM, the problem domain is lowered to 2D from 3D. However, it is challenging to use BEM to solve electromagnetic fields under saturation, because the coefficient matrices are not fully populated, or symmetric (Li et al. 2019). Therefore, to model SRMs, BEM and FEM or BEM and MEC are frequently coupled (Omekanda et al. 1997). For the nonlinear regions, the magnetic fields are estimated by the FEM or MEC, whereas the linear regions' magnetic fields are solved by the BEM. Another method for modeling SRMs is FDM. However, it has problems simulating complex geometries.

The MEC modeling creates an electric circuit model of the SRM geometry to evaluate the magnetic properties of a system by drawing comparisons between magnetic and electric circuits (Vahedi and Ganji 2021). Through the magnetic circuit's solution, the flux distribution inside the machine is determined. The electromagnetic torque, phase flux coupling, flux density, and magnetic field intensity can then be ascertained. Depending on how the MEC method is used, it might be classified as either an analytical or numerical technique. When used in conjunction with other analytical modeling approaches like Maxwell's equations, it is regarded as an analytical technique. When considering a magnetic material's nonlinearity, the MEC model is utilized in combination with numerical approaches (Wattthewaduge et al. 2020). The MEC technique can be improved to fairly accurately reflect the saturation, leakage flux, and other electromagnetic losses in comparison to FEM. In comparison to FEM, this method is faster. Increasing the number of reluctance elements improves the accuracy of the MEC model (Li et al. 2019). Nevertheless, this makes the model more difficult. Further, the flux paths within the machine must be specified well in advance of the modeling process (Krishnan 2001). Furthermore, modeling any SRM design with intricate geometries is challenging.

Static analysis (constant current analysis) and dynamic analysis are the two forms of analysis used to assess an SRM's performance. The static and dynamic

performance of SRM obtained from these analyses respectively must be carefully analyzed during the design phase before the lamination profile is finalized for mass production (Srinivas and Arumugam 2005). The performance of SRMs in both static and dynamic scenarios can be evaluated using the electromagnetic methods discussed above. The terminology “static” refers to the state in which the phase current remains constant during the whole electrical cycle. The initial runs of these static simulations serve as the foundation for dynamic analysis. The output of this static simulation includes the flux linkage curves, instantaneous torque profiles, magnetic flux density, etc (Wathewaduge et al. 2020). 2D electromagnetic static finite element analysis (FEA) is regarded as the most widely used modeling technique for SRMs out of all of them owing to its accuracy (Bostanci et al. 2017). Using this, SRMs are designed, analyzed, and optimized. The initial step in the procedure is to discretize the machine domain into a finite number of elements for a certain geometry. Then, the material properties are assigned to the various machine domain segments. After the boundary conditions are applied, the magnetic vector potential at every element node is calculated using the non-linear Poisson's equation. From the computed magnetic vector potentials, three electromagnetic parameters namely the flux linkage, torque, and flux density are then post-processed (Dawson et al. 1987). While static characteristics can partially reflect certain SRM performances, these performances are predicted based on the assumption of a constant current, which is insufficient and not entirely consistent with reality given that it is typically difficult to maintain a constant current, particularly during the commutation process. Therefore, static analysis cannot be used to model certain important aspects such as the field weakening capabilities and iron core loss.

The dynamic analysis is used to estimate the overall performance characteristics of the SRM. The dynamic simulation considers the SRM's transient behavior, accounting for elements like excitation control parameters, rotor and load inertia, and the impact of actual voltage and current waveforms on the motor's operation (Vijayakumar et al. 2008). It provides information on how the motor responds dynamically to unexpected changes in load or input parameters as well as during startup, acceleration, and deceleration. Circuit-coupled transient-finite element methods and circuit-based simulations are often utilized for transient analysis to capture the motor's response under changing operating conditions. The procedure of transient

FEA possesses a higher computational cost since it involves the simultaneous calculation of the motor's motion equations and the time-varying electromagnetic field equations (Srinivas and Arumugam 2005). The modern FEM-based software package makes accurate analysis of SRMs possible because of the significant advancements in computer technology, including the development of highly efficient, high-speed processors and improvements in computer memory technology. The transient FEA simulation yields a steady-state torque waveform, phase current, and voltage waveforms. Tuning the excitation control parameters using transient FEA simulations necessitates running these simulations several times, which takes considerable time. On the other hand, circuit-based simulations use simpler circuit models, which are usually easier and faster to solve, to simulate the dynamic behavior of the motor. Furthermore, this methodology accounts for the nonlinearity of the magnetic characteristics within the simulation (Vijayakumar et al. 2008). In these simulations, a system of differential circuit equations and the mechanical equations for suitable switching conditions are solved to estimate the dynamic behavior. Circuit-based simulations for SRMs have been carried out widely in the MATLAB/Simulink environment due to its flexible modeling framework, faster simulation development times, and availability of several libraries. In these simulations, the dynamic characteristics are determined based on the static characteristics imported in the form of look-up tables (LUTs) (Soares and Branco 2001). Despite being computationally efficient, the circuit-based simulations are not as accurate as the transient FEA simulations because they do not capture the complex magnetic interactions more precisely.

2.4 Employment of SRMs for EV applications

The design procedure for an electric traction motor is different from that of industrial motors. The main distinction between the performance specification and the load requirement of the traction and industrial motors is outlined below (Mehrdad et al. 2018);

- For short-term acceleration and hill climbing, the maximum torque produced by the traction motors should be four to five times the rated torque; in contrast, the

maximum torque produced by the industrial motors is typically double the rated torque.

- For highway cruising, traction motors must reach four to five times the base speed. Industrial motors can attain twice the base speed.
- The design of traction motors has to take into account the driving profiles of the vehicles and the habits of the drivers, whereas industrial motors are typically built around a standard operating zone.
- Traction motors require elevated power density and high-efficiency maps (superior efficiency across a wide range of torque and speed duty cycles) to reduce overall vehicle weight and increase the range per charge, while with industrial motors, efficiency is usually optimized at a rated operating point. Further, a trade-off between their power density, efficiency, and cost is necessary.

It is clear from the aforementioned pointers that traction motors have different performance requirements than industrial motors. Consequently, when designing an electric traction motor, a different methodology needs to be adopted. Using previously released publications as references, the steps involved in designing SRMs are described.

Determining the desired performance specifications and the necessary torque-speed performance curve is the first step in developing an SRM for an EV application. According to earlier published research, there are two approaches to accomplish this: by applying the vehicle dynamics model based on a driving cycle and vehicle parameters (Lin et al. 2015), or by taking into consideration the torque-speed performance curve of a different competitive benchmark motor (Kiyota and Chiba 2012). Secondly, the space limits for the traction motor in the EV mostly determine the stator diameter and stack length (geometrical constraints) of the SRM. The electrical constraints such as DC-link voltage and the peak RMS phase current are fixed based on the performance requirement (required peak power at the maximum speed and maximum torque at the rated speed). Thirdly, the number of phases is chosen by weighing the SRM drive's cost against the performance required. An electromagnetic performance comparison was carried out between an outer rotor 16/20 SRM (four-phase), 20/16 SRM (five-phase), and 24/20 SRM (six-phase) for a target torque-speed

performance curve to verify the suitability for an EV application. The comparison was carried out under the condition of similar electrical and geometric constraints, air gap, and slot fill factor. The four-phase 16/20 SRM was found to be suitable for the EV application since it provided the best trade-off between electromagnetic performance and SRM drive cost (Anvari et al. 2016). The pole count on the stator and rotor is determined in the fourth stage after the number of phases has been established. It is necessary to choose the pole count taking into account several electromagnetic performance metrics. A performance comparison of numerous three-phase IW topologies, including 12/8 SRM, 12/16 SRM, 12/20 SRM, and 12/28 SRM, was conducted based on overloading capabilities, efficiency, torque ripple, and field weakening capabilities. The comparison was conducted using identical geometric and electrical constraints, air gap, and slot fill factor. The 12/16 SRM configuration was chosen above alternative solutions because it provided the best possible balance between the aforementioned electromagnetic performance metrics (Howey et al. 2020a). Once the number of phases and pole count have been determined, the fifth stage entails determining the dimensions of the geometric design variables. Typically, the power output equation is used to calculate the stator bore diameter (D) (Terzic et al. 2018). The number of turns per phase (N) is adjusted to satisfy the target torque-speed envelope within the constraints of maximum RMS phase current and battery voltage (Chiba et al. 2012) (Zayed et al. 2021). The ranges of dimensions of the geometric design variables are constrained according to the empirical equations provided to prevent geometrical conflicts between the structures of different motor components (Anwar et al. 2001). Any alteration to one of these design variables will specifically affect the performance metrics, with varying degrees of potential benefit and drawback. Therefore, the dimensions of the geometric design variables are optimized by employing optimization techniques within the constraints of the slot fill factor and current density (Uddin et al. 2016).

Owing to its accuracy in predicting electromagnetic characteristics, FEA is the most commonly used modeling technique to assess the performance of SRMs. 2D electromagnetic FEA is preferred over 3D electromagnetic FEA due to its faster computation time. However, in the analysis of SRMs where the effects of end-turns and axial field fringing are predominant, 3D electromagnetic FEA is employed (Öksüztepe

2017a). To perform a preliminary analysis, 2D electromagnetic static FEA is typically utilized to predict a reasonable approximation of certain performance aspects such as average torque, torque density, copper loss, torque ripple, and overloading capabilities. Electromagnetic static FEAs are widely used in the design of IW-SRMs (low-speed motors) because they provide a good representation of low-speed shaft torque (Xue et al. 2010b) (Howey et al. 2020a). Nevertheless, electromagnetic static FEA cannot estimate other important performance aspects like iron core loss and field weakening capabilities. These aspects can be obtained using circuit-coupled time-stepping 2D transient FEA. The reference current (I_{ref}), and the commutation angles (excitation control parameters), for a constant motor speed are inputs to the transient FEA simulation (Madhavan and Fernandes 2013). Transient FEA simulations are known to require multiple runs to adjust these excitation parameters at different operating speeds, which is known to take a significant amount of time. Instead, to hasten this, the steady-state characteristics of the SRMs is commonly analyzed in the circuit-based MATLAB/Simulink environment (Sun et al. 2019). Further, for different values of reference currents, the commutation angles are optimized for the full operating range to find the best balance between the performance metrics (Jiang et al. 2016). Using the optimized values of the commutation angles, the iron core loss is estimated using the transient FEA simulation. The motor efficiency is estimated using the results of the calculations for the iron core and copper losses.

2.5 Implementation of optimization techniques to optimize the dimensions of the geometric design variables to enhance the overall performance of SRMs.

Design optimization, a crucial stage in the design process of an SRM is aimed to improve its overall performance. It has been previously determined that the electromagnetic performance metrics of an SRM are significantly influenced by the dimensions of the design variables as they influence the magnetic circuit. Any alteration to one of these design variables will specifically affect the performance measurements, with varying degrees of potential benefit and drawback. As a result, estimating the optimum motor dimensions forms a typical optimization problem. The optimization techniques can be broadly classified into deterministic and stochastic optimization

techniques (Rao 2009). Deterministic optimization techniques use the objective function's gradient information obtained by a predefined set of guidelines to find the optimal solution. The Lagrangian approach, sequential quadratic programming, and interior point method are examples of deterministic optimization techniques (Abdalmagid et al. 2022). These techniques quickly yield a unique and optimal solution as compared to the stochastic optimization techniques. However, the determined solution is not guaranteed to be the global optimal solution for nonconvex functions. Further, several conditions must be met to apply these techniques effectively: the objective functions must be continuous and derivable; both the constraints and the objective functions must be analytically defined; the implementation requires the Hessians matrix (Sun et al. 2020). On the other hand, stochastic optimization techniques obtain the optimal solution at random. Some of the popular stochastic optimization techniques include genetic algorithms, evolutionary algorithms, particle swarm optimization, etc (Bramerdorfer et al. 2018). Owing to the inherent randomness of these techniques, the optimal solutions are obtained at varied speeds during successive runs. They are usually used for non-convex, noisy, or complex optimization scenarios where deterministic techniques may have trouble covering large search spaces or have the chance of becoming stuck at the local optima. The choice between stochastic and deterministic optimisation approaches in real-world applications depends on a number of factors, such as the problem's nature and the requirements for the quality of the solution.

SRM design optimization is typically a nonconvex problem with numerous local solutions. Employing deterministic optimization techniques is not desirable as these techniques find it difficult to arrive at a global solution. Moreover, the electromagnetic analysis model for SRMs relies on FEA and there are no analytical equations within the optimization formulation. Owing to these circumstances, stochastic optimization techniques are preferable and are being widely employed for the design optimization of SRMs. In order to maximize the static average torque, a three-phase 6/4 SRM's stator bore diameter and pole arc angles were optimized using the genetic algorithm, a stochastic evolutionary method (SEM) (Raminosoa et al. 2010). The optimization problem formulation included constraints on the current density and geometrical relations for pole arc angles. A multi-objective optimization of a 4-phase

8/14 SRM was carried out by employing an SEM namely the genetic algorithm (GA) with 2D FEA (Smaka et al. 2013b) The study intended to maximize the chosen electromagnetic performance metrics by optimizing the pole arc angles, and taper angles. Geometric relations were used to constrain the limits of the pole arc and taper angles. In these studies, the design optimization was carried out using SEMs in conjunction with a computationally expensive FEA solver. To reduce the computational burden of the FEA during the optimization, SEMs were coupled with surrogate models like the response surface model, kriging model, radial basis function, etc. A multi-objective design optimization of a three-phase 6/10 SRM was performed by coupling the particle swarm optimization with 3rd-order response surface models to improve the electromagnetic performance metrics (Ma and Qu 2015). The suggested approach significantly lowers the amount of FEA iterations, which in turn significantly lowers the time and cost of calculation. In all the above-considered research studies, the multi-objective optimization was typically handled by a single objective function by considering the normalized weighted average of the objective functions, which reduced the flexibility since the optimization algorithm produced only one solution. Additionally, determining the weights for each design objective is a laborious process. Rather, it is preferable to have a collection of optimized designs from which a final design can be chosen. As a result, the designer has a choice of several optimal solutions. This approximation is termed Pareto-based multi-objective optimization (Tekgun et al. 2022). Oksuztepe demonstrated a Pareto-based multi-objective design optimization framework for a 3-phase 18/12 in-wheel SRM. The multi-objective design optimization was implemented by coupling an SEM namely the differential evolution algorithm with the magnetic equivalent circuit method (static performance) to calculate the performance metrics. The study intended to maximize the starting torque, torque per motor lamination volume, and efficiency by optimizing the stator bore diameter, pole arc angles, and yoke thicknesses (Öksüztepe 2017b). Recently, research studies have focussed on system-level multi-objective optimization of SRM drive, which optimizes the SRM's dynamic performance by taking into consideration both its design and control variables (Diao et al. 2020). Anvari et al. conducted a Pareto-based multi-objective system-level optimization of a 16/20 IW-SRM by considering both the design and the control variables within the optimization formulation. The average torque and

efficiency increased by 6.78% and 7.2%, respectively, while the torque ripple decreased by 61.2% when the optimized design was compared to the original design (Anvari et al. 2017). In a recently published study on the design optimization of SRM, the motor and the generating modes of operation were taken into consideration when optimizing the SRM drive (Diao et al. 2021). In all the aforementioned optimization studies intended to be used for EV applications, the variables of the SRM were only optimized at the rated/base speed for the defined design objectives. The machines that are optimized at these points demonstrate an improved performance around these points only. However, it is well known that the load operating points (LOPs) of a traction motor are dynamic and widely spread within the torque speed envelope. Considering the LOPs in the motor design optimization process can improve the machine's performance comprehensively over the whole torque-speed operating range.

Following this, research on electric motors for EVs in the recent past has concentrated on the assessment of motor performance and their optimization across a driving cycle. A permanent-magnet motor (PMM) whose design variables were optimized over the New European Driving Cycle (NEDC) indicated a greater cycle efficiency (1.1 % improvement) than the design optimized at the rated point (Lazari et al. 2014). Compared to the scenario when the design variables were optimized at a single rated point, the authors reported that integrating the LOPs into the optimization formulation increased the driving cycle efficiency (Carraro et al. 2016). The first step in the driving cycle-based design optimization process is typically to use the vehicle dynamics model to determine the LOPs based on a driving cycle and the vehicle parameters. Since the FEA solver has a greater computing cost, it is not computationally efficient to evaluate the performance metrics of each design candidate at every LOP. Hence, to approximately represent the driving cycle, representative points (RPs) are formed by clustering. It has been demonstrated that the improvement in electromagnetic performance metrics (post-optimization) is directly correlated with the number of RPs taken into account during the optimization process (Salameh et al. 2019). However, this comes at a higher computing cost as the performance metrics need to be evaluated at each of these RPs. The best trade-off between computational cost and performance metrics improvement must be taken into account while determining the suitable number of RPs. The clusters and, thus, the RPs can be found using a variety of methods, such

as visual inspection, the arbitrary split method, energy density distribution, and the k -means algorithm. However, the number of clusters that the visual inspection method yields based on the user-judgment may not be optimal. Using the arbitrary range split approach, the LOPs cannot be flexibly clustered according to their distribution density in the torque-speed plane. The energy density distribution method relies on the user's evaluation and visual inspection to ascertain the number of obtained clusters. Conversely, the k -means clustering algorithm employs a systematic approach, with the resulting clusters being determined by the distribution density of the LOPs. Further, within the optimization formulation, the optimization weights for each of the design objectives are determined based on the methodology used to obtain the RPs (Salameh et al. 2019).

A methodology to carry out the design optimization of a permanent magnet synchronous motor (PMSM) based on a driving cycle was laid down (Sarigiannidis et al. 2017). An adaptive differential evolution technique was employed to optimize the design variables of the two PMM topologies over NEDC. Several representative points (RPs) were extracted with regard to the fluctuation of the energy in the torque speed envelope. According to the energy distribution of the points inside a cluster, optimization weights were computed. At each RP, the design optimization was intended to improve the electromagnetic performance metrics. A driving cycle-oriented design optimization of an 18-slot 16-pole spoke-type permanent magnet motor was presented for an EV application (Fatemi et al. 2018). The representative points (RPs) were obtained using the k -means clustering algorithm. The study focused on maximizing the power density and efficiency by optimizing the design variables within the constraints of torque ripple and excessive demagnetization of the rotor PMs. A driving cycle-based design optimization study of an outer rotor PMSM was reported for an EV application (Sun et al. 2020). The four clusters and the corresponding representative points (RPs) were obtained using the visual inspection method based on the driving conditions. The study focused on maximizing the chosen electromagnetic performance metrics by optimizing both the design and control variables within the constraints of minimum required efficiency, current density, and slot fill factor. The optimization weights were derived based on the frequency of operating points at the different clusters. The multi-objective optimization of the PMSM was carried out by using the non-dominated

sorting genetic algorithm II (NSGA II) in conjunction with the constructed kriging models to determine the Pareto-optimal solution set. Between the optimized and initial designs, there was a 34.96% reduction in torque ripple, a 0.1% reduction in efficiency, and a 7.72% improvement in average torque.

After examining the body of research on driving cycle-based design optimization for electric traction motors, it is noticed that most studies have mostly focused on permanent magnet motors (PMMs), and permanent magnet synchronous motors (PMSMs) in particular. Not much work has been reported in this regard for SRMs. This is because PMSMs have well-established modeling techniques to assess their dynamic behavior. FEA in conjunction with the $d-q$ (direct-quadrature) electrical models has been well integrated within the optimization framework in these studies

2.6 Topological characterization of In-wheel (IW) SRMs for E-2Ws

Using an IW outer rotor motor configuration in an EV facilitates direct coupling to the wheel rim saving space and eliminating the requirement for a reducer and thereby the mechanical losses incurred (Xue et al. 2010b). However, because a reducer is not used, working circumstances and design constraints are more challenging for IW motors. Additionally, IW motors need to be lightweight since their mass influences the unsprung mass and, in turn, the ride comfort of the EVs. IW motors should possess a high torque density (due to limited space inside the wheel hub), high starting torque (for acceleration at lower speeds), superior efficiency over a vast range of speeds (for improved driving range), and a low torque ripple (for better ride comfort) (Sun et al. 2020). BLDC traction motors are highly suitable and are being widely employed for IW-EV applications due to superior torque density and efficiency, both of which are by virtue of rare earth (Tuncay et al. 2011). However, as compared to BLDC motors, SRMs have lower torque density, efficiency, and larger torque ripple (within the same volume constraints) due to high magnetic saturation in the core.

To address these issues among SRMs, several IW-SRM topologies have been evaluated and proposed to be employed for EVs and E-2Ws in particular. Amongst these, an 8/6 SRM with fewer number of rotor poles (N_r) lesser than the stator poles (N_s) was proposed to be used in an E-scooter (Singh et al. 2021). It has been reported

that SRM configurations with $N_r > N_s$ demonstrate improved efficiency and are highly suitable for E-2W applications (Vandana et al. 2012). The 6/10 $N_r > N_s$ SRM configuration exhibited higher torque density (due to an increase in the average torque and a drop in the motor's overall mass), efficiency (due to an increased slot area) with reduced torque ripple (due to an increased number of strokes per revolution) in contrast to the 6/4 SRM (Desai et al. 2010). The 6/10 IW-SRM was adopted for the E-bicycle application and the merit of the proposed idea was illustrated for the whole torque-speed range (Lin et al. 2015). Increasing the rotor pole count improves the slot area, which lowers copper loss and boosts efficiency (Vandana et al. 2012). Though an increase in N_r elevates the iron core loss, its influence on net loss is not pronounced due to the low-speed nature of the application. However, the $N_r > N_s$ SRM configurations have reduced peak torque and field weakening abilities due to higher levels of magnetic saturation and reduction in the saliency ratio respectively. Numerous three-phase IW-SRM designs, specifically 12/8, 12/16, 12/20, and 12/28, were examined based on peak torque capacity, efficiency, and torque ripple to ascertain the suitability for the E-bike under the same geometrical and electrical constraints (Howey et al. 2020a). The 12/28 IW-SRM design demonstrated a higher efficiency than the 12/20, 12/16, and 12/8 designs due to a lower copper loss. Additionally, even though its iron core loss was greater than that of previous designs, the efficiency remained unaffected. Compared to the other designs, the 12/28 SRM exhibited reduced torque ripple due to its higher number of strokes per revolution. However, because of its thinner yoke and narrower pole, it was more susceptible to magnetic saturation and had a lower peak torque capacity. A novel configuration of the three-phase 12/8 SRM with segmented rotors (SRSRM) was published in 2002 (Mecrow et al. 2002). An SRSRM's rotor is made up of several discrete segmented rotors, each of which is fixed in a nonmagnetic isolator. On phase excitation, this configuration allows magnetic flux to flow down one stator tooth, via the two rotor segments, and return through the adjacent stator tooth. The flux then returns via the portion of the stator core back between the two teeth. As a result of having double the active airgap area of a conventional SRM, the flux linkage per turn is almost twice as high, enhancing the machine's magnetic utilization (Mecrow et al. 2004). Additionally, since the rotor's yoke is eliminated, the topology has increased efficiency (Asgar and Afjei 2016). This lowers the weight of the rotor and shortens the

magnetic field's flux pathways, which lowers the MMF requirement. Under the same geometric limitations, the performance of the SRSRM arrangement was compared to a conventional 12/8 SRM. According to the authors' findings, the proposed SRM structure showed an average torque of 40% higher than the conventional SRM (Mecrow et al. 2004). Because of these advantages, a 12/26 SRSRM topology was suggested for an E-scooter (Nikam et al. 2012). A 12/10 multi-teeth (MT) SRM topology with a high torque density ($N_r < N_m$, where, N_m is the total number of MT) was initially proposed in 1995 (Miller 2002). The MT arrangement resulted in a larger flux variation over a shorter variation period, which led to a higher torque production per electrical cycle. Though this topology required lesser MMF to produce the desired torque, it was not further investigated due to a smaller slot area and a high iron core loss, which resulted in an inferior efficiency. A 6/16 IW-MTSRM ($N_r > N_m$) topology with high torque density was proposed for an EV application (Zhu et al. 2017b). Its performance was compared with that of conventional 6/8 and 6/10 SRM configurations under comparable volume constraints, current density, and slot fill factor. As compared to the 6/10 SRM, the proposed configuration showed a greater torque of 29.2%, a specific torque of 27.981%, and an 86.1% reduction in torque ripple.

Further, in recent studies PMs were incorporated between the adjacent stator poles in the 48/50 MTSRM topology (Hybrid SRM; HSRM), the addition of which boosted the torque density and efficiency (Farmahini Farahani et al. 2020). The principal reasons for the improved performance were the reduction in stator pole saturation levels and the enhancement of flux density in the air gap rendered by the PMs. Owing to these benefits, a 48/50 IW-HSRM topology for an E-bicycle application (Farahani and Mirsalim 2020). The authors used a variety of MTs to analyze various MTSRM and HSRM topologies to assess their suitability for the proposed application. Further, a comparison was also presented with their respective PM-less counterparts. For lower excitation currents, it was observed that an increase in the MTs led to an increase in average torque. However, because of tooth saturation (caused by decreased tooth width), their average torque was lower at higher excitation currents. Furthermore, by adding PMs to the 48/50 SRM topology, the average torque, torque per motor volume, and efficiency all increased by 65.22%, 65.22%, and 13.44%, respectively. Though the inclusion of PMs in this topology improved their performance, their total

cost was up by 17.6%. A unique SRM structure with U-shaped modular rotors was proposed (Chen and Yan 2018). Utilizing a modular rotor boosted the average torque and reduced the iron core loss in contrast to the conventional SRM owing to a shorter flux path.

Among the topologies described above, SRSRM, HSRM and modular SRMs, apart from being expensive and difficult to manufacture, have a complicated design thereby sacrificing the simplicity of the traditional SRM structure. Additionally, including PMs in the SRM produces cogging torque, which deteriorates the motor performance. Therefore, the MTSRM (with $N_r > N_m$) topology is a potential candidate for IW motor applications as it retains the inherent simplicity and cost-effectiveness offered by traditional SRM designs.

2.7 Summary of Literature Survey

An SRM's electromagnetic performance metrics are significantly influenced by the number of phases, pole count on the stator and the rotor, characteristics of the lamination material, dimensions of the geometric design variables, number of turns per phase, and excitation control parameters. SRM configurations with three phases or more demonstrate both self-starting and bi-directional capabilities. The average torque, power density, torque ripple reduction, and fault tolerance are all enhanced by increasing the number of phases. Nevertheless, this makes the drive becoming bulkier and more expensive. Increasing the pole count on the rotor improves the average torque and lessens the torque ripple. However, the diminished overload and field weakening capabilities are of major concern. Moreover, adding rotor poles increases the core loss and decreases the efficiency for high-speed applications. Key characteristics of the core material, including saturation flux density, magnetic permeability, and core losses, are known to have a major impact on an SRM's electromagnetic performance metrics. Considering both the torque-speed performance requirements and the total cost constraint for an EV, an appropriate lamination core material should be selected for an SRM. The magnetic circuit of an SRM is modified when the dimensions of the geometric design variables are altered. The impact of this may vary in degree and be either positively or negatively correlated with the performance indicators. Increasing

the number of turns per phase lowers the peak and RMS current requirement of the inverter to meet the peak torque requirements at operating speeds below the rated speed in an EV application. However, the rise in back-EMF reduces the SRM's power output at higher operating speeds. The choice of commutation angles for a definite reference current at an operating speed is crucial to attaining the required balance among the performance metrics.

To achieve a superior design and predict performance with a high degree of accuracy, a very accurate electromagnetic model of an SRM is required. The developed model can be used to predict numerous important electromagnetic performance characteristics, such as electromagnetic torque, magnetic flux density, flux linkage curves, electromagnetic losses, etc. In the literature, there are three primary subcategories of electromagnetic modeling related to SRMs: analytical modeling, numerical modeling, and MEC modeling. The analytical models based on Maxwell's equations are computationally efficient but provide a less accurate prediction of the electromagnetic performance. The electromagnetic performance characteristics can be precisely estimated by using numerical methods like FEM, BEM, and FDM. FEM is the most extensively used method among these methods as they account for the nonlinearity of the core material and 3D effects. Nevertheless, this approach has a significant computational expense. Even though the MEC approach has a lesser computational cost and reasonable accuracy when compared to FEM, simulating complex geometries is difficult. Additionally, this approach necessitates establishing the flow paths well in advance of the modeling procedure. It has been noted from the literature that the FEM is the most popular approach for creating an SRM's electromagnetic model. The two types of analysis that are used to evaluate an SRM's performance are static analysis and dynamic analysis. Electromagnetic static FEA is mostly used to evaluate the static performance of an SRM. However, the static analysis cannot be used to predict the field weakening capability and the iron core loss of an SRM design. The overall performance of an SRM is mostly evaluated using transient analysis. Predicting the transient performance using transient FEA involves a higher computational cost since tuning the excitation control parameters requires several iterations. To overcome this, circuit-based simulations have been carried out widely in the MATLAB/Simulink environment.

The peak torque, maximum speed, power density, and efficiency demands of traction motors are contrasting from industrial motors. Therefore, distinct considerations must be made when designing electric motors for traction purposes compared to industrial uses. According to the performed literature survey, SRMs have been proposed as motor solutions for EVs with both inner rotor and outer rotor configurations. Identifying the necessary torque-speed performance curve and performance parameters is the first step in designing SRM, which is intended for usage in EV applications. This is accomplished by using the vehicle dynamics model that is based on the specifications of the vehicle and a driving cycle, or by using the torque-speed performance curve of an alternative competitive benchmark motor. The stator outer diameter and stack length (geometrical constraint) along with the DC-link voltage and the peak RMS phase current (electrical constraint) have been fixed based on the space limits in the EV and the performance requirements demanded by the EV respectively. Next, the SRM's design parameters such as the number of phases, the number of poles on the stator and rotor, the lamination material, the dimension of the geometric design variables, and the number of turns per phase have been determined based on the performance criteria mandated by the EV. 2D electromagnetic FEA, owing to its accuracy, has been mostly employed to finalize the aforementioned design parameters and evaluate the performance of SRMs. Further, the steady-state performance has been analyzed using the circuit-based MATLAB/Simulink environment since it is faster than the transient FEA. Consequently, it has been used to optimize commutation angles (excitation control parameters) at various operating speeds.

It has been previously established that altering the dimensions of each of the geometric design variables of an SRM has a distinct effect on the performance metrics, with varying degrees of potential benefit and drawback. Therefore, determining the optimum motor dimensions for a constitutes a multi-objective design optimization problem. Considering the context of electric motor design optimization, stochastic optimization techniques are preferred over deterministic techniques because of the complex and nonlinear nature of the optimization problem. Numerous studies on the design optimization of SRMs for EV applications have been realized in the literature. It has been determined by the completed literature review that employing a Pareto-

based multi-objective design optimization (MODO), combining FEA with surrogate models, and integrating the excitation control parameters in the motor design optimization improves the flexibility, computational speed of the optimization process, and overall performance of the motor drive respectively. Additionally, it has been proven that a traction motor's performance can be fully enhanced throughout the torque-speed operating range by taking the load operating points (LOPs) into account (obtained from a driving cycle) within the motor design optimization formulation process. Following a review of the literature, it is observed that most studies on driving cycle-based design optimization for electric traction motors have concentrated on PMSMs. This is because the dynamic behavior of PMSMs can be evaluated using well-established modeling techniques. In these investigations, within the optimization framework, FEA and the d-q (direct-quadrature) electrical models have been well integrated.

The space constraints inside the wheel hub make it challenging for IW motors to meet the requirements for superior performance metrics. Also, IW motors must be lightweight because their mass affects the EVs' unsprung mass and ride comfort. Because BLDC traction motors have better torque density and efficiency, they are extremely appropriate and frequently used for IW-EV applications. On the other hand, SRMs have poorer torque density, efficiency, and larger torque ripple (all within the same volume limitations) as compared to the BLDC motors because of their higher levels of magnetic saturation in the core. Several IW-SRM topologies have been assessed and suggested for use with EVs and E-2Ws in particular to overcome these problems among SRMs. $N_r > N_s$ SRMs, SRSRMs, MTSRMs, HSRMs, and modular SRMs are a few of the IW topologies reported in the literature. SRM topology with $N_r > N_s$ shows potential benefits in regard to efficiency and torque ripple as compared to $N_s > N_r$ and is widely employed for E-2W applications. The aforementioned topologies—SRSRM, HSRM, and modular SRMs—have complex designs that undermine the simplicity of the traditional SRM structure in addition to being expensive and difficult to construct. The MTSRM (with $N_r > N_m$) topology is an attractive choice for IW motor applications since it preserves the inherent simplicity and cost of traditional SRM designs.

2.8 Motivation and Scope of the Present Work

Design and development of an SRM for an EV application necessitates a thorough comprehension of design and excitation control parameters, design optimization techniques, and topology characterization.

The electromagnetic performance metrics of an SRM are influenced by the dimensions of the geometric design variables. The impact of geometric variables on performance has been documented in research in the past, but the underlying causes have mostly gone unexplored. This is an observed gap in the conducted review of the existing literature.

After examining the body of research on driving cycle-based design optimization for electric traction motors, it is noticed that most studies have mostly focused on PMSMs. Not much work has been reported in this regard for SRMs. This is because PMSMs have well-established modeling techniques to assess their dynamic behavior. However, due to variations in the working principle, motor construction, design analysis, and control excitation procedure when compared to PMSMs, distinct modeling techniques are needed to understand the dynamic behavior of SRMs. A different methodology incorporating these techniques should be framed accordingly to accurately carry out a driving cycle-based design optimization for SRMs.

The MTSRM (with $N_r > N_m$) topology is a potential candidate for IW traction motor applications as it retains the inherent simplicity, cost-effectiveness, and robustness offered by traditional SRM designs. However, there is a lack of adequate literature detailing the design of MTSRM topologies and their electromagnetic performance. The MTSRM and conventional SRMs have not been subjected to a thorough electromagnetic performance comparison investigation that covers the complete torque-speed range for an EV application. Further, the performance of MTSRMs at higher speeds has not been explored. Most of the research on MTSRM has been restricted to three-phase machines. Four-phase machines are known to produce higher average torque, power density, reduced torque ripple, and relatively higher fault tolerance. Hence, the analysis of four-phase MTSRM is necessary and a valuable addition to the existing literature.

To address these aspects, the work being done aims to accomplish the following specific objectives.

- To investigate the influence of geometrical design variables on the electromagnetic performance metrics of an SRM and investigate the reasons responsible for the change in the performance metrics (Objective I).
- To demonstrate a procedure for realizing the multi-objective design optimization (MODO) of an SRM based on a driving cycle (Objective II).
- To carry out a performance comparison between MTSRM and conventional SRM topologies for the full torque-speed range within similar geometrical and electrical constraints (Objective III).

Chapter 3 INFLUENCE OF GEOMETRICAL DESIGN VARIABLES ON SRM PERFORMANCE

3.1 Introduction

A review of the past literature indicated that the electromagnetic performance metrics of an SRM are significantly influenced by the dimensions of the geometric design variables. While the effects of geometric variables on the performance of an SRM have been previously reported, the underlying causes for these influences have largely remained unexamined. A detailed analysis to study the effect of various important design variables on the performance of an SRM is essential for its improved design. In this chapter, the dimensions of the various geometric design variables like the rotor diameter, stator and rotor pole arc angles, and stator and rotor yoke thickness are subjected to a change, and their influence on the static characteristics (flux linkage and static torque) and the electromagnetic performance metrics is investigated (Objective I). The electromagnetic performance metrics such as the average torque and torque ripple have been evaluated. The outline of the procedure to accomplish this is depicted in Figure 3.1. In the first step, the SRM designs are generated as per empirical relations available in the literature. Static torque and flux linkage are obtained using 2D electromagnetic FEA in the second step. Further, the analytical-based magnetic equivalent circuit (MEC) model is employed to determine the reluctance of each segment in the SRM design. In the third step, a correlation between the FEA and MEC models employed in this study is established initially. Further, the variations in the static characteristics of the designs due to the changes in the dimensions of the geometric design variables are analyzed. Significant reluctance segments that have contributed to the change in the static characteristics have been identified by comparing the flux densities/flux paths and using the MEC model. Following this, the electromagnetic performance metrics namely average torque and torque ripple have been evaluated.

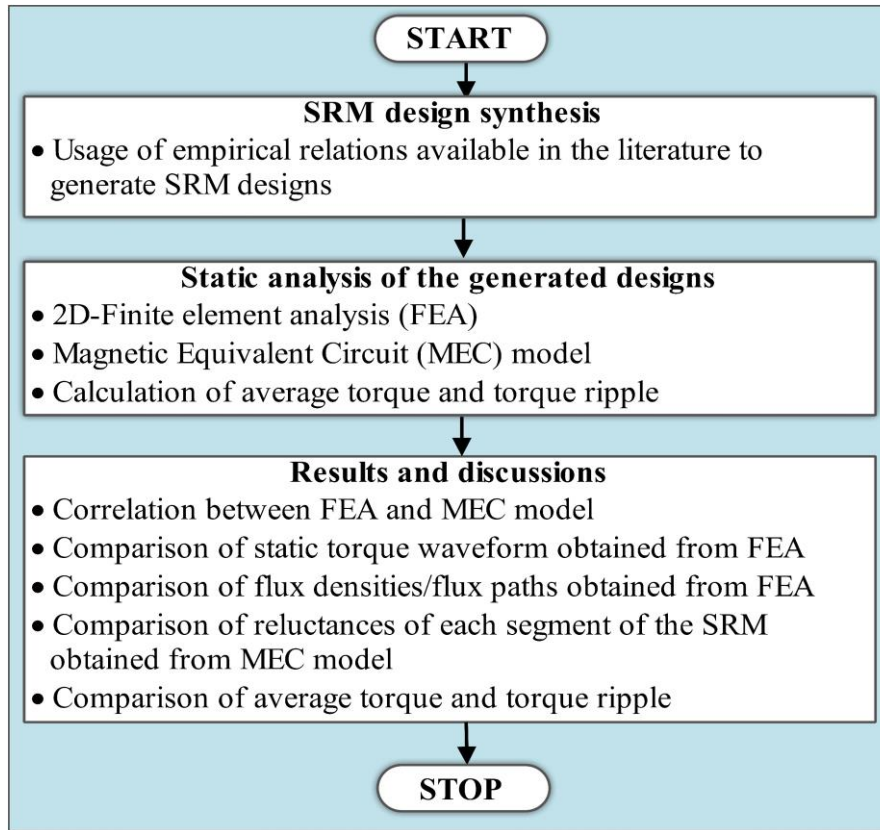


Figure 3.1 Outline of the procedure to study the influence of geometrical design variables on the electromagnetic performance metrics of an SRM

3.2 Theoretical background

3.2.1 Torque output of an SRM

The torque output of an SRM is quantified in terms of the variation in magnetic co-energy (∂W) due to saliency in the design when the rotor traverses to the aligned position from its unaligned position (Krishnan 2001). The shaded area in the flux linkage v/s current graph indicates the total magnetic co-energy (∂W_m) (Figure 3.2).

The instantaneous torque (T_e) (Nm) for a constant phase current (I) (A) is given by the expression;

$$T_e = \frac{\partial W}{\partial \theta} \quad (3.1)$$

This expression indicates the instantaneous torque is equal to the rate of change of co-energy with respect to the angular state of the rotor (θ).

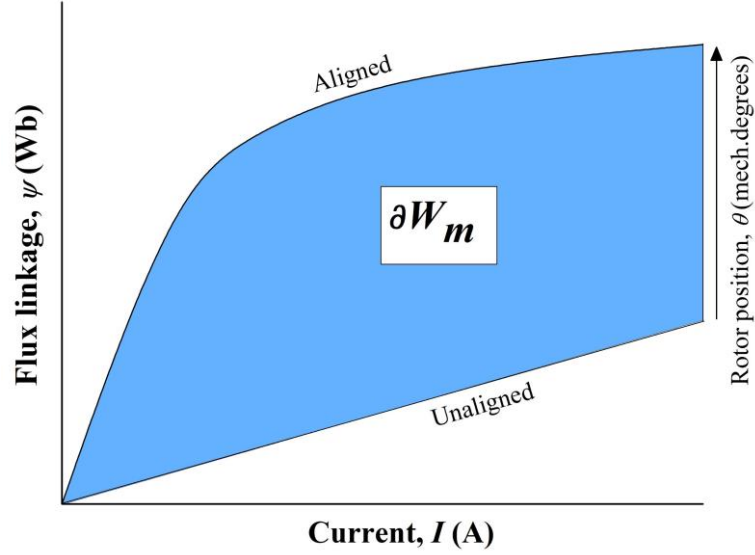


Figure 3.2 Flux linkage vs current characteristics

3.2.2 Magnetic Equivalent Circuit (MEC) of an SRM

The MEC model can be effectively used to analyze the variation of instantaneous torque with the rotor positions based on reluctance variation (Krishnan 2001). The reluctance of a flux tube in each segment is portrayed in the form of resistance. Magnetic reluctance (R) (AT/Wb) for any segment in the circuit is given by the expression;

$$R = \frac{l}{\mu_o \mu_r A} \quad (3.2)$$

where l is the length of the magnetic path, μ_o is the permeability of free space, μ_r is the relative permeability of the magnetic material and A is the area of the cross-section.

The MEC of a flux path (Figure 3.3a) is depicted in Figure 3.3b. The equivalent reluctance (R_{eq}) of the circuit can be expressed as;

$$R_{eq} = 2[R_{sp} + R_g + R_{rp}] + \frac{1}{2}[R_{sy} + R_{ry}] \quad (3.3)$$

For any angular position of the rotor, at a constant magnetomotive force (MMF), the flux established in the circuit is dependent on the equivalent reluctance.

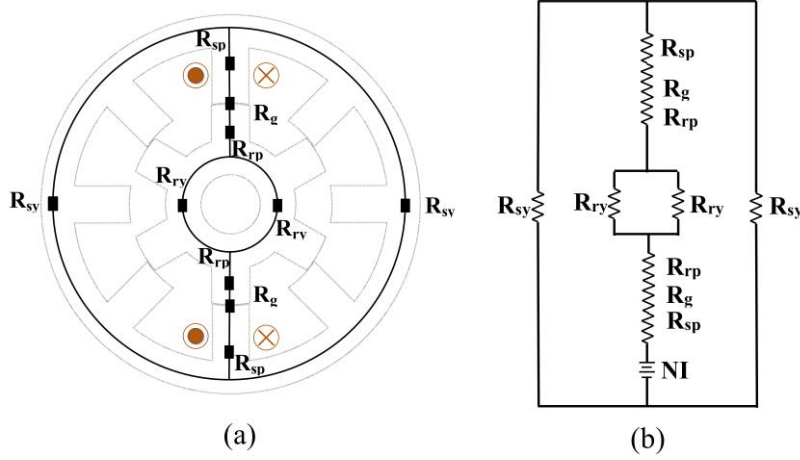


Figure 3.3 (a) Flux path (b) MEC for the flux path

The description corresponding to the reluctances of the flux path in each segment of the SRM has been tabulated (Table 3.1).

Table 3.1 Description of Reluctance

Notation	Description
R_{sp}	Reluctance of the stator pole
R_g	Reluctance of the airgap
R_{rp}	Reluctance of the rotor pole
R_{sy}	Reluctance of the stator yoke
R_{ry}	Reluctance of the rotor yoke

The MMF (AT) required to build the flux in the circuit is expressed as;

$$MMF = NI = \phi R_{eq} \quad (3.4)$$

where NI (product of the number of turns, N , and phase current, I) is the MMF and ϕ is the flux.

3.2.3 B-H characteristics of the core material

The core material used in the present study is M270_35A (Cogent 2023). From Figure 3.4, it is observed that the material offers the least reluctance for operating flux densities in the linear region due to the higher value of relative permeability. Beyond this, it exhibits nonlinear characteristics due to magnetic saturation leading to an increased reluctance owing to a drop in the relative permeability.

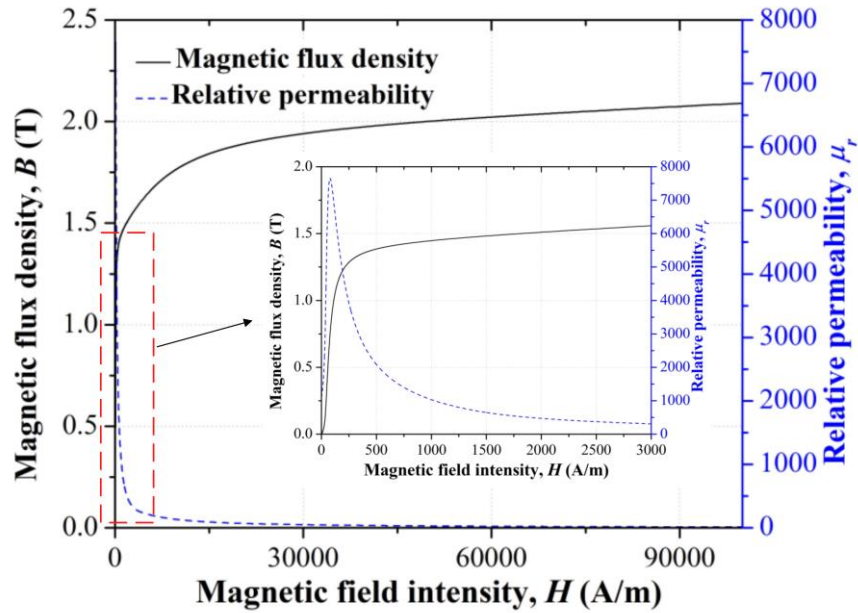


Figure 3.4 B-H curve of M270_35A (Cogent, 2023)

3.3 Methodology

This study intends to investigate the influence of change in the dimensions of the geometric design variables on the electromagnetic performance of an SRM. 2D-FEA is carried out to determine the static characteristics. The reluctance in different segments has been calculated by using the analytical-based MEC model. Based on the results obtained, electromagnetic performance metrics such as average torque and torque ripple are calculated. A four-phase 8/6 inner rotor type SRM configuration (Figure 3.5) is used in this study. The four-phase 8/6 inner rotor SRM was intended to be employed for an E-2W application. The power train unit for the considered application consists of the 8/6 inner rotor SRM coupled with a continuously variable transmission (CVT). This configuration led to the SRM exhibiting characteristics of a low torque, high-speed machine, with specifications of 9 Nm and 9000 rpm. Due to the high-speed requirements of the application, it is preferred to select an SRM configuration with fewer rotor poles. Configurations with a greater number of rotor poles tend to have increased iron-core losses, which negatively impact the efficiency. The notations of each design variable with their respective description have been provided in Table 3.2. Table 3.3 shows the entities that have been predetermined.

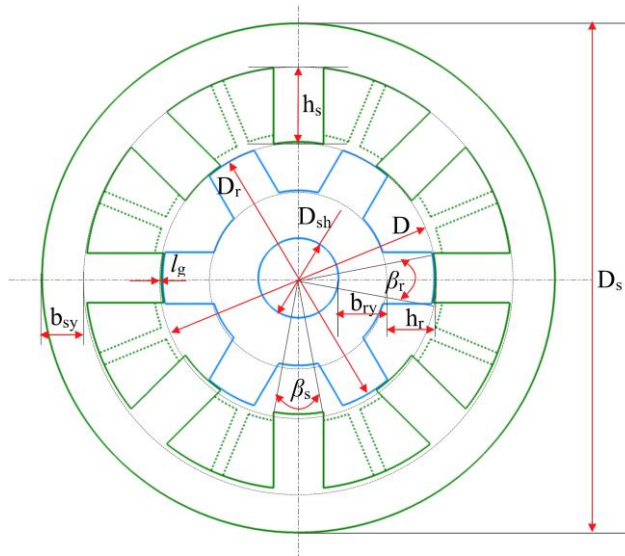


Figure 3.5 Geometric design variables of an 8/6 SRM

Table 3.2 Description of the geometric design variables

Notation	Description
D_r	Rotor diameter
h_r	Rotor pole height
b_{ry}	Rotor yoke thickness
β_r	Rotor pole arc angle
β_s	Stator pole arc angle
D_s	Stator outer diameter
D	Stator bore diameter
h_s	Stator pole height
b_{sy}	Stator yoke thickness
l_g	Airgap

Table 3.3 Predetermined design entities

Motor design variable	Value	Unit
Number of phases, N_{ph}	4	-
Number of stator poles, N_s	8	-
Number of rotor poles, N_r	6	-
Stator outer diameter, D_s	160	mm
Stack length, L	40	mm
Number of turns per phase, N	16	-
Airgap, l_g	0.4	mm
Shaft diameter, D_{sh}	25	mm
Rated speed	5250	rpm
Maximum speed	9000	rpm
Battery voltage	48	V
Peak phase current	250	A

3.3.1 Design of SRM

The procedure for the design of SRM follows those outlined in (Miller 1993) (Krishnan 2001) (Bilgin et al. 2019). Based on this, the empirical relations governing each geometric design variable are enlisted below:

(i) Rotor diameter (D_r): According to (Miller 1993), the ratio of D_r to the D_s is 0.5~0.55. Based on this, for a fixed D_s of 160 mm, D_r is varied from 80-88 mm with an increment of 2 mm. Here, $\beta_s = 22.5^\circ$, $\beta_r = 23.5^\circ$, $b_{sy} = 0.85\omega_{sp}$, and $b_{ry} = 0.85W_{rp}$ where W_{sp} and W_{rp} correspond to the stator and rotor pole width respectively.

(ii) Pole arc angles (β_s and β_r):

(a) Stator pole arc angle (β_s)

$$0.4 < \frac{\beta_s}{\theta_{sp}} < 0.5 \quad (3.5)$$

θ_{sp} is the stator pole pitch (45°). As per the above constraint, β_s is varied from 18° to 23° in steps of 1° . Here, $D_r = 84\text{mm}$, $\beta_r = \beta_s + 1$, $b_{sy} = 0.85W_{sp}$ and $b_{ry} = 0.85W_{rp}$.

(b) Rotor pole arc angle (β_r)

$$1.0 < \frac{\beta_r}{\beta_s} \leq 1.2 \quad (3.6)$$

β_r is varied from 22.5° to 27° in steps of 1.5° . For each trial, $\beta_s = 22.5^\circ$, $D_r = 84\text{mm}$, $b_{sy} = 0.85W_{sp}$ and $b_{ry} = 0.85W_{rp}$.

(iii) Yoke thicknesses (b_{sy} and b_{ry}):

(a) Stator Yoke thickness (b_{sy})

$$\omega_{sy} > b_{sy} \geq 0.5\omega_{sy} \quad (3.7)$$

b_{sy} varies from 11 to 17 mm with an increment of 1mm. For each trial, $\beta_s = 22.5^\circ$, $\beta_r = 23.5^\circ$, $D_r = 84\text{ mm}$ and $b_{ry} = 0.85W_{rp}$.

(b) Rotor Yoke thickness (b_{ry})

$$b_{ry} \geq 0.5\omega_{rp} \quad (3.8)$$

Based on this, b_{ry} is increased from 9 to 19 mm with a step size of 2mm. Here, $\beta_s = 22.5^\circ$, $\beta_r = 23.5^\circ$, $D_r = 84\text{ mm}$ and $b_{sy} = 0.85W_{sp}$.

It is to be noted that the above-mentioned empirical relationships are based entirely on considerations of electromagnetic performance.

3.3.2 2D-Finite-element analysis

Using the electromagnetic FEA-based ALTAIR FLUX software (ALTAIR 2023), a 2D magneto-static simulation is carried out to determine the static characteristics. The geometry of SRM is modeled using AutoCAD and then exported to the FEA software. A non-linear B-H curve is assigned for ferromagnetic materials. Following this, a finite

number of elements are obtained after discretizing the SRM model (Figure 3.6a). A fine mesh is employed in the core regions which are prone to magnetic saturation (stator and rotor pole tips) and in the air gap region since the airgap varies with the angular position of the rotor (Figure 3.6b). In regions away from the airgap, a coarse mesh is employed. A total of 93982 second-order triangular elements were used in the finite element model. The mesh in all the regions of the model was created using the same element type. The quality criteria of the triangular surface elements are based on their smallest angle (δ). The quality of the element is classified as excellent if $\delta > 30^\circ$, good if $\delta \in (15^\circ, 22.5^\circ)$, average if $\delta \in (22.5^\circ, 30^\circ)$, and low if $\delta \in (0^\circ, 15^\circ)$ (ALTAIR 2023). Details of the mesh for one of the simulations conducted have been mentioned in Table 3.4.

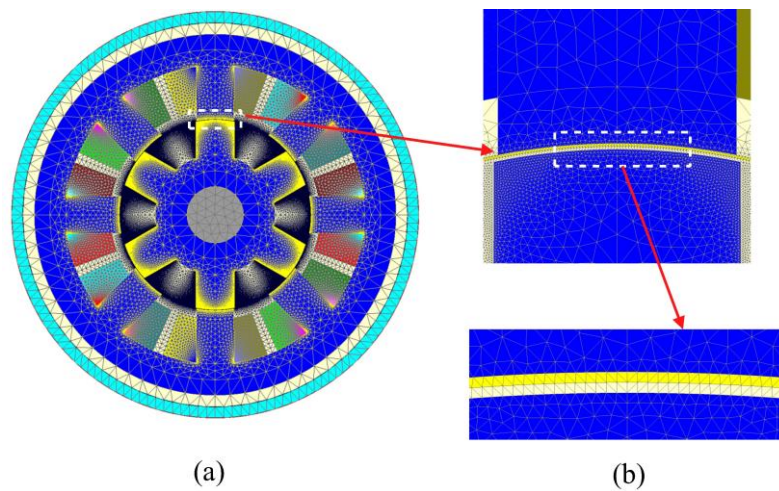


Figure 3.6 (a) FEA model of the SRM (b) Mesh quality in the airgap region

Table 3.4 Mesh details

Description	Value
Number of nodes	1,87,897
Number of surface elements	93892
Mesh order	2 nd
Number of excellent-quality surface elements	99.92%
Number of good-quality surface elements	0.08%
Number of average-quality surface elements	0.01%
Number of poor-quality surface elements	0%

The non-linear Poisson's equation governing the 2D magneto-static field problem in the x, y coordinates is expressed as (Bianchi 2005);

$$\frac{\partial}{\partial x} \left(\gamma \frac{\partial A_z}{\partial x} \right) + \frac{\partial}{\partial y} \left(\gamma \frac{\partial A_z}{\partial y} \right) = -J_z \quad (3.9)$$

where J_z corresponds to the current density comprising the component normal to the plane (x,y) , A_z is the magnetic vector potential in the z -axis, and γ is the magnetic reluctivity. The value of magnetic vector potential at the outer circumference of the SRM (homogenous Dirichlet's boundary condition) is fixed to zero ($A_z = 0$). Also, the distribution of the magnetic field in the axial direction of the SRM within the motor is constant. An excitation current is provided to stator windings. Equation 3.9 is solved to determine the magnetic vector potential at each node. Electromagnetic quantities namely torque, flux linkage, and flux density are then post-processed from the calculated magnetic vector potentials. In this study, the FEA model is solved to determine the static characteristics for 30 mechanical degrees (unaligned to aligned rotor position) with the phase being energized with a constant MMF of 4000 AT ($N = 16$ and $I = 250$ A). The magnetic flux density plot and the flux paths at the aligned position obtained from FEA are shown in Figures 3.7a and 3.7b respectively.

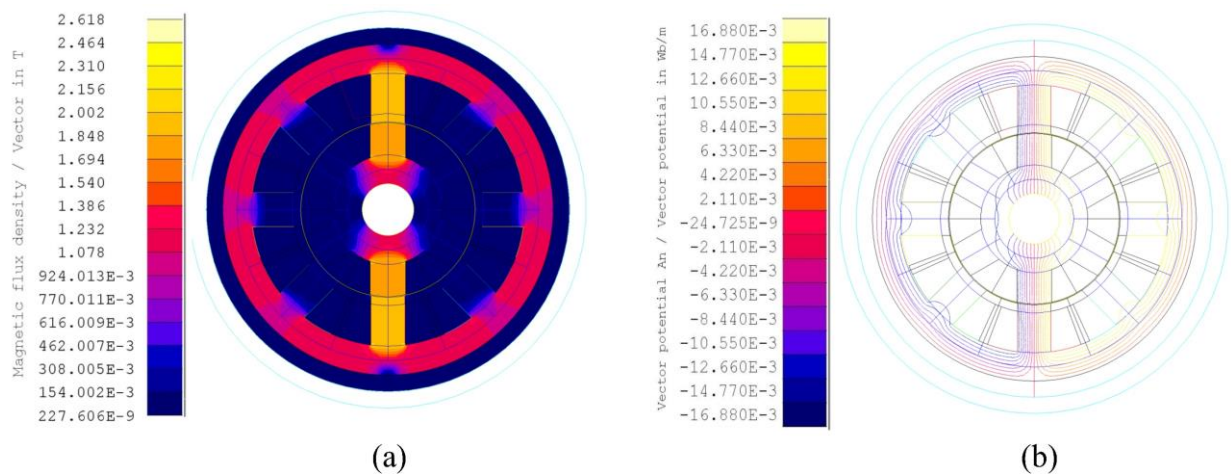


Figure 3.7 (a) Flux density plot (b) Flux paths at the aligned position

3.3.3 MEC Model

The reluctance in different segments of the motor in both the unaligned ($\theta = 0^\circ$) and aligned positions ($\theta = 30^\circ$) is calculated at 250 A using the MEC model (Krishnan

2001) in MATLAB R2020b. In the present model, seven flux paths have been considered (Figures 3.8a and 3.8b). For the unaligned position, the process is initiated by assessing a flux path with an assumption of an elementary value of flux density at the stator pole (B_{sp}). Using this, flux densities are evaluated at different segments. Ampere's circuital equation is applied and expressed as;

$$F_1 = NI = \sum HI \quad (3.10)$$

where NI is the applied MMF and $\sum HI$ is the computed total MMF. The resultant error ensuing between applied (F_1) and calculated MMF (F_c) is given as;

$$\Delta F = F_1 - F_c \quad (3.11)$$

To reduce the error (ΔF) to a minimum value, B_{sp} is reconsidered. Based on this, R_{eq} is calculated (Equation 3.3). Further, the inductance is calculated using equation 3.12.

$$L = \frac{N^2}{R_{eq}} \quad (3.12)$$

Similarly, the inductances corresponding to other flux paths are calculated and summed to obtain the total inductance. The procedure is repeated for the aligned position.

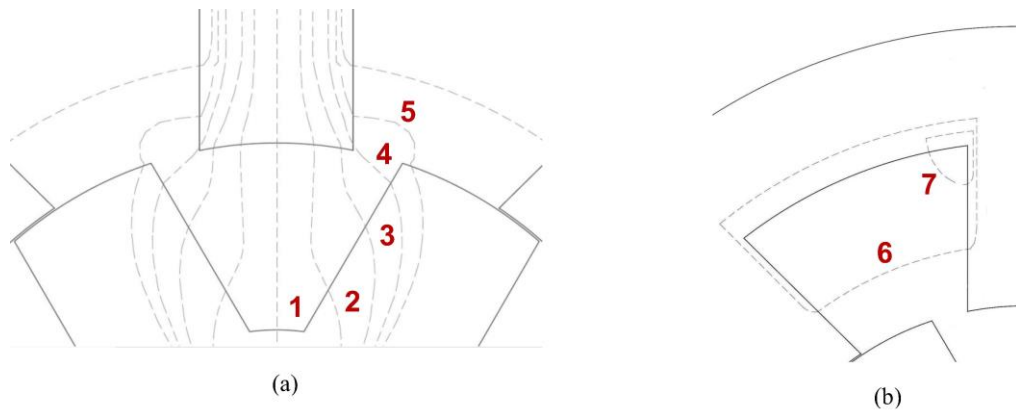


Figure 3.8 Flux paths at the unaligned position (a) 1-5, (b) 6-7

3.3.4 Performance metrics

Based on the static characteristics obtained, the following electromagnetic performance metrics have been calculated;

(i) Average torque (T_{average}): The average torque for one revolution is calculated using the expression (Miller 1993);

$$T_{\text{average}} = \frac{N_{\text{ph}} N_r}{2\pi} \partial W_m \quad (3.13)$$

In this study, since N_{ph} and N_r are both constant, T_{average} is a function of the magnetic co-energy (∂W_m).

(ii) Torque ripple (T_{rip}): The torque ripple is calculated using the expression (Sheth and Rajagopal 2003):

$$T_{\text{rip}} = \frac{T_{\text{max}} - T_{\text{min}}}{T_{\text{average}}} \quad (3.14)$$

T_{max} , T_{average} , and T_{min} are the maximum, average, and minimum torques respectively corresponding to the best 15° in the static torque characteristics. While considering the static torque profile for an 8/6 SRM design, of the 30 mechanical degrees, a single phase is theoretically energized for only 15 mechanical degrees. Hence, these best 15 mechanical degrees around the T_{max} ought to be approximately constant to maximize T_{average} and thereby minimize T_{rip} .

3.4 Results and Discussions

A correlation between FEA and MEC models was established following which the static torque characteristics for a given change in the design variable were obtained using FEA. The resulting differences due to the change in the dimensions of geometrical design variables are explained by investigating the reluctances in each segment of the motor. Subsequently, the electromagnetic performance metrics are calculated.

3.4.1 Correlation between FEA and MEC model

The correctness of the developed model is depicted by comparing the inductance values at the unaligned and aligned rotor positions for one of the designs. The results are tabulated in Table 3.5. A good correlation was found to exist between FEA and the MEC model with an error of about 4%.

Table 3.5 Inductance (mH) comparison

θ ($^\circ$)	FEA	MEC	% error
0	0.0313	0.0326	4.15
30	0.0807	0.0832	3.09

3.4.2 Influence of geometric design variables on the performance indicators

(i) Rotor diameter (D_r)

With an increase in D_r , the instantaneous torque (Figure 3.9a) was found to increase. The difference in torques was more enhanced at and above 7° (i.e. at the start of overlap between the stator and rotor pole corners). This is evident from the co-energy plots of the two extremities of 80 and 88 mm (D_r) at 250A (Figures 3.9b and 3.9c). At and above 7° , the dominance of R_g decreases due to its reduced mean path length and total flux path reluctance constitutes a larger segment of core material (Bilgin et al. 2019). Hence, this scenario necessitates an analysis of R_{sp} which was subject to variation corresponding to a change in D_r . For instance, R_{sp} at 14° was compared to understand the variation of co-energy between 7° - 30° . The operating flux densities for the 88 mm design were found to be lower than those for 80 mm (Figures 3.9d and 3.9e) in the stator pole signifying an increased relative permeability (Figure 3.4). This in conjunction with a shorter length (due to reduced stator pole height) and a higher cross-sectional area ($\beta_s = 22.5^\circ$ in both cases) of the flux path in the stator pole cumulatively decreases R_{sp} (Equation 3.2) and thereby R_{eq} . The above findings are also corroborated by results obtained with the MEC model (Table 3.6, $\theta = 30^\circ$). This augments the available MMF to drive the flux across the airgap thus increasing the rate of co-energy. Hence, the improvement in the instantaneous torque is mainly dictated by R_{sp} whose influence is pronounced between the start and full overlap condition. This caused the co-energy of the 88mm design to be higher than the 80mm design.

Following this, the performance metrics have been calculated. The increase in D_r resulted in an increase in the average torque (Figure 3.9f) due to a higher co-energy which has been detailed in the previous paragraph. Similar findings were also reported in the literature (Jiang et al. 2017). With an increase in rotor D_r , the torque ripple slightly decreases, which is primarily due to less magnetic saturation in the stator pole for

designs with higher D_r . Due to this, designs with higher values of D_r had utilizable 15 mechanical degrees that were broader, which decreased the torque ripple compared to designs with lower values of D_r .

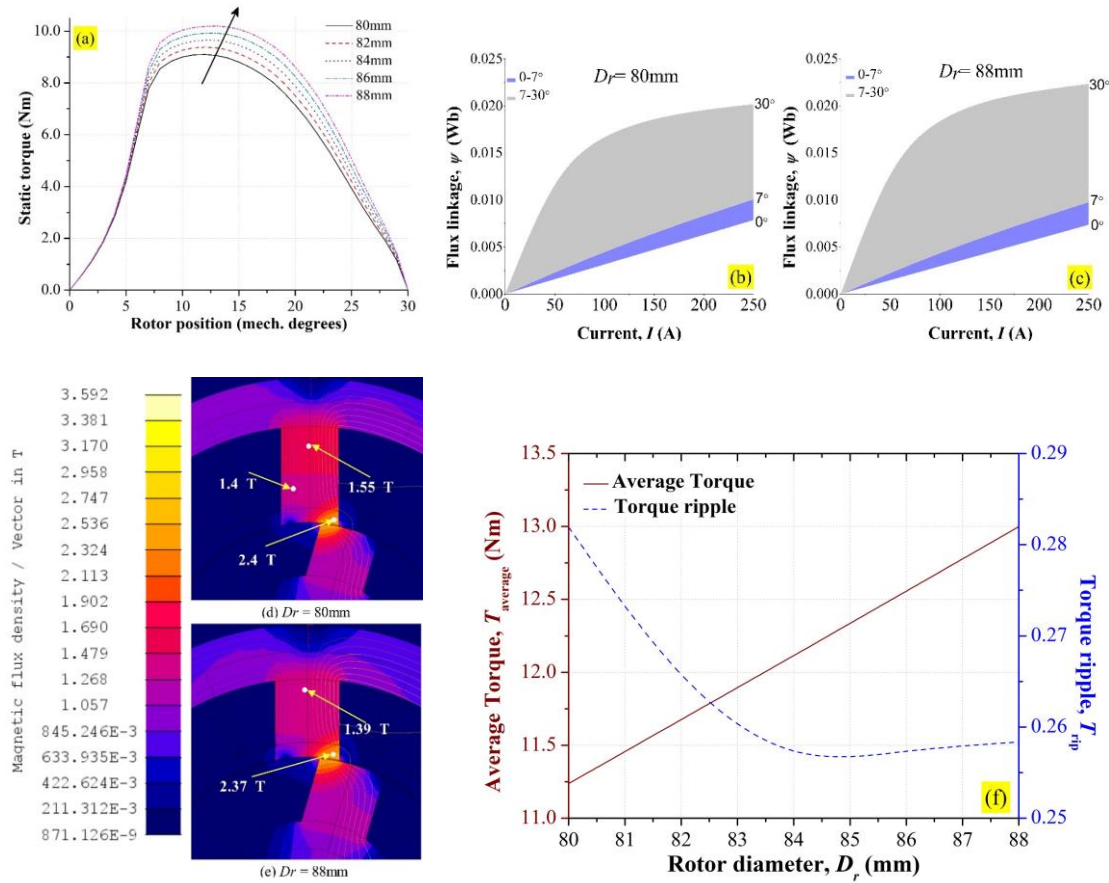


Figure 3.9 Influence of change in D_r ; (a) Static torque profile, (b) and (c) Co-energy comparison between 80 and 88 mm designs (d) and (e) Flux density comparison (f) Average torque and torque ripple

Table 3.6 Reluctance variation with the change in D_r

θ ($^\circ$)	D_r (mm)	R_{sy} (AT/Wb)	R_{sp} (AT/Wb)	R_g (AT/Wb)	R_{rp} (AT/Wb)	R_{ry} (AT/Wb)	R_{eq} (AT/Wb)
0	80	2900	1900	3921000	500	700	7847000
	88	3200	1800	4181000	600	800	8371000
30	80	40600	921000	551200	40600	2400	3048000
	88	41000	788000	536000	42000	2400	2754000

(ii) Pole arc angles

(a) Stator pole arc angle (β_s)

SRM designs with enlarged β_s has ameliorated instantaneous torque for rotor positions below 15° (Figure 3.10a). This contrast is apparent in the 18° and 23° β_s designs from their flux linkage characteristics (Figures 3.10b and 3.10c). The unaligned flux linkage at 250 A was higher in the 23° β_s design in comparison to the former mainly due to a lower value of R_g (Table 3.7). This can be attributed to the reduced length and increased cross-sectional area of the flux path in the air gap caused by the decrease in angular clearance between the rotor and stator pole corners (Mamede et al. 2019). An instance of this is evident from flux linkage distributions at the 8° rotor position obtained from FEA (Figures 3.10d and 3.10e). This phenomenon led to a sharp rise in the static torque, causing an increase in the length of the torque production zone which is noticeable from the static torque profiles of designs with higher β_s (Figure 3.10a).

This behavior caused an enhancement in the average torque (also observed in the co-energy plots, Figure 3.10b, and 3.10c) and a considerable reduction in the torque ripple (Figure 3.10f) which can be ascribed to the best utilizable 15 mechanical degrees during commutation approximating the maximum torque value in the static torque graph.

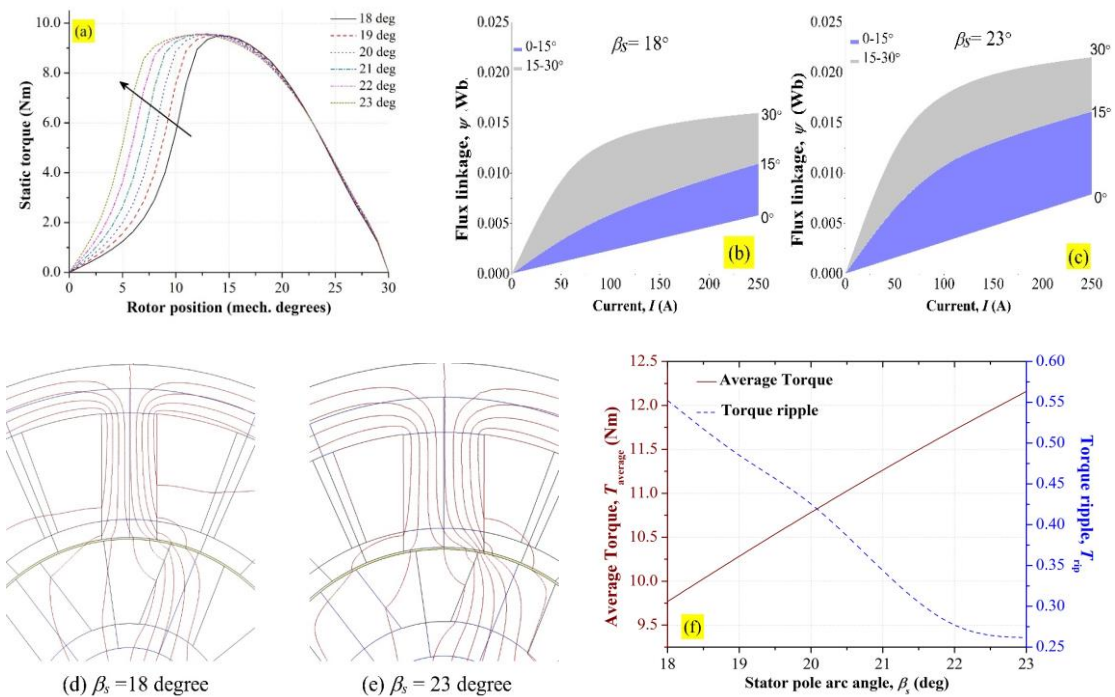


Figure 3.10 Influence of change in β_s ; (a) Static torque profile, (b) and (c) Co-energy comparison between 18 and 23° designs (d) and (e) Flux paths at 8° rotor position (f) Average torque and torque ripple

Table 3.7 Reluctance variation with the change in β_s

θ	β_s	R_{sy}	R_{sp}	R_g	R_{rp}	R_{ry}	R_{eq}
(°)	(°)	(AT/Wb)	(AT/Wb)	(AT/Wb)	(AT/Wb)	(AT/Wb)	(AT/Wb)
0	18	4300	2700	5306000	800	1000	10620000
	23	2700	1800	3899000	500	800	7806000
30	18	51900	1150000	704500	51900	2600	3849000
	23	45100	833000	535000	47100	2500	2855000

(b) Rotor pole arc angle (β_r)

With enlargement in the β_r , the static torque profiles show quick rise and fall (Figure 3.11a). This behavior can be appreciated from the co-energy plots for designs with β_r equalling 22.5° and 27° (Figures 3.11b and 3.11c). The design with 27° β_r had a higher flux linkage between the rotor position of 0° and 10° than the 22.5° β_r which was vice-versa between 10° and 30°. The former is due to the difference in R_g (due to reduced angular clearance between rotor and stator pole corners) between the designs which is evident from the flux distributions at the 5° rotor position (Figures 3.11d and 3.11e). Unaligned flux linkage of the 27° design was higher due to decreased R_{eq} which in effect is due to a lower value of R_g (Table 3.8). Also, its flux linkage for the aligned position was higher owing to lower R_{eq} which is marginally contributed by a lower value of R_{rp} .

Following this, with an increase in β_r , the average torque marginally increased up to 24° and decreased thereafter (Figure 3.11f) which was mainly influenced by the reduction in saliency caused by an enhancement of the unaligned flux linkage. From the static torque profiles, it is observed that the 15 mechanical degrees around the maximum torque point to be utilized during commutation is nearly a constant between all the SRM designs with varied β_r . Hence any change in β_r has minimal influence on the torque ripple which can also be deciphered from the graph (Figure 3.11f).

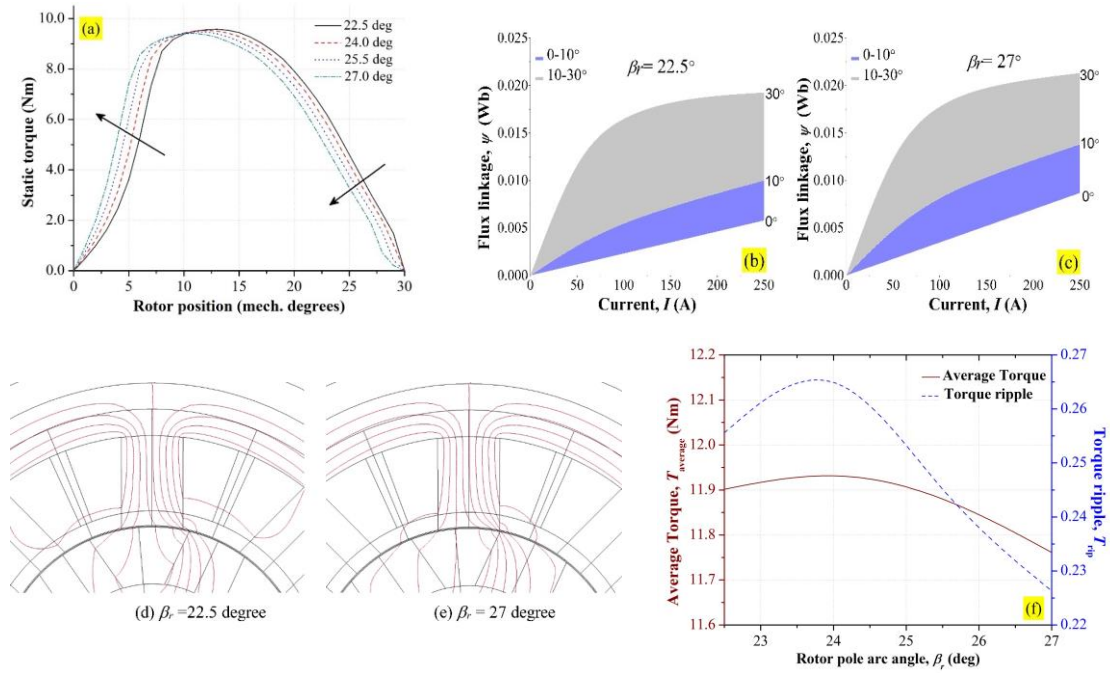


Figure 3.11 Influence of change in β_r ; (a) Static torque profile, (b) and (c) Co-energy comparison between 22.5 and 27° designs (d) and (e) Flux paths at 5° rotor position (f) Average torque and torque ripple

Table 3.8 Reluctance variation with the change in β_r

θ (°)	β_r (°)	R_{sy} (AT/Wb)	R_{sp} (AT/Wb)	R_g (AT/Wb)	R_{rp} (AT/Wb)	R_{ry} (AT/Wb)	R_{eq} (AT/Wb)
0	22.5	2900	1800	4135000	500	700	8278000
	27	2600	1700	3543000	400	700	7093000
30	22.5	31900	854000	564000	43200	2400	2923000
	27	32000	855000	552000	15000	1400	2886000

(iii) Yoke thicknesses

(a) Stator yoke thickness (b_{sy})

Static torque characteristics with different b_{sy} have been plotted in Figure 3.12a. The instantaneous torques at and below 14° were nearly the same for all the designs. Beyond 14°, designs with higher b_{sy} showcased increased instantaneous torques in contrast to those with lower b_{sy} which can also be demarcated in the co-energy plots (Figures 3.12b and 3.12c). Designs with 17 mm b_{sy} displayed lower operating flux densities (reduced magnetic saturation) than those with 11 mm at 21° rotor position in the stator yoke

segment (Figures 3.12d and 3.12e) indicating an increased relative permeability. Also, the former possesses a shorter length and a higher cross-sectional flux path area in the yoke section which collectively decreased R_{sy} (Equation 3.2) and thereby R_{eq} . The results obtained from the MEC model validated the above findings (Table 3.9). This resulted in increased instantaneous torque above 14° for 17 mm in comparison to the 11 mm b_{sy} design.

Based on this, it was noted that enlarging the b_{sy} enhanced the average torque output (Figure 3.12f). Consequently, the designs with higher b_{sy} due to decreased R_{sy} (as explained above) caused the utilizable 15 mechanical degrees in the static torque profile to be as flat as possible near the maximum torque point which resulted in decreased torque ripple. This was in contrast to the designs with lower b_{sy} which displayed higher torque ripple due to increased magnetic saturation in the stator yoke (Figure 3.12f).

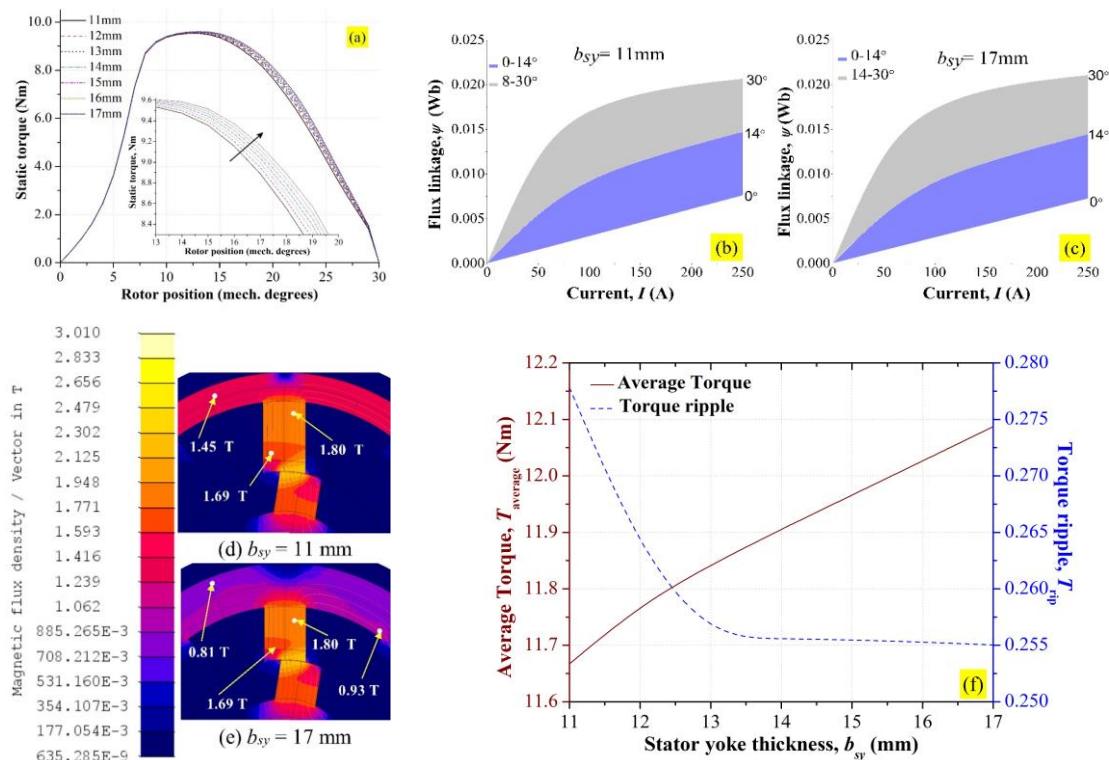


Figure 3.12 Influence of change in b_{sy} ; (a) Static torque profile, (b) and (c) Co-energy comparison between 11 and 17 mm designs (d) and (e) Flux density comparison, (f) Average torque and torque ripple

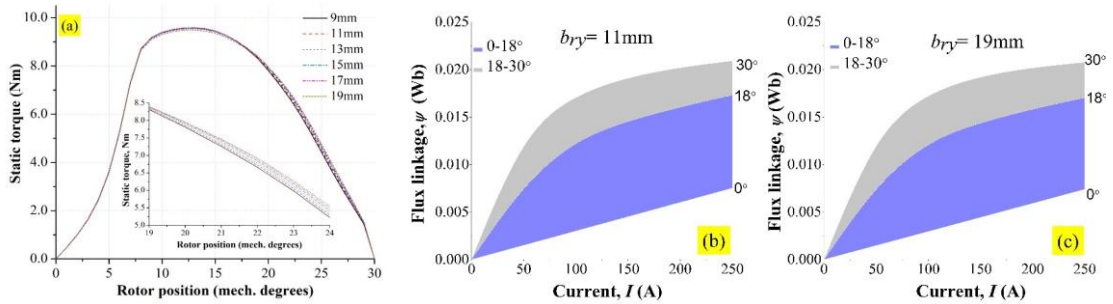
Table 3.9 Reluctance variation with the change in b_{sy}

θ (°)	b_{sy} (mm)	R_{sy} (AT/Wb)	R_{sp} (AT/Wb)	R_g (AT/Wb)	R_{rp} (AT/Wb)	R_{ry} (AT/Wb)	R_{eq} (AT/Wb)
0	11	3600	2000	4045000	500	700	8098000
	17	2400	1700	4241000	600	700	8487000
30	11	49900	796000	653300	37500	2900	2999000
	17	24700	781000	649000	38000	2800	2947000

(b) Rotor yoke thickness (b_{ry})

An increase in b_{ry} increases the instantaneous torques above the 19° rotor position (Figure 3.13a). However, this improvement is marginal and not significant. This is evident from co-energy plots for b_{ry} with 11 and 19 mm (Figures 3.13b and 3.13c). For a given fixed D_r , increase in rotor yoke thickness shortens the height of the rotor pole. This causes a dilution in the flux density from the rotor pole to the yoke (Figures 3.13d and 3.13e, $b_{ry} = 9$ mm and 19 mm at 21° rotor position) reducing the reluctance of the segments R_{rp} and R_{ry} and causing an improvement in the instantaneous torques. These observations are also corroborated by the results obtained from the MEC model (Table 3.10).

Also, with the increase in b_{ry} up to 17 mm the average torque was found to increase followed by a drop (Figure 3.13f). For designs with b_{ry} greater than 17 mm, the increase in unaligned flux linkage impacted the saliency remarkably causing a decrement in average torque. Designs with varied b_{ry} showed minimal effect on the torque ripple since the static torque profiles showed only a marginal change with varied b_{ry} (Figure 3.13f).



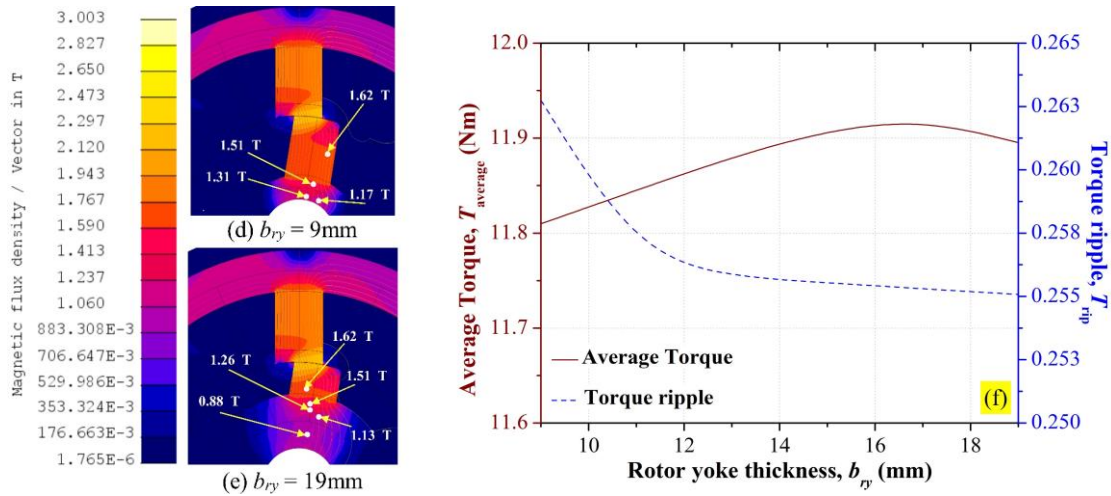


Figure 3.13 Influence of change in b_{ry} ; (a) Static torque profile, (b) and (c) Co-energy comparison between 9 and 19 mm designs (d) and (e) Flux density comparison (f) Average torque and torque ripple.

Table 3.10 Reluctance variation with the change in b_{ry}

θ (°)	b_{ry} (mm)	R_{sy} (AT/Wb)	R_{sp} (AT/Wb)	R_g (AT/Wb)	R_{rp} (AT/Wb)	R_{ry} (AT/Wb)	R_{eq} (AT/Wb)
0	9	3100	1900	4151000	700	1100	8308000
	19	2500	1700	4012000	400	500	8029000
30	9	42000	855000	565500	46700	3000	2958000
	19	41200	855000	565700	44800	1000	2946000

3.5 Summary

In this chapter, a comprehensive parametric study focussed on analyzing the influence of the dimensions of geometric design variables on the performance of an SRM was carried out. The empirical relationships available in the literature were used to generate the SRM designs. Using 2D electromagnetic FEA, the static characteristics of each design, such as static torque and flux linkage were generated. Key reluctance segments contributing to the change in the static characteristics have been determined by comparing the flux densities and by using the MEC model. The veracity of the developed MEC model has been verified by correlating their results with FEA. Various geometric design variables like the rotor diameter, stator and rotor pole arc angles, and stator and rotor yoke thickness have been analyzed based on changes in static characteristics. Electromagnetic performance metrics namely the average torque and

torque ripple were calculated. The major findings and significant conclusions of this chapter are detailed in Section 6.2 under Chapter 6.

Chapter 4 DRIVING CYCLE-BASED DESIGN OPTIMIZATION OF AN SRM

4.1 Introduction

Design optimization is an essential step in an SRM's design process that improves its overall performance. The literature survey in Chapter 2 revealed that in order to increase their performance comprehensively, the LOPs (obtained from a driving cycle) have to be included in the design optimization process. A novel procedure for implementing the multi-objective design optimization (MODO) of an SRM based on a driving cycle is described in this chapter (Objective II).

The flowchart of the proposed optimization strategy is depicted in Figure 4.1. In the first step, the LOPs and the target torque-speed envelope for the SRM are estimated based on the driving cycle and vehicle parameters using the vehicle dynamics model. To simplify the optimization process, a k - means clustering algorithm is employed to divide the LOPs into a finite number of representative points (RPs) in the second step. In the third step, the number of phases, pole count on the stator and rotor, and an initial design of the inner rotor type SRM are determined using empirical formulae available in the literature. In the fourth step, MODO is performed to obtain the Pareto-optimal set. An optimal design that provides the best balance between the design objectives is chosen from the Pareto-optimal set and the dimensions of design variables are used to build a prototype. In the fifth step, the static along with the dynamic performance of the prototype SRM is evaluated. The SRM prototype and the experimental setup for evaluating the static and dynamic performance has been developed in-house. The experimental results of the prototype SRM are compared with those of FEA simulations.

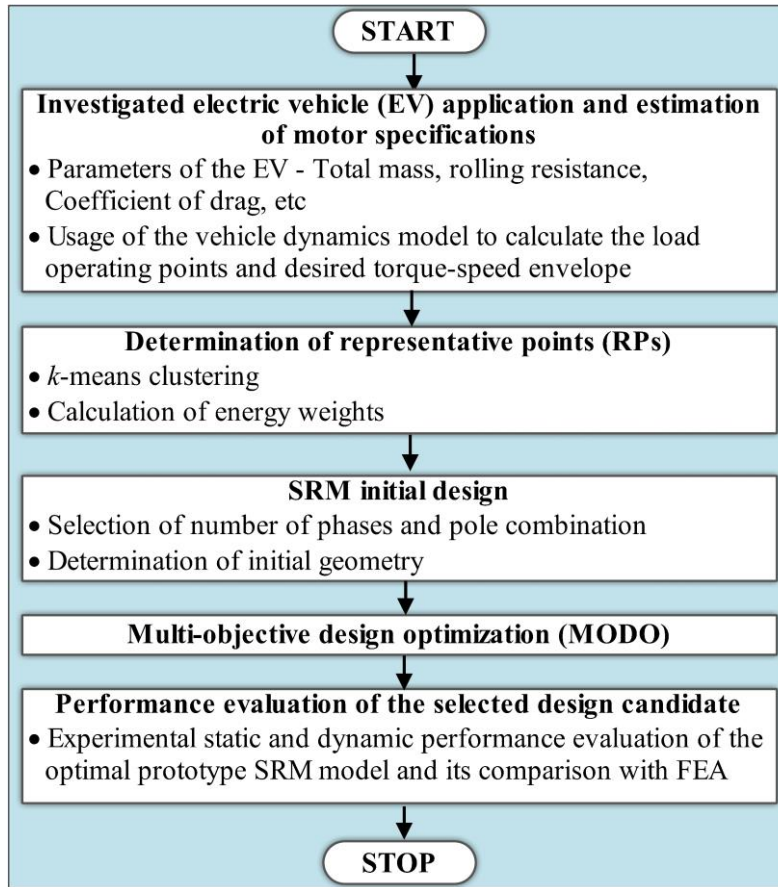


Figure 4.1 Outline of the MODO of an SRM based on a driving cycle

4.2 Investigated EV application and estimation of motor specifications

The EV under investigation in this study is an E-rickshaw (a three-wheeled vehicle), with the ability to ply in suburban environments with a power output of ~2 kW and a maximum speed of around 25 km/h. The E-rickshaw is a popular choice of paratransit in metropolitan India owing to its cost-effectiveness and flexibility. A review of the Indian E-rickshaw market reveals that inner rotor-type BLDC motors dominate the sales of electric traction motors in this category (Tsuyo 2023) (RetroEV 2023) (Ecomotors 2023). Table 4.1 summarizes the performance specifications of a few popular inner rotor-type BLDC machines used in Indian E-rickshaws with a power output of ~ 2 kW. Furthermore, these machines are integrated with a gearbox and a differential to transfer power to the wheels.

Table 4.1 Performance comparison between commercial E-rickshaw BLDC motors and the prototype machine

Manufacturer / Product user	Torque (Nm)	Mechanical power output (kW)	Maximum Speed (rpm)
Tsuyo (Tsuyo 2023)	24	1.96	2850
Mahindra Treo Yaari (RetroEV 2023)	22	1.95	2700*
Eco motors (Eco motors 2023)	-	2.2	3000
Prototype SRM (Present)	22	2	3000

*Estimated from references

In the present work, the LOPs and required motor performance specifications have been determined based on a driving cycle and vehicle parameters by using the vehicle dynamics model (Ehsani et al. 2018). Figure 4.2 illustrates the schematic of an E-rickshaw and the forces of the vehicle dynamics model. The parameters of the E-rickshaw are enlisted in Table 4.2. The driving cycle established in a Tier II city in India by the Council of Scientific and Industrial Research - Indian Institute of Petroleum (CSIR-IIP), India (Figure. 4.3(a)) for an E-rickshaw has been employed (Pathak et al. 2017). A driving cycle often depicts a vehicle's driving characteristics over time and accurately elucidates the actual operating conditions of the vehicle. The driving cycle in Figure 4.3(a) represents driving conditions in a Tier II city in India. It depicts an 18.75-minute, 4.31-kilometer trip with 1.95 stops per km, an average speed of 13.79 km/h, and a top speed of 28.43 km/h. Using Equation 4.1, the motor torque is calculated based on the traction force F_t , which is obtained by adding the inertia force F_j , rolling force F_{rr} , drag force F_w and climbing force F_g (Ehsani et al. 2018).

$$\left. \begin{aligned}
 F_j &= ma \\
 F_{rr} &= f_r mg \cos \alpha \\
 F_w &= \frac{1}{2} \rho C_d A v^2 \\
 F_g &= mg \sin \alpha \\
 F_t &= F_j + F_{rr} + F_w + F_g
 \end{aligned} \right\} \quad (4.1)$$

In the above equations, m represents the total mass of the E-rickshaw, a is the vehicle acceleration, g is the acceleration due to gravity, f_r denotes the rolling resistance coefficient, α indicates the gradient of the road, ρ is the density of air, A_f specifies the frontal area, C_d signifies the air drag coefficient and v represents the velocity of the E-rickshaw. It is important to mention that the vehicle dynamics model is conducted on a flat route. With the specified wheel radius (r) and differential gear ratio, the motor speed is calculated using the velocity (v) of the E-rickshaw. The regenerative area is not considered in this analysis since the machine is intended for a motoring application.

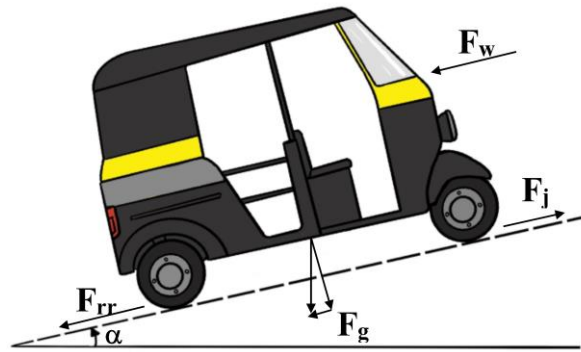


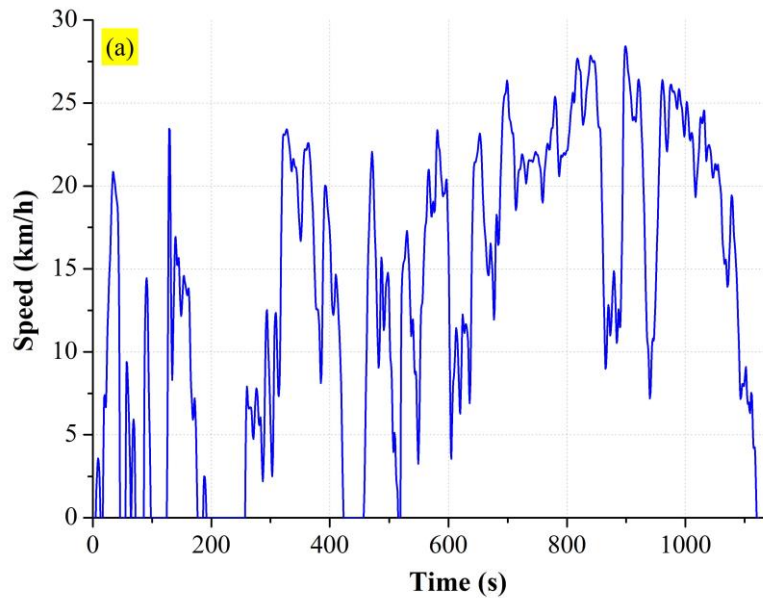
Figure 4.2 Forces acting on an E-rickshaw

Table 4.2 Parameters of the E-rickshaw (RetroEV 2023) (Sreejith and Rajagopal 2017)

Parameter	Value
Mass (kerb load / pay load) (m)	588 (276/312) kg
Rolling resistance (f_r)	0.015
Drag coefficient (C_d)	0.5
Frontal area (A_f)	2.09 m ²

Density of air (ρ)	1.25 kg/m ³
Acceleration due to gravity (g)	9.81 m/s ²
Wheel radius (r)	0.2475 m
Differential gear ratio	10:1
Efficiency of differential	0.98

Figure 4.3(b) depicts the distribution of operating points along the motor's torque speed range for the investigated driving cycle. The idealized target peak torque profile is shown, assuming a hyperbolic variation above the base speed to create an idealized constant power range. It can be noted that the performance requirements of the SRM thus obtained are similar to BLDC motors used to power some of the popular E-rickshaws in the Indian E-rickshaw market (Table 4.1). Further, from Figure 4.3(b), it can be observed that the LOPs are dispersed across the torque-speed envelope, with the focus being the high-speed, low-torque region. This unduly emphasizes the significance of locating the motor's best efficiency zone in this region.



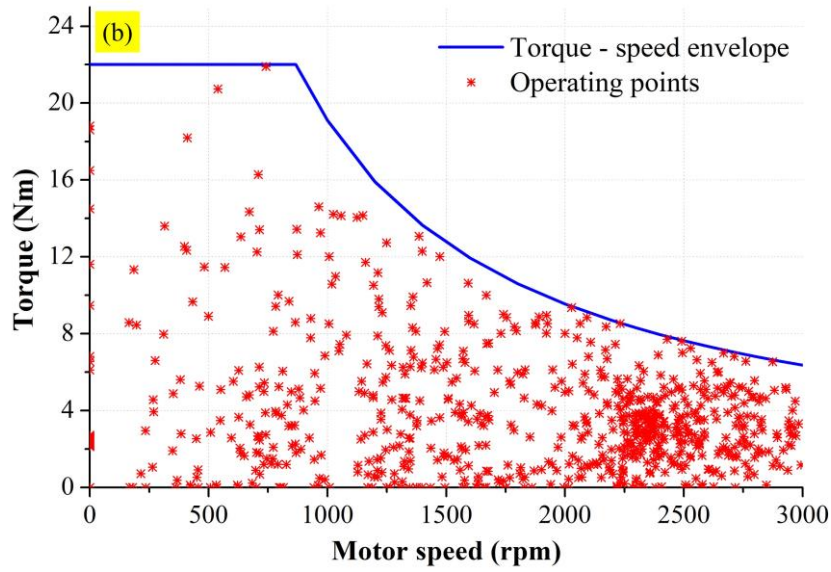


Figure 4.3 (a) CSIR-IIP driving cycle speed profile (Pathak et al. 2017) (b) Operating points of the E-rickshaw obtained from CSIR-IIR driving cycle

Based on the analysis, Table 4.3 summarises the design targets along with constraints for the inner rotor type SRM design. The designed SRM ought to, at the very least, achieve the peak average torque-speed envelope. Owing to hill climbing and unexpected overload situations during driving, and inaccuracies in motor manufacturing and assembly, it must be ensured that the peak average torque produced by the motor is adequately greater than the target torque (Ehsani et al. 2018) (Diao et al. 2022). In the present study, a current restriction (~ 20 A RMS) is imposed by the asymmetric half-bridge (AHB) inverter (SEMIKRON - 08470082AA) which is used to drive the SRM. For SRMs, the ratio between the RMS current and peak current lies in the range of 0.3~0.75 (Howey et al. 2020) (Jiang et al. 2017). Considering a value of 0.57 in the present case, the rated peak phase current is accordingly set to 35 A. The DC-link voltage is fixed to 144V. The stator outer diameter (D_s) and the stack length (L) in the present study are fixed to 160 mm and 190 mm respectively based on the space limitations. Because of the constraints imposed by manufacturing, the SRM's air-gap length (l_g) is fixed to the lowest possible value of 0.4 mm. Consequently, considering all the above-mentioned limitations, the maximum torque of the designed SRM for the E-rickshaw must exceed 22 Nm at the base speed of 868 rpm and 6.36 Nm at the maximum speed of 3000 rpm respectively.

Table 4.3 Target performance specifications and design restrictions for the SRM

Parameter	Value
Maximum torque	>22 Nm
Peak power	2 kW
Maximum motor speed	3000 rpm
Base speed	868 rpm
Stator outer diameter (D_s)	160 mm
Stack length (L)	190 mm
DC-link voltage (V)	144 V
Peak phase current (I_{peak})	35 A
Peak RMS phase current (I_{rms_lim})	~20 A
Air-gap length (l_g)	0.4 mm
Shaft diameter (D_{sh})	22 mm

4.3 Implementation of the k -means algorithm to determine the representative points (RPs)

Ideally, in an electric traction motor design optimization process that considers a driving cycle, the performance of each design candidate at each of the operating points (indicated in Figure 4.3b) needs to be evaluated. However, this approach is not computationally effective owing to the complications of the executed FEA-based design optimization algorithm. Alternatively, torque-speed data points can be split into various clusters based on the location and density of the operating points by employing data mining techniques like the k -means clustering algorithm (Fatemi et al. 2018). The k -means clustering algorithm has been selected in the current study over other methods since it uses a systematic approach and the number of final clusters obtained using this method is dependent on the distribution density of the LOPs (Salameh et al. 2019). More information about the different methods used to obtain the clusters and corresponding RPs, along with an evaluation of their advantages and disadvantages,

can be found in Section 2.4 of Chapter 2. The k -means clustering algorithm is an unsupervised machine learning algorithm employed for clustering the data points into ' k ' number of clusters (Selim and Ismail 1984). It has several advantages, including flexibility (ability to work with different types of data), simplicity (as it is based on simple mathematical ideas), fast convergence, high efficiency in clustering big data sets, and ease of implementation (Salameh et al. 2019). Owing to these benefits, k -means clustering is widely used in segmentation and recommendation engines, health care, fault detection and diagnosis of rotating machines, power system analysis, etc (Nandapala and Jayasena 2020) (Ravuvur et al. 2020) (Wang et al. 2020) (Green et al. 2014). This method is categorized under partitional clustering, where each cluster consists of a centroid. As per the equation given below, the algorithm seeks to minimize the total intra-cluster variance or the within-cluster sum of squares (J) defined for n data points and k clusters:

$$J = \sum_{j=1}^k \sum_{i=1}^n \|x_i^{(j)} - c_j\|^2 \quad (4.2)$$

where, $\|x_i^{(j)} - c_j\|^2$ is the distance between the centroid c_j of cluster j , and the data point $x_i^{(j)}$. The primary indicators of good clustering are low intra-cluster variance and high inter-cluster variation (Salameh et al. 2019). The tightness of the representative points within a cluster is denoted by the intra-cluster variance, while the distance between clusters is indicated by the inter-cluster variation. Both these indicators are dependent on the choice of k . To assist the user in selecting the k , methods like the elbow approach and silhouette analysis have been widely followed (Fatemi et al. 2018) (Mahmood et al. 2023). The elbow approach is used to estimate the intra-cluster variation of clustering using the J v/s k curve. As per this approach, the appropriate value of k is indicated at the point where the curve forms an elbow. Silhouette analysis can be used to assess both the inter-cluster and intra-cluster variance (Salameh et al. 2019). A high average silhouette width calculated from the silhouette analysis indicates the goodness of clustering. The average silhouette width value falls between -1 and 1. An average silhouette width of 1 indicates that data points are relatively compact within the cluster to which it belongs and separated from adjacent clusters. The necessary formulas and

the steps involved in calculating the average silhouette width are described in (Mahmood et al. 2023).

Using the k -means algorithm described above, the operating points within the torque-speed envelope obtained in Subsection 4.3 are grouped into a finite number of clusters, thereby yielding the RPs (Fig. 4.4). Each RP, which is the centroid of a cluster is associated with a value of torque and speed respectively (Table 4.4). From the elbow approach, the appropriate number of clusters has been determined to be four as seen in Fig. 4.5a. An elbow is formed at $k = 4$ as there was no significant variation in J for $k > 4$. Additionally, the findings of the silhouette analysis (Fig. 4.5b) corroborated with the elbow analysis and showed that four clusters were appropriate since the average silhouette width was found to be at its maximum for $k = 4$.

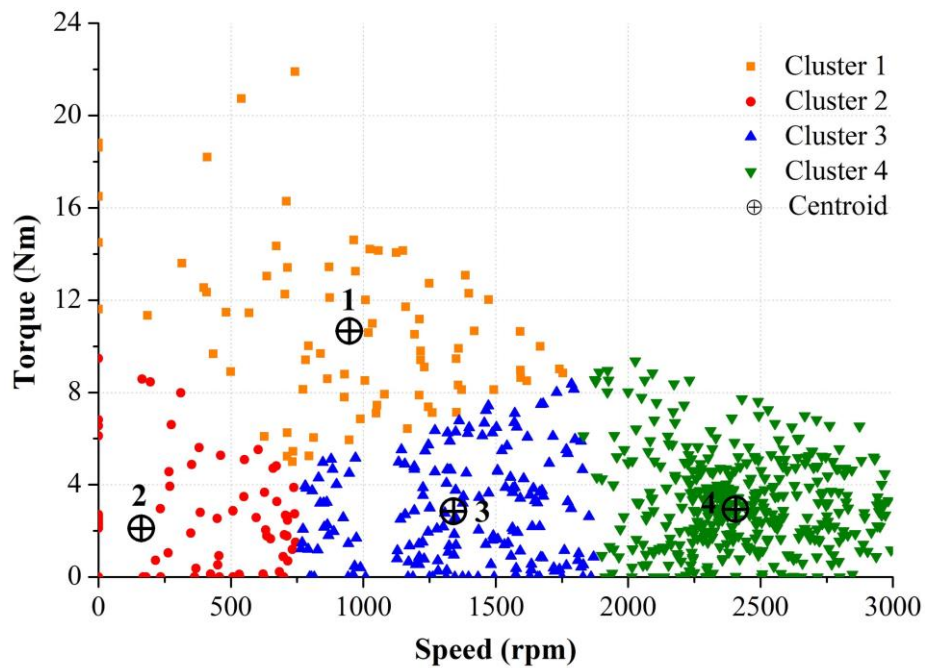


Figure 4.4 Determination of representative points (RPs) using k-means algorithm

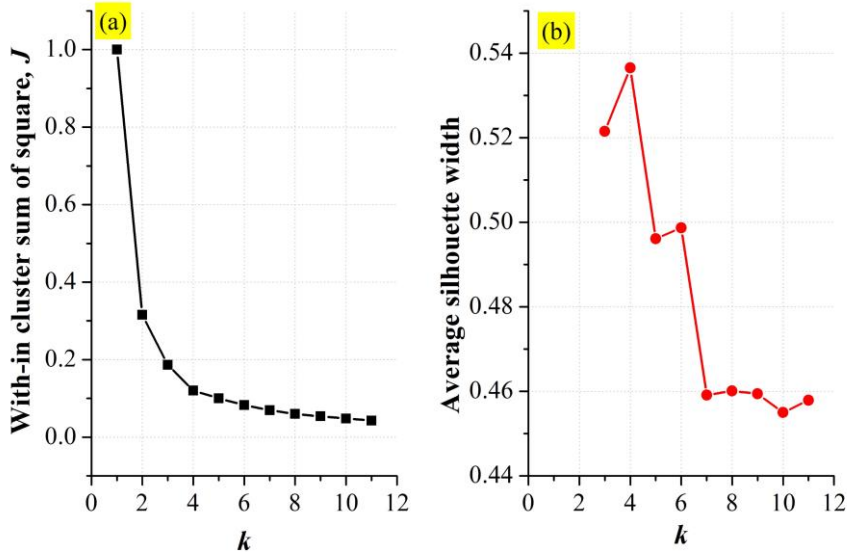


Figure 4.5 Selection of the appropriate number of clusters (a) Elbow approach (b) Silhouette analysis

Using the torque output and speed values depicted in Fig. 4.3b, the absolute value of the energy spread over the full torque-speed envelope is determined from the product of the torque, speed along with the time spent at every load operating point. The ratio of the total energy consumed across all points in each cluster to the total energy consumed across all clusters can be used to calculate the energy weights ($W_{E,i}$) for the RPs. This is expressed as (Salameh et al. 2019);

$$W_{E,i} = \frac{E_i}{\sum_{j=1}^k E_j} \quad (4.3)$$

where, E_i is the energy distribution of the points within the cluster and E_j is the total energy distribution of the points in all the clusters. The RPs along with their computed energy weights ($W_{E,i}$) are enlisted (Table 4.4).

Table 4.4 Representative points (RPs) and Energy weights

RP (k_i)	Speed (ω_i) (rpm)	Torque (T_i) (Nm)	Energy weight ($W_{E,i}$)
1	947.45	10.66	0.1611
2	161.26	2.11	0.0135

3	1340.26	2.81	0.1544
4	2405.41	2.93	0.671

4.4 SRM initial design

4.4.1 Selection of number of phases (N_{ph}) and stator/rotor pole (N_s/N_r) combination

The number of phases (N_{ph}) is known to have a substantial impact on the performance and cost of the SRM drive system (Miller 1993). It has been demonstrated that four-phase SRMs have an enhanced average torque, torque density, and lower torque ripple as compared to the three-phase SRM (Krishnan 2001). However, the number of converter phase units, drivers, voltage, and current sensors required for four-phase is higher which raises the cost. After weighing the trade-offs between all the criteria, performance is chosen over cost and the number of phases is fixed to four.

To limit the iron core loss to a minimum value, a four-phase configuration with the least stator pole count ($N_s = 8$) is selected. The rotor pole count (N_r) is set to 6 based on Miller's equation (Miller 1993), $N_r = N_s - 2$, thereby resulting in an 8/6 SRM configuration. Though increasing N_r further may reduce the torque ripple, their efficiencies for high-speed applications are lower owing to an elevated iron core loss (Krishnan 2001).

4.4.2 Initial sizing

Within the spatial and electrical constraints, it is proposed to develop a 2 kW four-phase inner rotor type 8/6 SRM that can satisfy the on-road operational requirements of an E-rickshaw. Figure 4.6 shows the design variables of the 8/6 SRM. Initially, using the output power equation provided below (Krishnan 2001), the stator bore diameter (D) is calculated.

$$P_{out} = k_e k_d k_1 k_2 B_s A_s D^2 L n_n \quad (4.4)$$

where P_{out} represents the output power; k_e and k_d are the efficiency and the duty cycle respectively (initially, both are fixed to 1); $k_1 = \pi^2/120$; k_2 is a variable, whose value is dependent on the ratio of the unaligned and aligned inductance; B_s specifies the

saturation flux density (2T); n_n is the base speed; A_s represents the specific electric loading which is expressed as;

$$A_s = \frac{2NI_{peak}q}{\pi D} \quad (4.5)$$

where N signifies the number of turns per phase, I_{peak} indicates the limit of the chopping current and q denotes the number of phases conducting concurrently (considered as 1). Considering the motor to be naturally cooled, the value of A_s is set to 25000 A/m. An initial value of N has been estimated by using Equation (4.5). Based on the empirical relations given in (Miller 1993), the initial values of the pole arc angles and pole heights, have been chosen. The procedure of initial designing is iterative and is accomplished using ALTAIR FLUX electromagnetic FEA (ALTAIR 2023). The initial dimensions of the design variables are enlisted (Table 4.5). Each SRM phase in the 8/6 topology under consideration comprises two coils wound on the two diametrically opposed poles of the stator, and these coils are connected in series. M270_35A has been chosen as the core material for the stator and rotor (Cogent 2023).

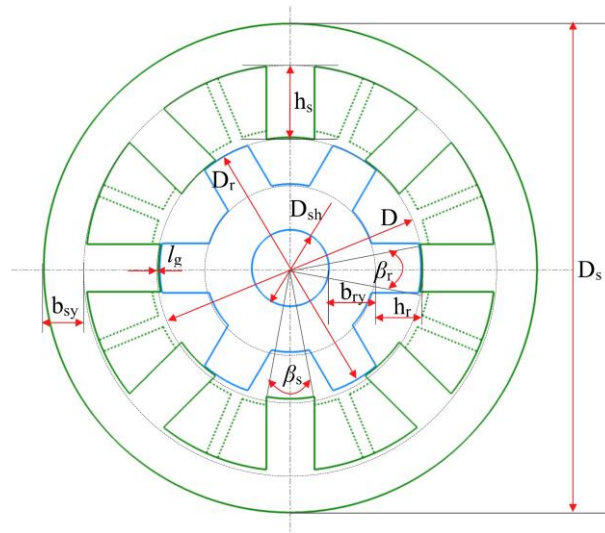


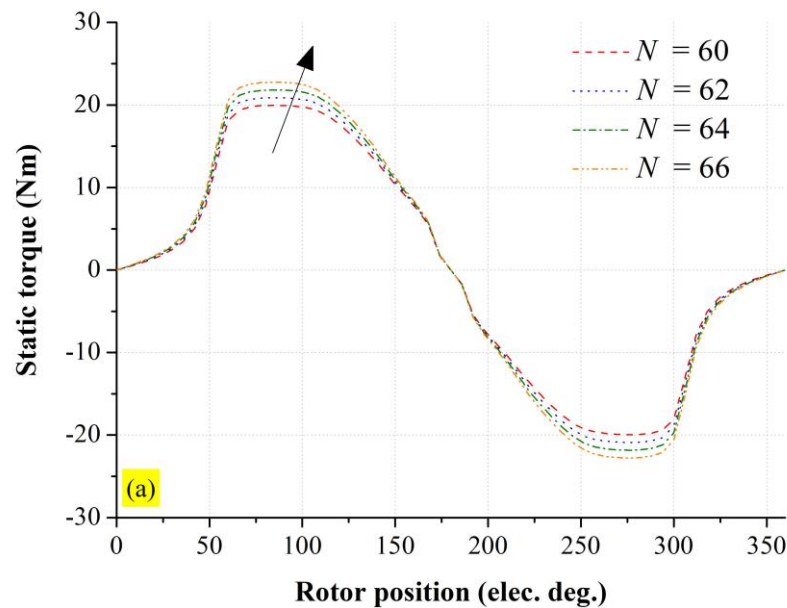
Figure 4.6 Design variables of the four-phase 8/6 SRM

Table 4.5 Initial SRM dimensions

Design variable	Value
Stator bore diameter (D) (mm)	83.01
Stator pole arc angle (β_s) ($^\circ$)	19.09

Rotor pole arc angle (β_r) ($^\circ$)	21.68
Stator slot depth (h_s) (mm)	26.96
Rotor slot depth (h_r) (mm)	10.94

Further, the value of N has been refined to satisfy the target torque-speed envelope within the set electrical constraints. The procedure put forth using the SRM drive mode (Bilgin et al. 2019) is used to achieve this. The static characteristics of the initial design with a varied number of turns per phase ($N=60-66$) are obtained using electromagnetic static FEA. These characteristics (*i.e.* static torque and flux linkage), as lookup tables (LUTs) are then provided as an input into the SRM drive model to determine the optimized commutation angles (θ_{on} and θ_{off}). The optimized θ_{on} and θ_{off} are obtained using a search algorithm-based single objective optimization intended to maximize the average torque at various speeds within the I_{rms_lim} . The static and dynamic results are shown in Figure 4.7. For operating speeds lesser than the base speed, it is noted that with the increase in N , the dynamic torque also improves (owing to an increase in the MMF which is also indicated in Figure 4.7a). Beyond the basic speed, these trends, however, reverse because of an increased effective back-emf (Figure 4.7b) (Chiba et al. 2012). The number of turns per phase is fixed to 66, as the motor displayed an optimum behavior *i.e.*, high average torque and power below and above the base speed respectively.



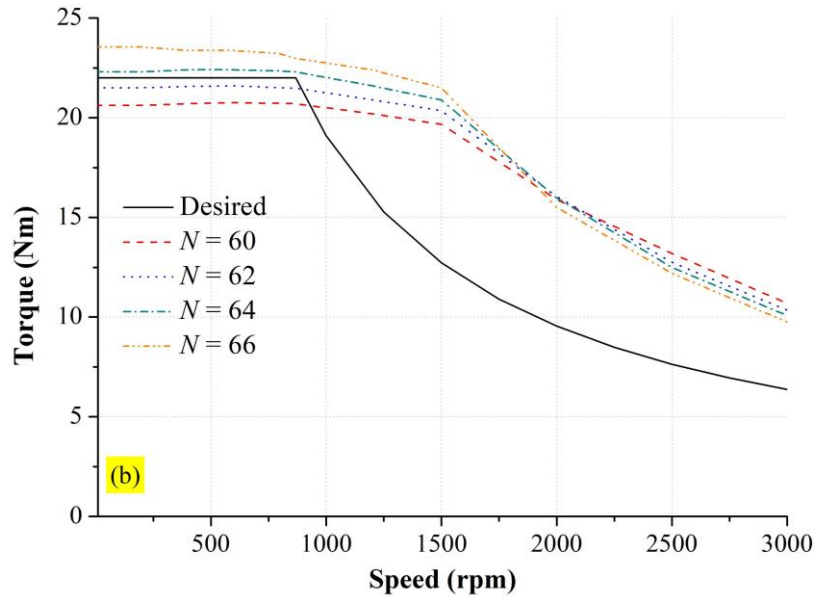


Figure 4.7 Influence of the number of turns per phase on the (a) Static torque and (b) Dynamic torque

Subsequently, the phase voltage (V_m) with $N = 66$ is calculated (Krishnan 2001) using Equation 4.6 to ascertain that the calculated value is lower than the dc-link voltage (144V).

$$V_m = \frac{\pi}{60} n_n k_2 DLNB \quad (4.6)$$

4.5 Multi-objective design optimization (MODO)

The different steps of the developed MODO process are outlined in the flowchart (Figure 4.8). Each step has been detailed in the following sub-sections.

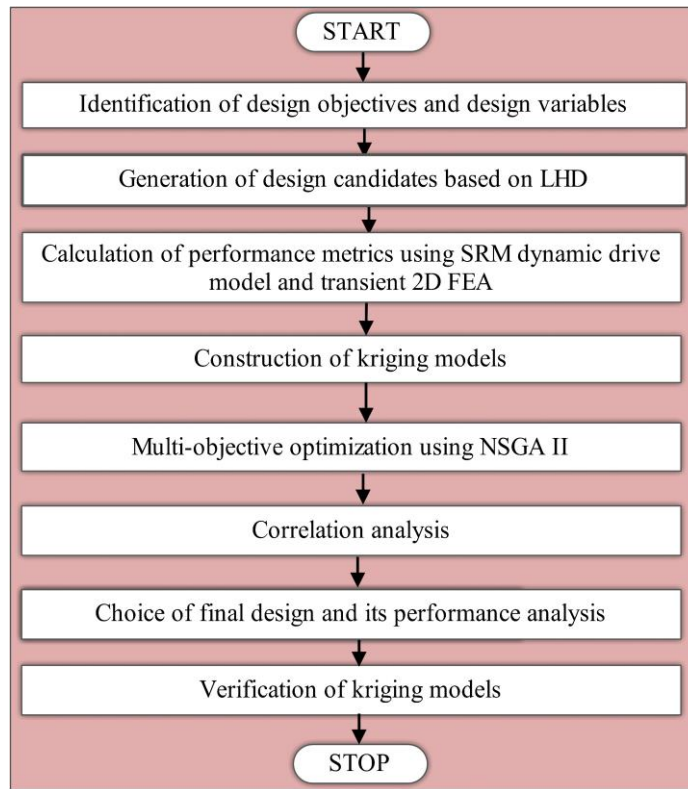


Figure 4.8 Flowchart of the Multi-objective design optimization (MODO)

4.5.1 Identification of design objectives

The choice of the appropriate performance metrics to be utilized in the formulation of the optimization model should be based on the application demands of the EV. According to a literature review on traction motors for E-rickshaws, high starting torque, torque density, and improved efficiency are the performance metrics to be prioritized for a successful deployment (Vaidehi et al. 2020) (Arun et al. 2021). A high starting torque is needed to guarantee that the large torque magnitude working points at lower operating speeds are met. E-rickshaws are intended to transport people, occasionally goods. In practical situations, the motors could experience temporary overload circumstances owing to an unexpected acceleration, hill climbing, or towing extra weight. Hence, to ensure that the motor can manage these transient loads, a high starting torque is essential (Vaidehi et al. 2020). Another crucial optimization target to be considered is torque density, whose maximization simultaneously increases the torque and/or reduces motor mass. In the current study, LOPs obtained from the driving cycle are taken into consideration while calculating electromagnetic losses. The

electromagnetic losses are estimated as total weighted losses by considering the sum of the copper and iron core losses as well as the energy weights assigned to each of the RPs (Fatemi et al. 2018). Therefore, maximizing the average torque (T_{avg}) during starting (i.e. at the base speed), maximizing the torque density (T_m), and minimizing the total weighted losses (P_w) over the drive cycle are chosen as the design objectives in the formulation of the optimization model for the SRM.

4.5.2 Design Variables for Optimization

The SRM, as depicted in Figure 4.6, comprises many design variables, and each one affects the performance metrics. The design variables such as the stator diameter (D_s), stack length (L), and air gap (l_g) had been fixed for the chosen application considering the geometrical and manufacturing constraints specified in Section 4.3. The remaining design variables such as the stator bore diameter (D), stator pole arc angle (β_s), rotor pole arc angle (β_r), stator pole depth (h_s), and rotor pole depth (h_r) are the design variables considered for optimization. These variables are known to have a significant influence on the performance metrics as established previously in Chapter 2 and Chapter 3 respectively. The ranges of each of these five chosen variables are constrained according to the empirical equations provided by (Miller 1993) (Xue et al. 2010b) to prevent geometrical conflicts between the structures of different motor components and increase the optimization efficiency (Table 4.6).

Table 4.6 Design variables and their ranges for optimization

Design variables	Range
Stator bore diameter (D /mm)	80 - 92
Stator pole arc angle ($\beta_s/^\circ$)	17 - 22.5
Rotor pole arc angle ($\beta_r/^\circ$)	$1 < \frac{\beta_r}{\beta_s} \leq 1.2$
Stator slot depth (h_s /mm)	$h_s = \frac{D_s}{2} - \frac{D}{2} - b_{sy}$

where, $b_{sy} = (0.7 \sim 1)\omega_{sp}$ and

$$\omega_{sp} = D \sin\left(\frac{\beta_s}{2}\right) \text{ is the stator pole width}$$

$$h_r = \frac{D_r}{2} - \frac{D_{sh}}{2} - b_{ry}$$

where, $b_{ry} = (0.7 \sim 1.2)\omega_{rp}$ and

Rotor slot depth (h_r /mm)

$$\omega_{rp} = D_r \sin\left(\frac{\beta_r}{2}\right) \text{ is the rotor pole width}$$

4.5.3 Generation of design candidates based on LHD and the evaluation of their performance metrics

A Latin hypercube design (LHD) sampling method (a type of DoE) (Ma and Qu 2015) owing to its flexibility and effective space-filling properties was used to obtain the design candidates. The number of turns per phase (N), as established previously in Section 4.4, was fixed at 66 for each design candidate. The methodology used to compute the performance metrics for each design candidate is described in this section and depicted in Figure 4.9. In this study, the performance metrics are evaluated based on their dynamic characteristics by giving due importance to θ_{ON} and θ_{OFF} . It is known that tuning them using transient FEA simulations necessitates carrying out these simulations several times, which takes considerable time. Instead, to hasten the process, a computationally efficient SRM drive model (Jiang et al. 2017) (Bilgin et al. 2019) is developed in MATLAB/Simulink. The SRM drive model is developed based on the hysteresis current control (HCC) strategy detailed (Rashid 2011). Unlike the commonly used traditional models based on closed-loop speed control with HCC, the SRM drive model does not require a speed controller. This eliminates the complexities associated with the adjustment of the tuning parameters. According to LHD, the periodic FEA models in ALTAIR FLUX are established. The static characteristics (static torque and flux linkage) were determined using the electromagnetic static FEA. These characteristics in the form of lookup tables (LUTs) are fed into the dynamic SRM drive model to assess the performance metrics. The coupling between ALTAIR FLUX and

MATLAB/Simulink is automated using Python scripting. The number of parallel strands is maximized for each design candidate (with $N = 66$) to achieve a slot fill factor (sf) of 0.6 (Howey et al. 2020) and the corresponding phase resistance (R_{ph}) is calculated.

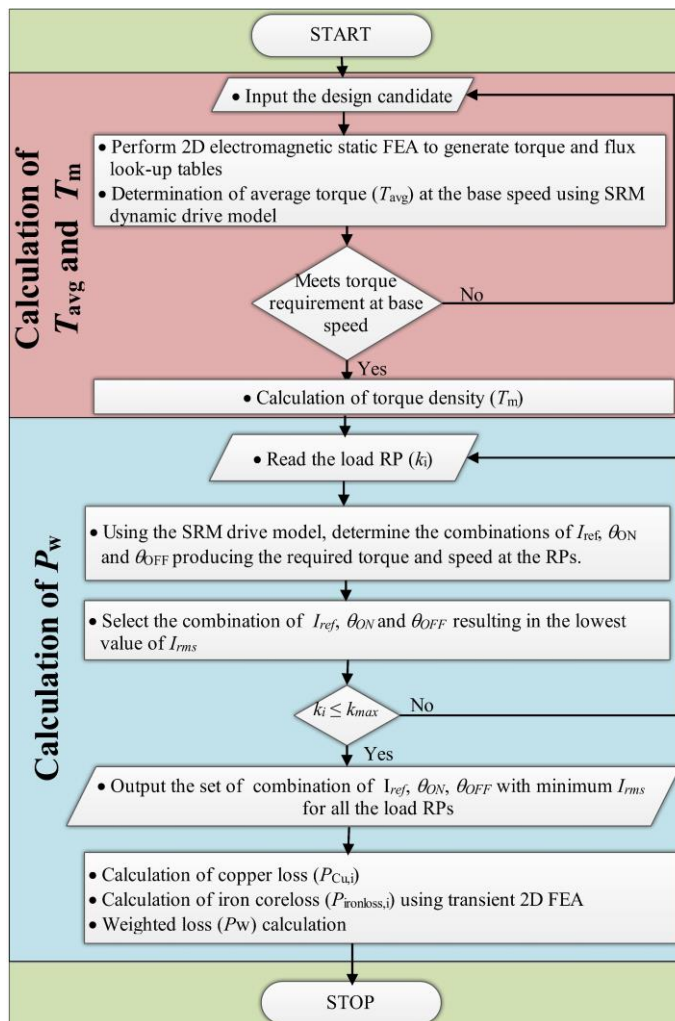


Figure 4.9 Flowchart indicating the calculation of the performance metrics of the design candidates

The maximum average torque (T_{avg}) of each design candidate at the base speed ($I_{peak} = 35$ A and 868 rpm) is computed based on the optimized commutation angles. A search algorithm-based single objective optimization to maximize the average torque is implemented in the SRM drive model to obtain the optimized commutation angles (Xue et al. 2010a). Accordingly, T_{avg} is calculated using the following expression (Jiang et al. 2017);

$$T_{\text{avg}} = \frac{1}{\theta_2 - \theta_1} \int_{\theta_1}^{\theta_2} T(\theta) d\theta \quad (4.7)$$

where $T(\theta)$ is the torque profile over the rotor position and $(\theta_1 - \theta_2)$ is equivalent to an electrical cycle. During the optimization of commutation angles, the RMS phase current (I_{rms}) is limited to 20 A and is one of the constraints (non-linear) considered.

$$I_{\text{rms}} \leq I_{\text{rms_lim}} \quad (4.8)$$

The boundaries of the commutation angles (linear constraint) are listed below (Jiang et al. 2017);

$$\begin{bmatrix} 1 & -1 \\ -1 & 1 \end{bmatrix} \begin{bmatrix} \theta_{\text{ON}} \\ \theta_{\text{OFF}} \end{bmatrix} < \begin{bmatrix} -\frac{360}{N_{\text{ph}}} \\ \frac{360l}{N_{\text{ph}}} \end{bmatrix} \quad (4.9)$$

where, l is constant governing the higher limit of the dwell and is limited to 1.33 in this work. As per this equation, the minimum dwell angle is set to 90 electrical degrees such that there is an overlap between the phase torques of the adjacent phases during commutation. Further, the maximum value of dwell is fixed to 120 electrical degrees. This ensures that, within this defined maximum dwell and for the determined values of θ_{ON} and θ_{OFF} , there is no current flowing in a phase in the decreasing inductance region. Both of these conditions are essential for reducing torque ripple and ensuring that the SRM operates smoothly (Miller 1993). Further, constraining the value of l to 1.33 ensures consistency in the calculation of the performance metrics of each of the design candidates. The design candidates that do not produce the required T_{avg} at the base and the maximum speed are excluded from the study.

The torque density (T_m) of each design candidate is calculated by considering the ratio of average torque to total mass (Ma and Qu 2015), which is expressed as;

$$T_m = \frac{T_{\text{avg}}}{m_{\text{Steel}} + m_{\text{Cu}}} \quad (4.10)$$

where, T_{avg} is the average torque calculated previously and m_{Steel} and m_{Cu} are the mass of the steel core and copper of each design candidate respectively.

For the calculation of the weighted loss (P_w) of each design candidate, the associated electromagnetic losses need to be evaluated at the RPs. This necessitates the careful determination of the excitation control parameters, namely the reference current (I_{ref}), θ_{ON} and θ_{OFF} that produce the required torque and speed value at each RP (Table 4.4). This is achieved by implementing a search algorithm in the SRM drive model. I_{rms} constraint and boundaries of the commutation angles are defined by utilizing Equations (4.8) and (4.9) respectively. The combination of I_{ref} , θ_{ON} and θ_{OFF} that produced the desired torque and speed values at each RP with the least I_{rms} is determined. Based on this, the copper loss ($P_{\text{Cu},i}$) at each load RP is calculated using the expression (Howey et al. 2020);

$$P_{\text{Cu},i} = N_{\text{ph}} I_{\text{rms}}^2 R_{\text{ph}} \quad (4.11)$$

Iron core losses ($P_{\text{ironcoreloss},i}$) at each RP are computed by using the transient FEA (ALTAIR 2023) based on the obtained excitation control parameters. In the transient FEA, an AHB converter is used to supply currents to the phases and these currents are controlled through HCC.

The total weighted loss (P_w) per output power for each design candidate, using the estimated values of $P_{\text{ironcoreloss},i}$ and $P_{\text{Cu},i}$ is calculated as (Fatemi et al. 2018);

$$P_w = \sum_i \frac{(P_{\text{Cu},i} + P_{\text{ironcoreloss},i}) W_{E,i}}{(T_i \omega_i)} \quad (4.12)$$

where, $W_{E,i}$ and ω_i is the energy weight and the rotor speed at the i^{th} load RP respectively (enlisted in Table 4.4).

4.5.4 Construction of Kriging models

As an alternative to FEMs given their high computing cost, the Kriging model is used to comprehensively and quickly ascertain the variation in trends between the optimization objectives and design variables (Diao et al. 2020). As compared to the response surface model and radial basis functions, the Kriging model is more effective at modeling local nonlinearities since it considers both the mean trend and variations of

the responses. They have been extensively employed in the modeling of electromagnetic devices (Diao et al. 2020) (Diao et al. 2021) . For the provided n sample points $[x_1, x_2, \dots, x_n]$ and their corresponding responses $[y(x_1), y(x_2), \dots, y(x_n)]$, the response $y(x)$ of the kriging model for an input \mathbf{x} is given by the equation;

$$\hat{y}(x) = f(x)^T \beta + z(x) \quad (4.13)$$

where, $f(x)$ indicates the approximation model which is mostly assumed a polynomial and is in the form $f(\mathbf{x}) = [f_1(x), \dots, f_q(x)]^T$, where q corresponds to the dimension of the polynomial. β is the model parameter vector to be estimated. It is assumed that $z(x)$ is a vector with zero mean, variance of σ^2 along with a covariance matrix cov_{ij} which can be expressed as;

$$\text{cov}_{ij} = \sigma^2 \mathbf{R}[R(x_i, x_j)] \quad (4.14)$$

where \mathbf{R} corresponds to the correlation matrix and R denotes the user-specified correlation function. In the current study, the performance metrics T_{avg} , T_m , and P_w have been determined for 600 design candidates produced by LHD to construct the Kriging models.

4.5.5 Multi-objective optimization using NSGA II

In most design scenarios, there is a conflict between the objectives in multi-objective optimization (Ma and Qu 2015). An improvement in one objective may lead to a decline in the other objectives. The Pareto front serves as an invaluable resource for decision-makers, offering a range of solutions that cater to various trade-offs between competing objectives. Numerous optimization techniques, including the multi-objective differential evolution algorithm (Öksüztepe 2017), NSGA, and their improved version NSGA II (Diao et al. 2020), have been used to solve multi-objective optimization problems. NSGA-II stands as a cornerstone in the domain of multi-objective optimization, providing a robust and efficient framework for solving complex problems characterized by conflicting objectives (Deb et al. 2002). The selection process in NSGA-II is crucial, as it involves ranking the candidate solutions based on non-dominance and diversity within each front. Crowding distance sorting measures the solution density within the Pareto front, favoring diversity by assigning higher distances

to less densely clustered solutions. Solutions for the next iteration are chosen to be both elite in terms of fitness and diverse to ensure that the resulting set of parent solutions for the next generation represents a well-distributed approximation of the Pareto front. This process effectively explores and exploits the trade-offs between multiple conflicting objectives in an optimization problem. Owing to these advantages, NSGA II is used as the optimization method in this study.

The multi-objective optimization model has been developed as follows;

$$Min : \begin{cases} f_1(-T_{avg}) \\ f_2(-T_m) \\ f_3(P_w) \end{cases} \quad (4.15)$$

$$Subject\ to : \begin{cases} J_c \leq 6A/mm^2 \\ sf \leq 0.6 \\ \beta_r \geq \beta_s \end{cases} \quad (4.16)$$

where the current density, denoted by J_c , is the ratio of the RMS value of the current waveform over the bare copper area. The upper bound of the selected current density restricts the SRM's working temperature for a specific cooling type. In the present study, under the conditions of natural air cooling, J_c is restricted to less than $6A/mm^2$ (Diao et al. 2020). The ratio of wire area to slot area is termed the wire slot fill factor (sf). Their maximum value is chosen based on practical considerations like the wire's cross-sectional shape and manufacturability (Bilgin et al. 2019). Given that the winding is being carried out using an automatic universal stator coil winding machine with round conductors, the maximum sf is limited to 0.6 (Howey et al. 2020) (Bilgin et al. 2019). Further, it is preferred to maintain the β_r larger than the β_s because it increases the aligned flux linkage and hence the average torque output of the SRM (Miller 1993). However, the increase in average torque is only effective up to the value of β_r , at which the saliency ratio is high (Jiang et al. 2017) (Howey et al. 2020). Also, providing a larger β_r than the β_s creates a dead zone around the aligned position which aids in providing more time for the flux to nullify after commutation ensuring that no negative torque is generated (Krishnan 2001). Designs that fail to deliver the desired torque (22 Nm) within the electrical constraints are consequently penalized. It should be noted

that the objectives that need to be maximized are negated because maximizing an objective f equals minimizing $-f$. Using a population size of 125, the NSGA II algorithm was run for 250 generations. The machine response within the NSGA II algorithm in the task of searching the optimal designs was predicted using the previously constructed Kriging models for each performance metric. The parameters used in the NSGA II optimization model are listed in Table 4.7.

Table 4.7 NSGA II Optimization model parameters

Parameter	Value
Population size	125
Number of iterations	250
Percentage crossover	0.7
Mutation rate	0.02
Mutation step size	1

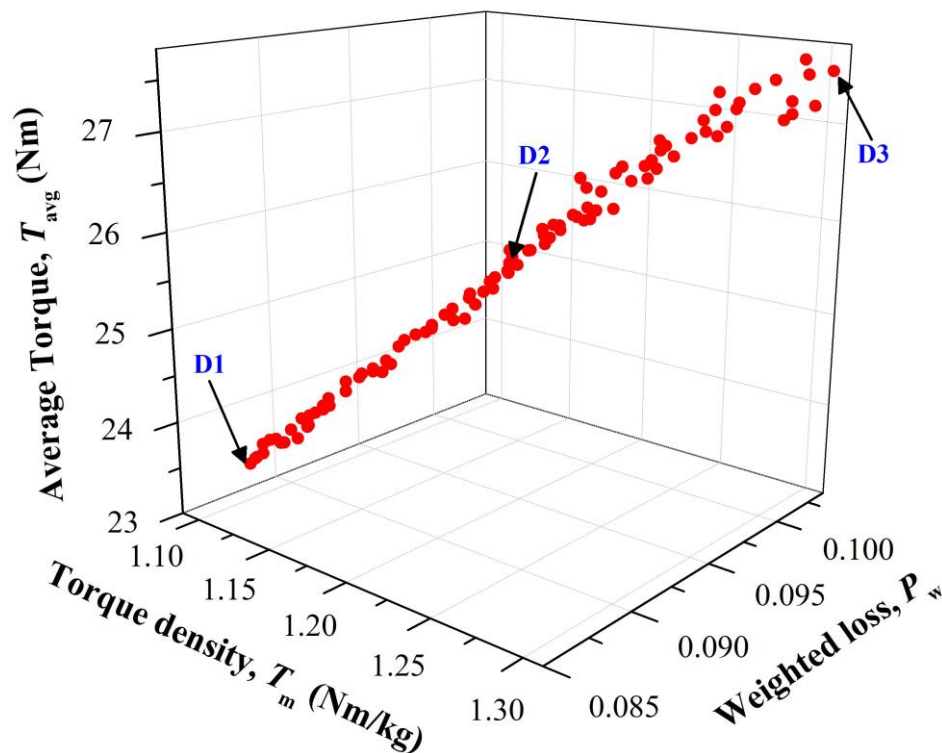


Figure 4.10 Pareto-optimal set obtained from NSGA II

The Pareto-optimal set obtained from the multi-objective optimization for the three objectives is shown in Figure 4.10, and it can be deciphered that the convergence and diversity are better in the spatial distribution. Each design from this solution set is optimum because of which, a preferred design can be chosen from the optimal solution set. According to the Pareto-optimal set, the average torque, torque density, and weighted loss range between 23.33 and 27.52 Nm, 1.09 and 1.28 Nm/kg, and 0.088 and 0.103 respectively. A comparison of the motor performances has been drawn between the initial and the three optimized designs D1, D2, and D3 (indicated in Figure 4.10) to demonstrate the effectiveness of the proposed MODO process. Table 4.8 displays the dimensions of the design variables and performance metrics for the initial and the three optimized designs. Torque ripple (T_{ripple}) calculated from their respective dynamic torque waveforms for each design at the base speed is also enlisted. The torque ripple was calculated using Equation 4.17 where T_{max} and T_{min} correspond to the maximum and minimum torque values respectively in the dynamic torque waveform.

$$T_{Ripple} = \frac{T_{max} - T_{min}}{T_{avg}} \quad (4.17)$$

Among the four design cases, it can be discerned that the initial design exhibits an inferior performance compared to others.

Table 4.8 Design variables and Performance metrics of the initial and the optimized designs

Parameter	Initial design	D1	D2	D3
Stator bore diameter (D) (mm)	83.01	82.40	88.53	91.54
Stator pole arc angle (β_s) ($^\circ$)	19.09	19.23	19.35	21.38
Rotor pole arc angle (β_r) ($^\circ$)	21.68	20.11	20.13	22.12
Stator slot depth (h_s) (mm)	26.96	26.36	23.11	20.88
Rotor slot depth (h_r) (mm)	10.94	14.14	15.41	18.3
Maximum current density (J_c) (A/mm^2)	4.51	4.47	5.22	5.96
Average torque (T_{avg}) (Nm)	22.98	23.33	25.58	27.52

Torque density (T_m) (Nm/kg)	1.07	1.09	1.20	1.29
Total weighted loss (P_w)	0.099	0.088	0.094	0.103
Torque ripple (T_{ripple}) (at the base speed) (%)	39.62	38.21	32.14	30.12

4.5.6 Correlation analysis between the design variables and the performance metrics

To decipher the correlations linking the design variables and the performance metrics, Pearson coefficient correlations are determined for the Pareto-optimal set. Pearson coefficient correlation is expressed as (Fatemi et al. 2018);

$$\rho_{x,y} = \frac{\text{Cov}(X,Y)}{\sigma_x \sigma_y} \quad (4.18)$$

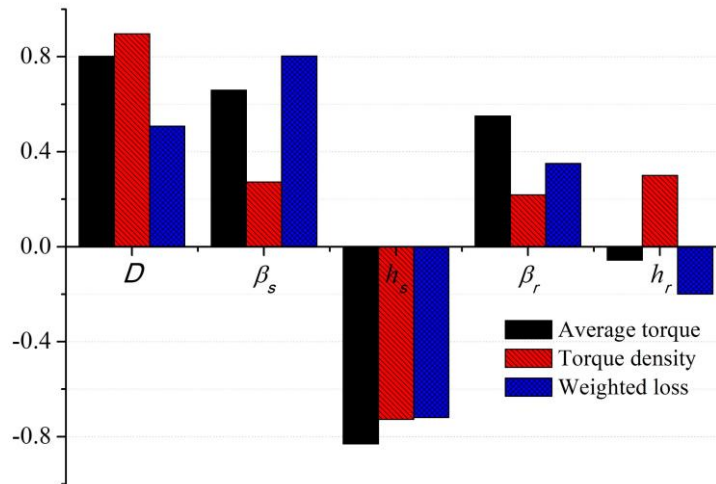


Figure 4.11 Pearson's correlation coefficient of the design variables

where X and Y represent the variables between which Pearson's correlation coefficient is determined. Cov and σ denote the covariance and standard deviation, respectively. Figure 4.11 shows the estimated Pearson's coefficients for the objective functions. The results indicated that design variables related to the stator core had a stronger correlation with the performance metrics as compared to the rotor core design variables. It can be noted that an increase in D , β_s and reduction in h_s enhanced the T_{avg} . An increase in D causes an increase in the lever arm that extends from the motor's center to the airgap. Increasing β_s leads to a greater overlap region between the stator pole and the

corresponding rotor pole. Further, a reduction in h_s reduces the reluctance of the stator pole owing to a shorter stator pole height. These observations corroborate the findings reported in (Jiang et al. 2017) (Mamede et al. 2019). Moreover, a detailed study investigating the influence of these geometric design variables on the average torque has been described in Chapter 3. The improvement in torque density with the rise in D , β_s and fall in h_s followed a similar trend. Also, any change in the stator design variables was shown to significantly impact P_w . A decrease in h_s and an increase in D and β_s decreased the slot area. Decreasing the slot area reduces the space for parallel strands, resulting in an elevated copper loss (Howey et al. 2020). It is well-known that among conventional SRMs, the stator core experiences more iron core loss than the rotor core due to the larger flux reversals in the stator core (Krishnan 2001). Therefore, it is evident that the changes in the stator design variables account for the major variations in the P_w . The contrasting correlations between the performance metrics and design variables interpreted from the above analysis also underline the significance of performing MODO to achieve the optimal design with the required trade-off.

4.5.7 Choice of final design and its performance analysis

The design D2 was chosen from the Pareto-optimal set, as it offered an optimum balance between average torque, torque density, total weighted loss and torque ripple (Table 4.8). The T_{avg} and T_m of the design D2 have been improved by 11.31% and 12.15% respectively, while the P_w is 5.1% lower in comparison to the initial design. At the base speed, the torque ripple for this design was 32.14%. By optimizing the commutation angles and the dwell, the torque ripple can be minimized further. Additionally, torque-sharing functions can be employed at lower speeds to reduce the torque ripple (Xue et al. 2010). However, this is beyond the scope of the present work.

Table 4.9 Excitation control parameters and the average output torque of the optimal design D2 at the RPs

Operating point	I_{ref} (A)	θ_{ON} (elec. deg)	θ_{OFF} (elec. deg.)	I_{rms} (A)	Average torque (Nm)
RP 1	23	54	144	10.72	10.79
RP 2	9	60	150	4.51	2.13

RP 3	10	54	144	4.89	2.84
RP 4	11	36	132	5.47	3.07

Table 4.9 indicates the control excitation parameters for the selected design D2 at the four RPs determined by emulating the procedure outlined in sub-section 4.5.3. The corresponding average torque that was obtained from transient FEA is also indicated. It can be noted that the design D2 for the computed control excitation parameters satisfies the desired torque and speed requirement at each RP. Further, the correlation between the transient FEA and the SRM drive model used in the present work is validated by comparing the dynamic torque waveforms for the design D2 corresponding to all the RPs (Figure 4.12). It is discernible that the instantaneous torque values exhibit a good agreement.

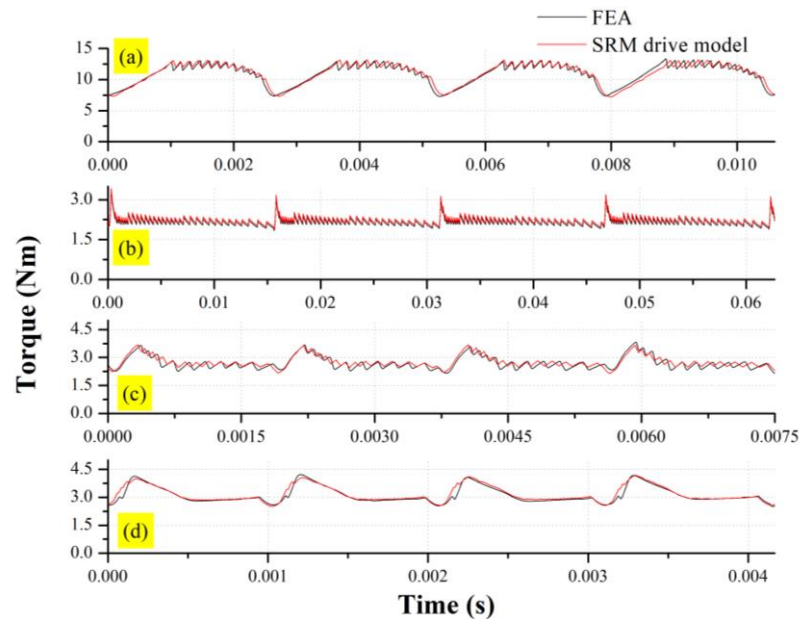


Figure 4.12 Comparison of dynamic torque waveforms obtained from FEA and SRM drive model at (a) RP1 (b) RP2 (c) RP3 and (d)RP4

Further, the analysis of the motor performance across the whole speed range for the design D2 has been accomplished from the perspective of torque-speed characteristics. Optimized values of θ_{ON} and θ_{OFF} over the entire speed range are determined from the SRM drive model by formulating a search algorithm-based single objective optimization to maximize the average torque (Xue et al. 2010). The reference

phase currents are swept between 1 and 35 A, while speeds are swept between 1 and 3000 rpm. Emphasis is placed on maximizing the average torque to prioritize the torque-producing capability of the motor. The respective reference phase current (A) and speed (rpm) instances are mentioned below;

$$\text{Reference phase current} = [35 \ 30 \ 25 \ 20 \ 15 \ 10 \ 5 \ 1]^T$$

$$\text{Speed} = [1 \ 200 \ 400 \ 600 \ 800 \ 867 \ 1200 \ 1500 \ 2000 \ 2500 \ 3000]$$

Equations (4.8) and (4.9) depict the constraints that are applied during the optimization process. Figure 4.13 illustrates the optimized θ_{ON} and θ_{OFF} LUTs for the design D2 over the full torque speed range. Here, 0 electrical degree refers to the unaligned position of the rotor pole with respect to the stator pole. About this reference point, the θ_{ON} and θ_{OFF} have been specified.

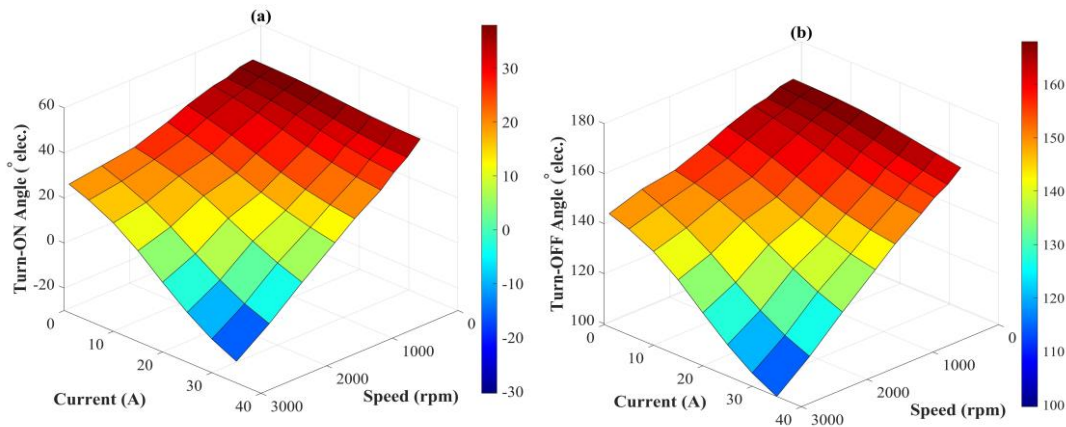


Figure 4.13 (a) Optimized Turn-ON angles LUT (b) Optimized Turn-OFF angles LUT

Figure 4.14 shows the torque-speed characteristics for the design D2 for different values of the reference phase currents. It can be observed that, within the constraints listed in Table 4.3, the chosen design satisfied the torque-speed envelope demanded by the Erickshaw.

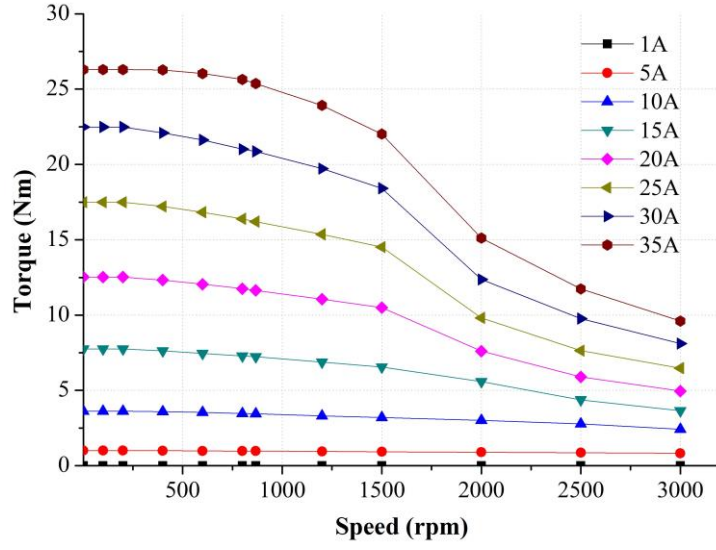


Figure 4.14 Torque-speed characteristics of the design D2

Additionally, the analysis of the motor performance across the whole speed range for the design D2 has been accomplished from the perspective of motor efficiency. The power loss analysis of the AHB converter, its efficiency, and consequently the overall system efficiency, are not taken into account in this study. The commutation angles obtained for various values of phase currents at different operating speeds determined previously are fed into the transient 2D FEA to determine the iron core loss ($P_{\text{ironcoreloss}}$). Correspondingly, the copper loss (P_{Cu}) is computed using Equation 4.11. Following this, the efficiency (η) at each operating point is calculated using the expression;

$$\eta = \frac{P_{\text{out}}}{P_{\text{out}} + P_{\text{loss}}} \times 100 \quad (4.19)$$

where, P_{out} denotes the output shaft power. The loss component (P_{loss}) includes both the copper (P_{Cu}) and iron core ($P_{\text{ironcoreloss}}$) losses expressed as;

$$P_{\text{loss}} = P_{\text{Cu}} + P_{\text{ironcoreloss}} \quad (4.20)$$

Figure 4.15 shows the motor efficiency map for the design D2. The high-efficiency region ($\geq 90\%$) roughly ranges from 1500 to 3000 rpm across the full torque range, and it can be noted that most of the LOPs depicted in Figure 4.3(b) lie in this region.

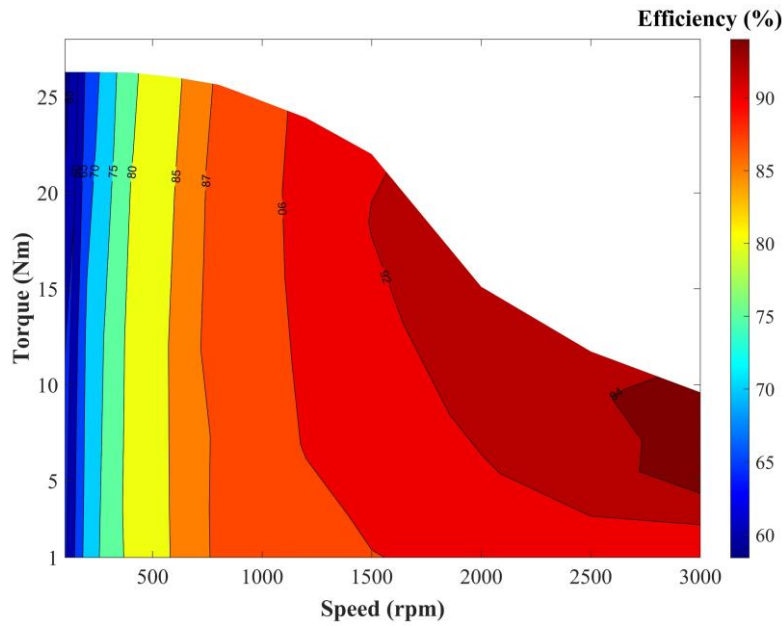


Figure 4.15 Motor efficiency map

Before prototyping the optimized design D2, fillets were added to the bottom of the stator and rotor poles to lessen magnetic saturation at the junction of the poles and the yoke and to increase the average torque. In addition, the inclusion of fillets at these locations reduces the effects of mechanical stress concentration (Miller 1993). Figure 4.16 depicts the ready-to-prototype design's magnetic flux distribution at the base point. It can be observed that the SRM works close to the knee point in this working condition. Further, the stator and the rotor yokes are not in deep saturation; an imperative consideration in the design of SRM (Mamede et al. 2019). The maximum flux densities were observed at the tips of the poles.

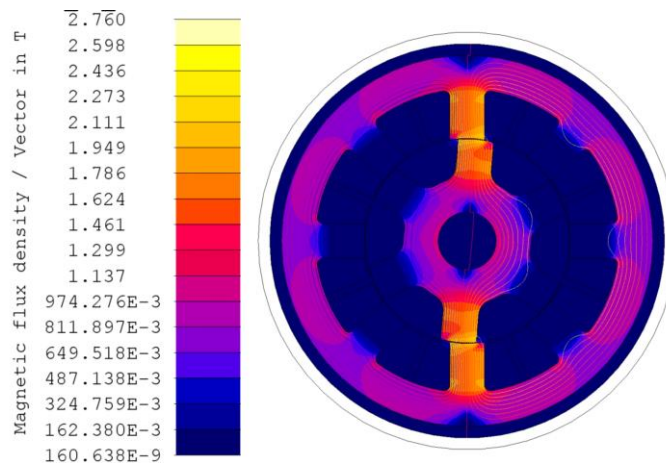


Figure 4.16 Flux density map of the optimized design at the base point

4.5.8 Verification of the Kriging Model

It is vital to corroborate the veracity of the Kriging model to guarantee the optimization's effectiveness. For this, the Pareto-optimal set's designs D1, D2, and D3 have been chosen. The results obtained from the FEA of these designs and the Kriging model are compared to ascertain the accuracy of the approximation model. The values of the three optimization objectives are enlisted (Table 4.10). As shown, the maximum errors of T_{avg} , T_m , and P_w for the three optimal designs are only 0.88%, 1.58%, and 2.83%, respectively. This verifies the accuracy of the constructed Kriging models.

Table 4.10 Comparison between FEM and Kriging model results

Performance metric	D1		D2		D3	
	FEA	Krig.	FEA	Krig.	FEA	Krig.
T_{avg} (Nm)	23.181	23.335	25.364	25.588	27.661	27.518
T_m (Nm/kg)	1.078	1.094	1.188	1.200	1.26	1.28
P_w	0.090	0.088	0.096	0.094	0.106	0.103
T_{avg} error	0.67 %		0.88 %		0.52 %	
T_m error	1.48 %		1.01 %		1.58 %	
P_w error	2.22 %		2.08 %		2.83 %	

4.6 Prototyping

A prototype of the optimum design D2 has been manufactured to experimentally verify the preceding simulation results. The drawings pertaining to the stator and rotor core of the optimal design D2 are shown in Figure 4.17. The exploded view of the SRM assembly is shown in Figure 4.18. The different assembled views of the SRM assembly are shown in Figure 4.19. The drawings pertaining to each of the child parts are shown in Appendix I. The purpose, material used, and manufacturing technique of each part are enlisted (Table 4.11). Figure 4.20 shows the prototyped primary components of the SRM prototype. M270_35A is the lamination material for the core. Figure 4.20a and Figure 4.20b depict the stator with the phase coil and the rotor assembly respectively. The winding is carried out with 2 parallel strands of SWG 17 resulting in a R_{ph} of 0.1902

Ω and sf of 0.55. Figure 4.20d depicts a four infrared (IR) sensor array and associated PCB for rotor position estimation. The PCB is mounted on the rear cover of the motor and is made to sense the position of the target plate, a miniature geometric shape resembling the rotor. The target plate is attached to the motor shaft. The sensor module consists of four optical reflective IR sensors spaced 20 degrees apart to detect the reflection of infrared beams from the rotor poles. Each sensor's output is assigned one of two digital values: 0 or 1, depending on the analog output of the sensor and a threshold. As the rotor rotates, the sensors generate a series of digital outputs i.e. logical lows (“0”) and highs (“1”). The output of each sensor is translated into a 4-bit binary code for a given state. Further, the binary representation is converted to its corresponding decimal equivalent. Based on this, a sensor state map is created by mapping the rotor position with respect to the sensor output. The controller then examines the sensor state map and phase excitation sequence based on the desired rotation of the direction of the motor to apply the appropriate phase commutation sequence. The photograph of the assembled prototype SRM mounted on the fixture is shown in Figure 4.20e.

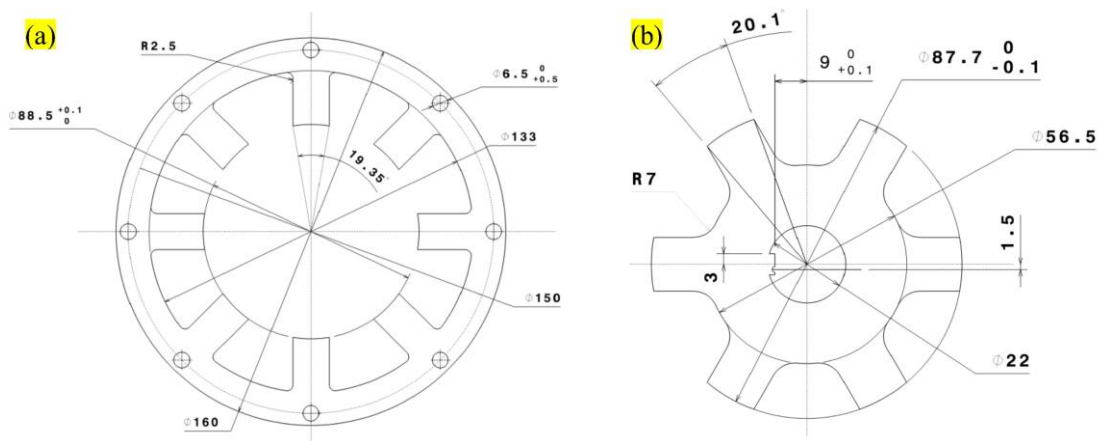


Figure 4.17 Drawings for fabrication (a) Stator and (b) Rotor core

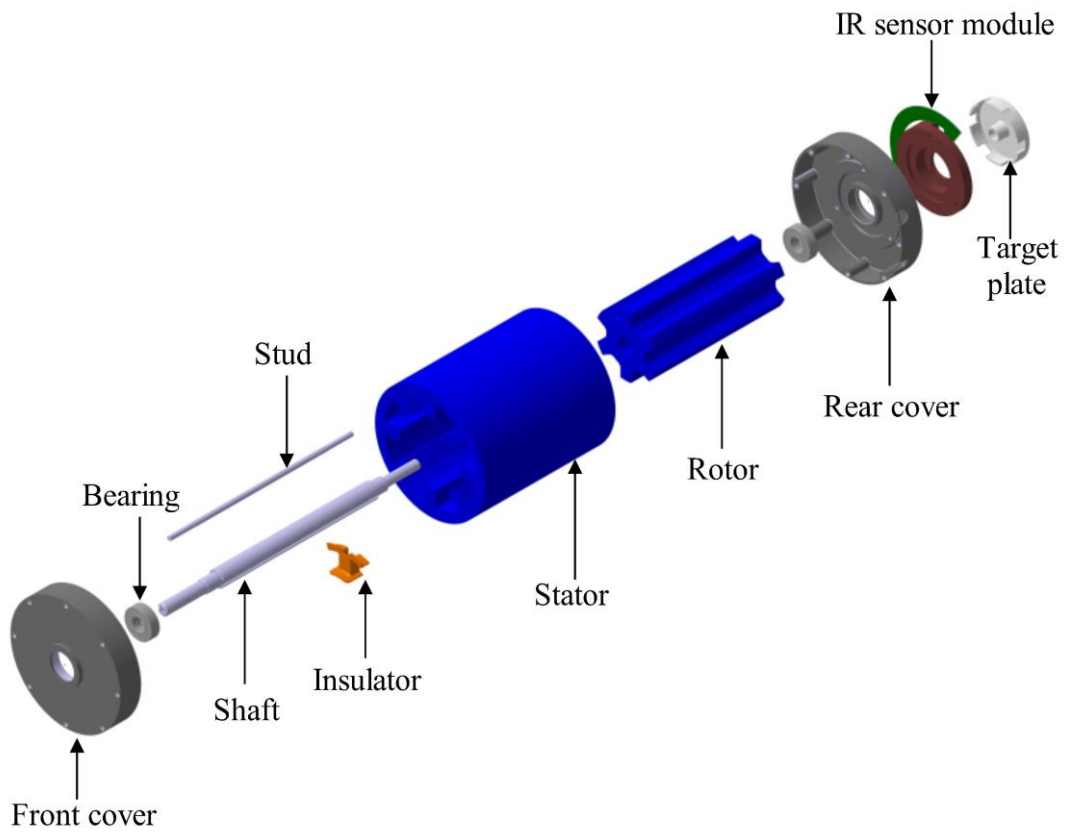


Figure 4.18 Exploded view of SRM components

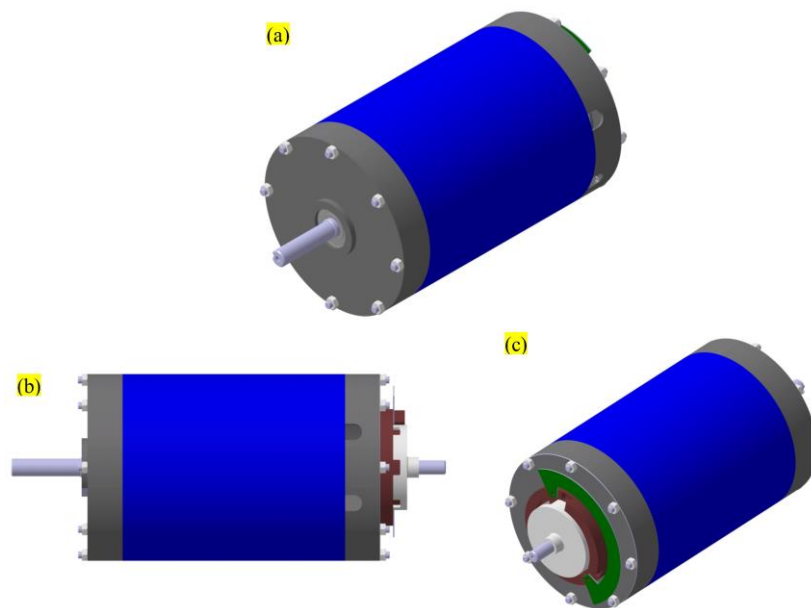


Figure 4.19 Views of the assembled SRM model (a) Isometric view (front) (b) Right side view (c) Isometric view (Rear)

Table 4.11 Different parts of the motor assembly, their purpose, material used, and manufacturing process employed.

Part name	Purpose	Material	Manufacturing process/ Heat treatment
Front cover	<ul style="list-style-type: none"> • To facilitate motor assembly and ensure the safety of the motor. • To protect the motor from dust, water, chemicals etc 	Aluminium 7075	Casting and machining
Shaft	<ul style="list-style-type: none"> • A shaft is used to support the different structures of the machine and transmit torque and speed to the external load. 	EN-24 steel	Machining, oil quenching and Hardening
Stud	<ul style="list-style-type: none"> • To support the motor assembly. 	EN-24 steel	Machining, oil quenching, and Hardening
Insulator	<ul style="list-style-type: none"> • Insulators are used to prevent contact between the lamination steel and the winding. • Acts as slot wedges to keep the windings intact and prevent from slipping. 	Nylon PA 6	Injection moulding
Stator	<ul style="list-style-type: none"> • The stator is the stationary part of the motor assembly. • Windings are accommodated in the stator poles. 	M270_35A non-oriented electrical steel	Laser cutting, stacking, and riveting
Rotor	<ul style="list-style-type: none"> • The rotor is the rotating part of the motor assembly. 	M270_35A non-oriented electrical steel	Laser cutting, stacking, and riveting
Rear cover	<ul style="list-style-type: none"> • To facilitate motor assembly and ensure the safety of the motor. • To protect the motor from dust, water, chemicals etc • To facilitate mounting of the IR sensor module for rotor position sensing 	Aluminium 7075	Casting and machining
Target plate	<ul style="list-style-type: none"> • A target plate mounted on the motor shaft is used for rotor position sensing 	Aluminium 6061	Machining

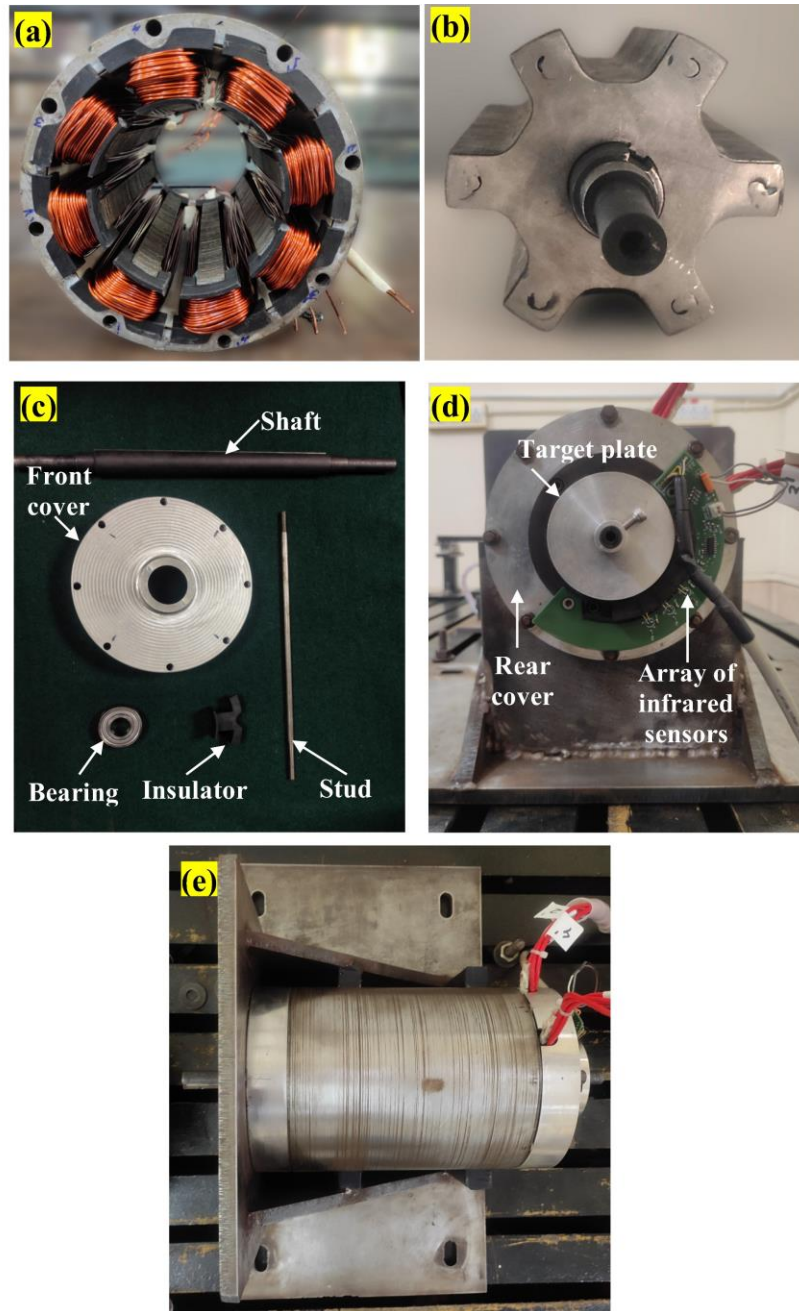


Figure 4.20 (a) Stator core with the phase windings (b) Rotor assembly (c) Basic components of the motor assembly (d) IR sensor array with target plate (e) Prototype SRM mounted on the fixture (top view)

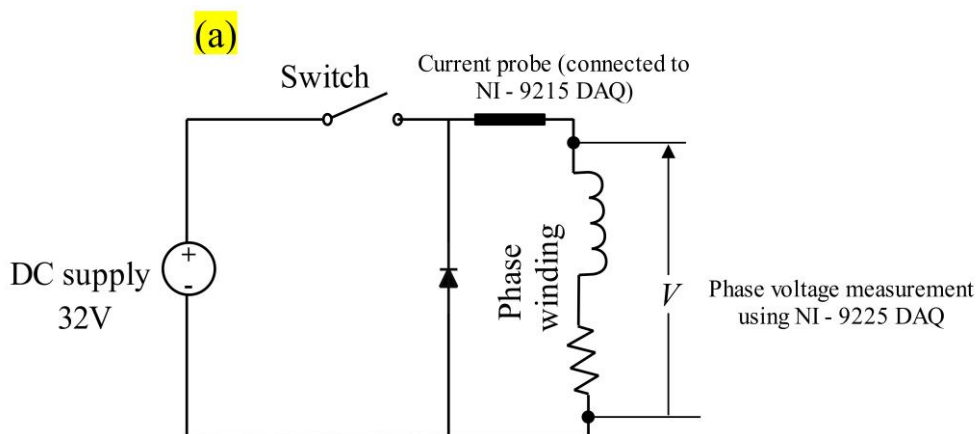
4.7 Experimental validation

4.7.1 Static Performance Validation

Using the DC excitation method (Song et al. 2015), the flux linkage characteristics of the SRM prototype are experimentally determined. The schematic and photograph of

the experimental setup for this are depicted in Figure 4.21a and Figure 4.21b respectively. A mechanical locking system is used to clamp the rotor at various angular instances between the unaligned and the aligned positions, and a DC power source (Aplab 3260 regulated dc power supply) is used to inject a current pulse into one of the phases at various amplitudes. A stepper motor (KOLLMORGEN make) which is mechanically connected to the SRM shaft is used to incorporate the parking of the rotor at evenly spaced angular instances between the unaligned and aligned state. The accuracy of this procedure is ensured by measuring the angular position of the rotor using an absolute rotary encoder (with 2500 ppr) installed on the stepper motor shaft and connected to NI-9401 DAQ. Phase resistance (R_{ph}) is accurately measured using the voltmeter-ampere method since any error in the measurement of the phase resistance impacts the flux linkage (Song et al. 2015) (Reddy et al. 2022). The rising current and the corresponding phase voltage (Figure 4.22a and Figure 4.22b) are measured using a current probe (Tektronix A622) connected to the NI-9215 and NI-9227 voltage DAQs, respectively, for each angular position of the rotor (θ) and the respective phase current. The flux linkage (ψ) is computed using Equation 4.21. The numerical integration of this equation is performed using Simpson's 1/3 rule.

$$\psi(\theta, i) = \int_0^{t_i} (V - iR_{ph}); \theta \text{ is fixed} \quad (4.21)$$



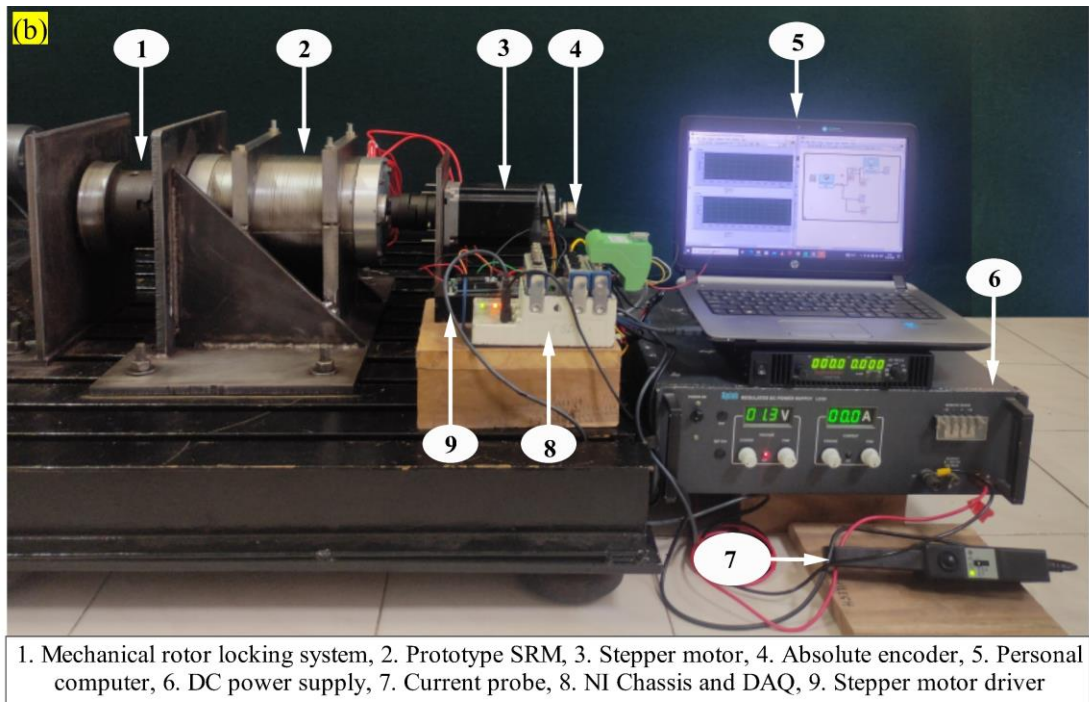


Figure 4.21 (a) Schematic and (b) Photograph of the experimental setup for determining the static performance of the SRM prototype

where V denotes the instantaneous voltage measured across the phase winding, t_I indicates the instantaneous time at which the phase current's magnitude reaches the value i . A comparison between the static FEA simulated and measured ψ at various θ for different values of i is shown in Figure 4.22c. The measured ψ near the aligned position for higher values of i are lesser than that of FEA values. This could be because of manufacturing and assembly deviations of the prototype motor. Moreover, the leakage and the end-winding flux are not accounted for in the FEA model. However, the maximum percentage error of the FEA compared to the measured ψ is less than 6.51%, which confirms the veracity of the FEA model employed in this study.

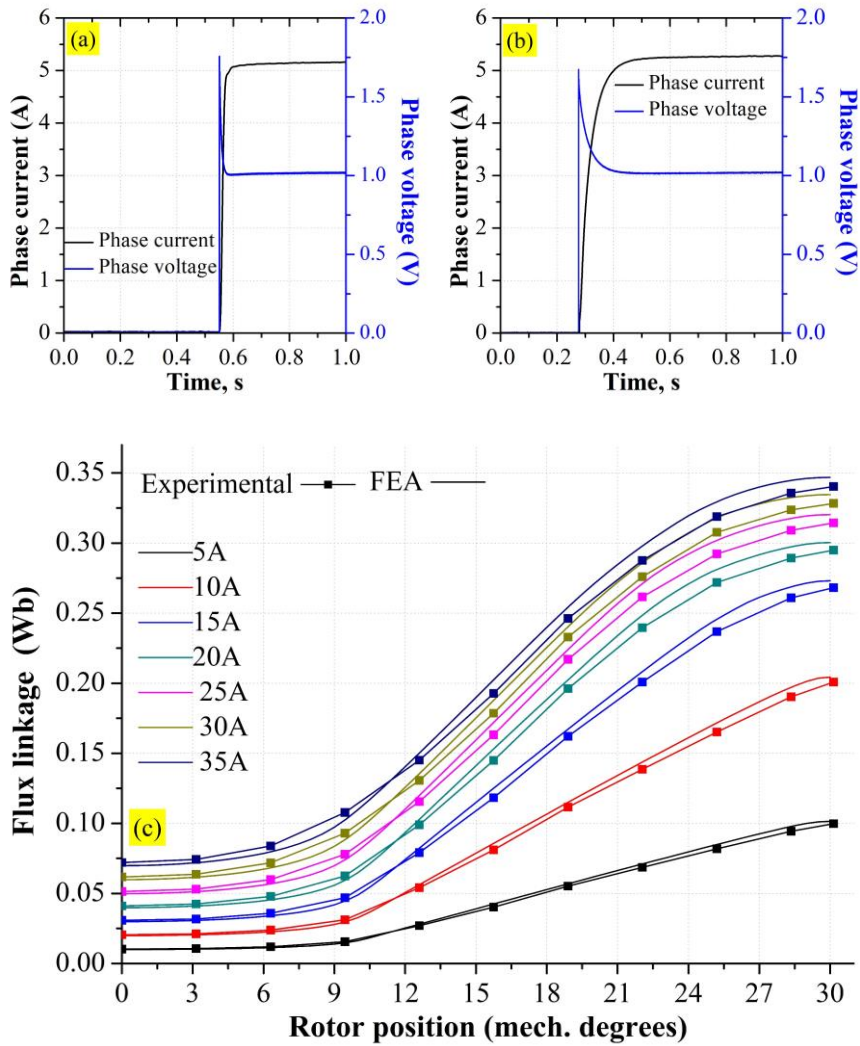
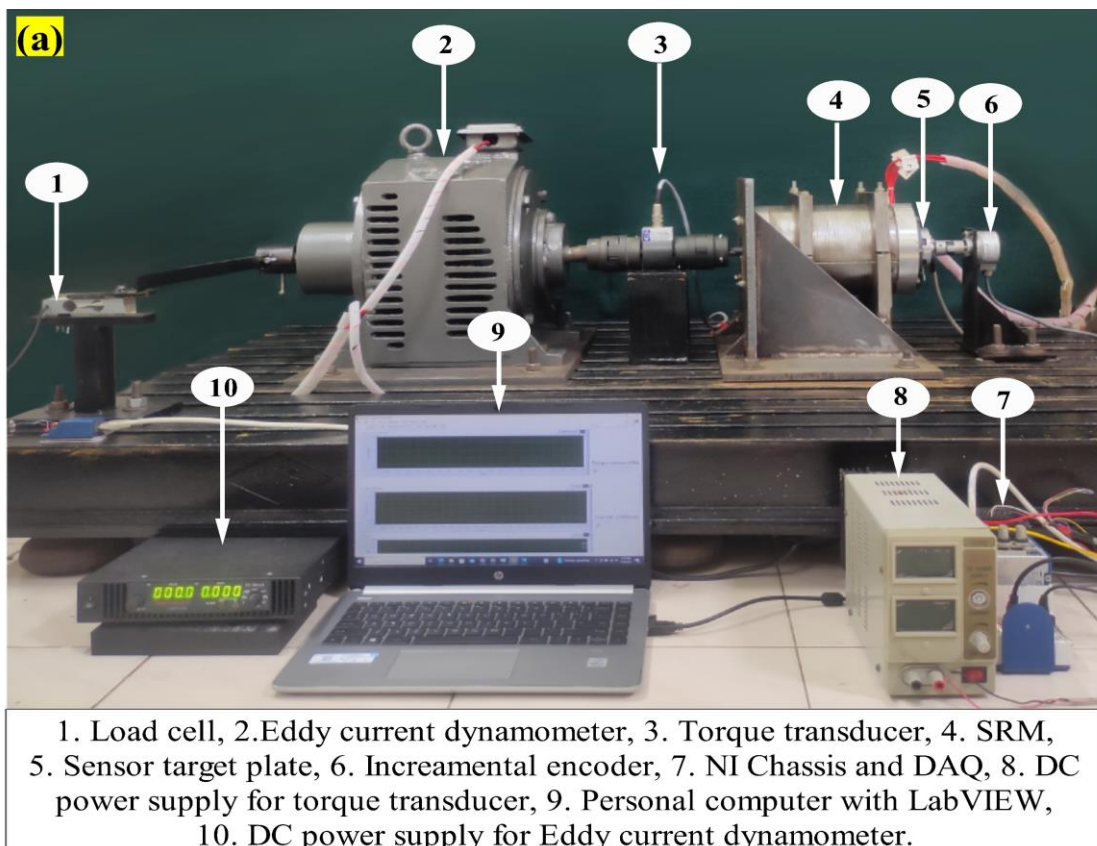


Figure 4.22 Measured phase current and voltage at (a) Unaligned (b) Partially aligned position and (c) Comparison between FEA and measured flux linkages.

4.7.2 Dynamic performance validation

Figure 4.23(a) depicts the experimental setup developed for assessing the dynamic performances of the SRM prototype. An eddy-current dynamometer, torque transducer (HBM T22), and the SRM prototype are mounted on the test bed and connected by two couplings. An AHB inverter (SEMIKRON make) is used to drive the SRM (Figure 4.23b). According to the closed-loop HCC method (with hard chopping) (Rashid 2011) implemented in the WAVECT WCU300 controller (WAVECT 2023), the inverter regulates the phase currents of the SRM to follow the desired waveforms. Figure 4.24 depicts the control diagram of the closed-loop HCC scheme. Based on various sensor states obtained by processing the outputs of the IR sensors in the controller, the

positional information of the rotor in the SRM is obtained. The controller suitably transmits the pulses to the converter with the use of a LUT that holds the data corresponding to the appropriate phase to be energized. An incremental encoder (Baumer optoPulse - EIL580P-SC, 1024 ppr) interfaced with the controller measures the motor's actual speed. The control strategy is briefly explained as follows; The PI controller compares the actual speed to the target speed to control the speed and determine the reference current. A 40 kHz sampling frequency is used by the voltage and current sensors to sample the phase voltages and currents. The hysteresis width was set to 2 A. The SRM is loaded using an eddy-current dynamometer. Using a DC power supply, the load applied by the dynamometer on the motor is controlled. The output average torque of the motor is measured using the torque transducer and the load cell-moment arm arrangement which are interfaced with the NI 9215 voltage DAQ and the NI 9237, respectively. LabVIEW 2017 is then used to process the data.



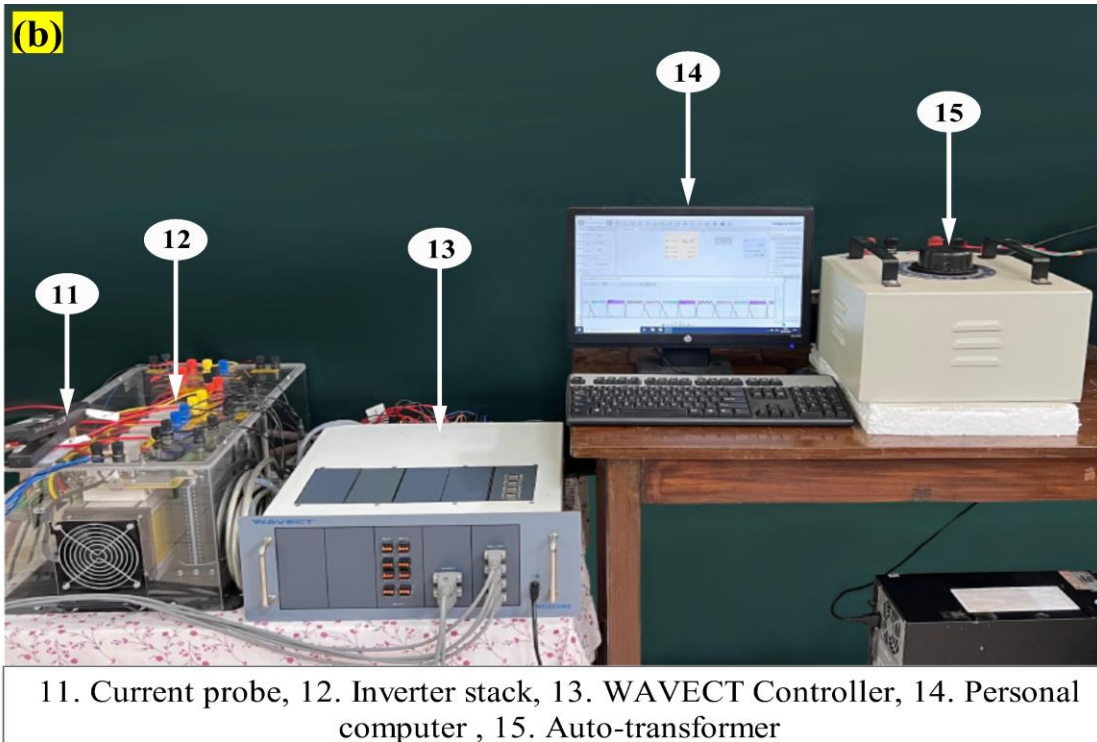


Figure 4.23 (a) Experimental setup for determining the dynamic performance of the SRM prototype (b) AHB inverter controlled by WAVECT controller

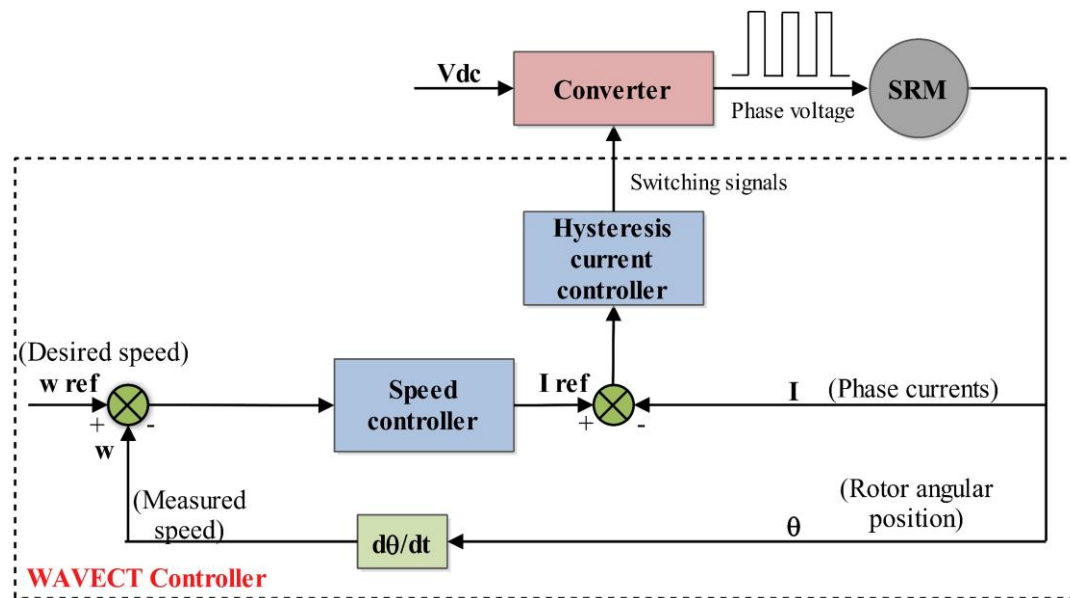


Figure 4.24 Closed loop hysteresis current control (HCC) block diagram

With this setup, the dynamic performance of the prototype SRM is assessed at the four RPs. The corresponding I_{ref} , θ_{ON} and θ_{OFF} were obtained from Table 4.9. The experimentally recorded waveforms of the current and voltage for one of the phases

that correspond to RP1 are shown in Figure. 4.25. It can be observed that hard chopping is implemented since the phase voltage traverses both the positive and negative in the current control region.

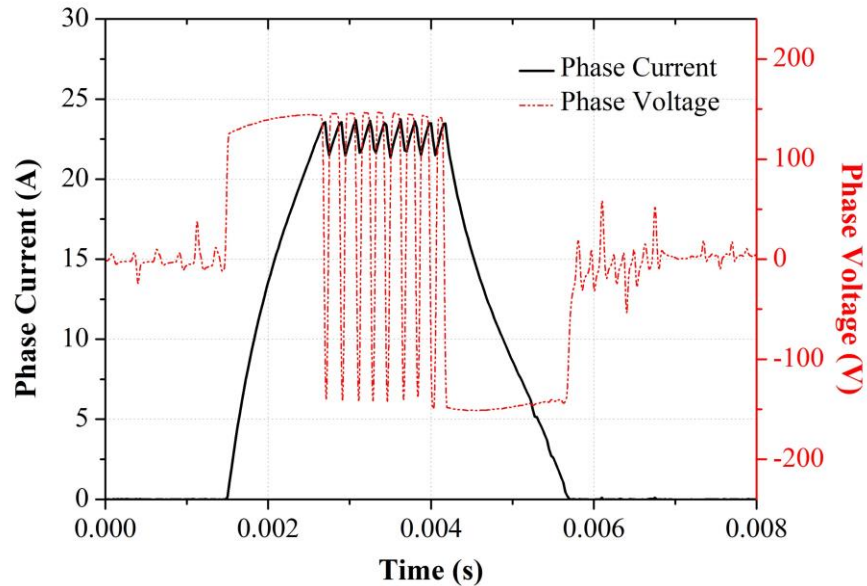


Figure 4.25 Experimental phase current and voltage waveforms at RP1 ($I_{ref} = 23$ A, $\theta_{ON} = 54$ elec. deg. and $\theta_{OFF} = 144$ elec. deg.)

Figure 4.26 compares the waveforms of the transient FEA simulation and the current waveform of the prototype SRM measured through experiments for the RP1. The simulated and experimental waveforms are observed to be very similar. The small deviations between them can be attributed to the negligence of end-winding leakage in the transient 2D-FEA model and the manufacturing and assembly imperfections of the prototype.

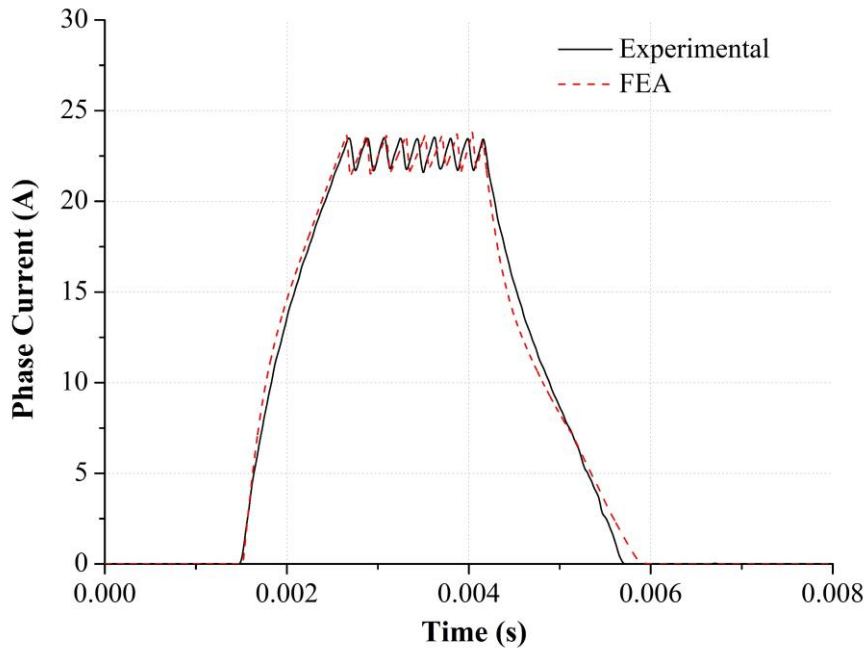


Figure 4.26 Experimental phase current comparison with transient FEA at RP1

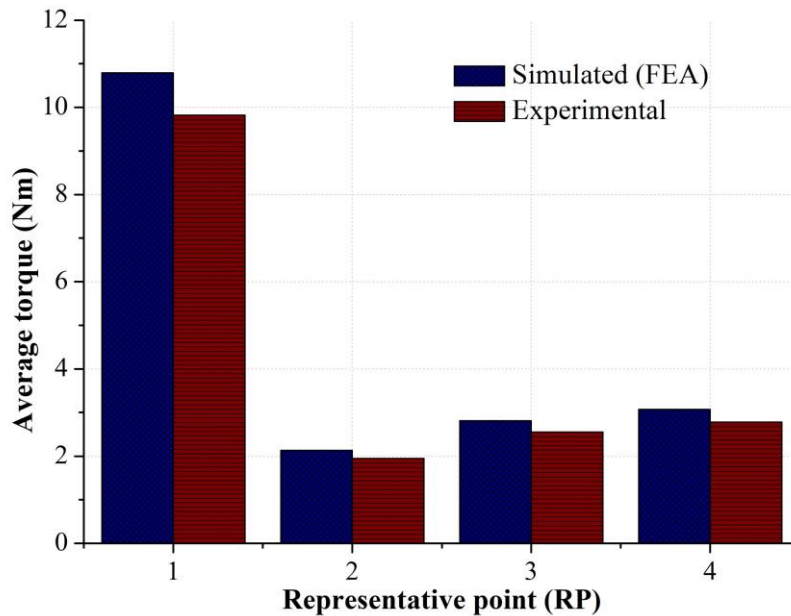


Figure 4.27 Average torque comparison between experiments and FEA at the 4 RPs

Figure 4.27 shows the comparison of the average torque determined from experiments and the transient FEA at the four RPs. It is observed that there is a minimal difference between the experimental and the FEA results (8.5-9.4% error) which may be due to the manufacturing and the assembly deviation which have not been considered within the FEA model. Additionally, friction and windage losses of the system are not

accounted for in the FEA model (Currie 2003). Figure 4.28 shows the experimental current waveforms for the four phases of the SRM prototype at the four RPs. The discussion above suggests that the dynamic experimental results are in close agreement with the transient FEA model employed.

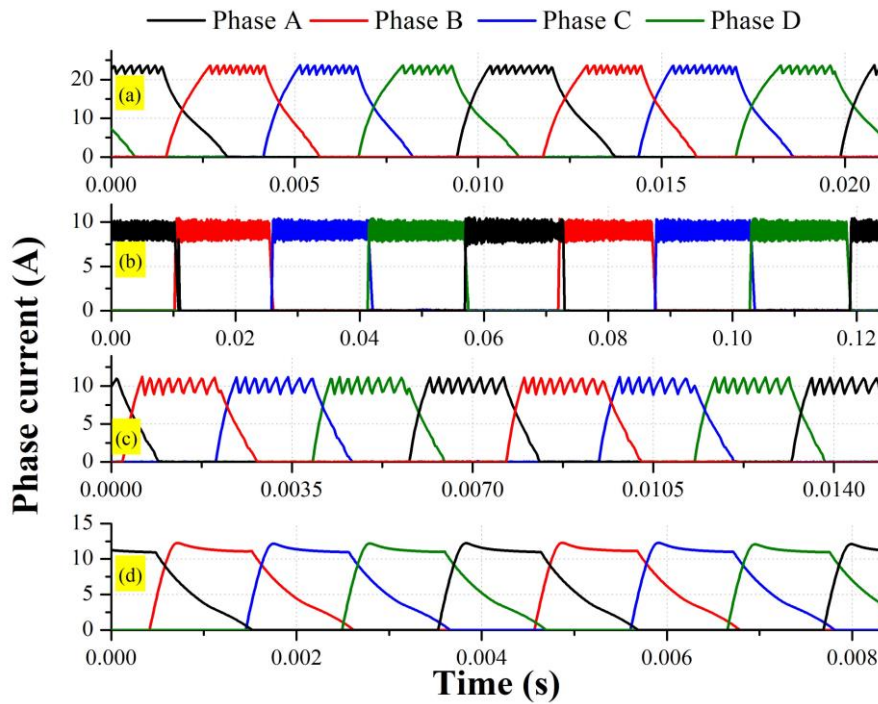


Figure 4.28 Experimental phase current waveforms at (a) RP1 (b) RP2 (c) RP3 (d) RP4

4.8 Summary

This chapter presented a methodology for realizing the Pareto-based MODO of an SRM (designed for usage in an E-rickshaw) by taking into account a driving cycle. The performance requirements and the load operating points of the SRM were estimated using the vehicle dynamics equations over the CSIR-IIP driving cycle. The desired motor performance metrics such as maximizing the starting torque, torque density, and minimizing the electromagnetic loss calculated across the load representative points in the driving cycle were set as the design objectives for the MODO. *k*-means machine learning algorithm was utilized to split the load operating points into a finite number of clusters and subsequently the RPs. Design objectives were accurately evaluated by running dynamic simulations in the computationally efficient MATLAB/Simulink SRM drive model and transient 2D-FEA considering the effect of control variables.

Kriging models built by carrying out the design of experiments were used to accurately depict the relationship between the design variables of the SRM and the design objectives to eliminate the computational cost of FEA during the optimization process. An NSGA II multi-objective optimization algorithm was performed based on the generated kriging models to obtain the Pareto-optimal set. From the generated Pareto-optimal set, an optimal design that provided the best balance between the design objectives was chosen and the dimensions of design variables were used to build a prototype for experimental static and dynamic performance verification. The results showed a close correlation between the static and dynamic performance of the prototype with the electromagnetic FEA simulations utilized with a minimum error. The major findings and significant conclusions of this chapter are outlined in Section 6.2 under Chapter 6.

Chapter 5 COMPARATIVE ASSESSMENT OF AN 8/18 MULTI-TEETH WITH CONVENTIONAL 8/10 IN-WHEEL SRM FOR AN E-SCOOTER

5.1 Introduction

As discussed in Chapter 2, the MTSRM (with $N_r > N_m$) topology is a potential choice for IW traction motor applications since it maintains the inherent robustness, affordability, and simplicity of traditional SRM designs. However, there is limited literature regarding the design of MTSRM topologies and their electromagnetic performance. A comprehensive electromagnetic performance comparison study covering the entire torque-speed range for an EV application has not been conducted between the MTSRM and traditional SRMs. In this chapter, a comprehensive electromagnetic comparison is carried out between the four-phase 8/18 MT and the conventional 8/10 IW-SRMs (Objective III). The 8/18 IW-MTSRM is novel and has not been reported in the literature so far. The considered topologies have been evaluated over the entire torque-speed range within the same electrical and geometrical constraints (current, voltage, and motor volume) for an E-scooter (E-2W) application. Based on the results obtained, the present work aims to establish the most apt SRM configuration for the E-scooter application.

An outline of the procedure to accomplish this objective has been depicted in Figure 5.1. In the first step, the target torque-speed envelope for the SRM is estimated based on the World harmonized motorcycle test cycle (WMTC) driving cycle and vehicle parameters using the vehicle dynamics model. In the second step, a design formula governing the selection of the number of MT and rotor poles for MTSRMs has been proposed. Using this formula, a four-phase 8/18 IW-MTSRM has been derived. Among the conventional SRM topologies, an 8/10 IW-SRM has been chosen for comparison. Initial designs of the considered topologies have been analyzed using electromagnetic FEA. For a fair comparison, the design variables corresponding to the SRM topologies have been optimized by applying the multi-objective particle swarm optimization (PSO). A search algorithm-based single-objective optimization (SOO) model has been implemented in the SRM drive model to determine the optimized

commutation angles across the entire driving range. In the third step, under the results and discussions section, the topologies have been compared based on their static and dynamic characteristics. The dynamic torque-speed efficiency maps, which are critical from the standpoint of an industrial application point have also been provided. Based on the comparative evaluation conducted, a configuration that provided the best balance between the electromagnetic performance metrics has been proposed for an E-scooter. In addition, a thermal analysis is carried out for the proposed configuration in the final stage to ensure its thermal reliability and safety.

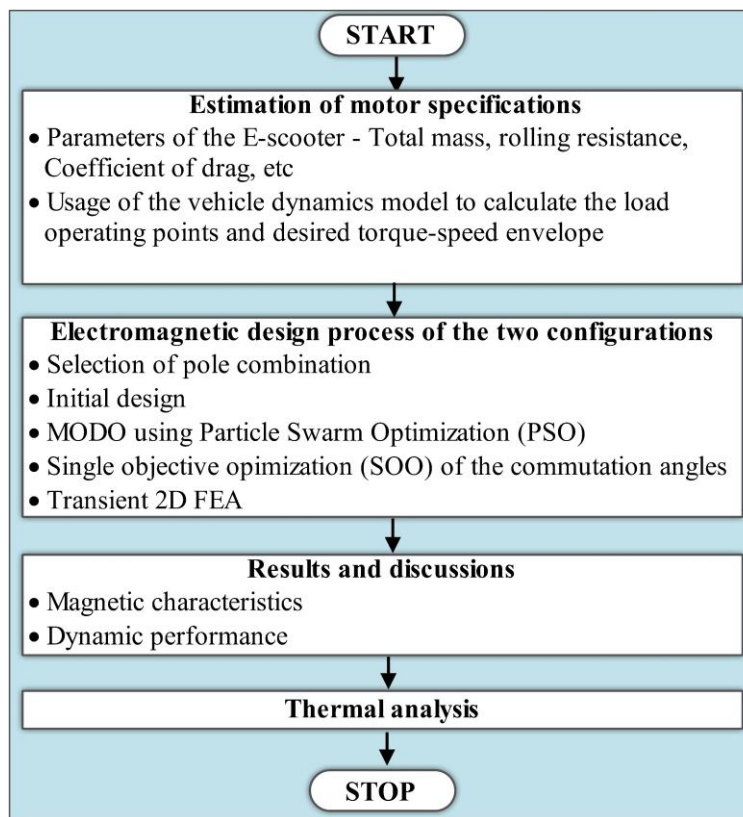


Figure 5.1 Outline of the procedure to carry out the comparative assessment of 8/18 MT with conventional 8/10 SRM

5.2 Theoretical Background

The torque output of an MTSRM at any angular instant can be theoretically calculated by using the magnetic equivalent circuit model (Prasad et al. 2022). The electromagnetic torque output (T) of an SRM operating in the magnetic linear condition (no magnetic saturation in the core) is given by;

$$T = \frac{1}{2} i^2 \frac{dL(\theta, i)}{d\theta} \quad (5.1)$$

where, i is the phase current, L is the phase inductance, and θ is the rotor position.

The phase inductance (L) is expressed as

$$L = \frac{N^2}{R_{eq}} \quad (5.2)$$

where, N is the number of turns per phase and R_{eq} is the equivalent reluctance of the SRM magnetic circuit as provided by the expression;

$$R_{eq} = R_{core} + R_g \quad (5.3)$$

R_{core} and R_g indicate the reluctances of the flux path in the core (stator and rotor) and airgap respectively. Since $R_{core} \ll R_g$,

$$R_{eq} \approx R_g \quad (5.4)$$

R_g is expressed as

$$R_g = \frac{l_g}{\mu_o L_{stk} L_{ol}(\theta) n} \quad (5.5)$$

where l_g is the magnetic path length of the airgap, μ_o is the permeability of free space, L_{stk} is the stack length of the motor, L_{ol} is the overlap length between the rotor and stator pole and n is the number of teeth per stator pole.

From Equations (5.1), (5.2), (5.4) and (5.5), the torque output (T) can be now expressed as;

$$\tau = \frac{1}{2} i^2 \frac{d}{d\theta} \left[\frac{N^2 \mu_o L_{stk} L_{ol}(\theta) n}{l_g} \right] \quad (5.6)$$

From Equation 5.6 it is evident that, for any given motor size having the same overall dimensions (D_{or} and L_{stk}) with a fixed g and magnetomotive force (MMF), the torque output can be enhanced by increasing the value of n . SRM configurations with $n = 1$ and $n = 2$ and their corresponding flux patterns have been shown in Figure 5.2. The

difference in the geometry of the IW-MTSRM, as depicted in Figure 5.2 (b) (each stator pole is bifurcated into two teeth and N_r is increased accordingly) causes the flux to distribute through each tooth. Further, these flux lines cross the airgap and flow into the corresponding rotor poles. This arrangement results in a larger flux variation over a shorter variation period leading to a higher torque production per electrical period (Zhu et al. 2017b).

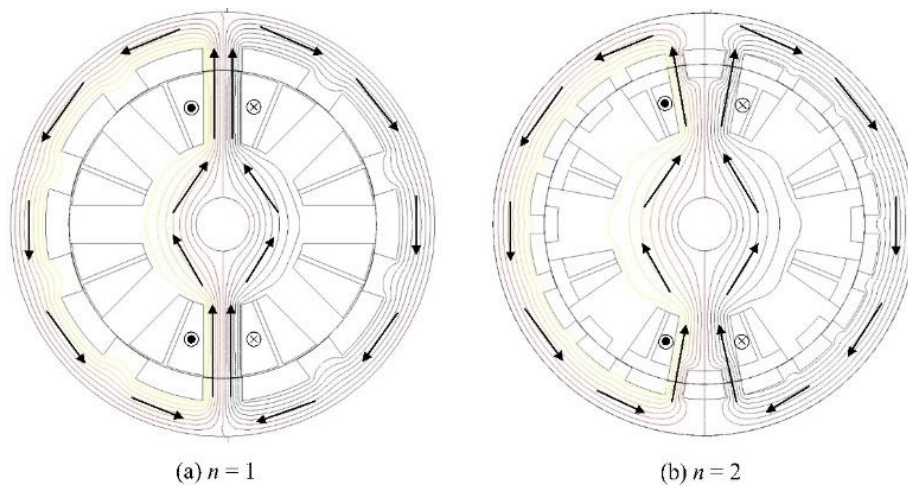


Figure 5.2 Flux path comparison of SRM configurations with (a) $n = 1$ (Conventional SRM) (b) $n = 2$ (MTSRM)

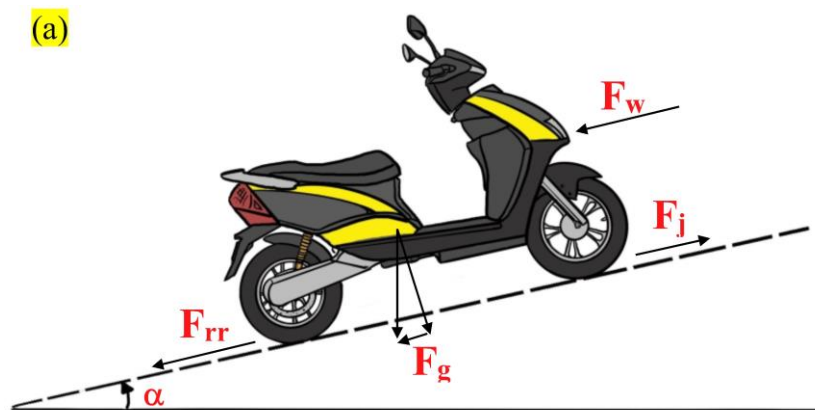
5.3 Investigated EV application and estimation of motor specifications

This section deals with the determination of the target motor specifications for the considered E-scooter (E-2W) application. Some of the popular E-scooters in the Indian E-scooter market (maximum speed of around 50 km/h) employing IW-BLDC motors along with their performance specifications are enlisted in Table 5.1. E-scooters are mainly employed for short-distance commutes within the city limits. The vehicle dynamics equations described in Chapter 4 are utilized and simulated over the WMTC to obtain the load operating points of the E-scooter (Ehsani et al. 2018). The WMTC (maximum speed of 50 km/h) has been extensively adopted by automotive manufacturers to determine the energy consumption and driving range of E-scooters (Steven 2002) (Bandivadekar 2021). Figure 5.3a illustrates the schematic of an E-scooter and the forces of the vehicle dynamics equations. Figure 5.3b represents the WMTC driving cycle. The parameters of the E-scooter are given in Table 5.2. Figure 5.3c depicts the torque-speed envelope and the LOPs of the E-scooter obtained by

simulating the vehicle dynamics equations over the WMTC driving cycle. The idealized target peak torque profile consisting of all the LOPs is also depicted, assuming a hyperbolic variation above the base speed to establish an idealized constant power range. From Table 5.1, it is observed that the performance requirements of the SRM thus obtained are similar to IW-BLDC motors used to propel some of the popular E-scooters in the Indian E-scooter market.

Table 5.1 Comparison between the specifications of the commercially available IW-BLDC motors and the proposed IW-SRM considered in the present work

E-Scooter name	Battery voltage (V)	Maximum speed of the E-scooter (kmph)	Peak Torque (Nm)	Peak power (W)
BGauss B8 (BGauss, 2023)	57.6	50	94.6	1900
Okinawa Ridge Plus (RIDGE+, 2023)	60	45	NA	1600
Hero Electric Photon (Photon, 2022)	48	45	NA	1800
Piaggio 1+ (Piaggio 1, 2023)	48	45	85	1200
Proposed IW-SRM (Present)	48	50	90	1900



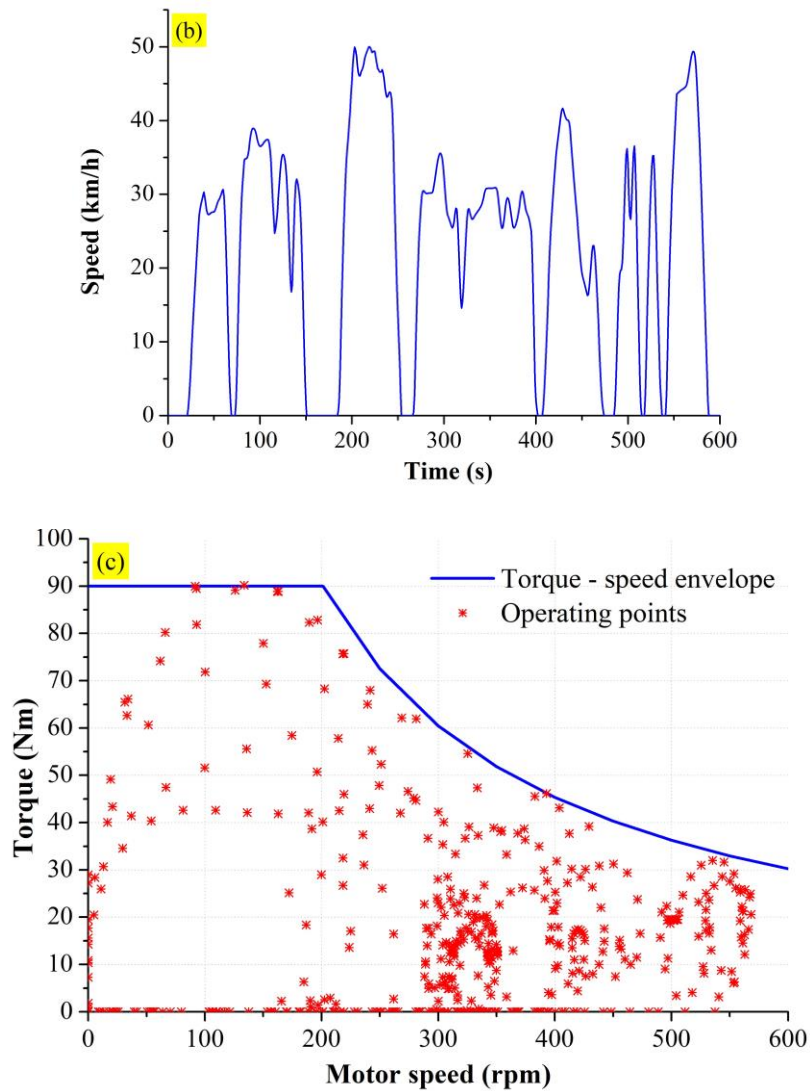


Figure 5.3 (a) Forces acting on an E-Scooter (b) WMTC driving cycle speed profile (Steven 2002) (c) Torque-speed envelope and load operating points of the E-scooter obtained from the vehicle dynamics equations.

Table 5.2 Parameters of the E-scooter (Andrada et al. 2016)

Parameter	Value
Mass (kerb load / payload) (M)	200 (100/100) kg
Rolling resistance (f_r)	0.01
Drag coefficient (C_d)	0.7
Frontal area (A_f)	0.6 m ²
Density of air (ρ)	1.23 kg/m ³

Acceleration due to gravity (g)	9.81 m/s ²
Tire size	90/90 R12

Based on this, the design targets with the constraints used for the SRM design are summarized in Table 5.3. The SRM designs should primarily target to meet the torque speed trajectory with a peak torque of at least 90 Nm until the base speed of 200 rpm and above 30 Nm at 600 rpm. Within a 12" rear wheel of the E-Scooter, the motor dimensions having an outer diameter of 278 mm with a stack length between 50-70 mm is a suitable and popular choice in the market (Sundaram et al. 2022) (Singh et al. 2021). For the proposed IW-SRM, the stack length is fixed at 65mm. It is a challenge in the SRM design process to attain such a high peak torque considering the limited space available inside the 12" wheel. Given the manufacturing constraints, the air-gap length (l_g) of the SRM is set to the lowest attainable value of 0.4 mm in the present study. The battery supply voltage is fixed to 48 V. Based on the demand peak load torque at the base speed, the required RMS phase current is calculated and constrained to 75 A (electrical constraint). For SRMs, the ratio between the RMS phase current and the maximum peak phase current lies in the range of 0.3~0.75 (Jiang et al. 2017) (Howey et al. 2020). Considering a value of 0.53 in the present case, the maximum peak phase current for chopping is accordingly set to 140 A.

Table 5.3 Design and electrical constraints for the SRM

Parameter	Value
Peak motor torque	>90 Nm
Mechanical power output	>1900 W
Maximum motor speed	600 rpm
Base speed	200 rpm
Rotor outer diameter (D_{or}) (12" wheel)	278 mm
Stack length (L_{stk})	65 mm
Battery voltage	48 V
Maximum peak phase current (I_{peak})	140 A
Maximum RMS phase current (I_{rms_lim})	~75 A

Air-gap length (l_g)	0.4 mm
Shaft diameter (D_{sh})	35 mm

5.4 Electromagnetics design process of the two configurations

This section discusses the design procedure for the 8/18 MT and the 8/10 SRM topologies. This section also includes some results for the 8/18 MTSRM wherever relevant.

The process employed in the design of the SRM topologies is defined in five discrete stages in the flowchart shown in Figure 5.4. Further, the design principles and analysis corresponding to each stage are also discussed. In both the SRM designs considered for comparison, the coils on the diametrically opposite stator poles are connected in series. Four-phase SRMs have been chosen in this study over the lower-phase configurations as they are known to demonstrate improved average torque, torque density, and lowered torque ripple (Krishnan 2001). As SRMs exhibit considerable nonlinearity due to magnetic saturation, FEA is used in this study to accurately analyze their electromagnetic characteristics (Wattthewaduge et al. 2020).

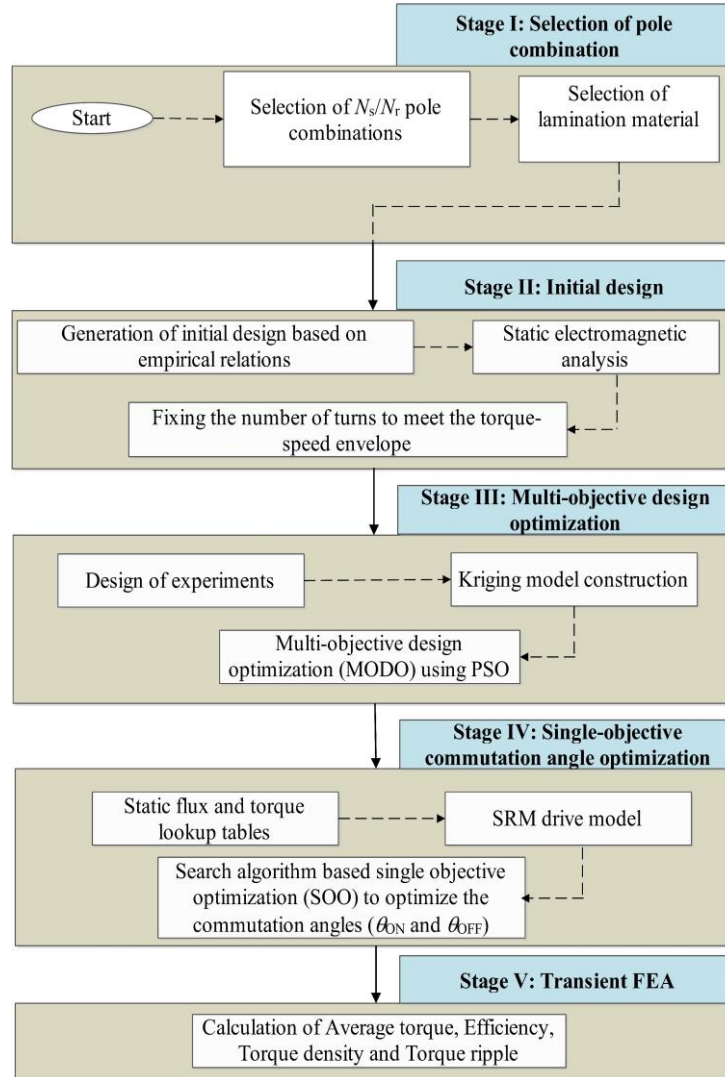


Figure 5.4 SRM design methodology

5.4.1 Stage I: Selection of pole combination and core material:

(i) Selection of N_s/N_r pole combination: The equation governing the selection of the total number of multi-tooth (N_m), number of multi-tooth per stator pole (n), and the rotor poles (N_r) for the MTSRM is distinct from that followed for the conventional SRMs and is expressed as;

$$LCM\left(\frac{N_m}{n}, N_r\right) = N_{ph} N_r \quad (5.7)$$

where LCM denotes the least common multiple and N_{ph} is the number of phases. Equation 5.7 can be applied for SRM configurations irrespective of N_{ph} and n .

According to the above expression, for four-phase MTSRMs, the number of rotor poles can be any of these values, *viz.* 12, 14, 18, 22, 26, 30. The configuration with $N_s = 8$, $n = 2$ ($N_m = 16$) and $N_r = 18$ was chosen. Among the conventional SRM designs, the 8/10 SRM (based on Miller's equation, $N_r = N_s + 2$) was chosen as it displayed an improved average torque, efficiency, specific torque, and lower torque ripple when compared to 8/6 SRM (Zhu et al. 2017a). An increase in the number of rotor poles boosts the slot area available for the winding. This reduces the copper loss and elevates the efficiency. The stator/rotor pole combinations were chosen such that $N_r > N_m$, N_s for both the topologies respectively. Further, N_r is kept close to N_m and N_s . Any further increase in N_r is known to reduce both their peak torque capacity and field weakening ability correspondingly (Howey et al. 2020). Accordingly, the dynamic results of the 8/14 and 8/22 MTSRM at different operating speeds are provided in Appendix II. Configurations with $n \geq 3$ have not been considered due to their reduced torque production capabilities and reduced efficiency owing to elevated core loss (Zhu et al. 2017b).

(ii) Selection of core material: M270_35A has been chosen as the core material for both the SRM topologies as it possesses an elevated saturation flux density (2T) and lower core loss (Cogent 2023). The B-H curve of the M270_35A is illustrated (Figure 5.5).

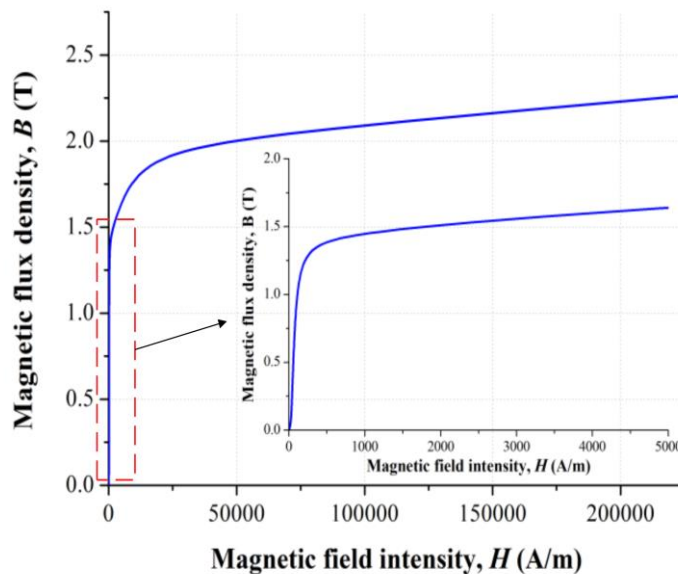


Figure 5.5 B-H curve of M270_35A (Cogent 2023).

5.4.2 Stage II: Initial design

(i) Generation of initial design: The classical analytical techniques put forth (Krishnan 2001) (Miller 1993) and 2D electromagnetic FEA were used to develop and analyze the initial designs for both the SRM topologies (Figures 5.6a and 5.6b). Constraints to this process include spatial limitation (D_{or} and L) and l_g . The different design variables corresponding to both the SRM topologies are indicated in Figure 5.6. A description of the design variables has been provided in the nomenclature section of this thesis.

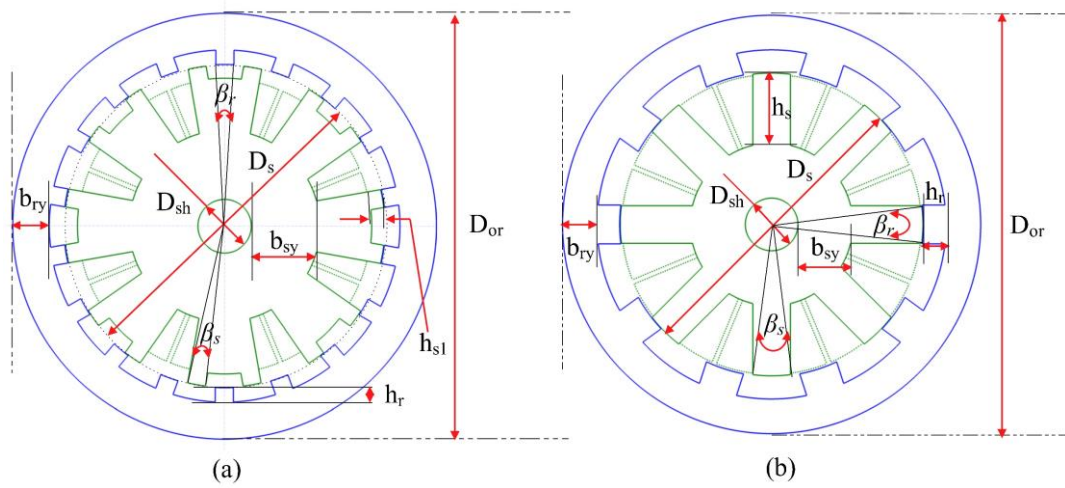
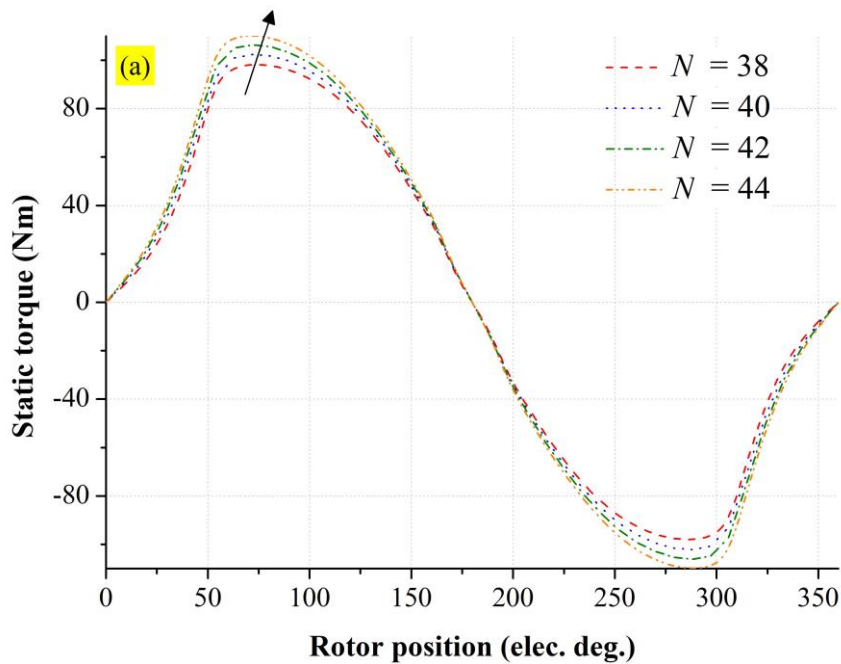


Figure 5.6 Initial design of (a) 8/18 MT ($n = 2$) and (b) 8/10 ($n = 1$) SRM configurations

(ii) Fixing the number of series turns per phase (N): The number of turns per phase for both the SRM topologies was adjusted to satisfy the peak torque-speed envelope within the constraints of maximum RMS phase current and battery voltage. The procedure put forth (Bilgin et al. 2019) was used to achieve this, and it has been illustrated for the 8/18 MTSRM. The static characteristics of the initial design of the 8/18 MTSRM with a varied number of turns per phase ($N=38-44$) are obtained using FEA (ALTAIR 2023). These characteristics (*i.e.* static torque and flux linkage), as lookup tables (LUTs) are then put into the SRM drive model to determine the optimized commutation angles (θ_{on} and θ_{off}). The optimized θ_{on} and θ_{off} are obtained using a search algorithm-based single objective optimization (SOO) intended to maximize the average torque at various speeds within the I_{rms_lim} . The dynamic results are shown in Figure 5.7b. For operating

speeds lesser than the base speed, it is noted that with the increase in N , the dynamic torque also improves (owing to an increase in the MMF, which is also indicated in Figure 5.7 (a)). Beyond the basic speed, these trends, however, reverse because of an increased effective back-EMF (Chiba et al. 2012). Although, it is preferable to use $N=38$ or 40 (as the motor exhibited an optimum behavior *i.e.*, high peak average torque below and above the base speed respectively), $N = 42$ was selected; the rationale for this is discussed in Section 5.5.1.



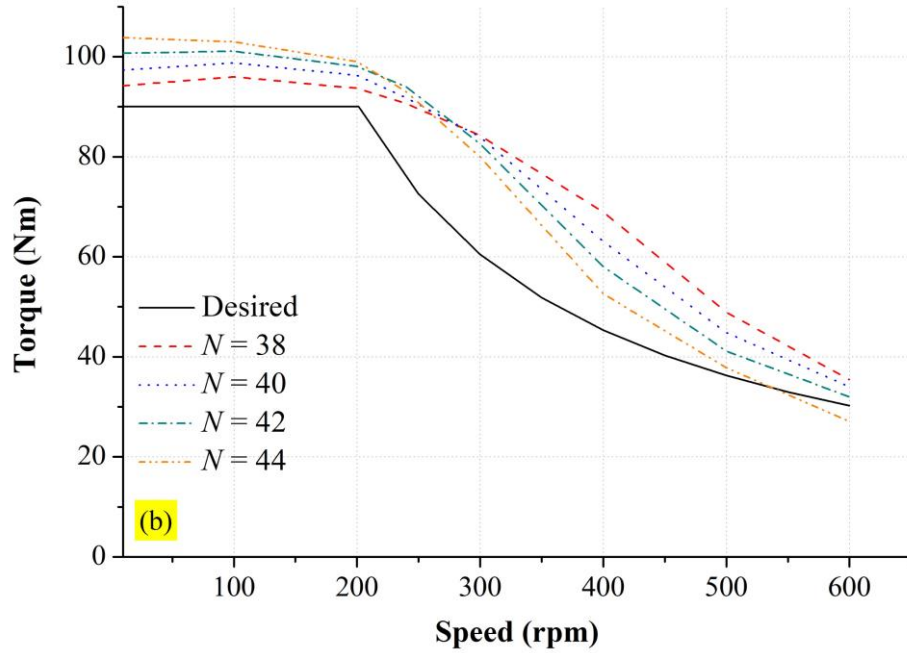


Figure 5.7 Influence of the number of turns per phase on the (a) Static torque and (b) Dynamic torque of the 8/18 MTSRM

5.4.3 Stage III: Multi-objective design optimization (MODO) using Particle Swarm Optimization (PSO)

For a fair comparison, MODO was performed for both the SRM topologies to determine the optimized values of the design variables. This was executed by coupling the PSO with a Kriging model constructed using the design of experiments (Figure 5.8) (Ma and Qu 2015). In the present study, the optimization was intended to maximize the static average torque and minimize the copper loss. Considering a practical range of dimensions of the design variables for an optimal design (Table 5.4), a Latin hypercube design (LHD) was employed in designing the experiments. With the number of turns per phase fixed for each design candidate, the number of strands is maximized to attain a practically attainable slot fill factor of 0.6 (Howey et al. 2020). The static average torque ($T_{average}$) for each design candidate at the maximum peak phase current (I_{peak}) is evaluated using 2D electromagnetic static FEA. $T_{average}$ is expressed as (Miller 1993);

$$T_{average} = \frac{N_{ph} N_r}{2\pi} \partial W \quad (5.8)$$

where, ∂W is the magnetic co-energy.

Peak copper loss ($Loss_{Cu}$) is calculated using the expression (Xue et al. 2010b);

$$Loss_{Cu} = m I_{peak}^2 R_{ph} \quad (5.9)$$

where, R_{ph} is the phase resistance for each design candidate. Based on the results obtained, Kriging models were generated for both $T_{average}$ and $Loss_{Cu}$ respectively.

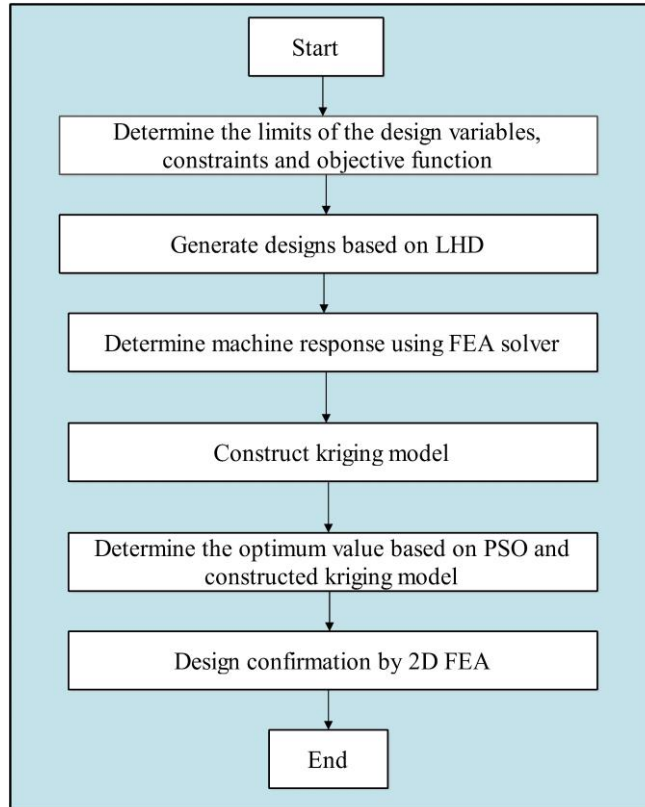


Figure 5.8 Flowchart of the MODO

Table 5.4 Optimization limits of the design for the 8/18 MTSRM

Parameter	Range
b_{ry}	19-25 mm
h_r	6.5-11 mm
β_r	6-10°
b_{sy}	39-50 mm
β_s	6-9°
h_{s1}	7.5-9.5 mm

The constraints adopted for design variables in the optimization (mentioned below) were based on SRM design principles provided (Zhu et al. 2017b) (Krishnan 2001). The constraints were also used to eliminate the unfeasible designs.

$$\beta_r \geq \beta_s \quad (5.10)$$

$$sf \leq 0.6 \quad (5.11)$$

The slot fill factor was constrained to 0.6. The MODO model was formulated, wherein the objective function consists of the weighted sum of individual objectives given as;

$$\min_x z(x_r) = w_1 \frac{T_{\text{averageb}}}{T_{\text{average}}} + w_2 \frac{Loss_{\text{Cu}}}{Loss_{\text{Cub}}} \quad (5.12)$$

where, w_1 and w_2 are the weight factors for average torque and loss such that $w_1 + w_2 = 1$; T_{average} and $Loss_{\text{Cu}}$ indicate the average torque and copper loss respectively. T_{averageb} and $Loss_{\text{Cub}}$ correspond to the baseline values of the average torque and copper loss respectively. w_1 and w_2 were assumed to be 0.6 and 0.4. A slightly higher weightage is given to average torque as compared to copper loss, to account for the high starting torque requirement in low-speed hill climbing and urban start-stop traffic for the E-scooter application. PSO was employed to determine the optimal solution of Equation 5.12 (Eberhart and Kennedy 1995). The population size of the PSO was set to 35 and the maximum number of iterations to 1000. The inertia of the particles and the acceleration coefficients were set to 0.6, 2, and 2 respectively. The convergence characteristic of the PSO is shown in Figure 5.9.

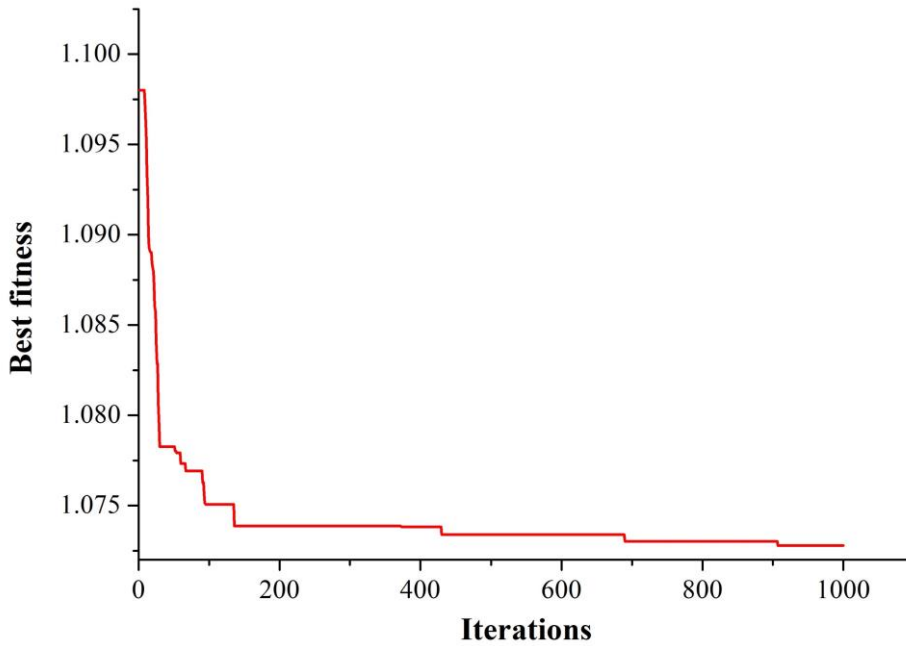


Figure 5.9 Convergence characteristic of the PSO

5.4.4 Stage IV: Single-objective firing angle optimization

In order to obtain the dynamic characteristics namely the average torque (T_{avg}), efficiency (η) and torque ripple (T_{ripple}) of the optimized SRM, it is important to accurately determine the optimized values of commutation angles (θ_{on} and θ_{off}) across the torque-speed range (Bilgin et al. 2019). The static characteristics of both the SRM topologies (optimized in Stage III) from FEA were fed into the SRM drive model developed in MATLAB/Simulink. More details regarding the SRM drive model can be seen in (Bilgin et al. 2019). The optimized values of θ_{on} and θ_{off} were determined from the SRM drive model by formulating a search algorithm-based SOO to maximize the T_{avg} (Xue et al. 2010a). To fully characterize the SRM's dynamic torque-speed profile, the process was repeated for all the evenly spaced reference current and speed points within the torque-speed range.

During optimization, an RMS phase current limit (I_{rms_lim}) of 75A (Table 5.2) was one of the constraints (non-linear) considered.

$$I_{rms} \leq I_{rms_lim} \quad (5.13)$$

An additional constraint of maintaining a positive T_{avg} magnitude at all operating speeds for various phase currents was also incorporated.

$$T_{avg} > 0 \quad (5.14)$$

The boundaries of the commutation angles (linear constraint) are also listed below;

$$\begin{bmatrix} 1 & -1 \\ -1 & 1 \end{bmatrix} \begin{bmatrix} \theta_{ON} \\ \theta_{OFF} \end{bmatrix} < \begin{bmatrix} -\frac{360}{N_{ph}} \\ \frac{360l}{N_{ph}} \end{bmatrix} \quad (5.15)$$

In the present study, the maximum phase conduction angle is set to 120 electrical degrees for both topologies to have an appropriate comparison. The LUTs showing the optimized θ_{on} and θ_{off} obtained from the above optimization for the 8/18 MTSRM are depicted in Figure 5.10.

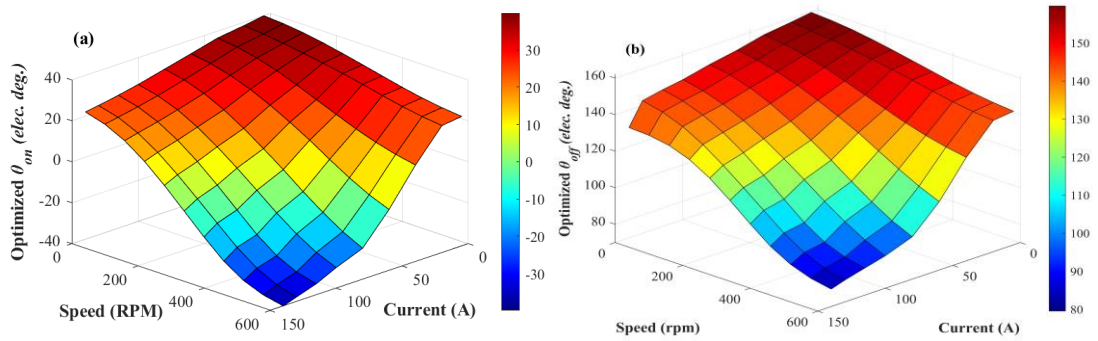


Figure 5.10 LUTs of optimized (a) θ_{on} (b) θ_{off} of the 8/18 MTSRM

5.4.5 Stage V: Transient 2D FEA

The optimized commutation angles (θ_{on} and θ_{off}) obtained for various values of reference currents at different operating speeds determined in stage IV for both the SRM topologies were fed into the transient 2D FEA to determine the T_{avg} , η and T_{ripple} respectively. The procedure described in Section 4.5.7 (Chapter 4) is followed to calculate the T_{avg} , η and T_{ripple} .

5.5 Results and Discussions

The optimized design variables and other parameters of both, 8/18 MT and 8/10 SRMs are provided in Table 5.5. It should be noted that the number of turns per phase (N) for the 8/18 MTSRM is 42 while that of the 8/10 SRM is 72. The significant reduction in N for the 8/18 MTSRM was mainly due to the MT geometry ($n = 2$) which produced the desired target torque at a lower MMF (as discussed in Section 5.2) and is evident. In this section, a comprehensive performance comparison between the two models is drawn based on the results obtained using 2D electromagnetic static and transient FEA.

Table 5.5 Parameters of the two optimized SRMs

Parameter	8/18 MTSRM	8/10 SRM
Rotor outer diameter (D_{or}) (mm)	278	278
Stack length (L_{stk}) (mm)	65	65
Air-gap length (g)	0.4	0.4
Rotor yoke thickness (b_{ry}) (mm)	23.1	20.5
Rotor pole arc angle (β_r) (degree)	7.9	15.1
Stator bore diameter (D_{os}) (mm)	218.6	215.5
Stator yoke thickness (b_{sy}) (mm)	40.5	35.5
Stator pole arc angle (β_s) (degree)	6.7	14.1
Slot depth in stator pole (h_{s1}) (mm)	8.51	-
Number of turns per phase (N)	42	72
Wire gauge	18 SWG	18 SWG
Number of parallel strands	8	9
Slot fill factor (sf)	0.59	0.58
Phase resistance (R_{ph}) (Ω)	0.019	0.031

5.5.1 Magnetic characteristics

(i) Static torque

The static torque curves obtained from electromagnetic static FEA for the two topologies at varied phase currents are illustrated in Figure 5.11. In this simulation, the

currents are maintained constant between the unaligned (0 electrical degrees) and aligned positions (180 electrical degrees). It can be noted that 8/10 SRM produces higher instantaneous torques for a current of 20 A in comparison to the 8/18 MTSRM. The instantaneous torques for 60 A were similar in both designs. However, at higher currents *i.e.*, 100 A and 140 A, 8/18 MTSRM produced higher instantaneous torques.

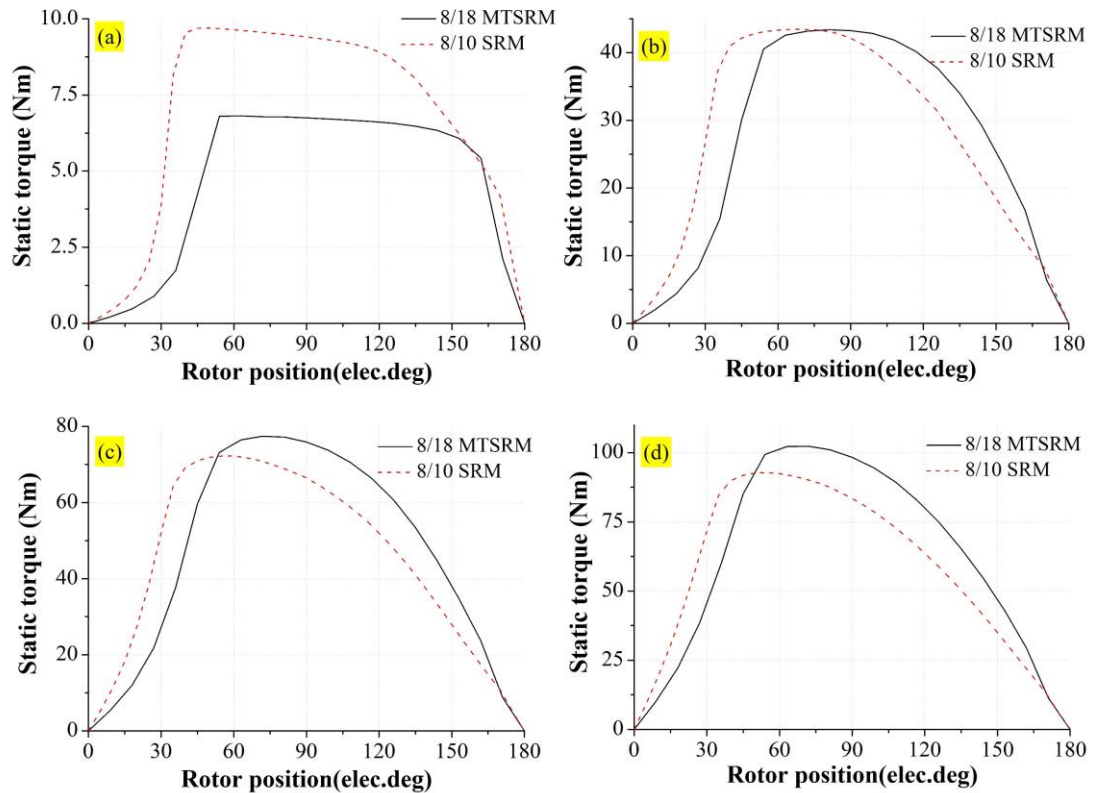


Figure 5.11 Static torque of the 8/18 and 8/10 SRM at varied currents (a) $i = 20$ A (b) $i = 60$ A (c) $i = 100$ A (d) $i = 140$ A

The average static torque per revolution is calculated using Equation 5.8. The calculated co-energies (∂W) from the flux linkage curves of the 8/10 and 8/18 MTSRMs were 18.8 J and 11.65 J respectively (Figure. 5.12). Though the co-energy represents the mechanical output per stroke, average static torque is dependent on the number of strokes per revolution ($m \times N_r$) in Equation 5.8). Accordingly, the comparison of average static torque for both designs at varied phase currents is depicted in Figure. 5.13. The 8/10 design was observed to produce a higher average torque for all values of currents until 50 A. However, a reversal in the trend is noted when the current is above 50 A.

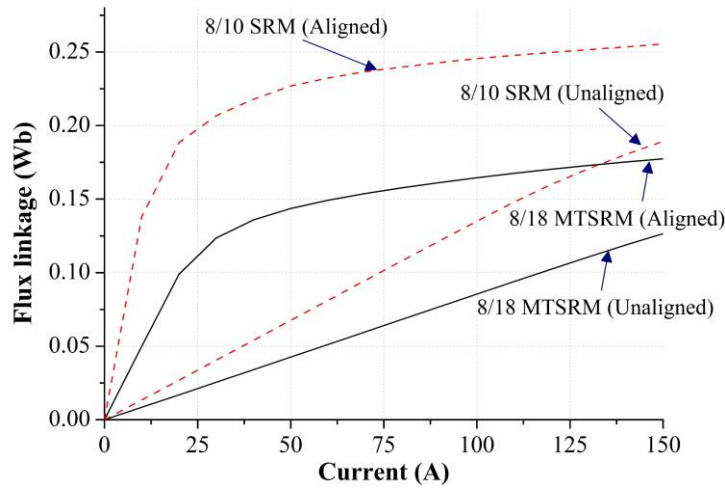


Figure 5.12 Flux linkage curves of the 8/18 MT and 8/10 SRM

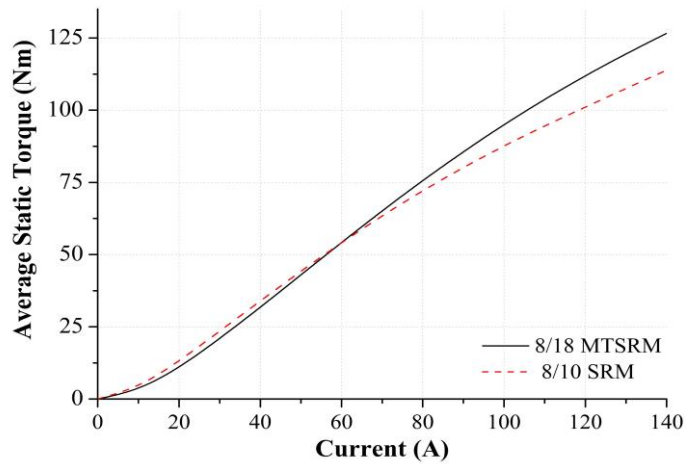


Figure 5.13 Average static torque of the 8/18 MT and 8/10 SRMs

An assessment of the flux densities associated with the magnetic core of both the SRM topologies at the partially overlapped rotor positions at 20 A and 140 A can be used to explain this behavior (Figure. 5.14). It is known that adequate saturation of the SRM magnetic core, particularly the corners of the stator and rotor poles is essential to enhance the co-energy increment and thereby boost its torque production capability (Jiang et al. 2006). At 20 A, the average operating flux densities in the stator pole of the 8/10 SRM were higher (~ 1.38 T) than the 8/18 MTSRM (~ 0.73 T) (Figure. 5.14a). The reduced flux density in the 8/18 MTSRM was due to lower MMF ($42 \times 20 = 840$ AT) which was insufficient to cause an adequate saturation of the pole corners in contrast to the 8/10 model ($72 \times 20 = 1440$ AT). The 8/18 MTSRM is thus

led to operate in the linear region (0.1 – 1.2 T) of the B-H curve (Figure. 5.5) resulting in decreased co-energy increment and the average static torque subsequently owing to ineffective use of the iron (Rahmani et al. 2021). This can also be deciphered in the flux linkage curves wherein the 8/18 MT and 8/10 SRM begin to saturate at a current of 30 A and 20 A respectively (Figure 5.12). Hence, to improve the saturation level of the 8/18 MTSRM, the number of turns per phase had been maximized to 42 (to maximize the MMF) as compared to 38 and 40 in Section 5.4.2, also ensuring that the desired torque-speed envelope is satisfied. At 140 A, 8/10 SRM is under deep magnetic saturation (Figure 5.14b, led to operate in the ineffective use of the current region in the B-H curve) in comparison to the 8/18 MT design thereby resulting in decreased average static torque. The higher average magnetic flux density in the stator pole of 8/10 SRM causes a major part of the MMF to be utilized to push the flux through this segment (due to increased reluctance). This depletes the MMF available to push the flux through the airgap thereby arresting the increase of average torque with increasing current (Rahmani et al. 2021). On the other hand, compared to the 8/10 design, the 8/18 MTSRM at 140 A produced a higher average torque due to lower magnetic saturation levels in the stator pole (Figure. 5.14b), indicating that they can demonstrate higher peak torque capacity. The characteristic of MTSRM showing resistance to magnetic saturation as compared to conventional SRM at higher excitation currents was also reported (Prasad et al. 2020). A reduced magnetic saturation in the 8/18 MTSRM at 140 A indicates that it can be downsized. This can enhance the torque density, a very important consideration for IW motor applications (Xue et al. 2010b).

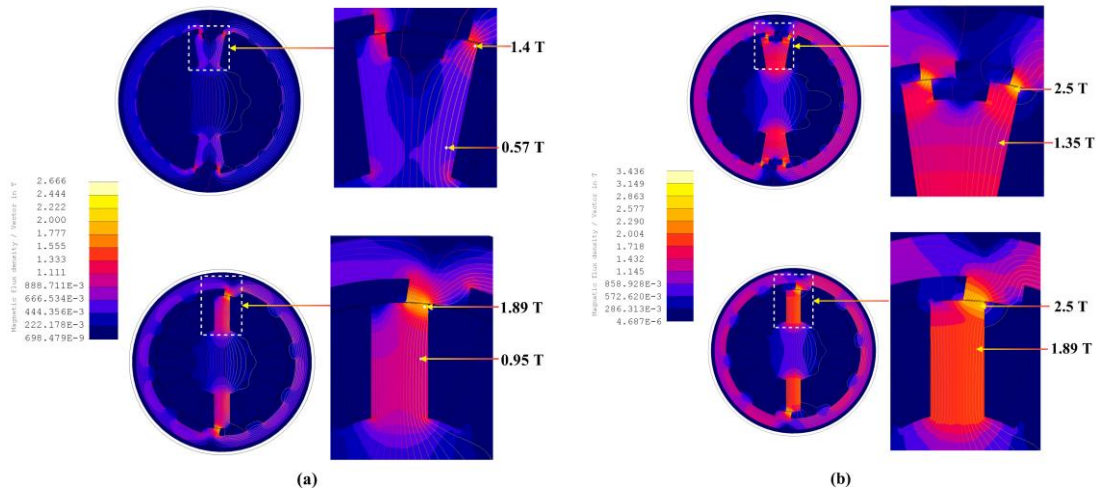


Figure 5.14 The flux density of the 8/18 MT and 8/10 SRM at the midway position at (a) 20 A and (b) 140 A

5.5.2 Dynamic Performance

Though the comparison of the static performance as elucidated previously can indicate the performance to a certain extent, it is imperative to assess the dynamic performance for a comprehensive understanding of the overall characteristics. Moreover, the static analysis considers the phase currents to be constant throughout the half electrical cycle which is not in accord with the practical scenario. In this section, the dynamic performance of the two SRMs is presented.

(i) Efficiency

The efficiency maps along with their respective copper and iron core losses and RMS currents for both the SRM topologies are depicted in Figures 5.15 - 5.18. It was observed that both the designs satisfy the torque-speed envelope as demanded by the E-scooter (Figure 5.3c) within the constraints mentioned in Table 5.2. The 8/18 MTSRM produced a higher peak torque at lower speeds *i.e.* below 250 rpm, as they showed higher resistance to magnetic saturation. However, their peak torque output was lower at higher speeds (>250 rpm) as compared to the 8/10 SRM. This was mainly due to the higher number of turns per phase considered ($N = 42$) for the 8/18 MTSRM which led to an increase in the effective back-EMF (Figure 5.7). This limited the rise of the RMS phase current and correspondingly the peak torque above this speed (Chiba et al. 2012). 8/18 MTSRM exhibited the best efficiency *i.e.*, > 90 % between 300 - 600 rpm

above 15.5 Nm. The efficiency at the base speed of 200 rpm for the 8/18 SRM was 81.9% while that of the 8/10 SRM was 72.1%. This difference was mainly due to the higher peak average torque (94.1 Nm) and reduced copper loss (363 W) of the 8/18 MTSRM in comparison to the 8/10 SRM (90.9 Nm, 671 W). The phase resistance of the 8/10 SRM was higher (Table 5.4) owing to a higher number of turns per phase considering the available slot area, which led to a higher copper loss. Throughout the envelope, the iron core loss of the 8/18 MTSRM was higher as compared to 8/10 SRM due to an increased stroke frequency. The iron core loss did not have a pronounced effect on the efficiency at the base speed. The 8/18 MTSRM demonstrated superior efficiency than the 8/10 SRM for higher torques for speeds lower than 400 rpm primarily owing to a reduced copper loss.

On the other hand, the 8/10 SRM exhibited its maximum efficiency *i.e.* > 90% in the operating region of 350 - 600 rpm and 11-55 Nm. In comparison to the 8/18 MTSRM, the 8/10 SRM exhibited superior efficiencies in the lower torque ranges (< 11 Nm) across a wide operating speed range. The inferior efficiency of the 8/18 MTSRM in this torque range can be ascribed to its reduced output average torque for lower currents because of inadequate magnetic saturation as discussed previously in Section 5.5.1 and shown in Figure. 5.14. It is well known that SRMs perform best in terms of output power and efficiency when the stator and rotor poles are sufficiently saturated (Rahmani et al. 2021). An inadequate pole saturation in the 8/18 SRM augmented the RMS current requirement (Figure. 5.18) to obtain the desired output average torque, significantly elevating the copper loss. An increased copper loss coupled with a higher iron core contributed to a decrease in the efficiency of the 8/18 MTSRM in this operating range. The above discussion suggests that, within the torque-speed envelope, the 8/10 SRM exhibits favorable efficiencies for lower torque duty cycles whereas the 8/18 MTSRM is more efficient for operating points with larger torque requirements.

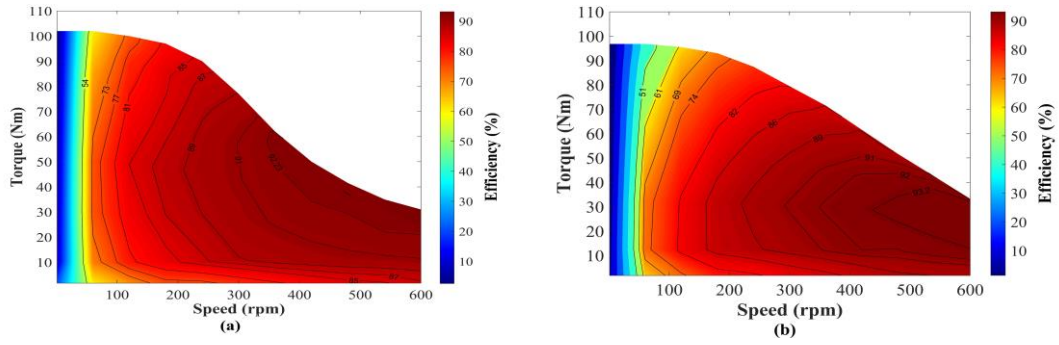


Figure 5.15 Comparison of efficiency maps (a) 8/18 MTSRM and (b) 8/10 SRM

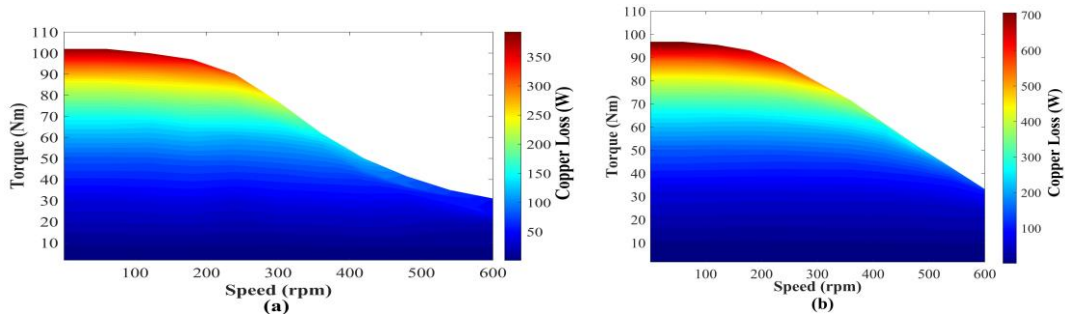


Figure 5.16 Comparison of copper loss maps (a) 8/18 MTSRM and (b) 8/10 SRM

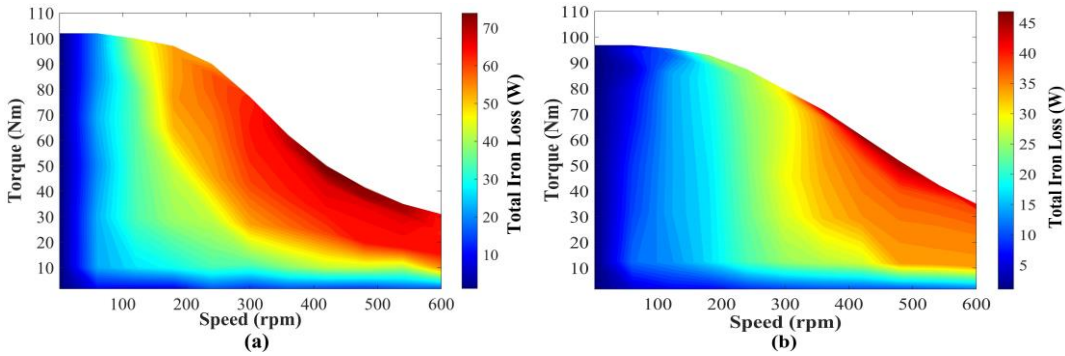


Figure 5.17 Comparison of Iron loss maps (a) 8/18 MTSRM and (b) 8/10 SRM

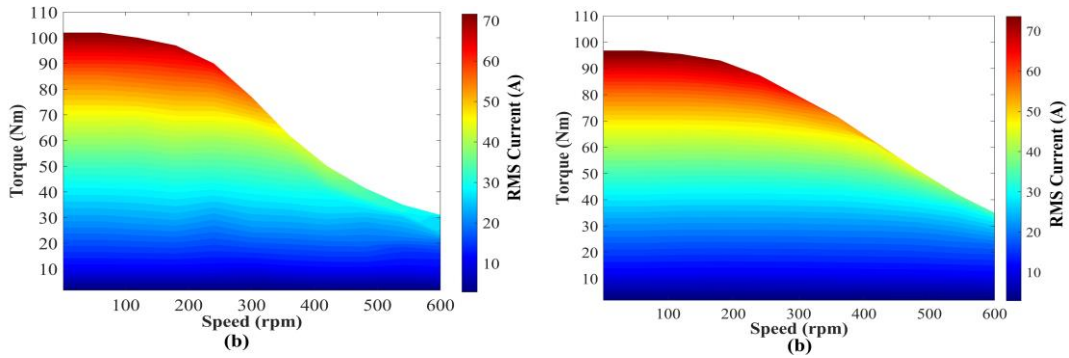


Figure 5.18 Comparison of RMS current maps (a) 8/18 MTSRM and (b) 8/10 SRM

Although the 8/18 MTSRM showed higher efficiencies than the 8/10 SRM in most regions of the torque-speed range, a comparison of their drive cycle efficiencies is necessary to discern the suitable SRM topology from an efficiency standpoint for the E-Scooter. The drive cycle efficiency (η_{cycle}) can be evaluated by dividing the summation of the output power and the summation of the input power at each operating point (j) of the driving cycle, which is expressed as (Carraro et al. 2016);

$$\eta_{\text{cycle}} = \frac{\sum_{j=1}^K P_{\text{out},j}}{\sum_{j=1}^K P_{\text{out},j} + P_{\text{loss},j}} \quad (5.15)$$

where, K indicates the number of operating points, $P_{\text{out},j}$ and $P_{\text{loss},j}$ indicates the output and the total loss at each operating point j . Accordingly, the η_{cycle} are calculated by running both the SRM topologies over the WMTC (Figure. 5.3c). A gridded interpolation is carried out in MATLAB over the operating speed, phase current, and losses to determine the losses at each operating point. The drive cycle efficiency of the 8/18 MTSRM was calculated to be 89.75% while that of 8/10 SRM was 87.94%. Although the difference in the η_{cycle} is not particularly substantial, an improvement of just 1.81% can significantly reduce energy consumption.

(ii) Steady-State characteristics of the motors

In this segment, the steady-state characteristics of the two motors have been compared at 200 and 600 rpm using transient FEA simulation. The vital performance parameters of both the motors obtained are enlisted (Table 5.5). The torque and current waveforms for both the SRM configurations with current chopping control (CCC) at the speed of 200 rpm are depicted in Figure 5.19. The chopping current was set to 140 A and the optimized commutation angles determined previously (Section 5.4.4) were used for simulation ($\theta_{\text{on}} = 0.15^\circ, 0.71^\circ$ and $\theta_{\text{off}} = 6.82^\circ, 12.71^\circ$ mechanical angles for the 8/18 MT and 8/10 SRM respectively). The conduction angles of the two SRMs were set to 120 electrical degrees for a fair comparison. Of the two design topologies evaluated, the average torque (T_{avg}) was higher in the 8/18 MTSRM (~3.52% higher) due to a lower saturation which also corroborates the static performance trends described in Section 5.5.1. Figure 5.20 shows the torque and current waveforms with single-pulse control (SPC) at the maximum speed of 600 rpm ($\theta_{\text{on}} = -2.35^\circ, -5^\circ$ and $\theta_{\text{off}} = 4.32^\circ, 7^\circ$

mechanical angles for the 8/18 MT and 8/10 SRM respectively). The 8/18 MTSRM produced a lower average torque owing to an increased effective back-EMF as compared to the 8/10 SRM (delineated in Section 5.5.2). A drop in the RMS phase current and the corresponding torque, caused by an increased effective back-EMF for the 8/18 MTSRM can be noted (Table 5.6). The 8/18 MTSRM exhibited higher power and specific torque at lower speeds. While, at higher speeds, the 8/10 SRM showcased better power and specific torque characteristics. Further, the 8/18 MTSRM demonstrated a lower torque ripple (T_{ripple}) (25.46%) as compared to the 8/10 SRM (41.61%). The decreased torque ripple exhibited by the 8/18 MTSRM is mainly due to the increased number of strokes per revolution which reduces the torque dips during commutation between the phases (also evident from instantaneous torque profiles in Figures 5.19 and 5.20).

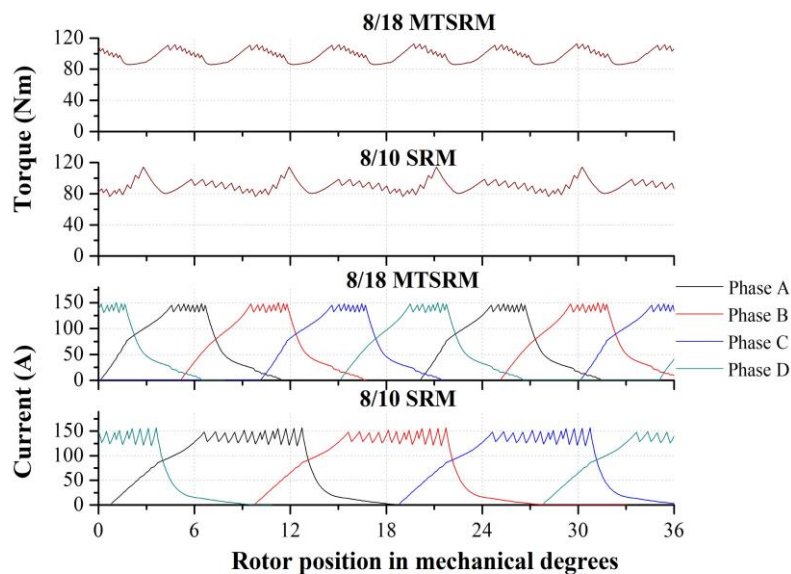


Figure 5.19 Torque and current waveforms operating on CCC at 200 rpm

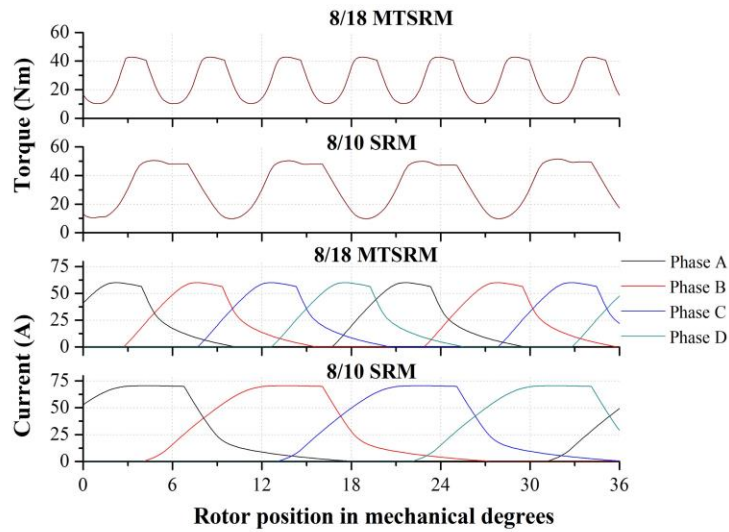


Figure 5.20 Torque and current waveforms operating on SPC at 600 rpm

Table 5.6 Comparison of steady-state performance of two SRM topologies

Control method	8/18 MTSRM		8/10 SRM	
	CCC	SPC	CCC	SPC
Speed (rpm)	200	600	200	600
Average torque, T_{avg} (Nm)	94.1	30.42	90.9	34.32
RMS current, I_{rms} (A)	68.69	30.8	71.19	33.21
Torque per ampere (Nm/A)	1.37	0.99	1.27	1.04
Specific torque (Nm/kg)	3.88	1.26	3.69	1.39
Output power (W)	1972	1911	1904	2156
Torque ripple, T_{ripple} (%)	25.46	123.7	41.61	127.1

For the E-scooter application, the 8/18 MTSRM was chosen as it offered an optimum balance between starting torque (higher peak torque at lower speeds), drive cycle efficiency, and torque ripple. Although its peak torque output is lower at higher speeds (>250 rpm) as compared to the 8/10 SRM, it satisfied the desired torque-speed envelope as demanded by the E-scooter.

5.6 Thermal analysis

The thermal capability is the second most vital constraint following their electromagnetic performance. The thermal performance of the chosen 8/18 MTSRM configuration has been determined by using a 2D FEA thermal model built in ALTAIR FLUX (ALTAIR 2023) at the base speed (200 rpm) for the maximum operating current. The stator slot in the FEA model comprises slot liners, impregnation, and copper wire along with its insulation (Figure 5.21). Their respective material properties namely thermal conductivities and volumetric heat capacities are correspondingly assigned in the analysis (Table 5.7). Cooling of the motor is accomplished by the flow of air around the rotor and convection in the airgap. The heat sources namely the copper loss (being dominant) and iron loss obtained from the transient FEA carried out previously are the load inputs for this simulation. The initial motor temperature is fixed at 40 °C (ambient condition). The temperature constraint of the windings is set to be 120 °C (“Class E” wire is considered in this analysis) (Howey et al. 2017). The simulation result presented in Figure 5.22 shows the time required for the windings of the chosen 8/18 MTSRM to attain the peak temperature of 120 °C at the base speed. Under such highly loaded conditions, the peak temperatures of the windings in the motor can remain below 120 °C for about five minutes which is quite adequate (usage of the motor at these operating conditions is for a shorter duration which is discernible from Figure 5.3c) (Howey et al. 2017). Considering this, the thermal performance of the 8/18 MTSRM can be concluded to be satisfactory. The temperature field model of the 8/18 MTSRM after five minutes of running at 200 rpm at the maximum phase current is shown in Figure 5.23. It can be observed that the temperature of the windings was the highest among all the machine segments. Since the stator pole is affected directly by the heat generated and transmitted by the winding, its temperature was higher than the rotor. The rotor temperature is lesser owing to lower iron loss.

Table 5.7 Material properties of the different components (ALTAIR 2023)

Component	Material	Thermal conductivity ($\text{Wm}^{-1}\text{C}^{-1}$)	Volumetric heat capacity ($\text{Jm}^{-3}\text{C}^{-1}$)
Air gap	Air	0.025	1012
Coil	Copper	394	3518000
Stator and rotor core	M270_35A	55	4600000
Impregnation	Epoxy	0.22	15000000
Insulator	Nomex 410	0.14	13000000
Liner	Nylon	0.24	16000000
Shaft	EN24 steel	52	4600000

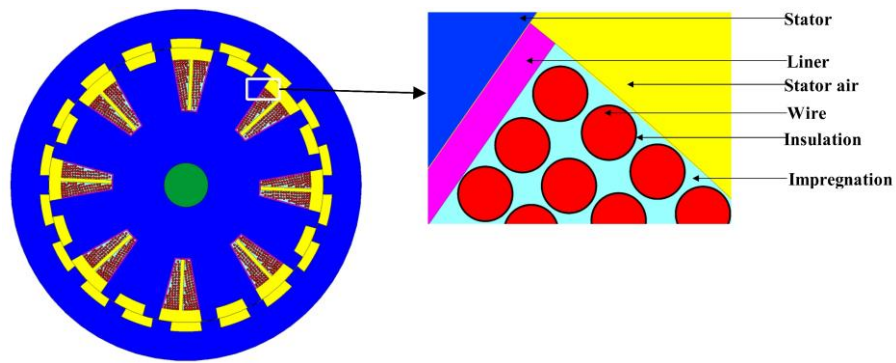


Figure 5.21 2D FEA thermal model of the 8/18 MTSRM

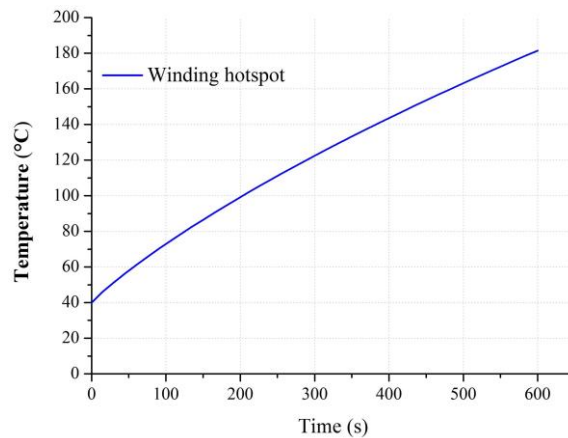


Figure 5.22 Temperature rise of the windings for peak torque condition at 200 rpm

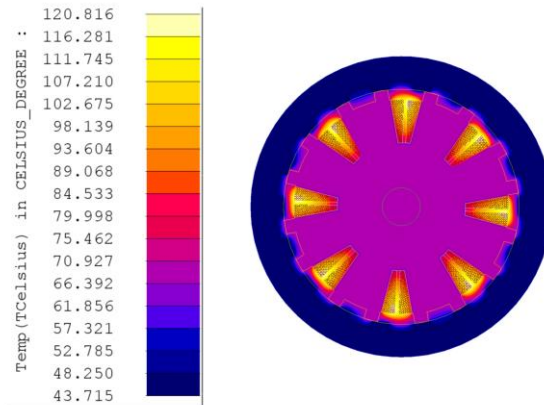


Figure 5.23 Temperature distribution of the 8/18 MTSRM after five minutes of running at 200 rpm

5.7 Summary

In this chapter, a thorough comparison of the electromagnetic performance of a four-phase 8/18 MT and conventional 8/10 SRMs operating under the same geometrical and electrical limitations over the whole torque-speed range was provided. A comparison analysis was performed to evaluate the two configurations' suitability for an E-scooter application. Using the vehicle dynamics model, the target motor specifications were determined based on the E-scooter parameters and the WMTC driving cycle. The SRMs' design variables were optimized by multi-objective PSO to ensure a fair comparison. Furthermore, a computationally efficient SRM drive model was used to precisely optimize the commutation angles across the torque-speed plane. The two SRM designs were evaluated based on their respective efficiency, magnetic characteristics, and steady-state performance. The findings showed that, in comparison to the 8/10 SRM, the 8/18 MTSRM was more suitable for the E-scooter application because it offered the best balance possible between peak torque capacity, drive cycle efficiency and torque ripple. Further, it is also observed that the chosen 8/18 MTSRM demonstrated an acceptable thermal performance. The major findings and significant conclusions of this chapter are provided in Section 6.2 under Chapter 6.

Chapter 6 SUMMARY AND CONCLUSIONS

6.1 Summary

The impact of the dimensions of the geometric design variables on the electromagnetic performance of an 8/6 SRM was presented in Chapter 3 (Objective I). The SRM designs were generated using the empirical relationships available in the literature. The static characteristics of each design, including static torque and flux linkage, were obtained using 2D electromagnetic FEA. By comparing the flux densities and applying the MEC model, the key reluctance segments responsible for the change in the static characteristics were identified. The veracity of the developed MEC model was validated by comparing their results with FEA. The influence of numerous geometric design variables, such as the rotor diameter, stator and rotor pole arc angles, and stator and rotor yoke thickness, have been investigated in terms of the corresponding differences in static characteristics and electromagnetic performance metrics (average torque and torque ripple).

A novel technique for performing a MODO based on a driving cycle of a 2 kW four-phase 8/6 SRM to be used as a traction motor for an E-rickshaw was presented in Chapter 4 (Objective II). The proposed methodology aimed to optimize the design variables of an SRM while considering a practical driving cycle, which is often ignored in conventional design optimization studies. The LOPs and the target motor specifications were estimated based on the CSIR-IIP driving cycle and E-rickshaw parameters by employing the vehicle dynamics model. To simplify the optimization process, the LOPs were divided into four clusters and the corresponding RPs using the k -means clustering algorithm. The elbow approach and the silhouette analysis were used to determine the appropriate number of clusters. The electromagnetic performance metrics, which included maximizing the starting torque, torque density, and minimizing the electromagnetic losses at the RPs were set as the design objectives and were accomplished using the SRM drive model and transient FEA. Further, to reduce the computational burden of FEA during optimization, the multi-objective NSGA II optimization method was coupled with the Kriging models. The Pareto-optimal designs

were compared in terms of design objectives, and the design that provided the best balance between them was selected for prototyping.

In Chapter 5, a comprehensive electromagnetic performance comparison was carried out between a novel four-phase 8/18 MT and the conventional 8/10 SRMs within the same geometrical and electrical constraints across the full torque-speed range to evaluate their suitability for an E-scooter application (Objective III). The target motor specifications were estimated based on the WMTC driving cycle and E-scooter parameters by employing the vehicle dynamics model. Both the SRM designs were compared based on magnetic characteristics, efficiency, and steady-state operation. For a fair comparison, the design variables of the SRMs were optimized using multi-objective PSO. Further, to accurately optimize the commutation angles across the torque-speed plane, a computationally efficient SRM drive model was employed.

6.2 Conclusions

From Chapter 3 (Objective I), the following conclusions are made; Both the stator and rotor pole arc angles influence the rise of static torque profiles due to variations in airgap reluctance. Further, a thorough analysis of stator pole reluctance is necessary while fixing the dimension of the rotor diameter. Average torque improves significantly with an increase in rotor diameter and stator pole arc angle. The average torque is improved by 15.67% with the increase in the rotor diameter from 80 to 88 mm. Further, an increase in stator pole arc angle from 18° to 23° improved the average torque by 24.4%. A rise in stator pole arc angle remarkably decreases the torque ripple. The torque ripple was reduced by 52% when the stator pole arc angle was increased from 18° to 23° . Both average torque and torque ripple are minimally affected by the increase in the rotor pole arc angle and rotor yoke thickness. To minimize the effect of magnetic saturation, it is imperative to set an adequate thickness for the stator and rotor yokes. FEA and the MEC model employed in this study showed a strong correlation, with a maximum error of roughly 4%.

From Chapter 4 (Objective II), it was observed that the average torque and torque density of the design candidate optimized based on a driving cycle were enhanced by 11.31% and 12.15% respectively, while the weighted loss was 5.1% lower

than the initial design. According to the correlation analysis, the stator core design variables (stator bore diameter, stator arc angle, and stator height) showed a substantial association with the performance metrics, in contrast to the rotor design variables. Based on the determined efficiency plot, it was seen that the optimized design exhibited a high-efficiency region ($\geq 90\%$) approximately between 1500 and 3000 rpm throughout the whole torque range. The majority of the obtained LOPs in the torque-speed curve were within this region. Further, the designed and optimized 8/6 SRM met the torque-speed envelope as demanded by the E-rickshaw within the set electrical and geometrical restrictions. Experimental testing of the static and dynamic performance of the SRM prototype revealed good agreement with the FEA simulations employed in this study. The maximum percentage errors for the static and dynamic performance, respectively, between the findings of the FEA simulation and the experiment, were less than 6.51% and 9.4%.

From Chapter 5 (Objective III), based on the results obtained, the following conclusions are drawn. The number of turns per phase required to satisfy the torque-speed envelope for the 8/18 MTSRM was significantly lesser compared to the 8/10 SRM (71.45 % lesser). A reduction in the number of turns per phase indicated that the 8/18 MTSRM required a lower MMF to produce the target torque. These findings corroborated the concept of MT topology. Owing to a reduced MMF, the average static torque of the 8/18 MTSRM in comparison to the 8/10 SRM was lower for phase currents below 50 A majorly due to inadequate magnetic saturation of the pole corners. Above 50 A, a reversal in the trends was observed. At the maximum phase current (140 A), 8/18 MTSRM exhibited a higher average static torque (11.21% higher) which was attributed to lower magnetic saturation levels in the stator pole as compared to the 8/10 SRM, thus indicating higher peak torque capacities. This indicates that the proposed design can be downsized to boost its torque density, a design consideration paramount for an IW motor. Within the geometrical and electrical constraints, both the proposed 8/18 MT and the conventional 8/10 SRMs satisfied the torque-speed envelope demanded by the E-scooter application. Since the 8/18 MTSRM was highly resistant to magnetic saturation, the topology produced a higher torque at lower speeds (below the base speed). Above the base speed, their torque output was lower owing to a higher

effective back-emf. The 8/18 MTSRM exhibited superior efficiencies at operating points with higher torque duty cycles while the 8/10 SRM demonstrated its highest operating efficiencies in the lower torque range. 8/18 MTSRM illustrated a greater drive cycle-oriented efficiency (~1.81 % higher) than the 8/10 SRM. Results from the steady-state analysis indicated that the 8/18 MTSRM exhibited higher average torque (3.52% higher) and specific torque (5.15% higher) at the base speed. While at the maximum speed, it produced a lower average torque (7.17% lower) and specific torque (5.18% lower) due to a higher effective back-emf. The above results indicate that the 8/18 MTSRM is suitable for greater torque drive cycles and lower speeds while the 8/10 SRM is favored for lowered torque requirements and higher speeds. Further, the 8/18 MTSRM demonstrated a lower torque ripple percentage (38.8% lower) at the base speed. For the E-scooter application, the 8/18 MTSRM was chosen as it provided an optimum balance between peak torque capacity, drive cycle efficiency, and torque ripple along with acceptable thermal performance. The obtained results indicate that the 8/18 MTSRM is a novel solution as it exhibited a higher peak torque capacity, torque density, and superior efficiencies in most operating regions with a reduced torque ripple. This makes it a strong contender for in-wheel applications in the future.

6.3 Scope for Future Work

In the present study, a 2kW SRM was designed and developed for the E-rickshaw application considering the electrical constraints imposed by the laboratory-based inverter (DC link voltage of 144 V and a peak RMS current of 20 A). However, commercially available BLDC motors are typically powered by electronic converters with varying voltage and current ratings, which also adhere to regulatory standards. To be considered a viable alternative to BLDC motors, SRMs must demonstrate performance that is either higher or comparable to BLDC motors within the same electrical and geometric constraints. Incorporating this factor into the design and development of an SRM offers a potential avenue for further investigation.

It has been reported in literature that SRMs generate inferior noise levels as compared to other traction motors. The noise is mainly produced by structural vibrations in the stator's outer surface caused by electromagnetic air-gap forces acting on the stator. The vibration and noise levels of the motor are influenced by

modifications to the geometric design variables and the excitation control variables. The electromagnetic air-gap forces operating on the stator are impacted by changes in these variables. Additionally, altering the geometric design variables related to the stator modifies its natural frequency. Therefore, a thorough analysis to determine how these factors affect the behavior of noise and vibration should be taken into consideration during the design phase of the SRM.

The thermal management of an SRM is the second most vital constraint following their electromagnetic performance. A detailed thermal analysis is essential to improve the motor's performance and ensure reliable motor operation should be considered in the future scope of the study.

The multiobjective design optimization technique described in this thesis does not account for the thermal and structural (noise and vibration) analysis. A multiphysics multiobjective design optimization incorporating electromagnetic, thermal, and structural analysis based on a driving cycle needs to be implemented in future studies.

In the present study, it has been established that the MTSRMs are less prone to magnetic saturation as compared to the conventional SRMs at higher excitation phase currents. This suggested that it is possible to downsize the MTSRMs, which will increase their torque density – a crucial aspect for IW-EV applications. For the MTSRM to be suggested as a possible replacement for the BLDC motor, a performance comparison with a commercially available BLDC motor must also be made under the same geometric and electrical limitations. Future work scope may take this into account.

References

- Abdalmagid, M., Sayed, E., Bakr, M. H., and Emadi, A. (2022). "Geometry and Topology Optimization of Switched Reluctance Machines: A Review." *IEEE Access*, 10, 5141–5170.
- ALTAIR, (2023), "Altair Flux, Package for electromagnetic and thermal analysis using finite elements FLUX 2D and FLUX 3D, Version 2019." <https://altair.com/flux/> (Jan. 31, 2023).
- Andrada, P., Martínez, E., Blanqué, B., Torrent, M., Perat, J. I., and Sánchez, J. A. (2016). "New axial-flux switched reluctance motor for e-scooter," *Proc., ESARS-ITEC 2016 - Int. Conf. Electr. Syst. Aircraft, Railway, Ship Propuls. Road Vehicles & Int. Transp. Electrification Conf.*, Toulouse, France.
- Anvari, B., Li, Y., and Toliyat, H. A. (2016). "Design of multiphase exterior rotor switched reluctance motor for traction applications," *Proc., ISIE 2016 - IEEE 25th Int. Symp. Ind. Electron.*, Santa Clara, CA, USA, 161-166.
- Anvari, B., Toliyat, H. A., and Fahimi, B. (2017). "Simultaneous Optimization of Geometry and Firing Angles for In-Wheel Switched Reluctance Motor Drive." *IEEE Trans. Transp. Electrification*, 4(1), 322–329.
- Anwar, M. N., Husain, I., and Radun, A. V. (2001). "A Comprehensive Design Methodology for Switched Reluctance Machines." *IEEE Trans. Ind. Appl.*, 37(6), 1684–1692.
- Arun, S., Koustubh, S., Abhijeet, R., Rai, S. (2021). "Optimization of Electric Powertrain for Auto-rickshaw," *SAE Technical Papers*, SAE International.
- Asgar, M., and Afjei, E. (2016). "Radial force reduction in a new flat-type double-stator switched reluctance motor." *IEEE Tran. Energy. Convers.*, 31(1), 141–149.
- Babajide, N. (2018). *Indian Energy Security Status: What are the Economic and Environmental Implications?*
- Bandivadekar, A. (2021). *Transition to BS VI vehicle emissions and fuel quality standards in India.*
- BGAUSS, (2023), "BGAUSS B8 E-Scooter in India." <https://www.bgauss.com/b8-overview/>
(Jun. 20, 2023).
- Bhandarkar, S. (2010). *Minimization of Vehicular pollution at NE-Karnataka Road Transport Corporation-Gulbarga by the use of CNG in place of diesel fuel.*
- Bhuvaneshwari, G., Rao, P. S., Thakurta, G., and Murthy, S. S. (2008). "Impact of Dwell Angle on the Electromagnetic Torque Ripples of the Switched Reluctance Motor." *Def. Sci. J.*, 58(3), 363–371.

- Bianchi, N. (2005). *Electrical Machine Analysis Using Finite Elements*. Boca Raton, FL 33487-2742: CRC Press, Taylor & Francis group.
- Bieńkowski, K., Szypior, J., and Bucki, B. (2004). “Influence of geometrical parameters of Switched Reluctance Motor on electromagnetic torque.”
- Bilgin, B., and Emadi, A. (2012). “Design Considerations for Switched Reluctance Machines With a Higher Number of Rotor Poles.” *IEEE Trans. Ind. Electron.*, 59(10), 3745–3756.
- Bilgin, B., Jiang, J. W., and Emadi, A. (2019). *Switched Reluctance Motor Drives*. Boca Raton, FL 33487-2742: CRC Press, Taylor & Francis group.
- Bilgin, B., Magne, P., Malysz, P., Yang, Y., Pantelic, V., Preindl, M., Korobkine, A., Jiang, W., Lawford, M., and Emadi, A. (2015). “Making the Case for Electrified Transportation.” *IEEE Trans. Transp. Electrif.*, 1(1), 4–17.
- Bostanci, E., Moallem, M., Parsapour, A., and Fahimi, B. (2017). “Opportunities and Challenges of Switched Reluctance Motor Drives for Electric Propulsion: A Comparative Study.” *IEEE Trans. Transp. Electrif.*, 3(1), 58–75.
- Bramerdorfer, G., Tapia, J. A., Pyrhonen, J. J., and Cavagnino, A. (2018). “Modern Electrical Machine Design Optimization: Techniques, Trends, and Best Practices.” *IEEE Trans. Ind. Electron.*, 65(10), 7672–7684.
- Broom, D. (2020). “6 of the world’s 10 most polluted cities are in India.”, <https://www.weforum.org/agenda/2020/03/6-of-the-world-s-10-most-polluted-cities-are-in-india/> (Dec. 1, 2023).
- Carraro, E., Morandin, M., and Bianchi, N. (2016). “Traction PMASR motor optimization according to a given driving cycle.” *IEEE Trans. Ind. Appl.*, 52(1), 209–216.
- Chen, H., and Yan, W. (2018). “Novel U-Shaped Structure Switched Reluctance Machine with a Module Outer Rotor.” *IEEE Trans. Appl. Supercond.*, 28(3).
- Chiba, A., Takano, Y., Takeno, M., Imakawa, T., Hoshi, N., Takemoto, M., and Ogasawara, S. (2011). “Torque density and efficiency improvements of a switched reluctance motor without rare-earth material for hybrid vehicles.” *IEEE Trans. Ind. Appl.*, 47(3), 1240–1246.
- Chiba, A., Takeno, M., Hoshi, N., Takemoto, M., Ogasawara, S., and Rahman, M. A. (2012). “Consideration of number of series turns in switched-reluctance traction motor competitive to HEV IPMSM.” *IEEE Trans. Ind. Appl.*, 48(6), 2333–2340.
- Cogent, (2023), “Electrical steel Non-oriented fully processed.”, <https://perso.uclouvain.be/ernest.matagne/ELEC2311/T2006/NOFP.pdf> (Jun. 21, 2023).

- Cohen, A. J., Samet, J. M., Straif, K., and International Agency for Research on Cancer. (2013). *Air pollution and cancer*. International Agency for Research on Cancer.
- Currie, I. G. (2003). *Fundamental Mechanics of Fluids Third Edition*. New York: Marcel Dekker.
- Dawson, G. E., Eastham, A. R., and Mizia, J. (1987). "Switched-Reluctance Motor Torque Characteristics: Finite-Element Analysis and Test Results." *IEEE Trans. Ind. Appl.*, IA-23(3), 532–537.
- Deb, K., Pratap, A., Agarwal, S., and Meyarivan, T. (2002). "A Fast and Elitist Multiobjective Genetic Algorithm: NSGA-II." *IEEE Trans. Evol. Comput.*, 6(2), 182–197.
- Deepak, M., Janaki, G., and Bharatiraja, C. (2022). "Analysing low speed efficiency of switched reluctance motor material grade for electric vehicle." *Mater Today Proc*, Elsevier Ltd, 1845–1852.
- Desai, P. C., Krishnamurthy, M., Schofield, N., and Emadi, A. (2010). "Novel switched reluctance machine configuration with higher number of rotor poles than stator poles: Concept to implementation." *IEEE Trans. Ind. Electron.*, 649–659.
- Diao, K., Sun, X., Lei, G., Guo, Y., and Zhu, J. (2020). "Multiobjective system level optimization method for switched reluctance motor drive systems using finite-element model." *IEEE Tran. Ind. Electron.*, 67(12), 10055–10064.
- Diao, K., Sun, X., Lei, G., Guo, Y., and Zhu, J. (2021). "Multimode Optimization of Switched Reluctance Machines in Hybrid Electric Vehicles." *IEEE Tran. Energy Convers.*, 36(3), 2217–2226.
- Diao, K., Sun, X., and Yao, M. (2022). "Robust-Oriented Optimization of Switched Reluctance Motors Considering Manufacturing Fluctuation." *IEEE Trans. Transp. Electrification*, 8(2), 2853–2861.
- Eberhart, R., and Kennedy, J. (1995). "A new optimizer using particle swarm theory," *Proc., MHS'95 - Sixth Int. Symp. Micro Machine Hum. Sci.*, Nagoya, Japan, 210-214.
- Ecomotors, (2023), "Ecomotors 48V 2200W BLDC E-Rickshaw motor." <https://www.tradeindia.com/products/premium-design-blDC-motor-2-2-kw-60-v7212660.html> (Sep. 20, 2023).
- Ehsani, M., Gao, Y., and Gay, S. (2003). "Characterization of electric motor drives for traction applications". *Proc., IEEE IECON*, Roanoke, VA, USA, 891-896.
- Ehsani, M., Gao, Y., Longo, S., and Ebrahimi, K. M. (2018). *Modern Electric, Hybrid Electric, and Fuel Cell Vehicles Third Edition*. Boca Raton, FL 33487-2742: CRC Press, Taylor & Francis group.
- Ehsani, M., Rahman, K. M., and Toliyat, H. A. (1997). "Propulsion system design of electric and hybrid vehicles." *IEEE Trans. Ind. Electron.*, 44(1), 19–27.

- Farahani, E. F., and Mirsalim, M. (2020). "Comprehensive study on divided-teeth and permanent magnet assisted outer-rotor switched reluctance motors." *IET Electr. Power Appl.*, 14(12), 2293–2300.
- Farmahini Farahani, E., Jalali Kondelaji, M. A., and Mirsalim, M. (2020). "A New Exterior-Rotor Multiple Teeth Switched Reluctance Motor with Embedded Permanent Magnets for Torque Enhancement." *IEEE Trans. Magn.*, 56(2), 8100405.
- Fatemi, A., Ionel, D. M., Popescu, M., Chong, Y. C., and Demerdash, N. A. O. (2018). "Design Optimization of a High Torque Density Spoke-Type PM Motor for a Formula e Race Drive Cycle." *IEEE Trans. Ind. Appl.*, 54(5), 4343–4354.
- Green, R., Staffell, I., and Vasilakos, N. (2014). "Divide and Conquer? k-means clustering of demand data allows rapid and accurate simulations of the British electricity system." *IEEE Trans. Eng. Manag.*, 61(2), 251–260.
- Hayashi, H., Nakamura, K., Chiba, A., Fukao, T., Tungpimolrut, K., and Dorrell, D. G. (2009). "Efficiency improvements of switched reluctance motors with high-quality iron steel and enhanced conductor slot fill." *IEEE Tran. Energy. Convers.*, 24(4), 819–825.
- Hennen, M. D., and De Doncker, R. W. (2007). "Comparison of outer- and inner-rotor switched reluctance machines". *Proc., IEEE PEDS '07*, Bangkok, Thailand, 702-706.
- Howey, B., Bilgin, B., and Emadi, A. (2020). "Design of an External-Rotor Direct Drive E-Bike Switched Reluctance Motor." *IEEE Trans. Veh. Technol.*, 69(3), 2552–2562.
- Howey, B., Rowan, E., Bilgin, B., and Emadi, A. (2017). "Thermal trade-off analysis of an exterior rotor e-bike switched reluctance motor," *Proc., ITEC 2017 - IEEE Transportation Electrification Conference and Expo.*, Chicago, IL, USA, 605–612.
- Hughes, Austin., and Drury, Bill. (2013). *Electric motors and drives : fundamentals, types and applications*. Waltham, MA 02451: Elsevier.
- Intergovernmental Panel on Climate Change. (2014). *Climate change 2014 : Synthesis report*.
- Jiang, J. W., Bilgin, B., and Emadi, A. (2017). "Three-Phase 24/16 Switched Reluctance Machine for a Hybrid Electric Powertrain." *IEEE Trans. Transp. Electrif.*, 3(1), 76–85.
- Jiang, J. W., Bilgin, B., Howey, B., and Emadi, A. (2015). "Design optimization of switched reluctance machine using genetic algorithm," *Proc., IEEE Int. Electric Machines Drives Conf. (IEMDC)*, 2015, Coeur d'Alene, ID, USA, 1671–1677.
- Kiyota, K., and Chiba, A. (2012). "Design of switched reluctance motor competitive to 60-kW IPMSM in third-generation hybrid electric vehicle." *IEEE Trans. Ind. Appl.*, 48(6), 2303–2309.

- Krishnan, R. (2001). *Switched Reluctance Motor Drives: Modeling, Simulation, Analysis, Design, and Applications*. Boca Raton, FL: CRC Press.
- Lawrenson, P. J., Stephenson, J. M., Blenkinsop, P. T., Corda, J., and Fulton, N. N. (1980). "Variable-speed switched reluctance motors," *IEE PROC.*, 253-265
- Lazari, P., Wang, J., and Chen, L. (2014). "A computationally efficient design technique for electric-vehicle traction machines." *IEEE Trans. Ind. Appl.*, 50(5), 3203–3213.
- Lin, J., Schofield, N., and Emadi, A. (2015). "External-Rotor 6-10 Switched Reluctance Motor for an Electric Bicycle." *IEEE Trans. Transp. Electr.*, 1(4), 348–356.
- Li, S., Zhang, S., Habetler, T. G., and Harley, R. G. (2019). "Modeling, design optimization, and applications of switched reluctance machines - A review." *IEEE Trans. Ind. Appl.*, 55(3), 2660–2681.
- Ma, C., and Qu, L. (2015). "Multiobjective optimization of switched reluctance motors based on design of experiments and particle swarm optimization." *IEEE Tran. Energy Convers.*, 30(3), 1144–1153.
- Mademlis, C., and Kioskeridis, I. (2003). "Performance optimization in switched reluctance motor drives with online commutation angle control." *IEEE Tran. Energy Convers.*, 18(3), 448–457.
- Madhavan, R., and Fernandes, B. G. (2013). "Axial flux segmented srm with a higher number of rotor segments for electric vehicles." *IEEE Tran. Energy Convers.*, 28(1), 203–213.
- Mahmood, H., Mehmood, T., and Al-Essa, L. A. (2023). "Optimizing Clustering Algorithms for Anti-Microbial Evaluation Data: A Majority Score-Based Evaluation of K-Means, Gaussian Mixture Model, and Multivariate T-Distribution Mixtures." *IEEE Access*, 11, 79793–79800.
- Mamede, A. C. F., Camacho, J. R., and Araújo, R. E. (2019). "Influence of geometric dimensions on the performance of switched reluctance machine." *Machines*, 7(4), 1–19.
- Mecrow, B. C., El-Kharashi, E. A., Finch, J. W., and Jack, A. G. (2004). "Preliminary performance evaluation of switched reluctance motors with segmental rotors." *IEEE Tran. Energy Convers.*, 19(4), 679–686.
- Mecrow, B. C., Finch, J. W., El-Kharashi, E. A., and Jac, A. G. (2002). Switched reluctance motors with segmental rotors," *Proc., IEE Proc.-Electr. Power Appl.*, Istanbul, 245–254.
- Miller, J., Bandivadekar, A., and Sathiamoorthy, B. (2019). *Health impacts of air pollution from transportation sources in Delhi key findings for the new Delhi region*.

- Miller, T. J. E. (2002). "Optimal design of switched reluctance motors." *IEEE Trans. Ind. Electron.*, 49(1), 15–27.
- Miller, T.J.E. (1993). *Switched Reluctance Motors and their Control First Edition*. London, UK: Oxford University Press.
- Mousavi-Aghdam, S. R., Feyzi, M. R., Bianchi, N., and Morandin, M. (2016). "Design and Analysis of a Novel High-Torque Stator-Segmented SRM." *IEEE Trans. Ind. Electron.*, 63(3), 1458–1466.
- Nandapala, E. Y. L., and Jayasena, K. P. N. (2020). "The practical approach in Customers segmentation by using the K-Means Algorithm," *Proc., 2020 IEEE 15th Int. Conf. Ind. Inf. Syst. (ICIIS)*, 2020, RUPNAGAR, India, 344–349.
- Nikam, S. P., Rallabandi, V., and Fernandes, B. G. (2012). "A high-torque-density permanent-magnet free motor for in-wheel electric vehicle application." *IEEE Trans. Ind. Appl.*, 48(6), 2287–2295.
- Nikam, S. P., Sau, S., and Fernandes, B. G. (2013). "Design of switched reluctance motor based electric drive-train for intra-campus two-wheeler," *Proc., IECON 2013 - 39th Annu. Conf. IEEE Ind. Electron. Soc.*, Vienna, Austria, 4612–4617.
- Oamen F., I. (2018). "Fossil Fuels and the Current Fuel Reserve in Developed and Developing Countries." *Science, Technology & Public Policy*, 2(1), 1–6.
- Öksüztepe, E. (2017). "In-Wheel Switched Reluctance Motor Design for Electric Vehicles by Using a Pareto-Based Multiobjective Differential Evolution Algorithm." *IEEE Trans. Veh. Technol.*, 66(6), 4706–4715.
- Omekanda, A. M., Broche, C., and Renglet, M. (1997). "Calculation of the Electromagnetic Parameters of a Switched Reluctance Motor Using an Improved FEM-BIEM-Application to Different Models for the Torque Calculation." *IEEE Trans. Ind. Appl.*, 33(4), 914–918.
- Pathak, S. K., Singh, Y., Sood, V., and Channiwala, S. A. (2017). "Drive Cycle Development for Electrical Three Wheelers." *SAE Technical Papers*, SAE International, 1–6.
- Petrus, V., Pop, A. C., Martis, C. S., Gyselinck, J., and Iancu, V. (2010). "Design and comparison of different Switched Reluctance Machine topologies for electric vehicle propulsion," *Proc., XIX Int. Conf. Elect. Mach. - ICEM*, Rome, Italy.
- Photon, (2022), "Hero electric Photon 48V." <https://www.bikedekho.com/hero-electric/photon-48v> (Jun. 18, 2023).
- Piaggio 1, (2023), "Piaggio 1+ electric scooter." https://e-vehicleinfo.com/piaggio-electric-scooter-price-range-and-specification/#google_vignette (May 29, 2023).
- Prabhu, S., Kalaimagal, V., Arun, V., Manikandan, A., Balaji, M., and Chandrasekar, V. (2023). "Impact of Laminating Core Materials on Switched Reluctance Motor for

Automotive Applications.” *2023 International Conference on Power, Instrumentation, Energy and Control, PIECON 2023*, Institute of Electrical and Electronics Engineers Inc.

Prasad, N., Jain, S., and Gupta, S. (2020). “Comparative analysis of new improved force split-teeth Linear Switched Reluctance Motor for high speed transit systems.” *Sadhana - Acad. Proc. Eng. Sci.*, 45(147), 1–13.

Rahmani, O., Sadrossadat, S. A., Mirimani, S. M., and Mirimani, S. H. (2021). “Optimization of efficiency and output power of 8/6 switched reluctance motor using new neural network-based adjoint L p metric method.” *IET Electr. Power Appl.*, 15(6), 769–783.

Rahman, K. M., Fahimi, B., Suresh, G., Rajarathnam, A. V., and Ehsani, M. (2000). “Advantages of switched reluctance motor applications to EV and HEV: Design and Control issues.” *IEEE Trans. Ind. Appl.*, 36(1), 111–121.

Raminosoa, T., Blunier, B., Fodorean, D., and Miraoui, A. (2010). “Design and optimization of a switched reluctance motor driving a compressor for a PEM fuel-cell system for automotive applications.” *IEEE Trans. Ind. Electron.*, 57(9), 2988–2997.

Rao, S. S. (2009). *Engineering Optimization Theory and Practice*. (Fourth Edition, ed.), Hoboken, New Jersey: John Wiley & Sons, Inc.

Rashid, M. H. (2011). *Power Electronics Handbook*. Oxford, UK: Elsevier.

Ravuvvar, H. N., Goda, H., Sumathi, R., and Chinnasamy, P. (2020). "Smart Health Predicting System Using K-Means Algorithm," in *Proc. ICCCI 2020 - Int. Conf. Comput. Commun. Informatics*, 2020, Coimbatore, India.

Reddy, B. S., Mayanja, B. G., Rhodah, B., Sindhu, K. S., Reddy, S. A., and Reddy, B. K. (2022). "Experimental Verification and Deep Learning Classification of A-V and V-A Methods for Resistance Measurement," *Proc., SMART GENCON 2022 - 2022 International Conference on Smart Generation Computing, Communication and Networking.*, Bangalore, India.

RetroEV, (2023), “Mahindra Treo Yaari SFT.” <https://retroev.in/overview.php?id=304&type=Auto> (Jan.5, 2023).

RIDGE+, (2023), “Okinawa Ridge plus electric scooter.” <https://okinawascooters.com/scooters/ridge-plus-gps> (May. 31, 2023).

Salameh, M., Brown, I. P., and Krishnamurthy, M. (2019). “Fundamental Evaluation of Data Clustering Approaches for Driving Cycle-Based Machine Design Optimization.” *IEEE Trans. Transp. Electrif.*, 5(4), 1395–1405.

- Sarigiannidis, A. G., Beniakar, M. E., and Kladas, A. G. (2017). "Fast Adaptive Evolutionary PM Traction Motor Optimization Based on Electric Vehicle Drive Cycle." *IEEE Trans. Veh. Technol.*, 66(7), 5762–5774.
- Schofield, N., Long, S. A., Howe, D., and McClelland, M. (2009). "Design of a switched reluctance machine for extended speed operation." *IEEE Trans. Ind. Appl.*, 45(1), 116–122.
- Selim, S. Z., and Ismail, M. A. (1984). "K-Means-Type Algorithms: A Generalized Convergence Theorem and Characterization of Local Optimality." *IEEE Trans. Pattern Anal. Mach. Intell.*, PAMI-6(1), 81–87.
- Sharma, R., Kumar, R., Singh, P. K., Raboaca, M. S., and Felseghi, R. A. (2020). "A systematic study on the analysis of the emission of CO, CO₂ and HC for four-wheelers and its impact on the sustainable ecosystem." *Sustainability (Switzerland)*, 12(17), 1–22.
- Sheth, N. K., and Rajagopal, K. R. (2003). "Optimum Pole Arcs for a Switched Reluctance Motor for Higher Torque with Reduced Ripple." *IEEE Trans. Magn.*, 39(5 II), 3214–3216.
- Singh, S., Jindel, J., Tikkiwal, V. A., Verma, M., Gupta, A., Negi, A., and Jain, A. (2022). "Electric vehicles for low-emission urban mobility: current status and policy review for India." *Int. J. Sustain. Energy*, 41(9), 1323–1359.
- Singh, V. K., Sharma, U., and Singh, B. (2021). "Design and Validation of SR Motor for Direct Drive In-Wheel using Ansys Simplorer," *Proc., 2021 IEEE 6th Int. Conf. Comput., Commun., Autom. (ICCCA)*, Arad, Romania.
- Smaka, S., Cosovic, M., and Masic, S. (2013). "The effects of magnetic circuit geometry on torque generation of 8/14 switched reluctance machine," *Proc., ICAT 2013 - 2013 XXIV Int. Conf. Inf. Commun. Autom. Technol.*, 2013, Sarajevo, Bosnia and Herzegovina, 1-5.
- Smaka, S., Konjicija, S., Masic, S., and Cosovic, M. (2013). "Multi-objective design optimization of 8/14 switched reluctance motor," *Proc., IEMDC 2013 - Int. Electric Machines Drives Conf.*, Chicago, IL, USA, 468–475.
- Smaka, S., Mašić, Š., Hadžimejlić, N., and Čosović, M. (2012). "Design considerations for novel 8/14 and comparison with conventional 8/6 and 8/10 switched reluctance machines," *Proc., SPEEDAM 2012 - Int. Symp. Power Electron., Power Electron., Electr. Drives, Autom. Motion*, Sorrento, Italy, 614-619.
- SMEV (2023). "EV sales in India." <https://www.smev.in/ev-sales> , (Dec. 10, 2023).
- Soares, F., and Branco, P. J. C. (2001). "Simulation of a 6/4 switched reluctance motor based on Matlab/Simulink environment." *IEEE Trans. Aerosp. Electron. Syst.*, 37(3), 989–1009.

- Song, S., Ge, L., Ma, S., Zhang, M., and Wang, L. (2015). "Accurate measurement and detailed evaluation of static electromagnetic characteristics of switched reluctance machines." *IEEE Trans. Instrum. Meas.*, 64(3), 704–714.
- Sreejith R., and Rajagopal, K. R. (2016). "An Insight into Motor and Battery Selections for Three-Wheeler Electric Vehicle," *Proc., ICPEICES 2016 - IEEE 1st Int. Conf. Power Electron., Intell. Control Energy Syst.*, Delhi, India
- Srinivas, K. N., and Arumugam, R. (2005). "Analysis and characterization of Switched reluctance motors: Part I - dynamic, static, and frequency spectrum analyses." *IEEE Trans. Magn.*, 41(4), 1306–1320.
- Statistica (2023). "Dysprosium oxide price worldwide from 2009 to 2020 with a forecast for 2021 to 2030.", <https://www.statista.com/statistics/450164/global-reo-dysprosium-oxide-price-forecast/> (Dec.5, 2023).
- Statistica (2023). "Neodymium oxide price worldwide from 2009 to 2020 with a forecast for 2021 to 2030.", <https://www.statista.com/statistics/450152/global-reo-neodymium-oxide-price-forecast/> (Dec.6, 2023).
- Steven, H. (2002). *Worldwide Harmonised Motorcycle Emissions Certification Procedure*.
- Sundaram, M., Anand, M., Chelladurai, J., Varunraj, P., Joshua Smith, S., Sharma, S., Haj Assad, M. El, and Alayi, R. (2022). "Design and FEM Analysis of High-Torque Power Density Permanent Magnet Synchronous Motor (PMSM) for Two-Wheeler E-Vehicle Applications." *Int. Trans. Electr. Energy Syst.*, 2022, 1–14.
- Sun, X., Diao, K., Lei, G., Guo, Y., and Zhu, J. (2019). "Study on segmented-rotor switched reluctance motors with different rotor pole numbers for BSG system of hybrid electric vehicles." *IEEE Trans. Veh. Technol.*, 68(6), 5537–5547.
- Sun, X., Shi, Z., Cai, Y., Lei, G., Guo, Y., and Zhu, J. (2020). "Driving-Cycle-Oriented Design Optimization of a Permanent Magnet Hub Motor Drive System for a Four-Wheel-Drive Electric Vehicle." *IEEE Trans. Transp. Electr.*, 6(3), 1115–1125.
- Tekgun, D., Tekgun, B., and Alan, I. (2022). "FEA based fast topology optimization method for switched reluctance machines." *Electr. Eng.*, 104(4), 1985–1995.
- Terzic, M. V., Bilgin, B., and Emadi, A. (2018). "Switched Reluctance Motor Design for a Forklift Traction Application," *Proc., ICELMACH 2018 - 2018 XIII Int. Conf. Electr. Mach.*, Alexandroupoli, Greece, 812–818.
- Tsuyo, (2023). "1 KW Electric Motor for E Rickshaw BLDC Motor E-Rickshaw Tsuyo Electric Paddle E-Rickshaw." <https://www.amazon.in/Electric-Rickshaw-Rickshaw-Tsuyo-Eickshaw/dp/B097TFLBLD> (Jan.3, 2023).
- Tuncay, R. N., Ustun, O., Yilmaz, M., Gokce, C., and Karakaya, U. (2011). "Design and Implementation of an Electric Drive System for In-Wheel Motor Electric Vehicle

Applications," *Proc., VPPC 2011 - IEEE Vehicle Power and Propulsion Conference*, Chicago, IL, USA

Turner, M. J., Wung, P. Y. P., and Wallace, R. S. (1997). "Comparing European 132 frame switched reluctance and induction motor drives". *Proc., IECON'97 23rd Int. Conf. Ind. Electron., Control, Instrum.*, New Orleans, LA, USA,403-408.

Uddin, W., Husain, T., Sozer, Y., and Husain, I. (2016). "Design Methodology of a Switched Reluctance Machine for Off-Road Vehicle Applications." *IEEE Trans. Ind. Appl.*, 52(3), 2138–2147.

Vahedi, P., and Ganji, B. (2021). "A simple magnetic equivalent circuit model for switched reluctance machine." *Electr. Eng.*, 103(2), 1307–1320.

Vaidehi, Dhar, S., Jayakumar, A., Lavanya, R., and Kumar, M. D. (2020). "Techno-economic assessment of various motors for three-wheeler E-auto rickshaw: From Indian context." *Mater. Today Proc.*, Elsevier Ltd, 6572–6579.

Vandana, R., Nikam, S., and Fernandes, B. G. (2012). "Criteria for design of high performance switched reluctance motor". *Proc., Int. Conf. Electr. Mach. (ICEM 2012)*, Marseille, France,129-135

Vijayakumar, K., Karthikeyan, R., Paramasivam, S., Arumugam, R., and Srinivas, K. N. (2008). "Switched reluctance motor modeling, design, simulation, and analysis: A comprehensive review." *IEEE Trans. Magn.*, 44(12), 4605–4617.

Wang, Q., Liu, J., Wei, B., Chen, W., and Xu, S. (2020). "Investigating the construction, training, and verification methods of k-means clustering fault recognition model for rotating machinery." *IEEE Access*, 8, 196515–196528.

Wattthewaduge, G., Sayed, E., Emadi, A., and Bilgin, B. (2020). "Electromagnetic Modeling Techniques for Switched Reluctance Machines: State-of-the-Art Review." *IEEE Open J. Ind. Electron. Soc.*, 1, 218–234.

WAVECT, (2023), "WAVECT WCU 300 – Control and Measurements." <https://www.entuple.com/products/wavect> (Feb.25, 2023)

Widmer, J. D., Martin, R., and Kimiabeigi, M. (2015). "Electric vehicle traction motors without rare earth magnets." *Sustain. Mater. Technol.*, 3, 7–13.

Xuan, J., Wang, X., Lu, D., and Wang, L. (2017). "Research on the safety assessment of the brushless DC motor based on the gray model." *Adv. Mech. Eng.*, 9(3), 1–15.

Xue, X. D., Cheng, K. W. E., Lin, J. K., Zhang, Z., Luk, K. F., Ng, T. W., and Cheung, N. C. (2010a). "Optimal control method of motoring operation for SRM drives in electric vehicles." *IEEE Trans. Veh. Technol.*, 59(3), 1191–1204.

Xue, X. D., Cheng, K. W. E., Ng, T. W., and Cheung, N. C. (2010b). "Multi-objective optimization design of in-wheel switched reluctance motors in electric vehicles." *IEEE Trans. Ind. Electron.*, 57(9), 2980–2987.

Yilmaz, M., and Krein, P. T. (2008). "Capabilities of finite element analysis and magnetic equivalent circuits for electrical machine analysis and design". *Proc., IEEE PESC*, Rhodes, Greece, 4027-4033.

Yu, Q., Bilgin, B., and Emadi, A. (2016). "Design considerations of switched reluctance machines with high power density," *Proc., 2016 IEEE Transportation Electrification Conf. Expo (ITEC)*, Dearborn, MI, USA, 4-8.

Zayed, M., Omar, M., Bakr, M., Narimani, M., Emadi, A., and Bilgin, B. (2021). "Switched Reluctance Motor Design for an EV Propulsion Application," *Proc., IECON, 2021*, Toronto, ON, Canada, 1-6.

Zeraoulia, M., Benbouzid, M. E. H., and Diallo, D. (2006). "Electric motor drive selection issues for HEV propulsion systems: A comparative study." *IEEE Trans. Veh. Technol.*, 55(6), 1756–1764.

Zhu, J., Cheng, K. W. E., and Xue, X. (2016). "Torque analysis for in-wheel switched reluctance motors with varied number of rotor poles," *Proc., ISEE 2016 - 2016 Int. Symp. Electr. Eng.*, Hong Kong, China, 1-5.

Zhu, J., Cheng, K. W. E., Xue, X., and Zou, Y. (2017b). "Design of a New Enhanced Torque In-Wheel Switched Reluctance Motor With Divided Teeth for Electric Vehicles." *IEEE Trans. Magn.*, 53(11), 1–4.

List of Publications based on Research work

Papers in Referred Journals

1. **Sandesh Bhaktha B**, Satish Kumawat, Jeyaraj Pitchaimani, K.V. Gangadharan, “Design and Performance Analysis of a Switched Reluctance Motor Using Finite Element Analysis and Magnetic Equivalent Circuit Model”, *Defence Science Journal* (2023), 73 (1): 29-40 [SCI], DOI: 10.14429/dsj.73.17828
2. **Sandesh Bhaktha B**, Neil Jose, Vamshik M, Jeyaraj Pitchaimani, K.V. Gangadharan, “Driving cycle-based design optimization and experimental verification of a Switched reluctance motor for an E-Rickshaw”, *IEEE Transactions on Transportation Electrification* (2024), (*Early Access*), Accepted on February 2024 [SCI], DOI: 10.1109/TTE.2024.3370401
3. **Sandesh Bhaktha B**, Gupta Rahul Ramnihor, Monika Sahu, Anil Jogi, Jeyaraj Pitchaimani, K.V. Gangadharan, “Comparative Assessment of a Novel 8/18 multi-teeth with conventional 8/10 in-wheel SRM for an E-Scooter”, *Automatika* (2024), 65 (3): 997-1012 [SCI], DOI: 10.1080/00051144.2024.2329492

Appendixes

Appendix I

This section contains the drawings for the child parts of the SRM assembly, such as the target plate, cover, shaft, insulator, and stud. All the dimensions are in millimeters. The angles are in degrees.

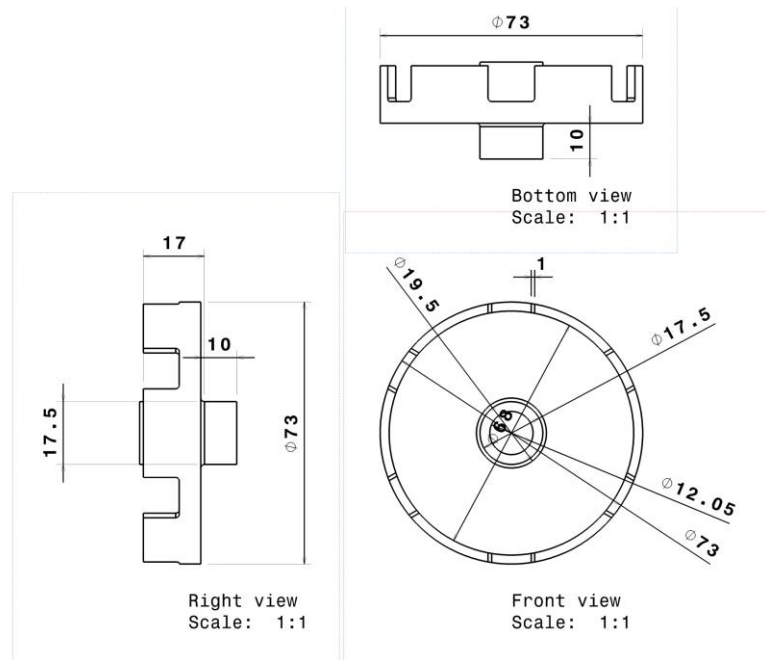


Figure 1. Target plate

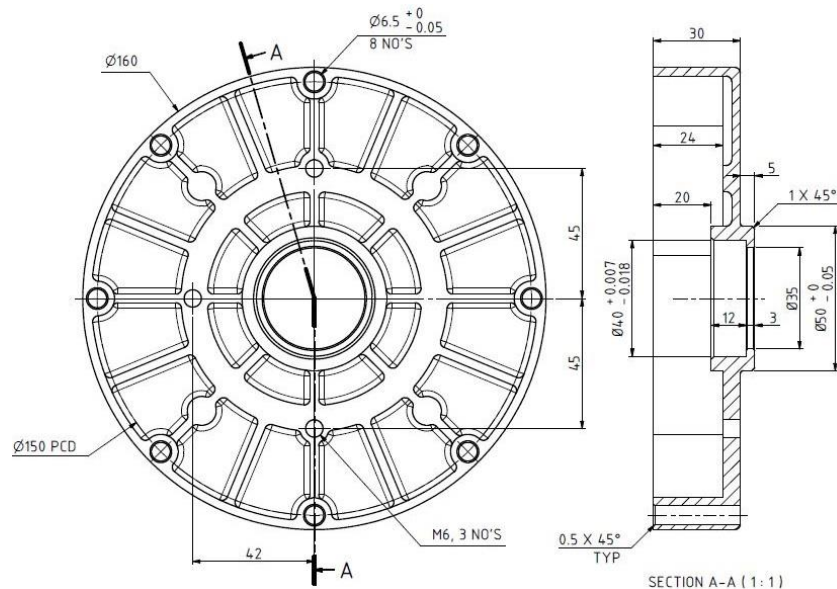


Figure 2. Cover

Appendix II

Dynamic performance of the 8/14 SRM and (b) 8/22 MT SRM configurations

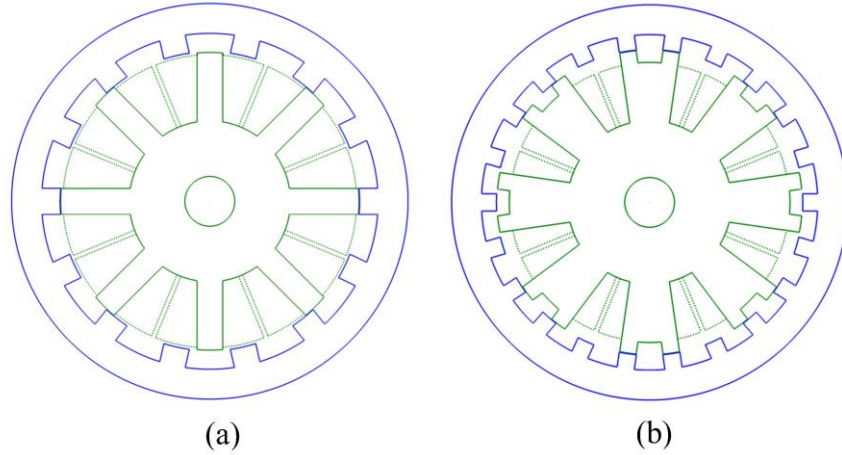


Figure 6. Initial designs of (a) 8/14 SRM and (b) 8/22 MT SRM configurations

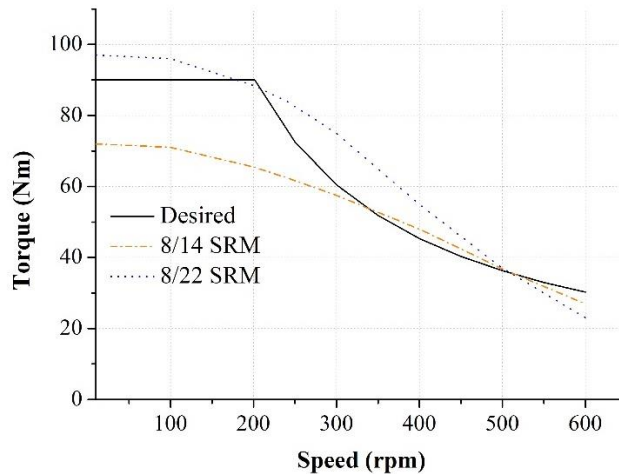


Figure 7. Influence of increase in rotor pole number on the dynamic torque

The initial designs of both the 8/14 and 8/22 MTSRM are shown (Figure 6). The number of turns per phase for both the design topologies was adjusted as per the methodology presented in Section 5.4.2 to meet the desired torque-speed performance envelope. However, from the graph (Figure 7), it is observed that the peak average torques at 200 rpm of both the 8/14 and 8/22 MTSRMs are lower than the desired value as they are prone to magnetic saturation in comparison to the 8/10 and 8/18 MTSRMs respectively.

Bio-Data

Name: Sandesh Bhaktha B
Date of birth: 27-09-1991
Marital status: Married
E-mail: sandesh.bhaktha@gmail.com
Mobile: +917838290497

Address:
“Sangeeth”, H. No. 4-127,
Sapthagiri Nagar, 4th Cross,
Manipal, Udupi district
Karnataka – 576104

Education

- M.Tech. in Manufacturing Engineering and Technology (2017)
Institute: Manipal Institute of Technology, Manipal
University: Manipal Academy of Higher Education (MAHE), Manipal
CGPA: 9.54
- B.E. in Mechanical Engineering (2013)
Institute: Manipal Institute of Technology, Manipal
University: Manipal Academy of Higher Education (MAHE), Manipal
CGPA: 8.02

